Tilting a ground-state reactivity landscape by vibrational strong coupling

Lucas Lethuillier-Karl

Université de Strasbourg

UNIVERSITÉ DE STRASBOURG

EDSC École Doctorale des Sciences Chimiques

ÉCOLE DOCTORALE DE CHIMIE (ED222)

UMR7006

THÈSE présentée par :

Lucas LETHUILLIER-KARL

soutenue le : **22 Novembre 2019**

pour obtenir le grade de : **Docteur de l'université de Strasbourg**

Discipline/ Spécialité : Chimie

TILTING A GROUND-STATE REACTIVITY LANDSCAPE BY VIBRATIONAL STRONG COUPLING

ÉTUDE DU BASCULEMENT DU PROFIL ÉNERGÉTIQUE D'UNE RÉACTION CHIMIQUE PAR COUPLAGE VIBRATIONNEL FORT POUR LE CONTRÔLE DE LA SÉLÉCTIVITE DE SITE

THÈSE dirigée par :

M. MORAN Joseph	Prof. Dr., ISIS, CNRS - Université de Strasbourg

RAPPORTEURS :

M. BERKESSEL Albrecht	Prof. Dr., Mathematisch-Naturwissenschaftliche Fakultät – Universität zu Köln
M. LAKHDAR Sami	Dr., LCMT, CNRS – Université de Caen

AUTRES MEMBRES DU JURY :

M. EBBESEN Thomas	Prof. Dr., ISIS, CNRS – Université de Strasbourg
M. JAVAHIRALY Nicolas	Dr., I-Cube, CNRS – Université de Strasbourg
M. SIEGEL Jay	Prof. Dr., Tianjin University

ACKNOLEDGMENT

First and foremost, I thank my supervisor Prof. Joseph Moran for giving me the opportunity to join his team. He believed in me when I just failed to get a doctoral scholarship from the French government and allowed me to work on two research projects that couldn't be more exciting and challenging.

I would also like to thank Professor Ebbesen, for letting me take part in the collaboration between our two teams. He was always available for discussion and very enthusiastic about my projects. I was fascinated by his approach to science and honoured to have been able to work in his research group.

I thank Prof. Albrecht Berkessel, Dr. Sami Lakhdar, Dr. Nicolas Javahiraly and Prof. Jay Siegel for accepting to participate in my thesis jury.

I now want to thank all my colleagues in both Prof. Moran and Prof. Ebbesen's teams for sharing these three years of hard work with me.

Starting with Anoop Thomas, who taught me everything I know about VSC, from both the technical and theoretical aspects. He lent me great moral support during hard times and helped me to remain positive and optimistic in all circumstances. Working with you has been an enriching human experience that I will never forget. Thank you for everything!

From Prof. Ebbesen's lab, I met other great people (and as many excellent scientists!) like Kalaivanan Nagarajan, Robrecht Vergauwe and Jérome Gautier (to name but a few) who always had a little word of encouragement, a short question to ask or help to give. This makes your laboratory a very pleasant place to work.

In Joseph Moran's laboratory, I initially worked with Kamila Muchowska, Sreejith Varma and Élodie Chevallot-Beroux on a very unique and original project: understanding the origin of life. Kamila and Sreejith, I was impressed by your scientific maturity and perseverance. Thank you for welcoming Elodie and me to the "prebiotic team" and for helping us take our first steps into the world of science.

I also thank all my other colleagues, past and present, who are still working in the lab. Abhijit Sau, who will now join me on the VSC project. I hope we will discover many new and interesting properties together! Anton Gudz, aka "The American Tornado" as effective in the lab as on a soccer pitch. Thank you for your energy and good mood. I'm sure I'll see you in a stadium or in front of a PS4! Edward Richmond, former post-doc who headed the

"catalysis team" with brio. I wish I had taken the time to get to know you a little better, but thanks for your advice and English humour! Florent Noel, always up for ~~one~~ beers. Thanks for helping me solve the mystery of the Rubik's cube. Jan Gorges, it was a pleasure to have you with us in the lab. I appreciated our discussions and your availability; you always had an advice or an idea to share. Thank you also for the beautiful Bismuth crystal that is now sitting on my desk! Jing Yi, thank you for introducing me to real Chinese tea. Paul Chatelain, aka "The Crook". Keep on delighting me with your travel stories and pretending that you always know what you're talking about (I'm ~~half~~ joking)! Shaofei Zhang, stay as you are, a humble and determined person. Thank you for the few words of Chinese you taught me and excuse me for my poor pronunciation. Welcome to the newcomers: Ankita Malik, David Leboeuf, Harprett Kaur, Robin Isnard and Sophia Rauscher. Thank you for helping me prepare for my defense; I look forward to getting to know you!

Je switch à partir de là en français et voudrais commencer par remercier trois collègues un peu particuliers.

Nathalie Monnin, secrétaire et gestionnaire au grand cœur, merci pour ta gentillesse et le soutien que tu nous as apporté à tous au labo. À bientôt pour les prochains 10 km de Strasbourg !

Vuk Vuković, mon plus ancien collègue, que j'ai connu en stage de M1. Merci pour ton aide précieuse, tes conseils et nos discussions très intéressantes. Tu as une rigueur et une culture scientifique qui font de toi un chimiste exceptionnel, et si tu changes de voie par la suite je te souhaite le meilleur. Peut être que l'on se recroisera dans quelques temps, qui sait…

Et enfin, Élodie Chevallot-Beroux, la meilleure collègue de thèse de l'histoire des doctorats ! Merci d'avoir été la moitié ponctuelle, prévoyante et consciencieuse de notre binôme. Tu as été à l'écoute de mes problèmes, au travail comme en dehors et un soutien sans faille dans tous les moments difficiles pendant 3 ans. Je n'en serais probablement pas là sans toi. Quelle aventure ! Difficile, mais à la fin, elle se termine plutôt bien, avec un diplôme, des souvenirs et surtout avec une amie. Je te souhaite de trouver la voie professionnelle qui te plaira et surtout le bonheur avec Boris et ta famille.

Un grand merci à ma famille, en particulier à ma mère qui m'a offert la meilleure éducation possible, à ma grand-mère qui est la personne la plus délicate et gentille que je connaisse et à mon père. Maman, je ne le dis jamais de vive voix, mais je n'aurais jamais rien pu accomplir sans tout le mal que tu t'es donnée pour moi depuis 26 ans maintenant.

J’espère que je te rends fier et heureuse à ma façon. J’ai une pensée pour mon grand-père et mon oncle que j’aurais aimé rendre fier également. Merci à Annie d’avoir été là pour ma soutenance de thèse.

Un mot pour remercier aussi mes amis qui m’ont permis de relâcher la pression en dehors du labo : Alix, Antonin, Rodrigue (que j’ai beaucoup embêté avec mes questions scientifiques parce que je le considère comme un excellent physicien avec énormément de bon sens et de logique), Sidney et Taoufik que je connais depuis l’enfance et qui m’accompagne depuis des années. C’est avec vous tous que j’ai faits les 400 coups comme on dit et avec les deux derniers, nous avons crée notre association de musique électronique, Underground Feelings, l’autre belle aventure de ces dernières années. Les amis rencontrés plus tardivement, Arnaud, Laurent, Thomas et Samuel ; avec qui je partage mes deux grandes passions que sont la musique et le football. Et mes potes de l’IUT de chimie : Cyrille, Loïc et Quentin ; c’est toujours un plaisir de délirer avec vous autour d’une bon repas équilibré à base de fromage bien gras. Vous êtes tous des personnes fascinantes et talentueuses que je respecte énormément !

Et pour finir Mathilde, mon amoureuse. Merci de m’avoir supporté pendant ce qui a probablement été la plus difficile année de ma (jeune) vie : la dernière année de ma thèse. Merci de m’avoir écouter parler le soir de tous ces problèmes techniques à dormir debout que je rencontrais au quotidien au labo. Tu me donnes une raison d’avancer et tu me ralentis dans mes excès. Tu me complète et fais partie de mon équilibre. J’espère devenir chaque jour une meilleure version de moi même pour toi. Notre vie ensemble ne fais que commencer mais je suis sur qu’elle sera pleine de beaux moments.

TABLE OF CONTENTS

RÉSUMÉ EN FRANCAIS

CHAPTER I

CHAPTER II

CHAPTER III

CHAPTER IV

CHAPTER IV

ANNEX & BIBLIOGRAPHY

LIST OF ABBREVIATIONS

Ag	silver
ap	antiperiplanar
ATR	attenuated total reflection
Au	gold
Bu_4NBr	tetra-*n*-butylammonium bromide
CCl_4	carbon tetrachloride
$CDCl_3$	deuterated chloroform
cQED	cavity quantum electrodynamics
DCM	dichloromethane
DMF	dimethylformamide
DPPA	diphenylphosphoryl azide
DFT	density functional theory
DTGS	deuterated triglycine sulfate
D_2O	deuterated water
EM	electromagnetic waves
ESC	electronic strong coupling
EtOAc	ethyl acetate
Eu	europium
FP	Fabry-Perot
FSR	free spectral range
FT-IR	Fourier transform infrared spectroscopy
FWHM	full width at half maximum
GC	gas-chromatography
GC-MS	gas-chromatography coupled with mass spectrometry
HFIP	1,1,1,3,3,3-hexafluoroisopropan-2-ol
HOMO	highest occupied molecular orbital
H_2O	water
H_2O_2	hydrogen peroxide
i-PrOH	isopropanol

I.S.	internal standard
IR	infrared
KIE	kinetic isotope effect
KSIE	kinetic solvent isotope effect
LUMO	lowest unoccupied molecular orbital
M	molar
MC	merocyanine
MCT	mercury cadmium telluride
min	minutes
mmol	millimole
MeOH	methanol
mg	milligram
MHz	megahertz
mL	milliliter
mM	millimolar
MnO_2	manganese dioxide
Na_2SO_4	sodium sulfate
NH_4Cl	ammonium chloride
nm	nanometer
NMR	nuclear magnetic resonance
OCN^-	cyanate Ions
O_2	dioxygen
$(OH)_{str.}$	O-H stretching mode
p-TsOH	*para*-toluenesulfonic acid
PET	polyethylene terephthalate
PMMA	poly(methyl methacrylate)
ppm	parts per million
PTA	1-phenyl-2-trimethylsilylacetylene
PVA	poly(vinylalcohol)
QED	quantum electrodynamics
QFT	quantum field theory
qNMR	quantitative nuclear magnetic resonance

RRF	relative response factor
sc	synclinal
SiO_2	silicon dioxide
SPI	1’,3’-dihydro-1’,3’,3’-trimethyl-6-nitrospiro[2H-1-benzopyran-2,2’-(2H)-indole]
TBAF	tetra-*n*-butylammonium fluoride
TBDMS	*tert*-butyldimethylsilyl
TFE	2,2,2-trifluoroethanol
THF	tetrahydrofuran
TIPS	triisopropylsilyl
TMS	trimethylsilyl
TS	transition state
UV	ultraviolet
VSC	vibrational strong coupling
V-USC	vibrational ultra strong coupling
ZPE	zero-point energy
ZnSe	zinc selenide
µL	microliter
µm	micrometer

RÉSUMÉ EN FRANÇAIS

I. INTRODUCTION GENERALE SUR LES INTERACTIONS LUMIERES-MATIERE

La nature de la lumière et des phénomènes qui lui sont associés est l'objet de recherches intellectuelles et scientifiques depuis l'Antiquité. De nos jours, la lumière est considérée comme étant composée de particules appelées photons - qui peuvent être comptées - et se comportant comme une onde électromagnétique (EM) - qui peut interférer - dans certaines conditions. Il est intéressant de noter que, très tôt, notre compréhension de la lumière est inextricablement liée à celle de son milieu de propagation. Par exemple, la vitesse de la lumière dans le vide est une constante universelle. Le terme "vide" est généralement utilisé dans un contexte scientifique pour décrire un espace créé par l'absence partielle ou totale de matière. Mais lorsqu'il a été démontré grâce à la physique quantique que même le vide n'était pas "rien", des modifications de plusieurs propriétés de la matière ont été réalisées, simplement en contrôlant son environnement. Le cœur de mon manuscrit porte sur le couplage vibrationnel fort (VSC). Il s'agit d'une nouvelle approche exploitant les interactions lumière-matière, que nous avons utilisée pour contrôler le déroulement et l'issue de réactions chimiques, en structurant le champ EM à l'intérieur de cavités optiques.[1,2] Depuis ses premiers développements en physique des atomes froids dans les années 1980[3], le régime de couplage fort, atteint en électrodynamique quantique de cavité (cQED) est devenu un nouvel outil scientifique offrant un contrôle sans précédent de la matière par la lumière et de la lumière par la matière[4]. Bien que le comportement de molécules en cQED ait été principalement étudié sous couplage électronique fort (ESC)[5], le couplage vibrationnel fort (VSC) présente également un fort potentiel[6–9]. En effet, l'hybridation des fluctuations quantiques du vide d'un mode de cavité optique et d'une molécule organique aboutit à la formation de deux nouveaux états vibro-polaritonique **(Figure 1, P+ et P-)**.

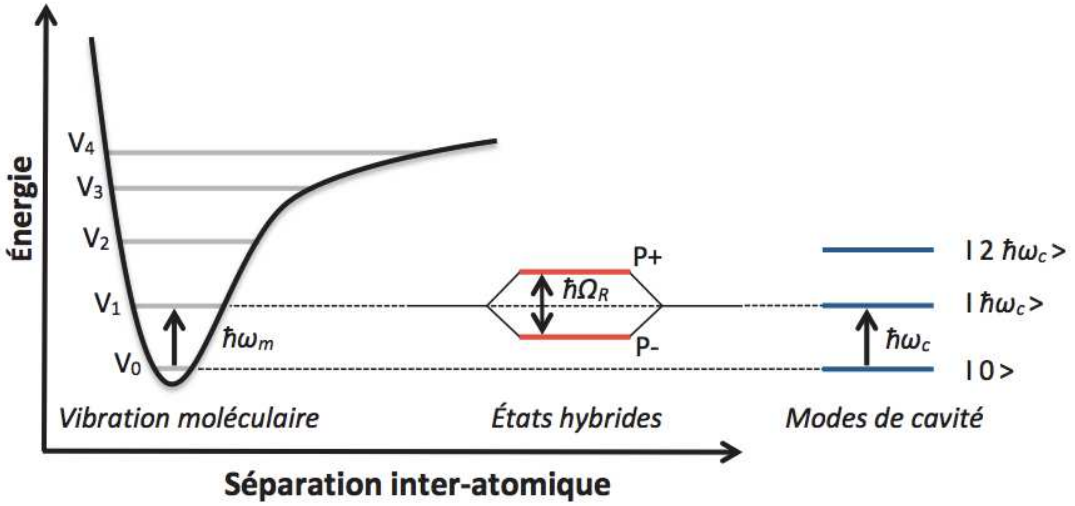

Figure 1. Illustration schématique du couplage lumière-matière entre une transition de vibration moléculaire et un mode de cavité aboutissant à la formation des états vibro-polaritoniques P+ et P- séparés par l'énergie de Rabi notée $\hbar\Omega_R$.

En 2016, une collaboration entre les groupes du professeur Ebessen et du professeur Moran a permis de montrer que le profil énergétique de la réaction de déprotection du 1-phenyl-2-trimethylsilylacetylene (PTA) par le fluorure de tetra-*n*-butylammonium (TBAF) **(Figure 2)** était différent dans une cavité optique résonante avec la vibration d'élongation de la liaison Si-C du PTA, ceci ayant pour conséquence une diminution de la vitesse de réaction d'un facteur 5,5.[1]

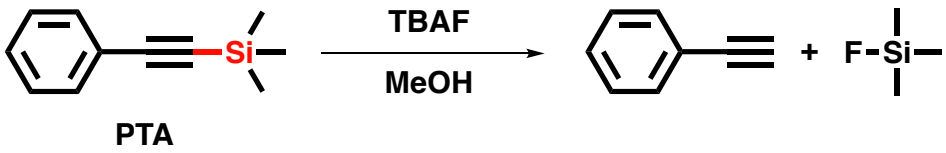

Figure 2. La réaction de déprotection du 1-phenyl-2-trimethylsilylacetylene (PTA) par le tetra-n-butylammonium fluoride (TBAF).

Les travaux présentés dans le deuxième chapitre de ce manuscrit de thèse constituent une preuve de concept montrant que le VSC offre la possibilité de faire basculer le profil énergétique d'une réaction chimique pour en contrôler la sélectivité de site. Le troisième chapitre fait état de travaux en cours, et dont les résultats préliminaires semblent indiquer une accélération de la vitesse de réaction étudiée sous VSC.

II. BASCULEMENT DU PAYSAGE REACTONNEL PAR VSC A L'ETAT FONDAMENTAL

II.1. INTRODUCTION

Ces dernières années, de nombreuses méthodes ont été développées par les chimistes pour la mise en œuvre de réactions chimio-, régio- ou stéréo-sélectives. Ces méthodes impliquent généralement des séquences réactionnelles basées sur des stratégies de protections-déprotections et/ou sur des fonctionnalisations souvent fastidieuses. Divers catalyseurs et réactifs ont été développés dans ce but mais ils permettent uniquement de différencier quelques groupements fonctionnels avec des différences stériques et électroniques très prononcées. Ici, nous avons tenté d'influencer la sélectivité de site d'une réaction par une approche tout à fait différente : le VSC entre une molécule organique et les fluctuations quantiques du vide à l'intérieur d'une cavité optique micro-fluidique. Pour explorer cette possibilité nous avons choisi de synthétiser le dérivé silane, *tert*-butyldimethyl{[4-(trimethylsilyl)but-3-yn-1-yl]oxy}silane **(R)**[10,11], comportant deux groupes silyles pouvant être retiré ultérieurement par réaction chimique. L'attaque nucléophile d'un des deux atomes de silicium par un ion fluorure aboutit respectivement à la formation du produit **(1)** après rupture de la liaison Si-C ou du produit **(2)** après rupture de la liaison Si-O **(Figure 3)**.

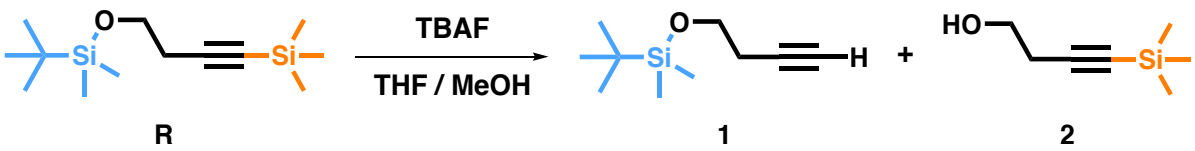

Figure 3. Les deux réactions de rupture de liaison silyles possibles (rupture de la liaison Si-C pour former **(1)**, rupture de la liaison Si-O scission pour former **(2)**) pour la réaction entre **(R)** et le TBAF à température ambiante dans un mélange de méthanol et de THF.

Les deux produits se forment via des voies mécanistiques similaires. Nous avons dans un premier temps cherché à savoir si le couplage fort sélectif des modes vibrationnels respectivement associés aux liaisons Si-C et Si-O avait une influence différente sur la réactivité. Dans un deuxième temps, et il s'agit là du point le plus important de cette étude,

nous avons vérifié que la modification du profil énergétique réactionnel par VSC pouvait permettre d'inverser le rapport de distribution des produits.

II.2. MATERIEL ET METHODES

La cavité optique utilisée dans les expériences réalisées ici est une cavité Fabry-Pérot (FP) formée de deux miroirs métalliques en or (Au) recouvert de séléniure de zinc (ZnSe) parallèles et séparés par une entretoise en poly(téréphtalate d'éthylène) (PET – Mylar ®) d'épaisseurs variables (6 à 8 mm) avec un canal central creux conçu pour l'injection d'échantillons liquides.[12] Pour s'assurer que les réactions ne soient pas affectées par la présence d'Au ou de ZnSe, une couche de verre (SiO_2) de 200nm d'épaisseur a été déposée sur la surface interne de chaque miroir. Le milieu réactionnel était constitué d'une solution homogène de réactif de départ **(R)** (0.90M) et de TBAF (0.86 M) dans un mélange 1:1 (v/v) de méthanol (MeOH) et de tétrahydrofurane (THF). Ces conditions ont été optimisées pour le couplage fort en maximisant la concentration de **(R)** pour atteindre l'énergie de séparation de Rabi $\hbar\Omega_R$ la plus élevée possible tout en conservant une bonne solubilité de **(R)** dans le système de solvants. Pour atteindre le régime de VSC, il est nécessaire d'avoir un mode de cavité en résonance avec une transition infra-rouge (IR) spécifique de **(R)**. Le spectre IR de **(R)** dans le mélange MeOH/THF a été enregistré hors cavité **(Figure 4)** et montre les bandes intenses caractéristiques des liaisons Si-C (842 cm^{-1}), Si–O (1110 cm^{-1}) et Si-CH_3 (1250 cm^{-1}) correspondant à leurs modes d'élongation (Si-C et SiO) et de torsion (Si-CH_3).

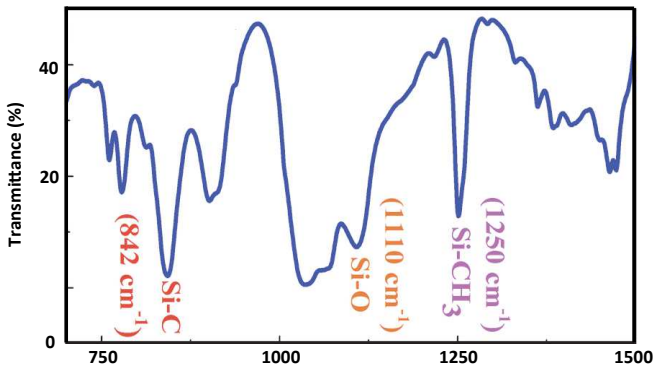

Figure 4. Spectre IR de **(R)** dans le mélange MeOH/THF, enregistré dans une cellule constituée de deux fenêtres en ZnSe recouvertes par du verre (SiO_2) et séparée par une entretoise de même épaisseur que pour la cavité Fabry-Pérot.

II.3. INFLUENCE DU VSC ENTRE UN MODE DE CAVITE ET DES VIBRATIONS DE LIAISONS QUI SONT ROMPUES LORS DU MECANISME REACTIONNEL

II.3.1. SUIVI CINETIQUE DES REACTIONS PAR SPECTROSCOPIE IR

L'évolution cinétique de la réaction a été suivie par spectroscopie IR. La vitesse globale des réactions de rupture des deux groupements silyles ayant lieu parallèlement a été quantitativement déterminée sous l'influence du VSC à partir du tracé logarithmique du décalage temporel d'un des modes de cavité d'ordre élevé (de $\bar{\nu}_0$ à $\bar{\nu}_t$). Lorsque la vibration d'élongation de la liaison Si-C est fortement couplée à un mode de cavité **(Figure 5, losanges rouges)**, la vitesse de réaction diminue d'un facteur 3,5 ± 0,2 par rapport aux mesures de contrôle effectuées hors cavité **(Figure 5, triangles bleus)** ou dans une cavité non-résonante qui n'est accordée à aucune des transitions vibratoires sélectionnées de **(R) (Figure 5, carrés verts)**. De même, le couplage fort de la vibration d'élongation de la liaison Si-O à un mode de cavité **(Figure 5, cercles orange)** donne lieu à un ralentissement de la vitesse globale de réaction d'un facteur de 2,5 ± 0,1 par rapport aux mesures faites hors cavité ou dans une cavité non-résonante.

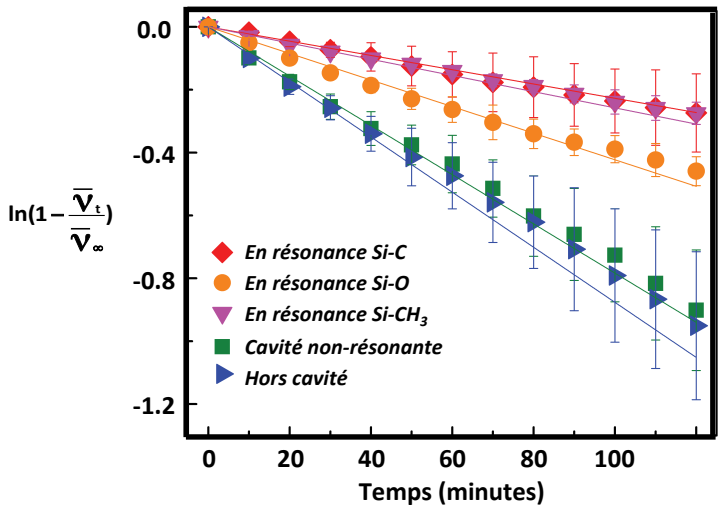

Figure 5. Données cinétiques de la réaction effectuée dans des cavités résonantes avec les modes de vibrations : d'élongation de la liaison Si-C (carrés rouges), d'élongation de la liaison Si-O (cercles oranges) et de torsion de la liaison Si-CH_3 (triangles roses) ainsi que dans une cavité non-résonante (carrés verts) et hors cavité (triangles bleus). Les marges d'erreur ont été déterminées à partir de l'écart-type d'au moins cinq expériences.

II.3.2. QUANTIFICATION DES PRODUITS (1) ET (2) PAR GC-MS

Après chaque expérience, le milieu réactionnel a été analysé quantitativement par chromatographie en phase gazeuse couplée à la spectrométrie de masse (GC-MS) afin de déterminer le rapport des concentrations [**1**]:[**2**] où [**1**] correspond à la quantité de produit **(1)** obtenue par rupture de la liaison Si-C et [**2**] à la quantité de produit **(2)** obtenue de rupture de la liaison Si-O. Pour les réactions effectuées hors cavité et dans une cavité non-résonante, les rapports de concentrations sont équivalents et indiquent que le produit **(1)** est formé majoritairement ([**1**]:[**2**] de 1,5 ± 0,2 et 1,4 ± 0.1 respectivement) **(Tableau 1, ligne bleue et verte)**. Une augmentation significative de la formation de produit **(2)** a été observée quand la vibration d'élongation de la liaison Si-C est fortement couplée à un mode de cavité, changeant ainsi complètement le rapport de distribution des produits [**1**]:[**2**] (0,3 ± 0,1) **(Tableau 1, ligne rouge)**. Un rapport de distribution des produits plus élevé (0,4 ± 0,1) a été observé quand la vibration d'élongation de la liaison Si-O est fortement couplée **(Tableau 1, ligne orange)**. Ainsi, le VSC de l'un ou l'autre des sites réactionnels directement impliqués dans la rupture des liaisons Si-C ou Si-O modifie le profil énergétique réactionnel de façon à favoriser la rupture de la liaison Si-O plutôt que la rupture de la liaison Si-C qui est normalement cinétiquement favorisée.

Tableau 1. Rapport de distribution des produits **(1)** et **(2)** obtenus par analyse GC-MS après réaction dans des cavités résonantes avec les modes de vibrations : d'élongation de la liaison Si-C (ligne rouge), d'élongation de la liaison Si-O (ligne orange) et de torsion de la liaison Si-CH_3 (ligne rose) ainsi que dans une cavité non-résonante (ligne verte) et hors cavité (ligne bleue). Les marges d'erreur ont été déterminées à partir de l'écart-type d'au moins cinq expériences.

Type d'expérience	Bande IR	Rapport de distribution des produits $\frac{[1]}{[2]}$
Hors cavité		1.5 ± 0.2
Hors résonance		1.4 ± 0.1
Cavité résonante	Si-C (842 cm^{-1})	0.3 ± 0.1
	Si-O (1110 cm^{-1})	0.4 ± 0.1
	Si-CH_3 (1250 cm^{-1})	0.3 ± 0.1

II.4. INFLUENCE DU VSC ENTRE UN MODE DE CAVITE ET DES VIBRATIONS « SPECTATRICES »

Les vibrations qui ne sont pas directement impliquées dans le mécanisme réactionnel peuvent également jouer un rôle essentiel dans l'issue d'une réaction.[13,14] Dans le cas présent, la forte bande d'absorption à 1250 cm^{-1} correspondant aux modes de torsion des groupes -CH_3 liés à l'atome de silicium[15], peut être considérée comme une vibration « spectatrice ». S'il s'agissait d'un groupe -CH_3 isolé, on pourrait s'attendre à observer cette bande d'absorption vers 1460 cm^{-1}. Son apparition à 1250 cm^{-1} indique qu'il interagit en réalité avec d'autres vibrations associées à l'atome de silicium. Le VSC de la vibration à 1250 cm^{-1} réduit la vitesse globale de réaction d'un facteur de 3,5 ± 0,1 **(Figure 5, triangles rose)** et donne un rapport de distribution des produits [**1**]:[**2**] de 0,3 ± 0,1 **(Tableau 1, ligne rose)**, ce qui est très proche des résultats obtenus sous VSC de la transition correspondant à la vibration d'élongation Si-C.

II.5. ACCES AUX CONSTANTES DE VITESSES INDIVIDUELLES DE FORMATION DES PRODUITS (1) ET (2)

Nous avons complété ces expériences en mesurant la constante de vitesse de réaction globale observée (k_{obs}) en fonction du réglage de la cavité tout le long du spectre IR de **(R)** pour obtenir un spectre d'action **(Figure 6)** qui confirme clairement quels modes vibrationnels influencent la réaction sous VSC.

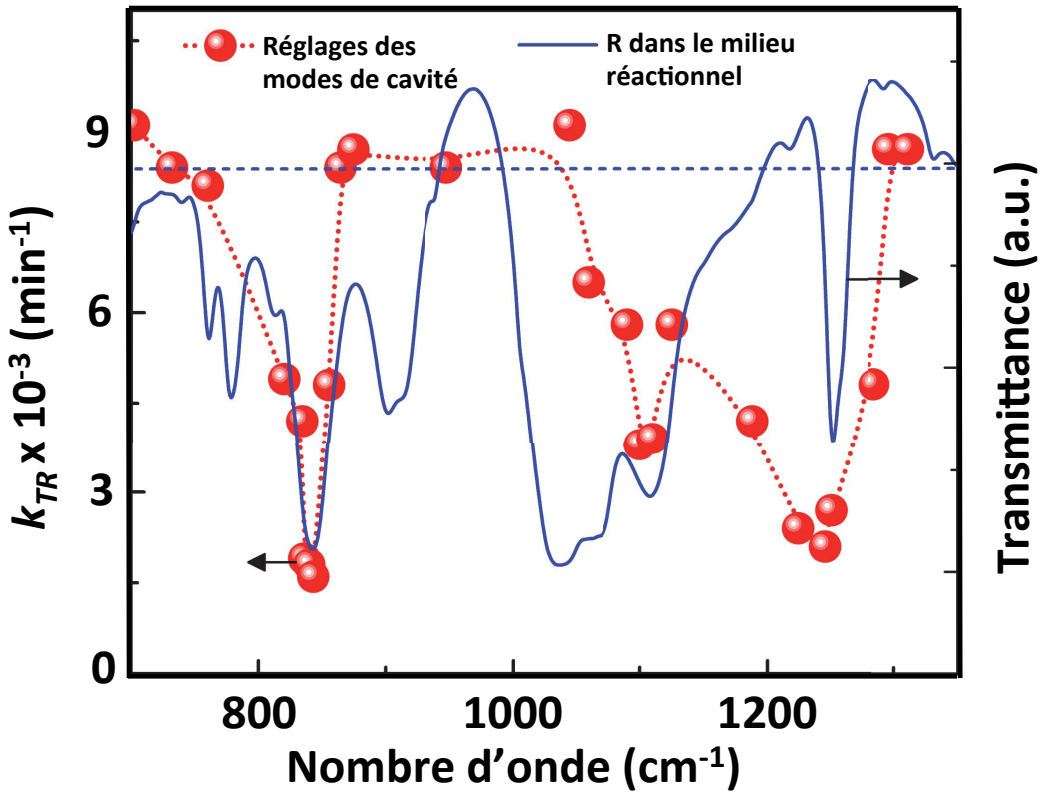

Figure 6. La vitesse globale de réaction à l'intérieur de la cavité varie en fonction des réglages de modes de cavités (sphères rouges). La ligne bleue pleine montre le spectre d'absorption IR de **(R)** dans le milieu réactionnel. La ligne en pointillé rouge qui connecte les sphères entre elles sert de guide pour les yeux. La ligne en tirets bleue représente la vitesse moyenne de la réaction en dehors de la cavité.

En combinant la constante de vitesse de réaction globale observée (k_{obs}) et les rapports de distribution des produits [**1**]:[**2**] obtenus par les mesures de GC-MS, nous avons pu extraire les constantes de vitesse individuelles k_1 et k_2 correspondant aux ruptures des liaisons Si-C et Si-O, respectivement. A partir de ces données, les rendements (ϕ) respectifs des produits **(1)** et **(2)** ont été calculés après diverses expériences en et hors régime de VSC **(Figure 7)**.

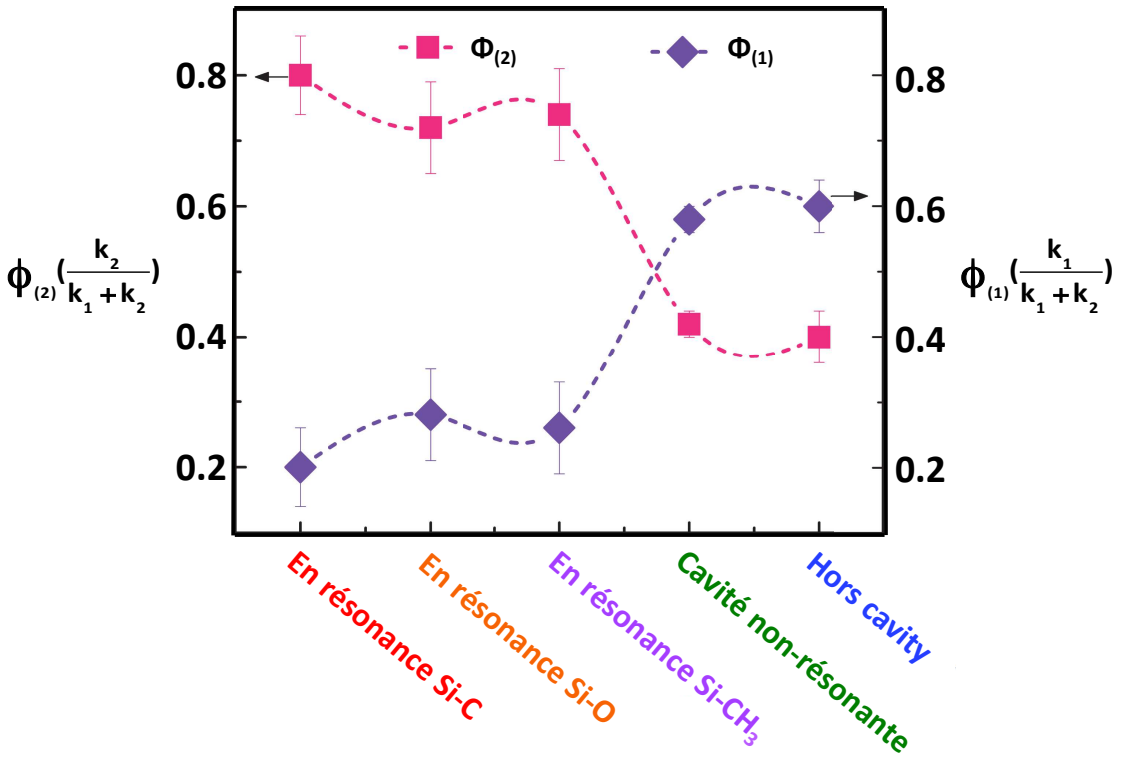

Figure 7. Graphique montrant le rendement du produit **(1)** (ϕ_1, losange violets) et **(2)** (ϕ_2, carrés rose) en régime de VSC de différents modes de vibrations de **(R)**, ainsi que dans une cavité non-résonante et hors cavité. Les marges d'erreur ont été déterminées à partir de l'écart-type d'au moins cinq expériences.

En dehors de la cavité et dans une cavité non-résonante, k_1 est supérieure à k_2, entraînant la formation préférentielle du produit **(1)** (**Figure 7**, losanges violets) alors que le VSC inverse la sélectivité, conduisant à une formation majoritaire du produit **(2)** (**Figure 7**, carrés roses). Il s'agit d'une preuve de principe directe montrant que le profil énergétique réactionnel peut être basculé sous l'action du VSC en ciblant trois modes vibratoires associés aux deux centres réactionnel formés par le deux atomes de silicium. Les valeurs de k_1 et de k_2 dans des conditions de couplage fort sont inférieures à celles observées hors cavité, ce qui indique une énergie d'activation plus élevée pour la réaction sous VSC.

II.6. ETUDES THERMODYNAMIQUES

Les paramètres thermodynamiques ont été déterminés pour chacune des deux réactions de rupture de liaison conduisant à la formation des produits **(1)** et **(2)** en mesurant leurs vitesses en fonction de la température hors cavité et dans les conditions de VSC des vibrations d'élongations des liaisons Si-C et Si-O. En utilisant la théorie de l'état de transition, l'énergie libre d'activation ($\Delta H^{\ddagger}$) et l'entropie d'activation ($\Delta S^{\ddagger}$) ont été déterminées. Les résultats résumés dans le **Tableau 2** indiquent que les paramètres thermodynamiques sont sensiblement modifiés dans le cadre du VSC pour les deux produits, mais conduisent à des valeurs différentes pour les produits **(1)** et **(2)**.

Tableau 2. Enthalpie et entropie d'activation en régime de couplage fort

Produits	Type d'expérience	$\Delta H^{\ddagger}$ (kJ.mol-1)	$\Delta S^{\ddagger}$ (kJ.mol-1)
(1)	Hors cavité	**34** ± 3	**-173** ± 11
	En résonance Si-C	**60** ± 2	**-95** ± 7
	En résonance Si-O	**57** ± 5	**-106** ± 17
(2)	Hors cavité	**23** ± 3	**-214** ± 8
	En résonance Si-C	**85** ± 5	**-6** ± 17
	En résonance Si-O	**76** ± 7	**-39** ± 24

Ce qui est surprenant, c'est que les nouvelles valeurs de $\Delta H^{\ddagger}$ et $\Delta S^{\ddagger}$ semblent être similaires, que l'on couple la vibration d'élongation de la liaison Si-C ou celle de la liaison Si-O. Cela pourrait être totalement fortuit pour la molécule choisie pour cette étude. Il a été montré dans la littérature que la présence de groupes partants éloignés les uns des autres pouvait modifier les vitesses de désilylation.[16]

L'élévation de la barrière d'activation pour la réaction de rupture des liaisons Si-C et Si-O sous régime de VSC est une des observations très intéressantes qui a été faite jusqu'à présent. Nous savions que le départ d'un groupement silyl induit par l'ion fluorure se fait par un mécanisme associatif *via* un intermédiaire pentacoordonné[17] et nous nous attendions donc à avoir un état de transition très encombré avec un $\Delta S^{\ddagger}$ très négatif, comme c'est le cas

pour la réaction hors de la cavité. La forte augmentation de $\Delta S^{\ddagger}$ vers une valeur se rapprochant de 0 sous régime de VSC implique que l'état de transition est modifié, en particulier celui qui conduit au produit **(2)**. Un $\Delta H^{\ddagger}$ élevé et un $\Delta S^{\ddagger}$ « moins négatif » indiquent que la structure des états de transitions sont probablement plus proche de celles des produits **(1)** et **(2)** que de celle du réactif de départ **(R)**, comme dans le cas des processus réactionnels à barrières retardées. Des études expérimentales et théoriques plus poussées sont nécessaires afin de pouvoir mieux comprendre, et généraliser, les effets du VSC sur différents types de réactions.

III. CATALYSE EN CAVITE PAR VSC DU SOLVANT

III.1. INTRODUCTION

Au cours de ma thèse, j'ai étudié le cas de systèmes chimiques dont la vitesse réactionnelle se voyait diminuée sous VSC. Les résultats présentés dans le **chapitre II** constituent une preuve de principe qui montre que le VSC peut même être utilisé pour modifier la sélectivité de site d'une réaction, devenant ainsi un outil très intéressant pour la chimie. Cependant, il n'en demeure pas moins que les chimistes cherchent la plupart du temps à optimiser les réactions chimiques en accélérant leur vitesse plutôt qu'en les diminuant.

Une récente étude sur la solvolyse de l'acétate de *p*-nitrophényle a permis de montrer qu'en fonction du paysage réactionnel, les vitesses réactionnelles pourraient aussi bien être accélérées sous VSC.[18] Dans ce cas précis, une accélération d'un ordre de grandeur a été observée après couplage coopératif des modes d'élongations de la liaison C=O du réactif et du solvant, démontrant ainsi que le VSC pouvait être transféré du solvant au soluté tant qu'au moins une de leur fréquences vibrationnelles correspondent et se superposent. De plus, des accélérations de la vitesse de réaction allant jusqu'à l'ordre de 10^4 ont été mesurées dans des expériences où l'eau (H_2O) agit aussi bien en tant que réactif qu'en tant que solvant pour l'hydrolyse d'ions cyanate (OCN^-).[19] Dans cette étude, le mode d'élongation de la liaison OH de H_2O a été hybridé à un mode de la cavité FP, entraînant une énergie de séparation de Rabi $\hbar\Omega_R$ de 92 meV. Cette valeur exceptionnellement élevée correspond au régime de couplage vibrationnel ultra-fort (V-USC).

Néanmoins, compte tenu de la myriade de réactions chimiques et de leur nature diverse, il est nécessaire de comparer davantage d'exemples de différents types de réactions sous VSC et/ou V-USC afin de comprendre dans quelle mesure la catalyse par cavité peut être réalisée. Il serait par exemple intéressant de vérifier si la catalyse en cavité peut être réalisée par VSC du solvant seul. Dans cette perspective, et compte tenu de l'intérêt de l'équipe du Prof. Joseph Moran pour les effets de solvant observés avec le 1,1,1,3,3,3,3-hexafluoroisopropan-2-ol (HFIP), j'ai décidé d'étudier ce dernier dans le cadre du VSC.

III.2. EPOXYDATION DU *CIS*-CYCLOOCTENE (R2) DANS LE HFIP ET SOUS REGIME DE VSC

Le HFIP a été très souvent utilisé comme solvant permettant l'activation de H_2O_2 pour l'époxydation des oléfines avec[20] or sans[21] la présence d'un catalyseur métallique. J'ai décidé d'étudier l'époxydation du *cis*-cyclooctène en oxyde de cyclooctène, catalysée par HFIP avec H_2O_2 **(Figure 8)**, sous régime de VSC pour plusieurs raisons. Tout d'abord, cette réaction purement organo-catalytique est bien connue puisqu'elle a été étudiée en profondeur sur le plan cinétique et théorique par Berkessel *et al.* qui ont élucidé son mécanisme, soulignant ainsi le rôle catalytique clé du HFIP.[22,23] Lors de ces travaux, les auteurs ont conclu que la réaction d'époxydation se produisait dans une sphère de coordination comprenant environ 12 molécules de HFIP, expliquant ainsi la hausse considérable de la vitesse de réaction à haute concentration ($n_{HFIP}/n_{Total} \geq 0,5$). De plus, une article plus récent indique aussi que le schéma de solvatation lui-même joue un rôle crucial dans le processus réactionnel.[24] Cette particularité nous a semblé particulièrement intéressante compte tenu de la propriété des états collectifs du VSC. Ensuite, la réaction devrait pouvoir être étudiée sans problème à l'intérieur d'une cavité de FP, car elle se produit à température ambiante. Et enfin, le cis-cyclooctène étant disponible à l'achat, aucune synthèse fastidieuse n'est nécessaire pour la préparation du réactif de départ.

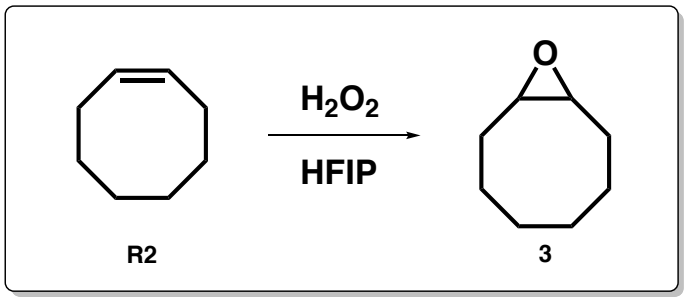

Figure 8. Époxydation du *cis*-cyclooctène **(R2)** par H_2O_2 dans HFIP

III.2.1.CHARACTERISATION IR DU MODE D'ETIREMENT O-H DU HFIP

Avant d'effectuer la moindre réaction catalysée par HFIP sous VSC, il a fallut élucider le spectre IR du HFIP **(Figure 9)**. La discussion portera sur la région des hautes fréquences (3000-3700 cm^{-1}) où l'on s'attend à trouver la bande d'absorption correspondant au mode d'étirement O-H du HFIP.

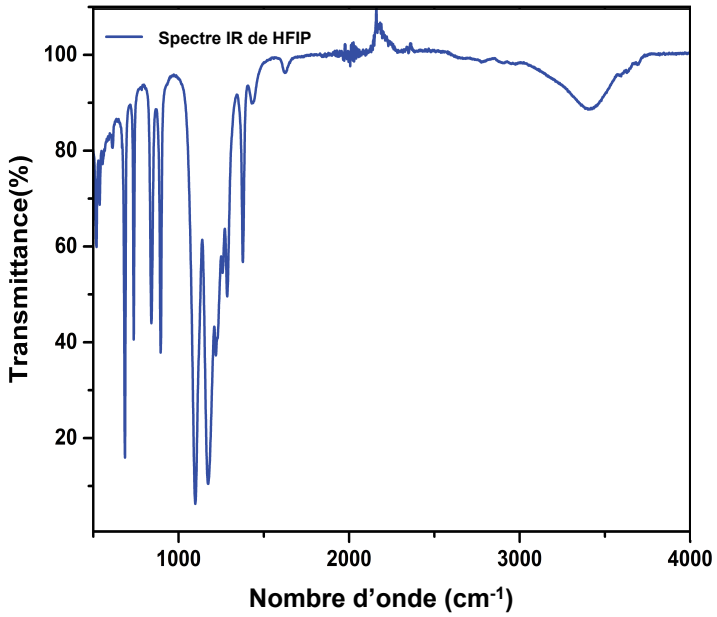

Figure 9. Spectre IR du HFIP mesuré avec un spectromètre ATR-IR. Le mode d'étirement O-H apparaît à 3400 cm^{-1}

Il est intéressant de souligner ici que l'angle α entre les deux atomes d'hydrogène du monomère HFIP définit ses différentes conformations. Ces dernières ont une influence sur sa capacité à donner des liaisons hydrogène **(Figure 10)**.[23]

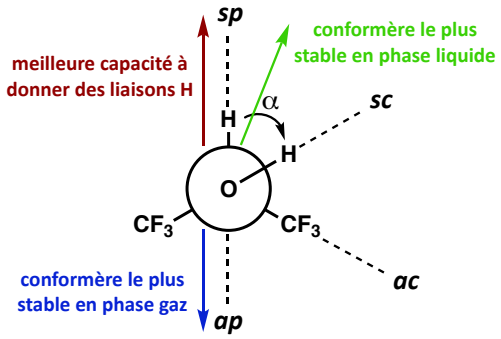

Figure 10. Dépendance des propriétés du HFIP dans sa forme monomérique par rapport à l'angle α entre les deux atomes d'hydrogène. Adapté de la référence 23.

Plusieurs études ont révélé la présence de deux bandes d'absorption bien séparées dans la région des hautes fréquences du spectre IR du HFIP, lorsqu'elles sont mesurées en phase vapeur ou en solution dans le tétrachlorure de carbone (CCl_4), ce qui permet d'analyser ce dernier sous sa forme monomèrique. Ces deux bandes d'absorption correspondent au mode d'étirement O-H des conformères synclinal (±sc) et antipériplanaire (ap) du HFIP. En solution dans CCl_4, la bande IR issue de l'étirement de la liaison O-H a une fréquence plus basse et une intensité un peu plus faible dans la conformation ap que dans la conformation sc (**Figure 11**). [25–27]

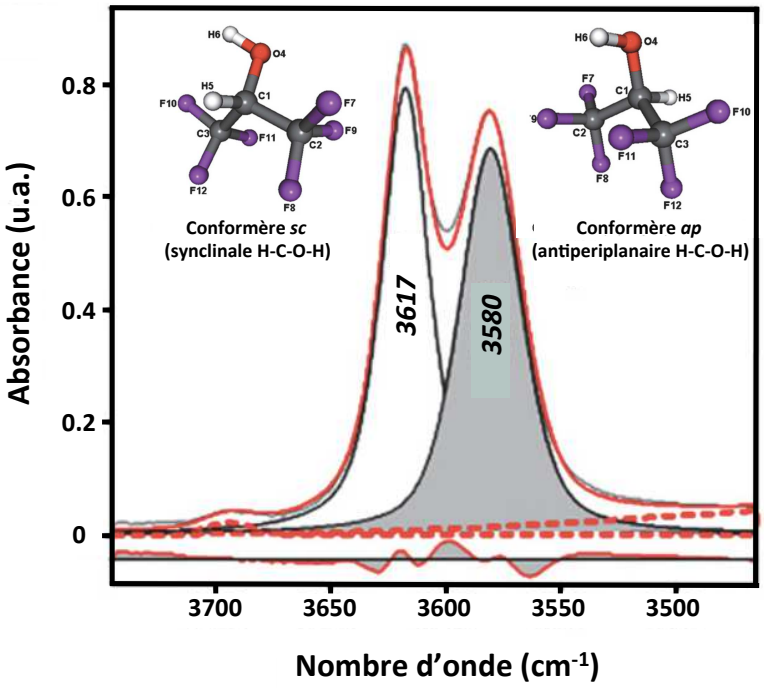

Figure 11. Région des hautes fréquences du spectre IR d'une solution de HFIP à 0.1M dans CCl_4, montrant les bandes d'élongation des liaison O-H de différents conformères du HFIP. La bande assignée au conformère ap est ombrée en gris. Les structures des conformères ap et sc du HFIP sont illustrées dans l'encadré. Adapté de la référence 25.

En mesurant le spectre IR d'une solution de HFIP à 0.1M dans CCl_4 **(Figure 12A)** et en le comparant à celui obtenu avec du HFIP pur **(Figure 12B)**, on peut voir que les deux bandes correspondant aux conformères *ap* et *sc* du HFIP sont clairement visibles lorsqu'elles sont enregistrées en solution dans le CCl_4, alors que dans le HFIP pur, elles apparaissent comme de petits épaulements à peine visibles. Dans ce dernier cas, la bande d'absorption large et décalée vers les fréquences basses est attribuée au mode d'étirement des liaisons O-H des agrégats de HFIP.

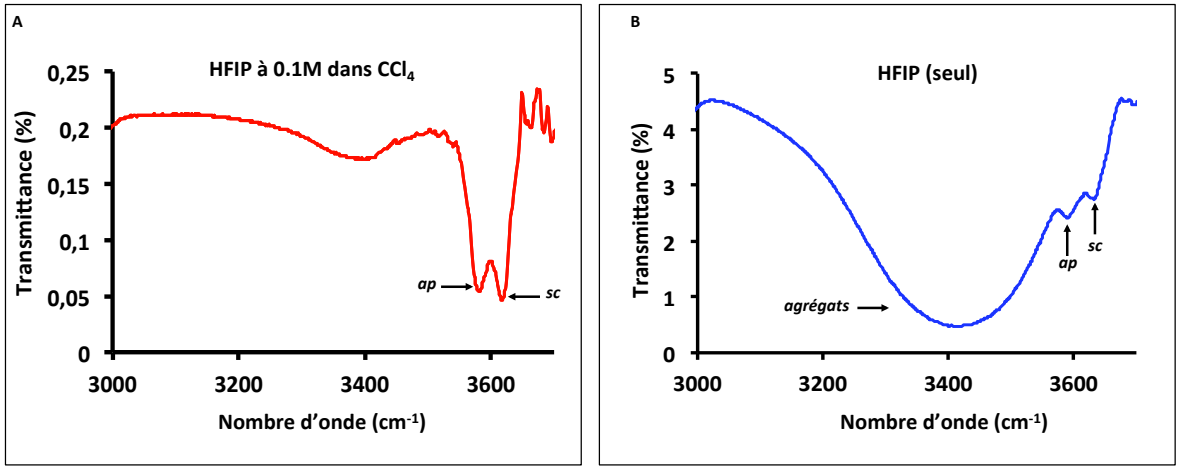

Figure 12. Région des hautes fréquences du spectre IR d'une solution de HFIP à 0.1M dans CCl_4 **(A)** et d'une solution de HFIP pure **(B)**.

III.2.2.EXPERIENCES ET ANALYSES QUANTITATIVES PAR GC-MS

Le mode d'étirement des liaisons O-H des agrégats de HFIP a été fortement couplé à un mode de cavité FP **(Figure 13A)**. Les deux nouvelles bandes correspondant aux états polaritoniques P+ et P- sont mises en évidence sur le spectre IR du HFIP à l'intérieur d'une cavité accordée à 3389 cm^{-1} **(Figure 13B)**. L'énergie de séparation de Rabi $\hbar\Omega_R$ de 225 cm^{-1} qui a été observée montre que le HFIP répond aux critères de couplage fort car $\hbar\Omega_R$ est plus élevée que la largeur à mi-hauteur (FWHM) du mode cavité (34 cm^{-1}) et de la bande correspondant au mode d'élongation de la liaison O-H (206 cm^{-1}).

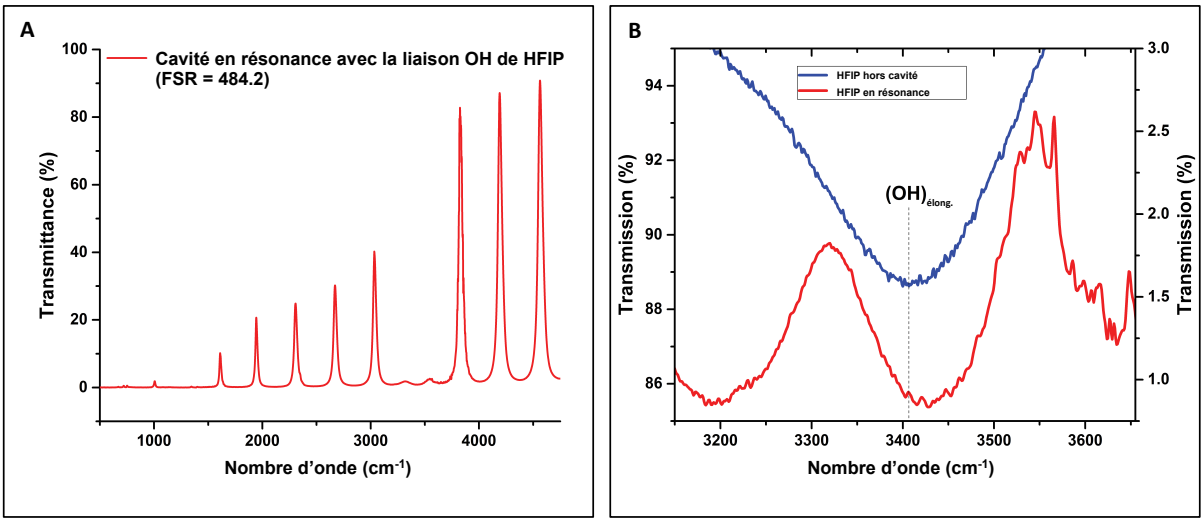

Figure 13. A. Spectre de transmission FT-IR du HFIP sous couplage fort de sa liaison O-H avec un mode de cavité FP **B.** Zoom sur la fenêtre spectrale où les nouvelles bandes vibratoires polaritoniques P+ et P- apparaissent sous VSC (rouge) avec un zoom sur celle du HFIP pur, dans la région de la bande O-H, mesuré avec un spectromètre ATR-IR (bleu).

La cavité optique FP utilisée dans les expériences suivantes a été assemblée à partir de deux miroirs métalliques parallèles en Au (10 nm) pulvérisés sur des fenêtres émettrices IR ZnSe (2 mm). Pour s'assurer que la réaction n'était pas affectée par la présence de Au et de ZnSe, une couche de verre (SiO_2) de 200 nm a été déposée sur la surface interne de chaque miroir. Les miroirs métalliques ont été séparés par une entretoise en polypropylène d'épaisseur variable avec un canal central creux conçu pour l'injection d'échantillons liquides. Pour préparer les différentes cavités en résonance et hors résonance dans les expériences décrites ci-après, l'épaisseur des entretoises en polypropylène utilisées a varié de 4 à 12 µm. La surface de la cavité était de 1 cm x 2,5 cm. La partie accordée représentait typiquement 40% de cette surface car les quatre vis que nous utilisons pour accorder la

cavité exercent une pression sur les fenêtres plates, les déformant légèrement. La réaction a été surveillée dans une zone accordée de la cavité à l'aide d'une ouverture de 5 mm de diamètre. Pour les expériences de contrôle, qualifiées d'expériences "hors cavité", les cellules ont été préparées de la même manière que précédemment, mais les miroirs métalliques ont été remplacés par des fenêtres en ZnSe revêtues de verre uniquement. Une solution homogène du réactif de départ **(R2)** (0,65 M), de H_2O_2 (0,18 M) et de l'étalon interne, le bromooctane (0,06 M), dans le HFIP (8,50 M ; n_{HFIP}/n_{total} = 0,90) a été utilisée comme milieu réactionnel tout au long des expériences présentées ici. Les mélanges réactionnels ont été neutralisés avec du dioxyde de manganèse (MnO_2) et analysés quantitativement par GC-MS après chaque expérience, dans le but de déterminer le ratio de concentrations $\frac{[3]}{[R2]}$ où **[3]** est la quantité de produit **(3)** obtenue après epoxidation du réactif de depart **(R2)** dont la quantité n'ayant pas réagi est notée **[R2] (Tableau 3)**.

Tableau 3. Ratios $\frac{3}{R2}$ mesurés quantitativement par GC-MS après chaque expérience

Entrée	Expérience	Ratio $\frac{[3]}{[R2]}$
1	Hors cavité	**0,147** ± 0,08
2	Hors résonance	**0,12** ± 0,02
3	En résonance O-H	**0,82** ± 0,17

La présence dans tous les chromatogrammes du réactif de départ **(R2)** n'ayant pas réagi indique que la réaction n'était pas complète après une période de 50 min **(Figure 14)**. Pour les réactions effectuées hors cavité et dans les cavités hors résonance, les ratio de concentrations $\frac{[3]}{[R2]}$ étaient équivalents dans la limite des erreurs expérimentales **(Tableau 3, entrées 1 et 2)**. Comme le montre le chromatogramme rouge de la **Figure 14**, une

augmentation significative de la formation du produit **(3)** a été observée lorsque le mode d'élongation de la liaison O-H a été fortement couplé à un mode cavité, indiquant une accélération de la formation du produit dans les cavités résonantes par un facteur 4,8 **(Tableau 3, entrée 3)**. Les valeurs reportées dans le **Tableau 3** tiennent compte de la fraction de la cavité FP sous VSC, soit 40% de sa surface totale. La fraction restante était désaccordée au-delà de la largeur du mode vibrationnel et, par conséquent, se trouvait dans un état hors résonance.

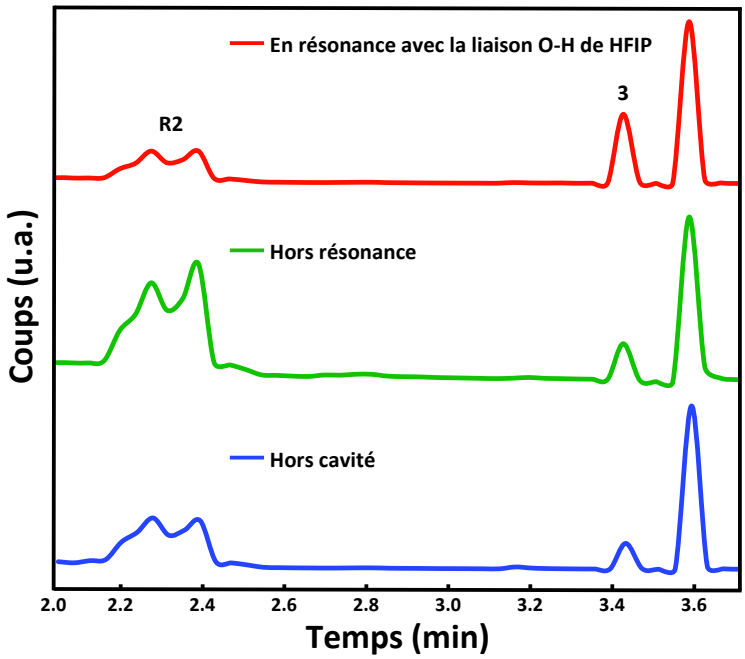

Figure 14. Les chromatogrammes GC des réactions effectuées dans les cavités accordées pour être en résonance avec le mode d'élongation de la liaison O-H (rouge) ainsi que les données pour une cavité hors résonance (vert) et hors cavité (bleu). Les pics correspondant au cis-cyclooctène et à l'oxyde de cyclooctène sont marqués **(R2)** et **(3)**, respectivement. Le pic à 3,6 min correspond au bromooctane, qui a été ajouté dans le mélange réactionnel comme étalon interne pour une analyse quantitative ultérieure. Ces chromatogrammes sont zoomés sur les composés d'intérêt pour plus de clarté.

Sur la **Figure 15**, les ratios de concentrations $\frac{[\mathbf{3}]}{[\mathbf{R2}]}$ sont tracés en fonction des réglages de la cavité FP obtenus en faisant varier l'espacement entre les fenêtres diélectriques (points rouges) par rapport à la bande d'absorption correspondant au mode d'élongation de la liaison O-H des aggrégats de HFIP (courbe bleue) afin d'obtenir un spectre d'action. Le rapport moyen obtenu pour les expériences effectuées à l'extérieur de la cavité est représenté par une ligne en pointillés verts. L'effet le plus important est clairement visible sous VSC à 3386 cm^{-1} où le rapport $\frac{[\mathbf{3}]}{[\mathbf{R2}]}$ était égal à 1.30, ce qui est 7.6 fois plus élevé que le rapport moyen de 0.17 mesuré hors cavité.

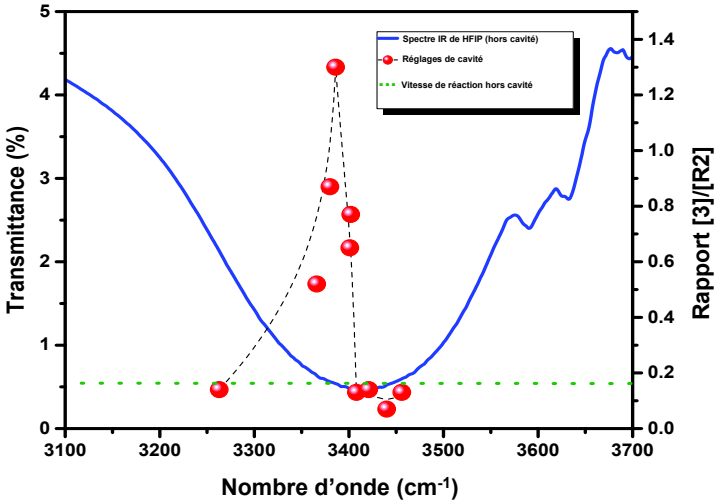

Figure 15. Influence relative du VSC dans la région du mode d'élongation de la liaison O-H du HFIP. La ligne bleue continue montre le spectre d'absorption IR du HFIP, zoomé dans la région des hautes fréquences où se trouve la bande d'absorption correspondant au mode d'élongation de la liaison O-H des agrégats de HFIP. La ligne pointillée verte représente la vitesse moyenne de la réaction à l'extérieur de la cavité. Les rapports de concentrations $\frac{[3]}{[R2]}$ sont tracés en fonction des réglages de la cavité pour les réactions à l'intérieur de la cavité (sphères rouges). La ligne pointillée noire reliant les sphères est un guide pour l'œil.

Étonnamment, la forme du spectre d'action ne correspond pas parfaitement à la forme de la bande d'absorption du mode d'élongation de la liaison O-H du HFIP **(Figure 15)**. Comme mentionné ci-dessus, une augmentation importante du rapport $\frac{[3]}{[R2]}$ a été observée dans les cavités résonantes, ce qui indique une réaction plus rapide sous VSC. Toutefois, si le rapport augmente progressivement entre 3263 et 3386 cm^{-1}, il ne devrait pas diminuer aussi brusquement à une fréquence plus élevée. Une explication possible de ce résultat pourrait être liée au fait que, de manière similaire à ce qui est observé pour la forme monomèrique du HFIP, on peut distinguer plusieurs types d'agrégats de HFIP en fonction de la conformation des monomères qui interviennent dans leur formation. Ainsi, la large bande d'absorption observée correspondant au mode d'élongation de la liaison O-H dans les agrégats de HFIP est probablement le résultat d'une combinaison de plusieurs composants. Ici, compte tenu de la forme du spectre d'action **(Figure 15)**, il est suggéré qu'un seul d'entre eux est sensible aux VSC. Selon Berkessel *et al.*, le HFIP est susceptible d'adopter une conformation *sc* (conformation la plus stable en phase liquide) ou même *sp* (meilleure capacité à donner des liaisons H) lorsqu'il doit agir comme donneur de liaisons H **(Figure 10)**.[23] On peut donc supposer, à titre d'hypothèse, que les agrégats formés par l'une ou l'autre des deux conformations sont ceux qui sont sensibles aux VSC et qui participent donc à l'activité catalytique.

III.2.3. SUIVI CINETIQUE DE LA VITESSE DE REACTION PAR SPECTROSCOPY IR

Comme dans nos études précédentes, nous voulions suivre l'évolution de la réaction en mesurant les décalages des résonances d'ordre élevés de la cavité. Malheureusement, dans la plupart des expériences où la cavité était en résonance (parfois aussi hors résonance) avec la bande d'absorption correspondant au mode d'élongation de la liaison O-H des agrégats HFIP, un phénomène inhabituel a été observé. Comme le montre la **Figure 16**, la zone sondée de la cavité, où la réaction a été suivie à travers une petite ouverture, semblait être vide après une période de temps allant de 15 à 30 min. Le spectre de transmission IR du mélange réactionnel juste après l'injection dans la cavité était parfaitement normal **(Figure 16A, spectre bleu)** et restait stable jusqu'à 10 min après l'injection **(Figure 16B, spectre rouge)**. Ensuite, un processus qui n'a initialement pas été compris a conduit à une modification anormale du spectre IR **(Figure 16C, spectre orange)** jusqu'à ce que la zone sondée génère un spectre correspondant à celui d'une cavité vide, indiquant l'absence de tout matériau moléculaire dans cette région de la cavité **(Figure 16D, spectre violet)**.

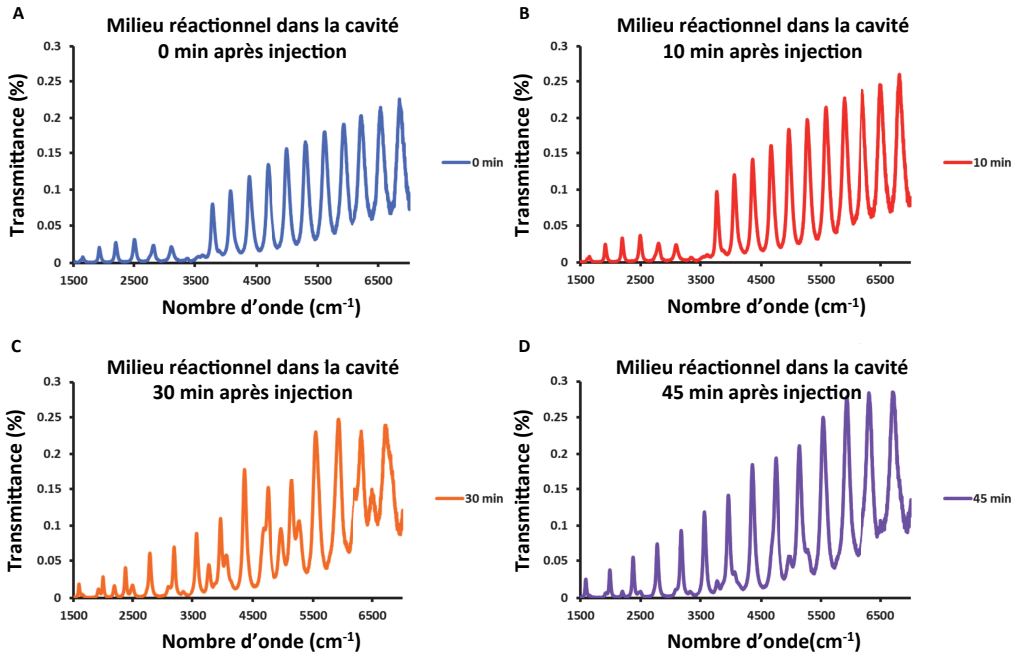

Figure 16. Evolution du spectre de transmission IR d'une cavité en résonance en fonction du temps. Dans cet exemple particulier, la cavité a été réglée à 3386 cm-1. Les spectres montrés ici ont été enregistrés immédiatement **(A)**, 10 min **(B)**, 30 min **(C)** et 45 min **(D)** après injection du mélange réactionnel dans la cavité.

Après avoir examiné la cavité à la fin des expériences, j'ai réalisé que ce phénomène était dû à la formation d'une bulle près de la région sondée. Pendant la réaction, H_2O_2, l'un des réactifs du mélange réactionnel, peut libérer de l'O_2 et former des bulles à l'intérieur de la cavité. Étonnamment, ce phénomène ne s'est jamais produit dans les expériences de contrôle, mentionnées plus haut comme des expériences hors cavité, dans lesquelles le mélange réactionnel est resté parfaitement stable à l'intérieur de la cellule micro-fluidique. Il convient de souligner ici que la catalyse hétérogène ou toute autre interaction avec Au peut être exclue, car la couche de Au déposée sur les miroirs de la cavité est revêtue de SiO_2 pour éviter tout contact avec le milieu réactionnel.

IV. CONCLUSION GENERALE

Ce manuscrit de thèse a été écrit par et pour un chimiste découvrant le monde des interactions lumière-matière. L'introduction générale commence par une description historique et chronologique de la compréhension de la lumière par l'homme, de l'Antiquité à l'avènement de la physique quantique. On constate que très tôt, la conception de la lumière a été associée à l'environnement dans lequel elle se propage. Plus tard, lorsque l'on s'est rendu compte grâce à la physique quantique que même le vide n'était pas "rien", des modifications de plusieurs propriétés de la matière ont été réalisées simplement en contrôlant son environnement. Je cite dans le manuscrit le cas des premières expériences cQED où le champ EM du vide entourant des atomes individuels était structuré de manière à étudier et à réguler les propriétés quantiques de la matière.[28–32] La recherche fondamentale dans ce domaine a conduit à des avancées majeures dans la compréhension des interactions lumière-matière et à des applications sociétales importantes comme la communication optique[33–35], l'imagerie optique[36–38] et les lasers[39–41]. Dans la lignée de ces travaux pionniers, il a été démontré par la suite que différentes propriétés des systèmes moléculaires pouvaient être régulées par un couplage fort avec les modes de cavité. L'essentiel de ce manuscrit de thèse porte sur le VSC puisqu'il s'agit d'une nouvelle approche pour contrôler les paysages réactionnels chimiques. Par exemple, en 2016, la collaboration entre les équipes des professeurs Ebbesen et Moran a démontré la capacité du VSC à réduire la vitesse d'une réaction chimique.[42]

Pendant la majeure partie de ma thèse, j'ai contribué de façon significative à l'étude d'un système réactionnel un peu plus complexe qui a été élaboré pour démontrer la capacité du VSC à favoriser la formation de produits par rapport à un autre. En effet, le réactif utilisé pour ces expériences comportait deux groupes fonctionnels distincts, un silyle (Si-CR_3) et un éther silylé (Si-OR_3) qui pouvaient être déprotégés simultanément par TBAF. Une analyse cinétique a montré que le VSC de l'un ou l'autre site (Si-C ou Si-O) favorisait la rupture de la liaison Si-O par rapport à celle de la liaison Si-C qui est autrement cinétiquement favorisée. Une analyse thermodynamique a révélé que la barrière d'activation et l'entropie d'activation du système augmentaient sous VSC, suggérant un état de transition ayant une structure plus proche de celle du produit qui serait légèrement moins tendu que l'état de transition standard connu pour ce type de réaction de déprotection. Ces travaux ont été discutés dans le chapitre II et publiés dans *Science*. Il constitue une preuve de concept démontrant qu'il est possible d'influencer la sélectivité d'une réaction par le biais du VSC.[2]

Dans le but de découvrir de nouvelles caractéristiques du VSC, nous avions comme objectif d'évaluer sa capacité d'accélérer la vitesse des réactions chimiques. J'ai choisi de travailler sur une réaction bien connue de la littérature : l'époxydation d'oléfines avec H_2O_2 dans HFIP. Une étude cinétique de cette réaction par Berkessel *et al.* a révélé le rôle catalytique crucial du solvant (HFIP) à haute concentration, qui est induit par un assemblage en clusters.[22] Les résultats préliminaires présentés au **chapitre III** semblent indiquer une augmentation de la vitesse de réaction sous VSC par un facteur 4.8. Cependant, une optimisation des conditions expérimentales est nécessaire pour confirmer ce résultat intéressant. En outre, compte tenu de la réponse obtenue en couplant la bande d'absorption correspondant au mode d'élongation de la liaison O-H des agrégats HFIP dans les expériences préliminaires, il est supposé qu'un seul de ses conformères serait sensible aux VSC et il serait donc le seul à être catalytiquement actif. L'étude sera approfondie afin de vérifier si le VSC permet une différenciation entre les deux conformères.

Un effet cinétique isotopique inverse a été observé lorsque HFIP-d_1(O-D) a été utilisé comme solvant dans une réaction de Friedel-Crafts étudiée par un de mes collègues.[43] À l'avenir, un tel modèle de réaction pourrait être utilisé pour explorer la possibilité d'utiliser le VSC comme mime de l'effet cinétique isotopique qui ne nécessiterait aucune modification chimique du substrat.

Tous ces résultats contribuent à montrer que le VSC constitue une méthode à température ambiante et à champ faible qui a le potentiel pour devenir un outil quotidien utilisable par les chimistes afin de contrôler physiquement la réactivité chimique sans catalyseurs, sans pré-fonctionnalisation ou sans changements chimiques des conditions de réaction et pourrait également fournir un nouvel outil pour les études mécanistiques.

CHAPTER I

I. GENERAL INTRODUCTION ON LIGHT-MATTER INTERACTIONS

I.1. A BRIEF HISTORY OF LIGHT

The nature of light has been the subject of intellectual and scientific inquiry since antiquity. Nowadays, light is understood as being composed of particles called photons - which can be counted - and behaves as electromagnetic (EM) waves - that can interfere - under certain conditions. Interestingly, the understanding of light is inextricably linked to that of its propagating medium. For example, the speed of light in *vacuum* is a universal constant. The term "*vacuum*" is generally used in a scientific context to describe a space created by partially or totally removing matter. We will see later in this manuscript that, with the advent of quantum electrodynamics (QED), modern physics has started to attribute new properties, sometimes disconcerting, to *vacuum*.

Here, I will briefly recall how these two concepts of light and *vacuum*, which are key for the understanding of light-matter interaction, have been grasped over the course of history.

I.1.1. ANCIENT IDEA OF LIGHT AND THE CONCEPT OF AETHER

From ancient texts, it is clear that in the 3rd century B.C. the ancient Greeks questioned the nature of light in particular in regard to sight. At a time when philosophers thought that the nature and complexity of all matter could be explained by four classical elements: earth, water, fire and wind, Empedocles (495-435 B.C.) was convinced that sight was based on the existence of an "inner fire" emitting visual rays from the eye. By adopting this idea, Euclid (≈300 B.C.) managed to geometrize optics creating a model where light rays propagate in straight lines.[44]

On the other hand, Democritus (460-370 B.C.), by extending Leucippus' ideas, developed a mechanistic materialist theory known as atomism. He considered matter to be made up of indivisible atoms (literally: "unbreakable") swirling in the void, which allows their movement. According to his theory, light comes from atoms emitted by luminous bodies, leaving an impression of light in our eyes as soon as they meet. A few centuries later, a Persian

scientist, Ibn al-Haytham (965-1039) definitively refuted the “inner fire” hypothesis made by Empedocles by stating that light rays spread from objects to eyes and not from eyes to objects. In his remarkable work, he even hypothesized that light was made up of corpuscles moving at very high speed, capable of bouncing off a surface or moving from one medium to another by changing direction.[45] René Descartes and Isaac Newton will use the exact same reasoning, six centuries later.

In the same period, Aristotle (384-322 B.C.) was studying the motion of objects. His results led him to conclude that the movement speed of an object was proportional to its weight and inversely proportional to the density of the medium in which it was moving.[46] Such statements implied that any objects surrounding the void would immediately fill it, moving at an infinite speed. This seemed to be nonsense and convinced Aristotle to formulate the *horror vaccui* hypothesis according to which the idea of total emptiness was impossible. Rather then *vacuum*, a fifth classical element was invented: the celestial body that was first referred to as *aether* by Plato.[47] Aristotle's *horror vaccui* hypothesis lasted even until the arrival of modern science in 17th century and the well-known vacuum experiments by Evangelista Torricelli, Blaise Pascal and Otto von Guericke using air pumps.[48–52] The observation of light propagation through evacuated glassware, reinforced the idea that *aether* was the medium of empty space.

I.1.2. THE BEGINNING OF WAVE-CORPUSCLE DUALITY

Major advances were made in geometric optics during the following centuries[53] and new light-involving phenomena, such as the interference and diffraction, were discovered.[54,55] Christian Huygens and Isaac Newton draw the consequences of that in an attempt to understand the nature of light, but their conceptions were different.

Huygens showed that Snell-Descartes’ laws could only be valid if light was considered as waves propagating in a rectilinear manner. He compared light to sound and concluded that light was a vibratory phenomenon propagating as waves in a subtle and invisible propagation medium. The existence of luminiferous *aether* seemed justified.[56]

Newton's point of view was completely different. Using a prismatic lens, he achieved the decomposition of light and revealed the spectrum of white light. He postulated that light was made up of very fast corpuscles, which when they reach the eye, generate vibrations

that are transmitted to the brain giving sensations of varying colors depending on their size. Ironically, Newton's overall work demonstrates the lack of corpuscular theory to explain the optical phenomena known at his time, but the wave theory aroused very strong opposition from him, particularly because he failed to conciliate the linear path of light and wave propagation. Newton was so respected that most physicists of the 18th century adopted his conception.[57]

I.1.3. THE SUCCESS OF WAVE THEORY AND MAXWELL'S ELECTROMAGNETISM

It was not until 1801 that the wave theory came back to the forefront and was used to interpret the interference pattern obtained in the famous double-slit experiment performed by Thomas Young.[58] Ten years later, Augustin Fresnel developed a wave optics theory that quantitatively explains the phenomena of interference but also those of diffraction previously observed by Francesco M. Grimaldi. Young and Fresnel's work proved that Newton's corpuscular model failed where wave theory worked perfectly.

Probably the most important breakthrough in the scientific understanding of light came with the theory of James C. Maxwell, published in 1865.[59] Based on André-Marie Ampère and Michael Faraday's work on electricity and magnetism, Maxwell progressively generalized the laws of electromagnetism and predicted the existence of EM waves. This led him to propose that light belongs to the EM spectrum and is only the visible part of it **(Figure 17)**.

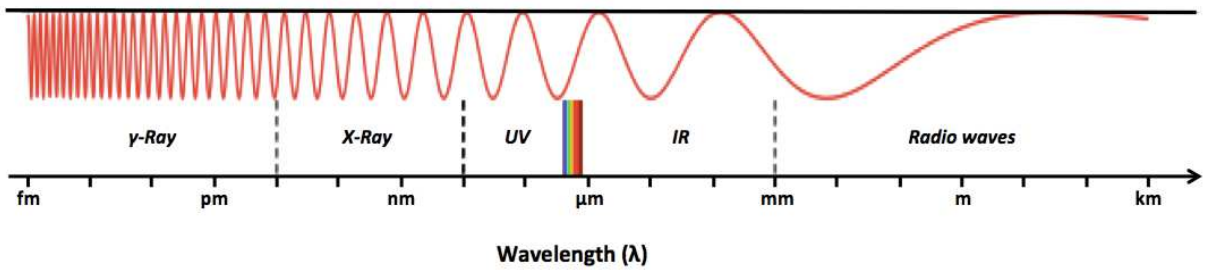

Figure 17. Electromagnetic spectrum. What we usually refer to as "light" is only a very small part of EM waves that is visible to the human eye. Our retina contains receptors that are only sensitive to wavelengths between about 0.4 and 0.7 µm. The signal transmitted from the eye to the brain via the optic nerve is interpreted in terms of color from violet to dark red for wavelengths ranging from 0.4 to 0.7 µm. IR rays, microwaves and radio waves correspond successively to wavelengths greater than 0.7 micrometers. UV rays, X-rays (discovered by Wilhelm Röntgen)[60] and γ-rays of radioactivity (discovered by Henri Becquerel)[61] correspond successively to wavelengths shorter than 0,4 µm.

The experimental evidence for the existence of EM waves across a larger spectrum will be provided some twenty years later by Hertz, who observed reflection, refraction, diffraction, interference and polarization phenomena on the waves produced by EM oscillators, following the same laws as those for optical light.[62] In parallel, the development of spectroscopy enabled research on the relationship between radiation and matter to be extended to a wider field beyond the visible spectrum. Herschel and Witter concluded, with a series of experiments on the thermal effects of bodies and the photochemical reactions of silver salts, on the existence of invisible waves: infrared (IR) and ultraviolet (UV) **(Figure 17)**.[63,64]

I.1.4. THE END OF THE CONCEPT OF *AETHER*

From 1881 to 1887, Albert A. Michelson and Edward Morley attempted a series of experiments to measure Earth's speed in *aether* in order to prove that the Earth was moving through it. They found no significant difference between the speed of light in the direction of movement through the presumed *aether* and the speed of light at right angles. Thus, they concluded that the relative speed of *aether* to the Earth was zero or close to.[65,66] Faced with these results, which were contradictory to the theories of the time, the scientific community began to doubt the true existence of *aether*. Finally, in 1905, Albert Einstein put a definitive end to the concept of *aether* by formalizing the theory of special relativity. His new theory of space and time was based on the fact that the speed of propagation of light in *vacuum* remains constant in every frame of reference, in accordance with Michelson and Morley's experiment.[67]

I.1.5. REVIVAL OF THE CORPUSCULAR THEORY OF LIGHT AND BIRTH OF A NEW MECHANICS

The wave character of light was universally accepted at the end of the 19th century when another major event of physics occurred: the birth of quantum theory. In 1900, Max Planck tried to interpret the variation in the intensity of the light emitted by incandescent bodies as a function of the wavelength in order to solve the issue of the "UV catastrophe" in

the black-body radiation model proposed by John W. S. Rayleigh and James Jeans **(Figure 18)**.[68]

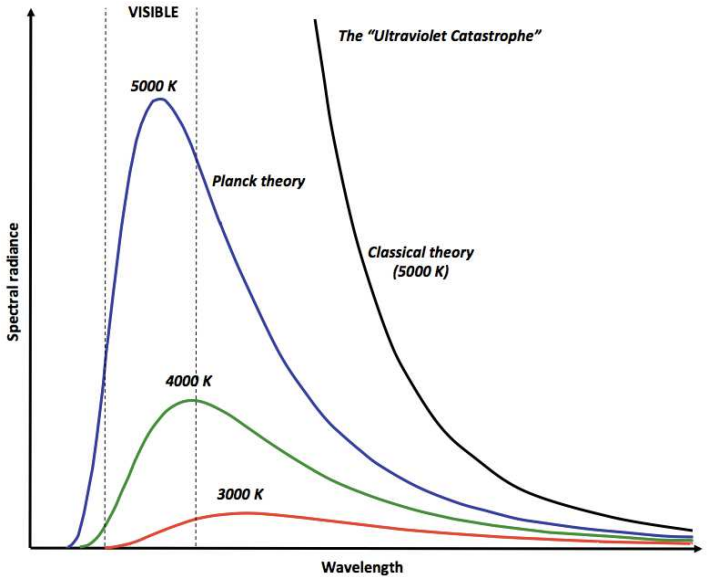

Figure 18. The "UV catastrophe": according to the classical Rayleigh-Jeans law, the energy emitted by an ideal blackbody tends to an infinite value at short wavelengths (black curve). Planck's law accurately describes blackbody radiation: the energy emitted decreases as its temperature decreases, its intensity also decreases and its maximum moves to longer wavelengths (blue, green and red curves).

Planck showed that the patterns of the corresponding spectra could only be interpreted by assuming that light was not exchanged continuously with matter, but only in energy packets called quanta.

$$\Delta E = nh\nu \quad with \quad n = \frac{1}{e^{\frac{h\nu}{k_B T}} - 1} \qquad \textbf{(Equation 1)}$$

where ΔE is the exchanged energy, h is the Planck constant (6.626070 x 10^{-34} J.s), ν is the frequency of the emitted radiation, k_B is the Boltzmann constant and T is the temperature. Although he did not directly introduce the notion of quantification, Planck's approach was a precondition for the birth of quantum mechanics. At that time, no one really took this theory seriously except Albert Einstein, who identified these energy packets as grains of light; the term "photon" which refers to the quanta of the EM field will be imagined later. He took up the idea of quanta in 1905, notably, in order to explain the photoelectric effect by considering that the energy of the photon was related to the frequency of the radiation and not to its intensity.[69] In 1913, Niels Bohr designed a model for the hydrogen atom based on this theory **(Figure 19)**.[70]

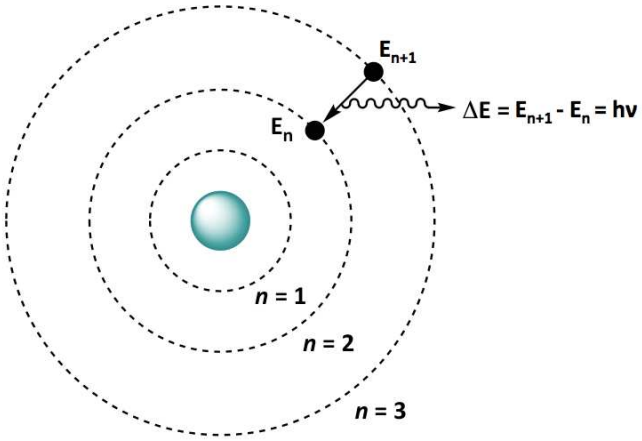

Figure 19. Bohr atomic model as shown in high school textbooks. The passage of an electron gravitating in a given orbit *n* (principal quantum number) corresponding to an energy level E_{n+1} towards an orbit corresponding to a lower energy level E_n is followed by the emission of a photon, whose energy is precisely equal to the difference in energy between the two levels: $E = E_{n+1} - E_n = h\nu$, where h is the Planck constant and ν is the frequency of the electromagnetic wave associated to the considered photon.

His planetary-model was built on a classical mechanics reasoning but he added a quantification condition that aimed to define preferential orbits of the electron corresponding to specific energy levels of the atom. This model was perfectly suitable for describing the position of the lines emitted by the hydrogen atom, but it was not appropriate to describe a large part of the spectra of larger atoms, to explain the existence of fine and hyperfine structures in the spectral lines, or some other features which are due to complicated quantum principles. It should be noted that **eq. 1** comes from corpuscular theory but still contains a frequency of a wave nature. These two aspects do not necessarily conflict and are complementary to each other. In 1923, Louis de Broglie extended the wave-corpuscle duality observed for light to any particle of matter.[71] He puts forward a hypothesis according to which any moving particle can be associated with a wave whose wavelength is the ratio of the Planck constant to the amount of motion of the particle:

$$\lambda = \frac{h}{p} = \frac{h}{mv} \quad \textbf{(Equation 2)}$$

where λ is the wavelength, h is the Planck constant and p is the momentum. Louis de Broglie's hypothesis was the starting point of a vast debate in which the most eminent physicists (Albert Einstein, Werner Heisenberg, Erwin Schrödinger, Paul Dirac, etc.) participated; a debate that led to the creation of a new mechanics, quantum mechanics, which describes all atomic and nuclear phenomena.

I.2. QUANTUM ELECTRODYNAMICS (QED)

In 1927, by integrating relativity into quantum mechanics, Dirac initiated the creation of a new branch of physics called quantum electrodynamics (QED).[72] QED addresses the interaction between electromagnetic radiation and matter. More precisely, it is a quantum approach to electromagnetism describing the interaction of the EM force and electrically charged particles. The QED theory was further developed in the late 1940s by Richard Feynman, Julian Schwinger and Sin-Itiro Tomonaga.[73]

Here as a trained chemist, I will not try to explain in details the underlying physics behind QED theory, which is at the heart of the modern comprehension of light-matter interactions. I will rather introduce some concepts that have emerged from this field of physics and that are important to understand before reading the following sections.

I.2.1. THE *VACUUM* FIELD: ENERGY, FLUCTUATIONS AND VIRTUAL PHOTONS

It is known that our universe is filled with energy that manifests itself in the form of radiation and matter. What is perhaps more surprising is that it is also filled with invisible quantum fluctuations, the so-called "*vacuum* field" which has it roots in Heisenberg's uncertainty principle. The simplest way to understand the origin of the *vacuum* field is to draw an analogy with molecular vibrational theory and its *zero-point energy* (ZPE).

In molecular vibrational theory, bonds are often represented as a harmonic oscillator made of two atoms connected by a spring and oscillating between a "maximum potential energy -minimum kinetic energy" state and a "minimum potential energy - maximum kinetic energy" state **(Figure 20)**.

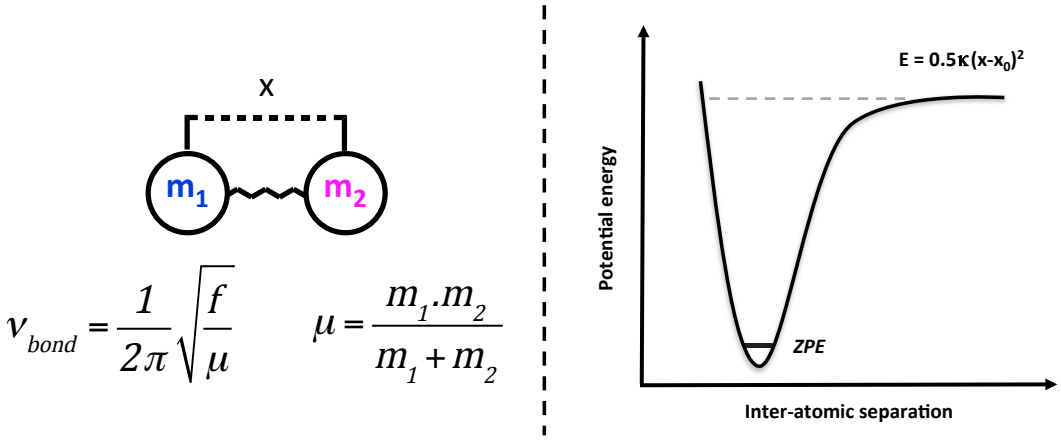

Figure 20. On the left is shown a schematic representation of a molecular bond as a harmonic oscillator made of two atoms m_1 and m_2 connected by a spring. Below this scheme, the expression of ν_{bond}, the classical vibrational frequency of the bond under consideration is given. f is the bond strength constant and μ is its reduced mass. On the right is shown a potential energy diagram showing the ZPE of a molecular bond, which is the lowest energy state of the system, characteristic of its ground state.

In quantum mechanics, the energies of a vibrational mode E_{vib} are quantized **(see eq. 3)** and can be seen as levels in a potential energy well **(Figure 20)**

$$E_{vib} = \left(n + \frac{1}{2}\right) h\nu_{bond},\ n = 0,1,2,\ldots \quad \textbf{(Equation 3)}$$

where n is the energy level, h is the Planck constant, ν_{bond} is the vibrational frequency of the bond. As microscopic systems, molecular oscillators have a ZPE, which is the lowest energy state in which it can be found. Similarly, and as we will see next, the EM field has a ZPE of $\frac{1}{2}\hbar\omega$ per mode of frequency ω.[74]

In quantum field theory (QFT), the EM field can be represented as a quantum harmonic oscillator[75] and defined by the coupling between a magnetic $\vec{B}$ and an electric field $\vec{E}$. In *vacuum*, the average energy value of these fields fluctuates permanently around zero according to Heisenberg's uncertainty principle[76]:

$$\Delta E \cdot \Delta t \geq \frac{\hbar}{2} \quad \textbf{(Equation 4)}$$

where ΔE refers to the energy variation, Δt to a time interval and $\hbar$ to the reduced Planck constant. Thus, even in a *vacuum* there are EM fields associated with their fluctuating ZPE.[77] This is known as *vacuum* quantum fluctuations, which correspond to nothing more than brief and permanent local variations of the field's energy level. The EM *vacuum* field is but a subset of *vacuum* quantum fluctuations that are predicted by QFT. For instance, there is a non-zero probability that the *vacuum* quantum fluctuations give rise to the spontaneous

appearance of virtual particle-antiparticle pairs that disappear almost immediately by annihilating each other, forming virtual photons, thus satisfying the principle of charge and energy conservation. In other words, for a very short period of time, energy is "borrowed" and "returned" to the *vacuum*. In the QED perspective, charged particles interact through processes of emission and absorption of photons, the particles of light that transmit electric and magnetic forces. The interaction with virtual photons is of very short duration, as they do not exist outside their interaction. All such particle interactions by virtual photon exchange can be graphically represented using the diagrams developed by Richard Feynman **(Figure 21)**.[78]

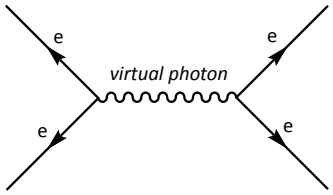

Figure 21. An example of one very simple Feynman diagram. Virtual photons (represented as wavy line) serve as force carriers for the interacting particles (here, electrons are represented as straight lines) that undergo changes in their velocity and direction of motion when they release or absorb the energy of a photon.

In summary, with the advent of QED, the notion of *vacuum* has taken a whole new dimension. Even the most perfect *vacuum* must no longer be considered as a completely empty and inert physical entity but rather as an energy field at its minimal level (ZPE) that occupies every point in space. In the quantum world, there is a sea of virtual photons disappearing as soon as they are formed, leaving, as a trace of their existence, only a shadow of their action on matter.[79] In this thesis, we are only concerned with the EM vacuum field and next, two key experiments that provided experimental proof of their existence will be presented.

I.2.2. REVEALING THE EFFECT OF EM *VACUUM* QUANTUM FLUCTUATIONS

The Lamb shift and the Casimir effect are two famous cases that are generally used to illustrate the effect of EM *vacuum* quantum fluctuations.

I.2.2.1. LAMB SHIFT

The presence of virtual particle-antiparticle pairs has an impact on the energy levels of atoms. This was first noticed from work on the hydrogen atom, an experimental model whose understanding has led to the development of a large part of quantum mechanics. According to predictions made from Dirac's quantum mechanics formulations, both states were initially considered degenerate **(Figure 22A)**. But in 1947, Willis E. Lamb and R. C. Retherford measured an energy shift between the $2^2S_{1/2}$ and $2^2P_{1/2}$ states of the fine structure of the hydrogen atom **(Figure 22B)**. In Lamb's experiment, hydrogen atoms were excited in the $2^2S_{1/2}$ metastable state with an electron beam. Under an applied magnetic field, microwaves for which $h\nu$ corresponded to the energy difference between one of the Zeeman components **(Figure 22C)** of $2^2S_{1/2}$ and any component of either the $2^2P_{1/2}$ or $2^2P_{3/2}$ levels were used to induce and measure the corresponding transitions. Such measurements provided a precise method for the location of the $2^2S_{1/2}$ state relative to the P states, as well as the distance between the latter states. Therefore, Lamb was able to determine the energy offset of $2^2S_{1/2}$ compared to $2^2P_{1/2}$.[80]

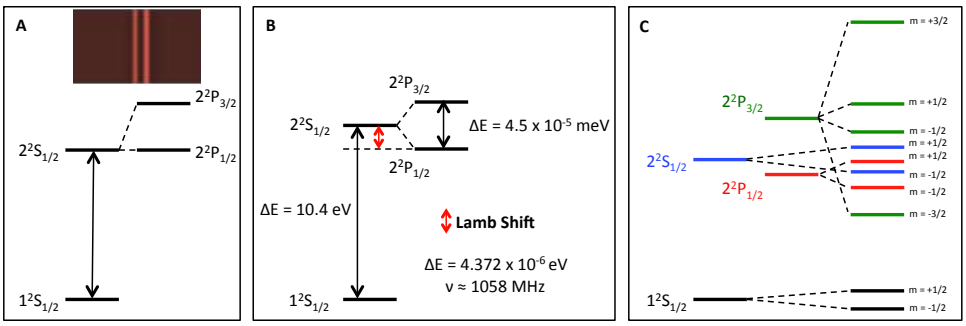

Figure 22. A. Energy level diagram of the hydrogen atom according to Dirac's theory. It explained the fine structure, which is due to the combined effects of relativistic variation of mass with velocity and spin-orbit coupling **B.** The Lamb shift. It is necessary to take into account the coupling with the electromagnetic vacuum to lift the degeneracy between $2^2S_{1/2}$ and $2^2P_{1/2}$. **C.** Energy level diagram of the hydrogen atom into an external magnetic field. Zeeman effect causes degeneracy lifting.

This discovery of the shift in energy between the two levels of the fine structure of hydrogen atoms, for which Lamb was awarded the Nobel Prize for physics in 1955, is now known as the “Lamb shift”. Hans Bethe was the first to suggest that the Lamb shift was due to the interaction between the electron of the hydrogen atom and the quantum fluctuations in the EM field, which disturbs the electron, causing a slight change in the position of the orbits and thus, in its energy levels.[81]

I.2.2.2. CASIMIR EFFECT

In 1948, Hendrik B.G. Casimir postulated, in a theoretical work based on a QFT mathematical approach, that the existence of quantum fluctuations in *vacuum* would lead to a force exerting a radiation pressure on the outside of two parallel conductive plates which would thus tend to be attracted toward each other **(Figure 23)**.[82]

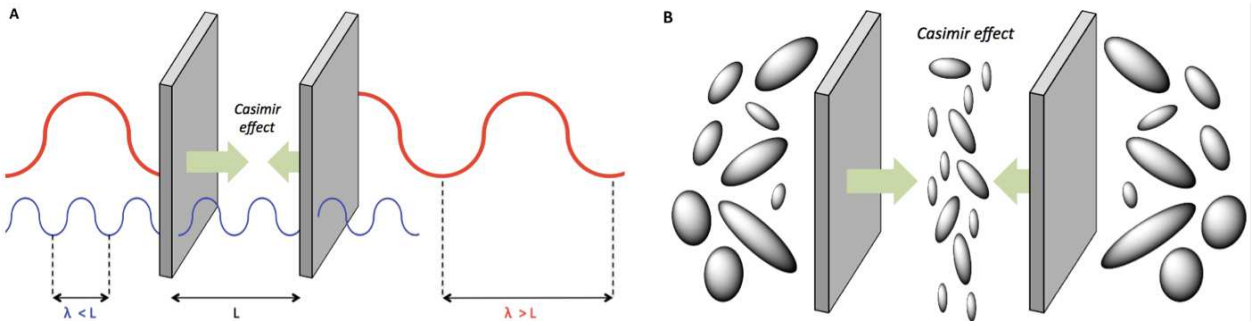

Figure 23. A. Electromagnetic radiation represented as virtual photons characterized by their wavelength (blue and red waves). Between the two conductive plates, only photons whose wavelength λ is shorter than the distance L between the two plates can exist (blue wave). There are therefore fewer waves within the two plates than outside, and this generates a non-zero pressure that tends to bring the plates together. **B.** Electromagnetic radiation represented as virtual photon particles. The density of virtual photons between the two plates is necessarily less than outside the plates, where there are no constraints. The higher external radiation pressure exerted on the two plates creates a force that brings them together.

This phenomenon is now called the “Casimir effect” and has been demonstrated experimentally for the first time in 1997 by Steve K. Lamoreaux.[83] The EM *vacuum* fluctuations were directly observed and measured, using femtosecond lasers in 2015.[84]

I.3. CAVITY QUANTUM ELECTRODYNAMICS (CQED)

In the previous section, I have outlined some pioneering works that have contributed to significant advances in our understanding of the environment with which matter interacts, and which should be considered as a quantified EM field **(see section I.2.1)**. In the same line, from the late 1970's to nowadays, a new generation of experiments carried out inside cavity resonators **(for a schematic representation of a simple cavity resonator, see section I.3.1.2., Figure 27)** to study quantum properties.[28–31] This led to the emergence of an entirely new field of research called cavity quantum electrodynamics (cQED)[32] and to a wide number of applications in optical communications[33–35], optical imaging[36–38], lasers[39–41].

In cQED, two coupling regimes between molecular transitions and confined electromagnetic fields can be distinguished: the weak and strong coupling regimes. Here, I will first present historical groundbreaking experiments carried out under a weak coupling regime and in which the spontaneous emission of excited molecules has been greatly modified. Then, I will present the characteristics of a strong coupling regime and review briefly its consequences for chemistry.

I.3.1. WEAK COUPLING REGIME: MODIFYING RADIATIVE PROPERTIES

We have seen in section 1.2. that the universe is full of *vacuum* quantum states. In fact, light emission properties depend not only on the emitter properties but also on its environment, i.e., on the availability of these *vacuum* quantum states that accommodate the emitted photons. This implies that if the density of states can be varied, in a cavity resonator for example **(see section I.3.1.2., Figure 27)**, the spontaneous emission rate of an emitter can potentially be significantly changed compared to free space. This effect was first discussed in 1946 by Purcell in the context of radio-frequencies and is now known as the Purcell effect.[85] After a short reminder about emission in free space, I will briefly present an experiment from Karl H. Drexhage in which the fluorescence of an Europium (Eu) ion complex was modified when placed near a metallic surface. The difference between weak and strong coupling will be discussed in more detail in **section I.3.2.**.

I.3.1.1. A BRIEF REMINDER ABOUT EMISSION IN FREE SPACE

Spontaneous emission is a process of light emission in which excited emitters return to their fundamental state spontaneously. There is another type of emission known as stimulated emission where a photon striking an excited emitter can force it to go back to the ground state, by emitting an incident photon with the exact same characteristics (same energy, same frequency, same momentum) and in the same direction **(Figure 24)**.[86]

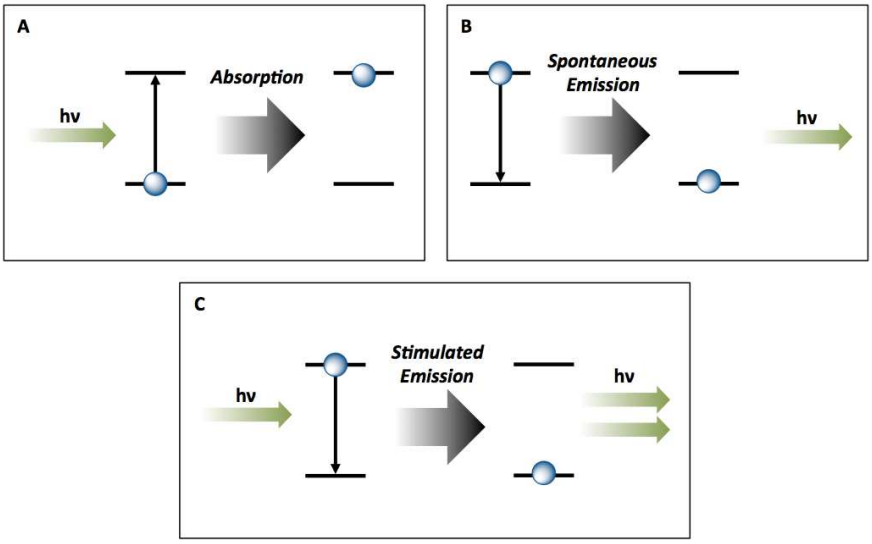

Figure 24. Distinction between absorption (**A**), spontaneous emission (**B**) and stimulated emission (**C**)

In a pedagogical article about cQED, Haroche and Kleppner provided a nice review of spontaneous emission in free space[32] in which the emission process resulting from the decay of one electron from the electronic level *e* to level *g* separated by the energy interval $\Delta E = E_e - E_g = \hbar\omega$, is described as the result of the coupling between the electron and the electromagnetic field in its *vacuum* quantum state. Thus, the optical quantum states available in *vacuum* act as a gigantic "reservoir" in which the emitter excitation decays away. We will see now that emission processes are strongly dependent on the density of optical quantum states available in the close environment of the emitter.

I.3.1.2. CAVITY ENHANCED / INHIBITED EMISSION (PURCELL EFFECT)

Fluorescence is the result of a radiative transition between two electronic states of the same multiplicity (e.g. singlet excited state to singlet ground state). Typically, this emission occurs at lower energy than the absorption of the exciting photons, because of an energy loss due to intramolecular relaxation and interaction with the environment, typically the solvent. The fluorescence is in competition with non-radiative processes such as internal vibrational relaxation and inter-system crossing to the triplet state, as illustrated in the Jablonski diagram **(Figure 25).**

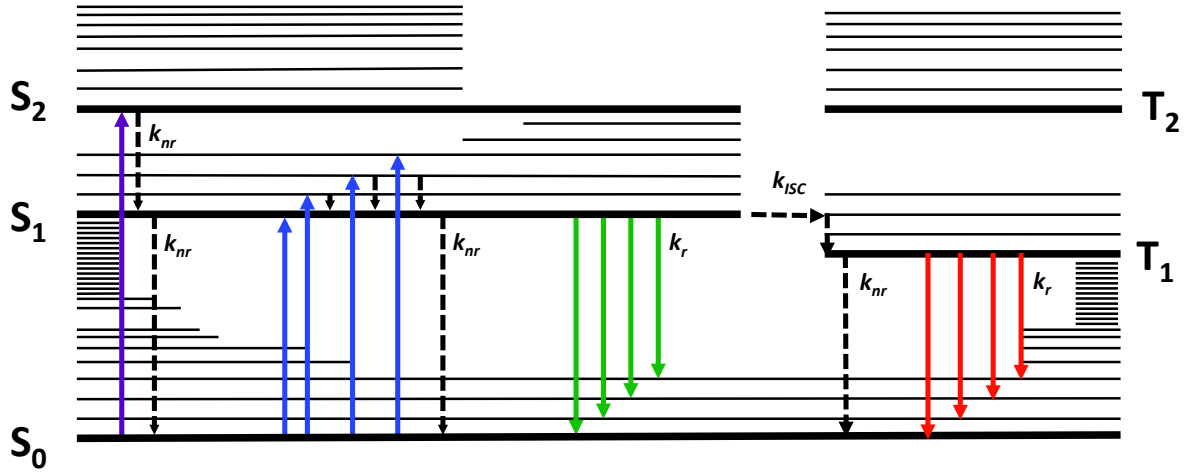

Figure 25. Jablonski diagram. Bold horizontal lines represent the energy levels. Thin horizontal lines correspond to the vibrational sub-levels of singlet (S_0, S_1 and S_2) and triplet (T_1 and T_2) electronic states. Dotted arrows symbolized non-radiative (nr) processes: internal conversion and inter-system crossing (ISC)

A fluorescent emitter is generally characterized by two fundamental parameters: its lifetime τ, which is the average time during which the emitter remains in its excited state before returning to its fundamental state by the emission of a photon, and its fluorescence quantum yield ϕ, which is the probability for the emitter to generate a photon.[87] The lifetime and the quantum yield can be respectively written as:[88]

$$\tau = \frac{1}{k_r + k_{nr} + k_{ISC}} \quad \textbf{(Equation 5)} \quad \text{and} \quad \phi = \frac{k_r}{k_r + k_{nr} + k_{ISC}} \quad \textbf{(Equation 6)}$$

where k_r represents the radiative rate constant, k_{nr} is a single constant regrouping all the possible non-radiative decay processes and k_{ISC} represents the rate constant for inter-system crossing processes. Something that can only be understood in a QED context is that

k_r, and therefore τ and ϕ of a fluorescent emitter, are not inherent features of the molecule but are highly dependent on its local EM environment, or, in other words, on the density of optical states **(see Eq. 7)**.

The presence of a metallic interface in the vicinity of a fluorophore can alter the fluorescence processes through the modification of its local EM environment. The first experiment showing that the spontaneous emission of a quantum system depends on its density of optical states was carried out by Drexhage in the 1960s.[89] This experiment consisted of measuring the fluorescence lifetime of monomolecular layers of a Eu complex near a silver mirror (coated with CdC_{20} layers which provided a certain distance *d* according to their number) as a function of the distance *d* from the complex to the surface of the mirror. The result of the measurement is shown in the **Figure 26**. Lifetime oscillations were observed for a distance *d* of between 30 and 500 nm. They result from the interaction between the emission by the complex and the density of optical states that varies with the distance from the mirror. The sudden drop in lifetime when *d* decreases below 20 nm is due to the non-radiative energy transfer to the metal.

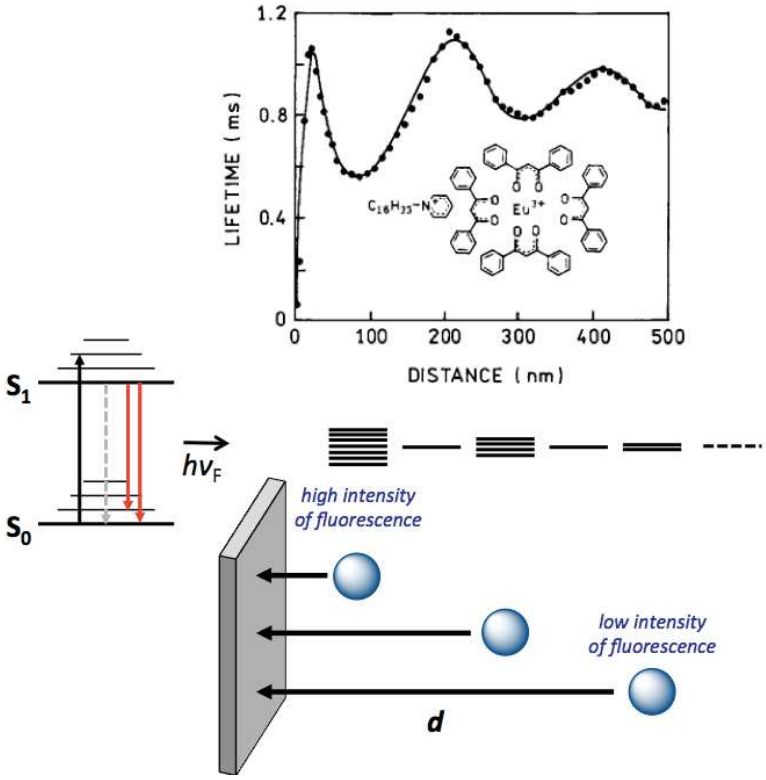

Figure 26. Fluorescence lifetime of the Eu^{3+} ions from the Eu complex (blue spheres) as a function of the emitter-mirror distance *d* measured experimentally (black dots) and theoretical calculations (black continuous curves). The distance *d* is provided by CdC_{20} layers of different length (black arrows). The structure of the Europium complex is shown below the continuous curve. The smaller *d* is, the higher the density of the states, resulting in higher fluorescence intensity. Adapted from reference [89].

In the early 1980's and in the aftermath of Drexhage's experiments, other teams have conducted QED experiments placing atoms in optical cavities, known as Fabry-Perot (FP) cavities, and which are composed of two parallel mirrors **(Figure 27)**.[28–31] Such FP cavities produce standing waves only for certain resonant frequencies called normal modes of the cavity. One can make an analogy with guitar strings that can only vibrate at frequencies, called harmonics, which are multiples of the fundamental frequency. The unique feature of these devices is that they allow a radical change in the mode structure of the *vacuum* field when their size is close to the wavelength of the standing waves. Indeed, for an electric field polarized parallel to the mirror, optical cavity modes only exist if $\lambda < 2L$, otherwise, when $\lambda > 2L$ the lowest-order mode cuts off abruptly. An excited atom whose radiation arises from an electric dipole moment oscillating parallel to the mirrors become long-lived when $\lambda > 2L$.

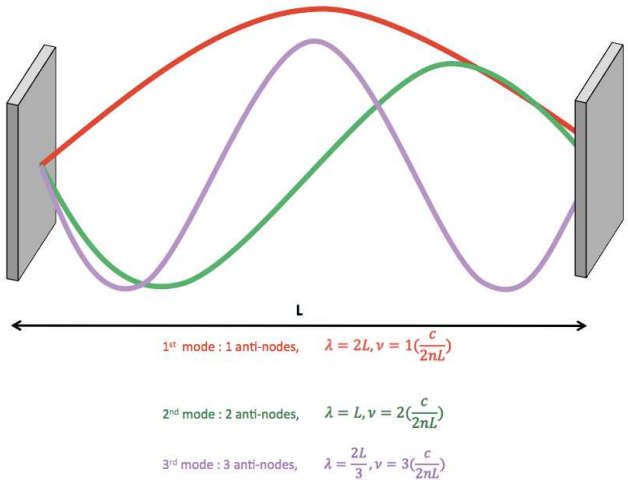

Figure 27. Schematic representation of a cavity resonator. L is the distance between the two mirrors. λ and ν are respectively the wavelength and the frequency of the corresponding standing waves. When confined inside cavity resonators, EM wave produces standing waves for certain resonant frequencies called normal modes of the cavity. The three first modes are represented here (red, green and purple curves).

As mentioned earlier, the Purcell effect can be explained by the fact that the density of states is narrowed down inside such optical cavities. The emitting system inside the resonator emits only within the existing constrained field, in contrast to free space. The formula known as Fermi's "golden rule" indicates that the probability of photon emission Γ_0 is proportional to the density of final states ρ_0:[32]

$$\Gamma_0 = \frac{2\pi}{3}\Omega_R^2\rho_0 \quad \textbf{(Equation 7)}$$

where, Ω_R is the Rabi frequency at which the emitter and the electromagnetic field confined inside the cavity exchange energy.

I.3.2. STRONG COUPLING REGIME: MODIFICATION OF THE ENERGY LEVELS OF MATTER

I.3.2.1. AN INTRODUCTION TO STRONG COUPLING

In the previous section, the mentioned examples of emission processes examples are regulated by weak coupling: the energy exchange rates between the emitter and the cavity modes were slower than the damping rate of the field in the cavity. In other words, the cavity and the emitter do not act as coupled oscillators. As a result, only the spontaneous emission rate was modified, whereas the emission frequency remained unaltered. In the strong coupling regime, however, the interaction is so strong that energy levels themselves are altered.

For an easy understanding of the strong coupling effect, one can think of a very simple model: the classical case of two coupled harmonic oscillators. Two harmonic oscillators become coupled if they have the possibility to exchange energy faster than any decay process in the system. It was observed for the first time on a classical system by Huygens, the inventor of pendulum clocks. He realized that pendulums could be synchronized by coupling *via* a wooden structure **(Figure 28A)**.[90] The energy profile of the coupled pendulum system is modified compared to the one of the individual original pendulums **(Figure 28B)**. Two new oscillation modes whose frequencies are different from those of the original oscillator modes are obtained. The two pendulums oscillating in phase by exchange of mechanical energy will form a new, lower energy level. The out-of-phase movement constitutes the excited state of the coupled pendulums.[91]

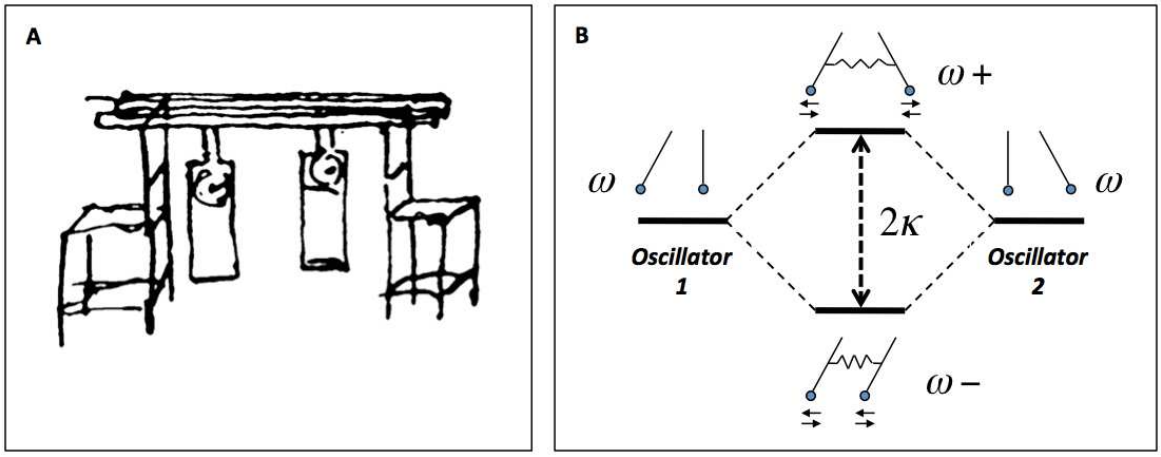

Figure 28. A. Classical coupled oscillators. Original drawing made by Huygens in 1665 to describe his experiment. Two pendulum clocks oscillate in synchronicity when hung from the same wooden structure **B.** Energy diagram of classical coupled oscillators. The coupling gives rise to two new states (eigenstates) of oscillations ($\omega +$ and $\omega -$) separated by an energy of 2κ where κ is the coupling constant of the system. Adapted from reference [90] and [91]

The light-matter strong coupling regime in cQED is analogous to the coupled oscillators, and likewise forms two new eigenstates of lower and higher energy, as we will see below. It can be generated in a cavity resonator tuned to have the same frequency as that of a molecular transition **(see section I.3.2.2.2., Figure 29)**. Since the first quantum strong light-matter interaction, reported for a single atom in a microwave cavity[92], several experimental[6,7,9,42,93–105] and theoretical[106–113] studies from many groups have shown that light-matter strong coupling could give rise to modification of spectra and relaxation processes of organic molecules. As a result, and as we will see next, strong coupling produces molecular properties that are different than those of the original uncoupled constituents. From now on, the discussion will only concern light-matter interactions involving molecular materials instead of single atoms. Indeed, the main topic of this thesis is the recent advance made by our teams on the control of chemical reactions under strong coupling. These results open possibilities for future applications of strong coupling as a new tool for chemistry.

I.3.2.2. CHARACTERISTICS OF THE STRONG-COUPLING REGIME

I have to mention here the difference between Electronic Strong Coupling (ESC), in which electronic transitions are coupled to a mode of the electromagnetic field inside a cavity and Vibrational Strong Coupling (VSC), which consists in coupling a cavity mode to a molecular vibration. In the following sub-sections, the electronic or vibrational nature of the molecular resonance is not very important, and I will talk about coupled molecules as molecular resonators. The ability of ESC **(see part I.4.)** and VSC **(see part I.5.)** to modify the EM environment of organic molecules has been used to modify typical molecular properties and even chemical landscapes, allowing to control chemical reaction rates.[1,5] During my PhD, I have contributed to a study revealing that VSC could also be used to tilt the selectivity of a chemical reaction.[2] This work will be presented in details in the next chapter. I will now present the general characteristics of the strong coupling regime.

I.3.2.2.1. HYBRID LIGHT-MATTER STATES (POLARITONIC STATES)

In this work, an interaction takes place between the electromagnetic fluctuations of the cavity and the organic molecules under strong coupling by exchange of virtual photons. If the energy exchange rate in the coupled system is very fast and dominates over the loss processes, the originally coinciding states split into two new states. These new hybrid light-matter states, also called polaritonic states (P+ and P-), are described by the following wave functions:[42]

$$|P+\rangle = c_{11}|e\rangle_m|0\rangle_{cav} + c_{12}|g\rangle_m|1\rangle_{cav} \quad \textbf{(Equation 8)}$$

and

$$|P-\rangle = c_{22}|e\rangle_m|0\rangle_{cav} - c_{21}|g\rangle_m|1\rangle_{cav} \quad \textbf{(Equation 9)}$$

where P+ and P- are linear combinations of the molecule in the excited state (e) with 0 photons in the cavity and the molecule in the ground state (g) with 1 photon in the cavity. **Eq. 8** and **Eq. 9** show that polaritonic states are truly hybrids in the sense that they are a real combination of light ($|0\rangle_{cav}$ and $|1\rangle_{cav}$) and matter ($|e\rangle_m$ and $|g\rangle_m$). That is where light-matter strong coupling gets its name.

I.3.2.2.2. RABI SPLITTING

The new hybrid states are separated by an energy $\hbar\Omega_R$ known as the Rabi energy, which is proportional to the coupling strength **(see Eq. 13) (Figure 29)**.[42]

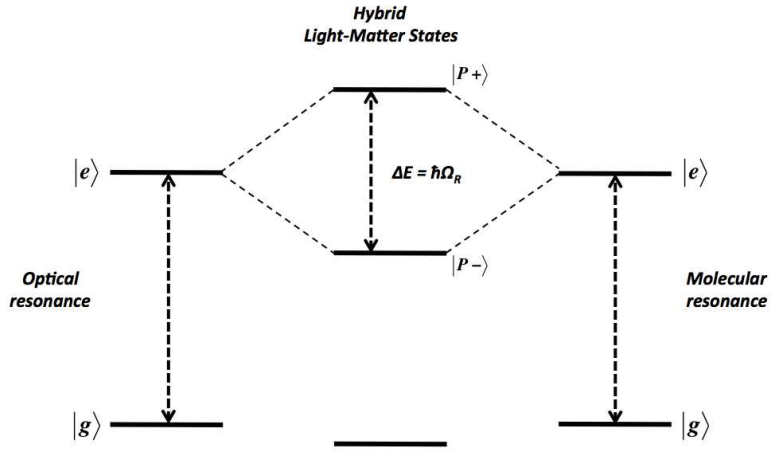

Figure 29. Energy diagram of a strong coupling interaction between an optical mode of a cavity and molecular resonances. The new states that are formed by Rabi splitting are hybrid light-matter states or polaritonic states (P+ and P-). They arise from the resonant interaction between the electromagnetic field confined in the optical resonator and the two-level molecular resonator. The energy gap ΔE between the polaritonic states is equal to $\hbar\Omega_R$ and is called the Rabi energy. Adapted from reference [42]

This degeneracy-lifting phenomenon is called Rabi splitting and modifies the absorption spectrum of molecules placed inside a cavity when it is resonant with a molecular transition. **(Figure 30)**

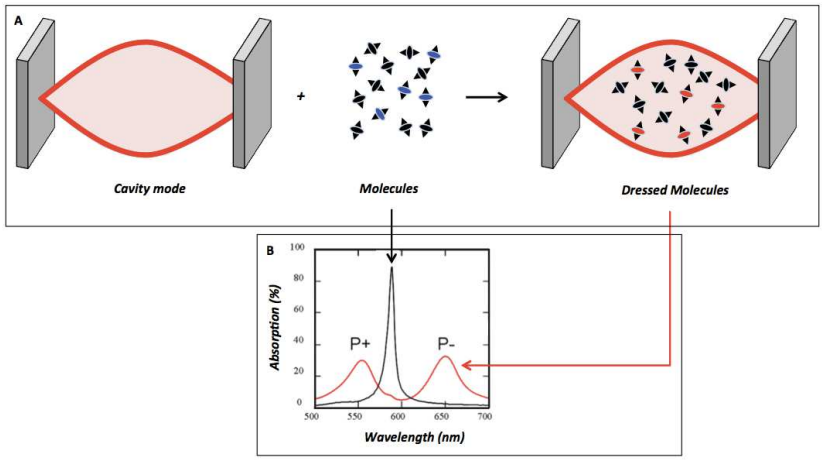

Figure 30. A. Schematic representation of the first mode of the cavity λ/2 formed between two metallic mirrors (optical cavity) (red area). When the cavity mode is resonant with the absorption of molecules (shown as little dipoles), they are said to be dressed by the electromagnetic field with which they strongly interact, resulting in the formation of light-matter hybrid states. **B.** Experimental absorption spectrum of a cyanine dye molecule before (black curve) and after (red curve) undergoing light-matter strong coupling with a cavity. Adapted from reference [42]

I.3.2.2.3. IMPORTANT PARAMETERS AND DEPENDENCE ON THE CONCENTRATION (COLLECTIVE STATES)

As already mentioned earlier, to reach the strong-coupling regime, it is necessary for dissipation processes to be negligible compared to the strength of the interaction between the resonant components. Indeed, the key parameters for the identification of the nature and strength of light-matter interactions are: the coupling strength g, the relaxation rate from the excited state in open space Γ_e and the inverse of the lifetime of a virtual photon in the empty cavity Γ_c **(Figure 31)**.

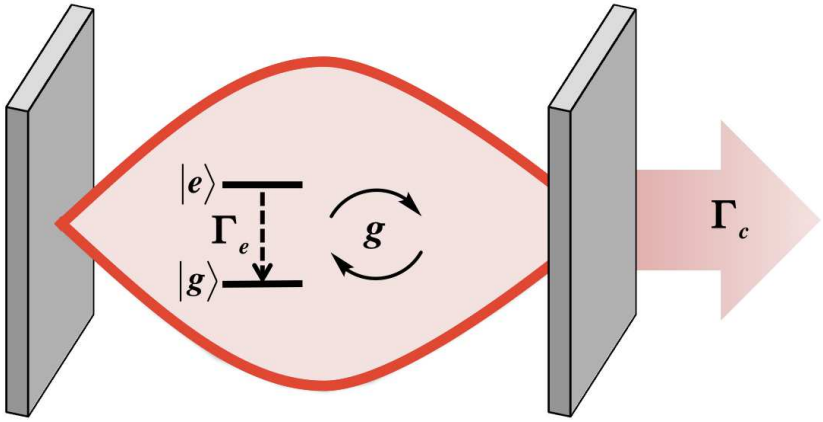

Figure 31. Schematic representation of a resonator coupled to a cavity mode. g is the coupling strength, Γ_c and Γ_e are the respective decay constants of the photon in the cavity and of the excited state. The distinction between weak and strong coupling regimes can be made on the basis of the following conditions: $g < \Gamma_e, \Gamma_c$ in the case of weak coupling and $g > \Gamma_e, \Gamma_c$ for strong coupling. Adapted from reference [114]

The decay constants Γ_e and Γ_c are respectively given by:

$$\Gamma_e = \frac{1}{\tau} \quad \textbf{(Equation 10)} \quad \text{and} \quad \Gamma_c = \frac{1}{t_p} \quad \textbf{(Equation 11)}$$

where τ is the lifetime of the excited state and t_p is the lifetime of the photon in the empty cavity. In the simplest case, the Rabi energy $\hbar\Omega_R$ is given by the Jaynes-Cumming two-state model:[115]

$$\Delta E = E_+ - E_- = \hbar\Omega_R = \sqrt{4g^2 - (\Gamma_c - \Gamma_e)^2} \quad \textbf{(Equation 12)}$$

where $E_+$and E_- are the respective energies of $P+$ and $P-$. From the **Eq. 13**, it can be seen that if dissipation processes are negligible in front of the strength of interaction between the resonant components (when $g \gg \Gamma_c - \Gamma_e$), the Rabi splitting is proportional to g, which is

the interaction energy between the electric component of the electromagnetic field E_{cav} in the cavity and the transition dipole moment d of the material: [116]

$$\hbar\Omega_R = 2g = 2d \cdot E_{cav} = 2d\sqrt{\frac{\hbar\omega}{2\varepsilon_0 V_m}} \times \sqrt{n_{\mathrm{ph}} + 1} \quad \textbf{(Equation 13)}$$

where $\hbar\omega$ is the resonant energy, ε_0 is the vacuum permittivity, V_m is the volume of the electromagnetic mode and n_{ph} is the number of photons involved in the coupling process. In the **Eq. 13**, the last term $\sqrt{n_{\mathrm{ph}} + 1}$ shows that even in the absence of "real" photons (when $n_{\mathrm{ph}} = 0$), $\hbar\Omega_R$ has a residual value $2d\sqrt{\frac{\hbar\omega}{2\varepsilon_0 v}}$ known as the *vacuum* Rabi splitting. It is important to understand that the word *vacuum* here refers to *vacuum* EM field in the cavity, i.e. its *ZPE* **(see section I.2.1.)** and not to the absence of matter.[117]

In the case of many molecular resonators, it is known that the Rabi splitting energy depends on the number of molecules interacting with the cavity mode **(Figure 32)**.[93,116,118]

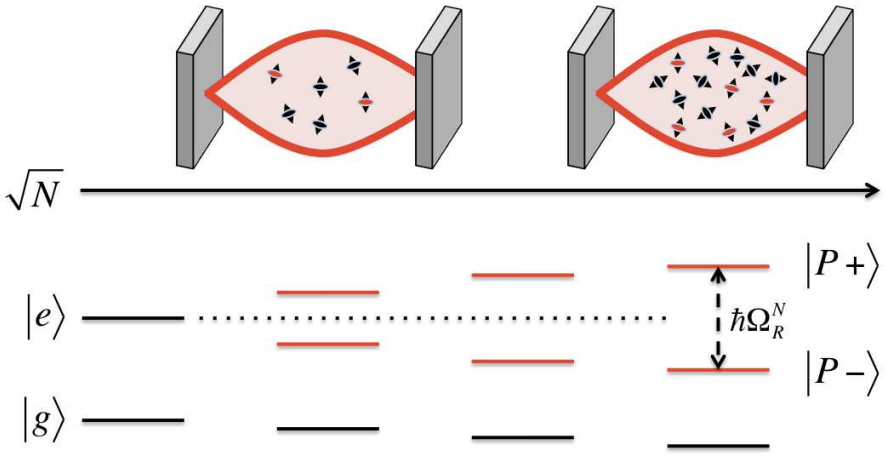

Figure 32. Collective states. The strong coupling of a large number of molecules to a given optical mode significantly enhances $\hbar\Omega_R$. The large splitting perturbs the energy levels of the other molecular eigenstates that are not directly involved in the coupling.

The Rabi energy involving N coupled molecular resonator becomes:

$$\hbar\Omega_R^N = \sqrt{N}\hbar\Omega_R = \sqrt{N} \times 2d\sqrt{\frac{\hbar\omega}{2\varepsilon_0 V_m}} \times \sqrt{n_{\mathrm{ph}} + 1} \quad \textbf{(Equation 14)}$$

where $\hbar\Omega_R$ is the contribution of each molecular resonator. When many molecules are coupled to a single mode, adding photons does not significantly increase $\hbar\Omega_R^N$. The volume V_m of an electromagnetic mode of a micro cavity resonator is typically very large (~µm^3) compared with the volume occupied by a molecule (~nm^3), so it is possible for the number

N of molecules within one mode, and interacting with it, to be very large, resulting in a significant enhancement of the Rabi splitting since $\hbar\Omega_R \propto \sqrt{\frac{N}{V_m}}$. The important point here is that the EM field concentrated in the single mode of the cavity resonator provides in-phase oscillations of all molecular transitions in this mode, leading to the formation of a collective dipole.[49]

I.4. ESC FOR THE CONTROL OF CHEMICAL REACTIONS

As already mentioned earlier, when it comes to the coupling of organic molecules to the electromagnetic *vacuum* fields, two cases can be distinguished: ESC, in which electronic transitions are coupled to a mode of the EM field inside a cavity, and VSC, which consists in coupling a cavity mode to a molecular bond vibration. I have already introduced electronic transitions in **sub-section I.3.1.2.**, so I will start directly by presenting the effect of ESC on chemistry. Finally, I will briefly introduce molecular vibration before discussing the effect of VSC on chemistry.

I.4.1. MODIFYING CHEMICAL LANDSCAPES BY ESC TO *VACUUM* FIELDS

The ability of ESC to modify the EM environment of organic molecules has been widely used to modify typical molecular processes and properties such as the rate of nonradiative energy transfer[119], the conductivity and work function of semiconducting materials[120,121] and their nonlinear optical response[122–124]. In this section, I have decided to present the proof-of-concept work from Ebbesen and co-workers showing how the chemical landscape can be modified under ESC, thus allowing the control of chemical reaction rate[5]. This work paved the way towards a better understanding of the potential implications of strong coupling for chemical reactivity.

Under ESC, just as atoms exchange electrons to form molecular orbitals, an organic molecule can interact through interaction (exchange of virtual photons) between its

electronic transition and a mode of the electromagnetic field inside a cavity resonator, leading to the creation of polaritonic states by Rabi-splitting **(see sub-section I.3.2.2.2.) (Figure 33)**. The combination of molecules and cavity must be considered as a distinct entity with its own new energy levels and therefore with its own unique chemistry.

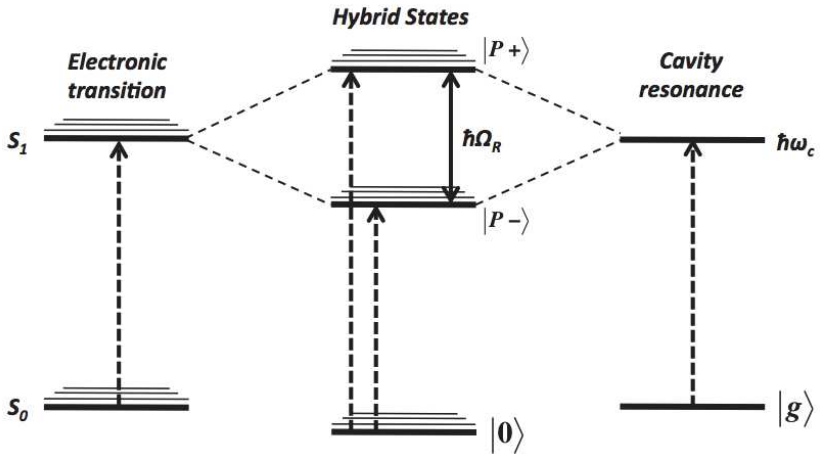

Figure 33. Simplified energy diagram showing the interaction of a Highest Occupied Molecular Orbital (HOMO) – Lowest Unoccupied Molecular Orbital (LUMO) transition (S_0 to S_1) of a molecule resonant with a cavity mode $\hbar\omega_c$. The two hybrid light–matter (or polaritonic) states, $|P+\rangle$ and $|P-\rangle$, are separated by the Rabi splitting energy $\hbar\Omega_R$.

The model system chosen for this study was a photochromic spiropyran derivative, the 1',3'-dihydro-1',3',3'-trimethyl-6-nitrospiro[2H-1-benzopyran-2,2'-(2H)-indole] (SPI). Photochromic molecules, or photochromes, are a class of molecule that can undergo photochromism, i.e., a reversible transformation, photoinduced in at least one direction, between two states A and B having different absorption spectra.[125] Upon irradiation at 330 nm, the SPI photoisomerizes by ring cleavage to form a merocyanine (MC) **(Figure 34)**. The reverse reaction can be achieved photochemically or by thermal means.

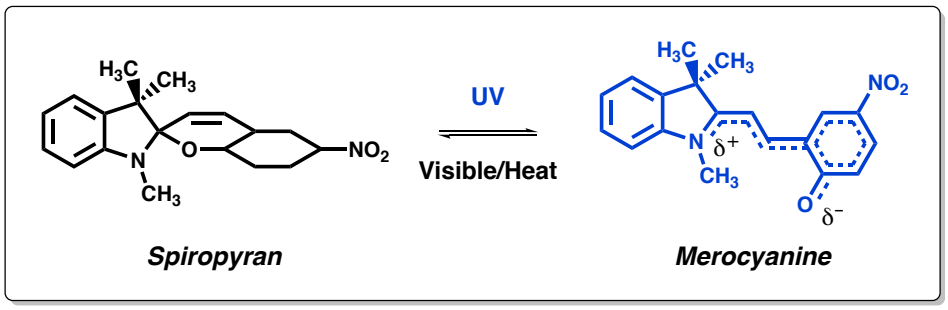

Figure 34. Reversible photoisomerization of spiropyran (SPI) to merocyanine (MC)

The experiment consisted in recording the transmission spectrum of the system inside and outside a FP cavity resonator **(Figure 35A)**, as a function or irradiation time at 330 nm, where silver (Ag) mirrors have a transparency window. UV irradiation at 330 nm tirggered the formation of MC both “inside cavity” (poly(methyl methacrylate) (PMMA)/photochrome film between two Ag mirrors) and “outside cavity” experiments (isolated PMMa/photochrome film). The key result of this study is that the rate of the photoisomerization process was modified when the molecules were placed under ESC regime in a resonant cavity.

The two transmission features of the initial cavity structure are shown in Figure 35B (t = 0 minute (min), black curve). A first absorption band is found at 560 nm and corresponds to the fundamental cavity mode whose position depends on the thickness of the cavity. The FP mode is reduced and splits as the MC concentration increases because, in the particular experimental conditions (poly(vinylalcohol) (PVA)/PMMA/PVA thickness of 130 nm), the fundamental cavity mode was resonant with the strong absorption of the highly conjugated MC (λ_{max} = 560 nm) **(Figure 35, red curve)** that is formed upon irradiation. The strong coupling to the *vacuum* field in the cavity, leads to the formation of the polaritonic states evidenced by the splitting of the absorption at 560 nm into two new peaks **(Figure 35C, green curve and Figure 35B, apparition of the new bands around 480 and 660nm)**

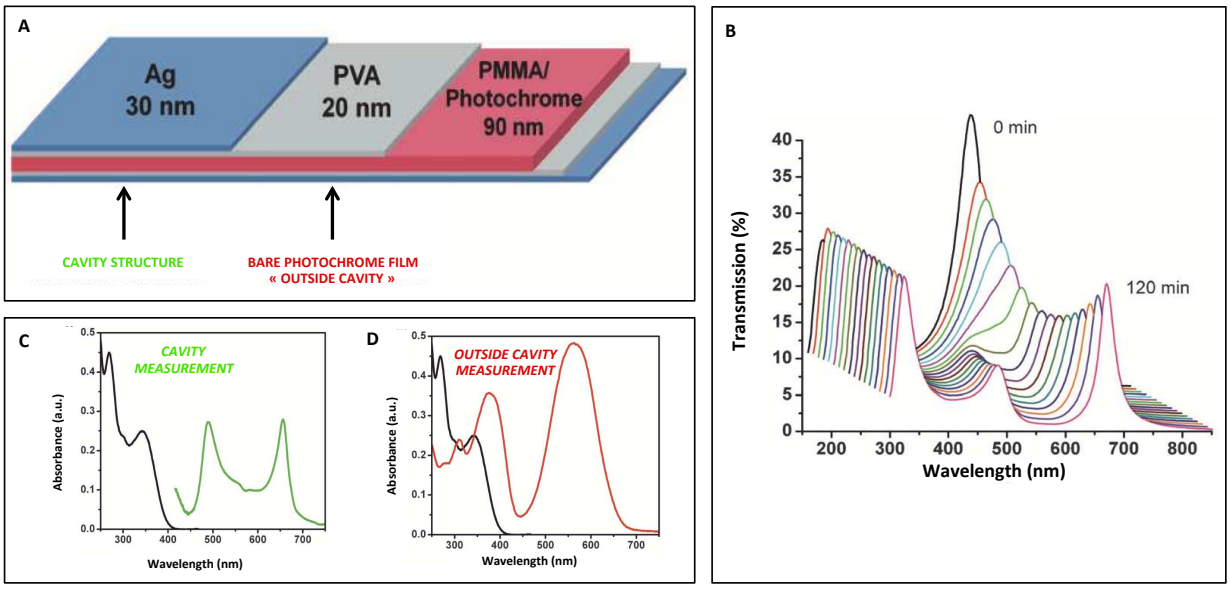

Figure 35. A. Schematic representation of the cavity structure. On the left, the PMMA film containing the photochrome is sandwiched between two Ag mirrors insulated from direct contact to the Ag by thin PVA film. The assembly of the two mirrors provides the cavity structure for the so-called cavity experiments. The non-cavity experiments are performed by using only one Ag mirror to avoid cavity resonance to be established (right region). The cavity (two Ag mirror) and outside cavity (one Ag mirror) experiments were done on the same film. **B.** Transmission of the coupled system (cavity measurement) as a function of irradiation time at 330 nm. The absorption band of the initial cavity mode at ca. 560 nm (black curve) splits into two new absorption bands as the SPI to MC photoisomerization proceeds. **C.** Absorption spectrum of SPI (black curve) in PMMA film and of strongly coupled MC inside the cavity (green curve) determined experimentally in the available wavelength window by measuring the transmission T and reflection R of the sample (Abs = 1-T-R). The absorption spectrum of the SPI form (black curve) is not affected. **D.** Absorption spectrum of SPI (black curve) and MC (red curve) in PMMA film outside the cavity.

Transmission data accounting for the progression of the formation of MC in cavity **(Figure 35B)** and in outside cavity experiments (not shown) were used to calculate the absorbance, and thus, the concentration of MC at each time. A comparison was done between the kinetic build-up of MC during irradiation of the resonant cavity and of the bare molecular film with UV light of constant intensity at 330 nm. At the start of the reaction, the measured rates were similar for the two systems but as the photoisomerization proceeded, the observed rate was slowed down significantly in the case of the cavity structure. This delay is a consequence of the onset of strong coupling conditions and the formation of hybrid light-matter states. The larger the splitting, the slower the overall reaction. Hence, the change in rate cannot be attributed to a simple optical effect. At the photostationary state[126], the final concentrations of the species were also modified, increasing the MC yield in the cavity by ca. 10%. Furthermore, it was verified that when the cavity was designed in such a way to be ouf of resonance (at all angles) with the MC absorption transition, there was no change in rate compared to the “outside cavity” experiments.

The effect of strong coupling in the vacuum field must be differentiated from phenomena such as the acceleration of photochemical reactions in the strong field, which is generally achieved by means of controlled laser pulses, precisely defined in time and intensity and where the molecules retain their electronic structure. Instead, it can be seen as analogous to a catalyst, which changes the reaction rate by modifying the energy landscape **(Figure 36)**.

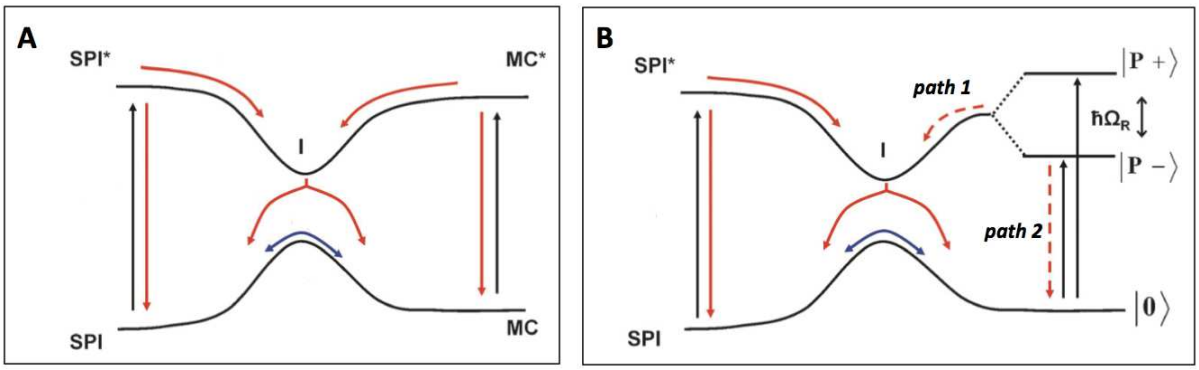

Figure 36. A. Simplified energy landscape diagram connecting the two isomers SPI and MC in the ground and first excited state SPI* and MC*. **B.** Simplified energy landscape diagram connecting the two isomers in the ground and first excited state. Due to strong coupling the MC* state is turned into the polaritonic states $|P+\rangle$ and $|P-\rangle$, separated by the Rabi splitting energy $\hbar\Omega_R$.

The full kinetic study will not be discussed in details here, but it revealed that the $|P+\rangle$ state was too short-lived to be detected. In fact, it decayed rapidly to $|P-\rangle$, which is less energetic than the MC* uncoupled excited state **(Figure 36)**. As a result, return to the ground state **(Figure 36B, path 2)** was favored over photoisomerization to the SPI form **(Figure 36B, path 1)**. The ESC effect is favored by higher concentrations but not just simply by increasing the collision rates, as it is the case for regular chemical reactions; it also modifies the energy landscape of the molecular ensemble.

The strong coupling was done here to an electronic transition but, after a reminder about molecular vibrations **(see section I.5.1.)**, we will see that it can also be reached in the case of specific vibrational transitions, even in the liquid phase **(see section I.5.2.1.)**, for instance to modify the ground-state reactivity of a chemical compound **(see section I.5.2.2.)**.

I.5. VSC FOR THE CONTROL OF CHEMICAL REACTION

I.5.1. MOLECULAR VIBRATIONS AND VIBRATIONAL ENERGY

Because they absorb energy from their surroundings, mainly in the form of heat or electromagnetic radiation, molecules are permanently moving. They can rotate, translate or vibrate. Rotation and translation, which I will no longer discuss in this section, move a molecule in space while its atoms stay the same distance apart. Vibrations, on the other hand, change those distances and alter the shape of the molecules. If there is a change in vibrational energy that is high enough, the molecule can transition from its ground state to what is called an excited vibrational state.

Let us consider the case of a very simple diatomic bond formed by combination of two atoms. When the electronic clouds of the atoms overlap, it lowers the energy of each partner. This enables the formation of the bond, whose energy is then lower than the sum of the individual energies of its constituent atoms. The potential energy diagram of a diatomic bond (Morse potential) is shown in **Figure 37**.

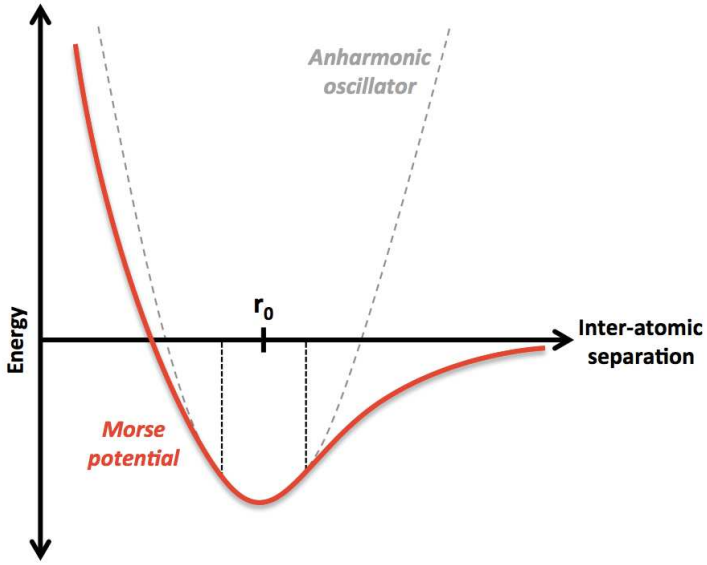

Figure 37. Potential energy diagram of a diatomic bond. The red curve represents the variation of potential energy of a diatomic bond as a function of the inter-atomic separation and is often referred to as the Morse potential. The optimum interatomic separation distance r_0 corresponds to the lowest possible energy state of the bond. The grey dash line represents the potential energy curve of a simple harmonic oscillator. The region between the two black dashed lines is where the inter-atomic separation fluctuates permanently in the ground state.

According to quantum mechanics, electron clouds are not stationary but they are rather always fluctuating. The separation distance between the two atoms of a diatomic bond oscillate back and forth between separation values that are very close to an optimum value r_0 where the potential energy decreases to its lower in energy and most stable state **(Figure 37)**. Thus, there is a very high probability that the separation distance of the considered diatomic bond lies within the region bounded by the black dashed lines in **Figure 37**, while there is a very low probability of it being outside this region. This delimited portion of the curve resembles the curve of a simple harmonic motion **(Figure 37, grey dash line)**. Therefore, regarding the displacement around r_0, a diatomic bond is considered to behave as a simple harmonic oscillator with a frequency of oscillation ν_{bond} and a vibrational energy E_{vib} **(see part I.2.1).** When the bond is in the ground state (v = 0), it still has a certain vibrational energy known as the ZPE. A set of quantum mechanical rules known as the selection rules determines whether transitions are allowed or forbidden. For vibrational transition, the selection rule states that the change in quantum number Δv must be +1 or -1 and necessitate a change in the dipole moment of the bond. This leads to several different types of vibration, such as bending, twisting, scissoring, and others.

I.5.2. VSC OF MOLECULAR RESONATORS IN MICRO-CAVITIES

Molecular resonators can undergo VSC by interaction with a mode of the electromagnetic field inside a micro-cavity resonator, leading to the creation of polaritonic states by Rabi-splitting. While the interaction happens through an electronic transition in ESC, it proceeds through a vibrational transition in VSC **(Figure 38)**.

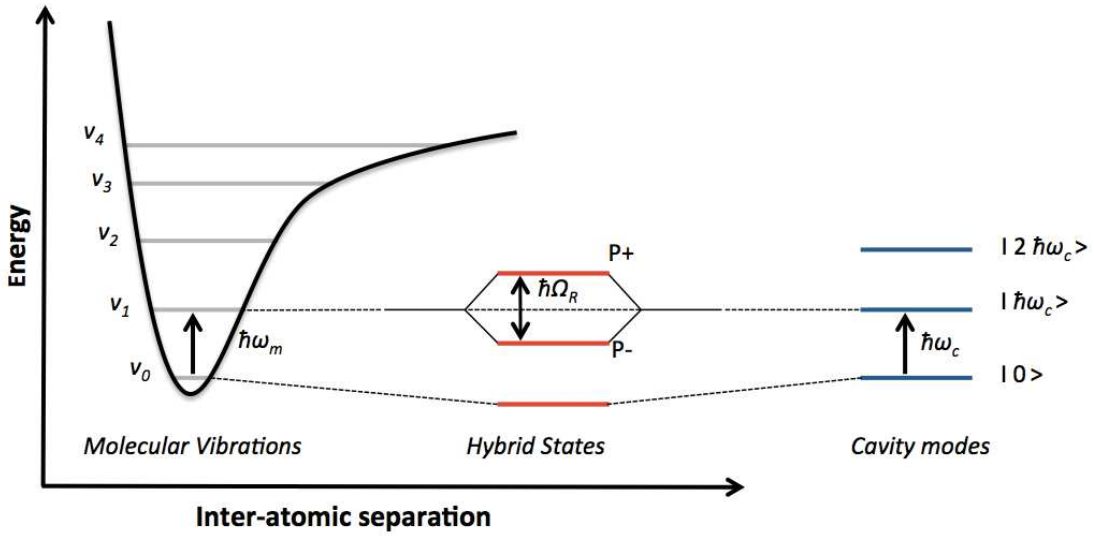

Figure 38. Simplified energy diagram showing the interaction of a vibrational transition (v_0 to v_1) of a molecule resonant with a cavity mode $\hbar\omega_c$. The two hybrid light–matter (or polaritonic) states, $|P+\rangle$ and $|P-\rangle$, are separated by the Rabi splitting energy $\hbar\Omega_R$.

In organic molecules, vibrational transitions typically occur between 400 and 4000 cm^{-1}. This wavenumber interval corresponds to vibrational frequencies ω_m ranging from $1.2x10^{13}$ s^{-1} to $1.2x10^{14}$ s^{-1} (as $\omega_m = \left(\frac{1}{\lambda}\right) c = \bar{\nu} c$). The frequency of FP cavity modes is given by:

$$\omega_c = m\left(\frac{c}{2nL}\right) \quad \textbf{(Equation 15)}$$

where m is the mode order, c is the speed of light, n is the refractive index of the medium inside the cavity and L is the distance between the two mirrors. If we consider the first mode of a cavity whose inner medium has a refractive index of 1 (m = 1, n = 1), ω_c can be tuned to be in resonance with ω_m by varying cavity lengths L between 1.25 and 12.5 µm. Thus, as the refractive index n of organic molecules is typically found between 1.3 and 1.8,[127] coupling between resonance modes of a cavity and vibrational transitions of a molecular resonator

can be easily achieved in micrometric FP cavities **(see section IV.1.5.)**. It can be expected that the resonant interaction between a cavity mode and a molecular vibration, resulting in the formation of two new vibrational polaritonic states by Rabi splitting, would have an impact of the bond strength f as $\omega_m \propto \sqrt{\frac{f}{\mu}}$, where μ is the reduced mass of the atoms involved and thus, on the chemical properties and associated chemistry.

I.5.2.1. LIQUID-PHASE VSC

In 2015, Ebbesen & co-workers demonstrated experimentally for the first time that light-matter strong coupling of simple organic molecules could be extended to vibrational transitions,[6] including in the liquid phase by using a micrometric flow-cell FP cavity (**Figure 39A**).[12] Prior to this, light-matter strong coupling was mainly used in the context of ESC, for instance in order to modify solid-phase photochemical reaction rates **(see section I.4.1)** and the work function or the conductivity of organic semiconductors.[5,120,121,128,129] The flow-cell device allows the injection of liquid samples inside the FP cavity. An inert polymer spacer can be placed between the two mirrors in order to tune the length of the cavity by varying the size of the spacer. A fine-tuning of the length of the cavity can be done by tightening or loosing the four screws of the flow-cell **(Figure 39A)**. The mirrors of the FP cavity that were used in this study were made of zinc selenide (ZnSe) windows coated with a 10 nm gold (Au) layer **(Figure 39B)**. Such a cavity has a series of resonances, which are multiples of the fundamental cavity mode and depend on the refractive index of the medium inside the cavity as seen in **Eq. 15**. An example of the Fourier transform IR (FT-IR) transmission spectrum obtained for a FP cavity with a path length of 8.6 µm is shown in **Figure 39C**.

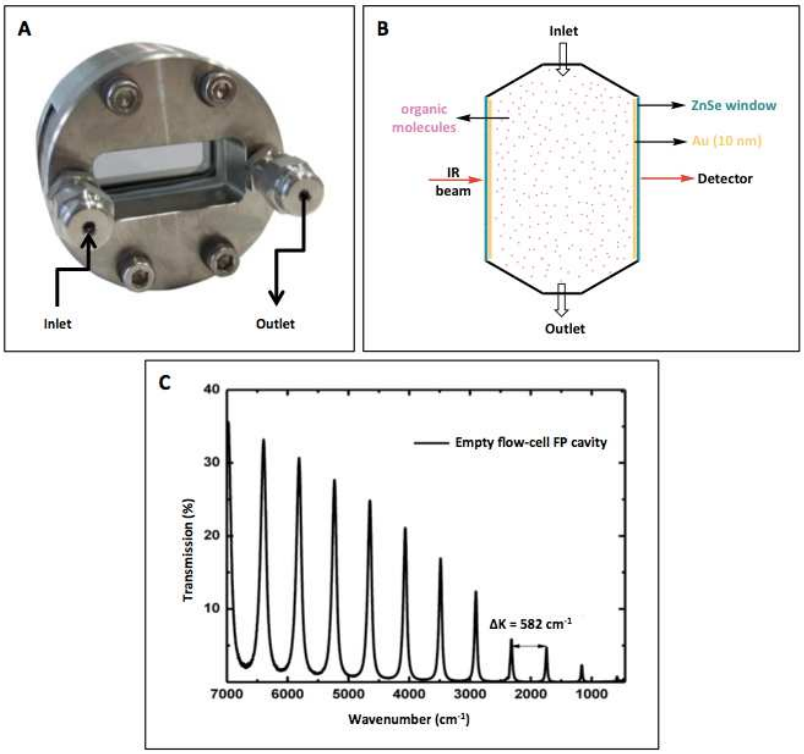

Figure 39. A. Photograph of a flow-cell FP cavity **B.** Schematic representation of the flow-cell FP cavity. **C.** FT-IR transmission spectrum of an empty flow-cell FP cavity showing its measured optical resonances. The length L between the two mirrors is 8.6 µm. The decreasing peak intensities at short wavenumbers are due to the evolution of the dielectric constants of the Au mirrors in this spectral region. Adapted from reference [12]

Four different organic compounds were strongly coupled separately in the liquid phase. Their respective structures are shown on the insets of **Figure 40**, which show their IR absorption spectra **(Figure 40, black curves)** together with those under VSC **(Figure 40, red curves)**. The procedure for the cavity tuning will be explained in detail in the experimental part of this thesis **(see section IV.1.5.)**.

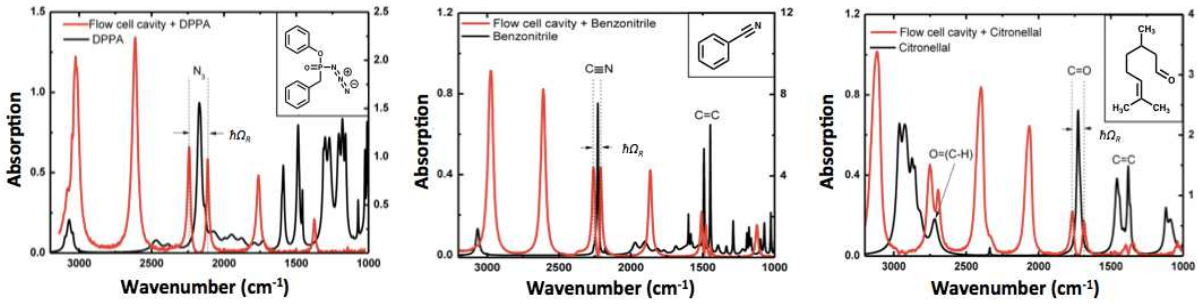

Figure 40. IR absorption spectra of three molecules (black curves, in absorption) that have been strongly coupled with the Fabry-Perot cavity modes (red curves). From left to right: diphenyl phosphoryl azide (DPPA), benzonitrile and citronellal.

The IR absorption spectrum of diphenyl phosphoryl azide (DPPA) displays a number of sharp vibrational peaks but the strong and isolated azide ($R\text{-}N{=}N^{+}{=}N^{-}$) stretching mode at 2169 cm^{-1} was of particular interest **(Figure 40, left spectrum)**. The cavity was tuned to have one of its modes in resonance with this peak, resulting in the formation of two new hybrid modes on either side of the original frequency. The measured *vacuum* Rabi splitting (127 cm^{-1}) satisfied the criteria for strong coupling as it was higher than both the FP cavity mode (43 cm^{-1}) and the vibrational band (39 cm^{-1}).

In the case of benzonitrile, the cavity was adjusted so that more than one mode was strongly coupled, as can be seen in the red spectrum on the middle of **Figure 40**. The cyanide group (R-CN) has a stretching frequency at 2229 cm^{-1} whose absorption band split into two new peaks at 2260 and 2206 cm^{-1}. It was assumed that the smaller splitting (54 cm^{-1}) as compared with DPPA was probably due to both the lower absorption and the smaller full width at half maximum (FWHM) of the original vibrational mode. Interestingly, at ~1500 cm^{-1}, the two aromatic C=C modes are close to each other. When coupled to the same optical mode, they revealed a double splitting.

Finally, the C=O stretch of two very similar compounds, hexanal (not shown) and citronellal **(Figure 40, right spectrum)** were strongly coupled. They exhibit a Rabi splitting of 105 and 80 cm^{-1} respectively. Furthermore, the authors showed an interesting correlation between the calculated integrated absorption coefficients of the different bonds and the splitting observed in the experiments. As predicted by **Eq. 15 (see sub-section I.3.2.2.3)**, these experimental results clearly show that the splitting scales with the integrated extinction coefficient, emphasizing the effect of the transition dipole moment on the interaction strength.

I.5.2.2. GROUND-STATE CHEMICAL REACTIVITY UNDER VSC

In the 1980s, Pimentel and co-workers demonstrated that it was possible to influence the result of simple reactions by using IR lasers at cryogenic temperatures, in order to minimize competing thermal effects and relaxation processes.[130,131] Alternatively, and as we have seen in the previous section, by offering the possibility of perturbing the energy levels of a given chemical molecule in one or more of its chemical bonds in the liquid phase and

under mild temperature conditions, VSC opens up an unprecedented opportunity for the control of chemical reactions in the ground state, since IR light excitation is no longer necessary. This topic is of particular interest as it can lead to site-selectivity, as we will see in the next chapter, or enable the elucidation of reaction mechanism. The effect of VSC on chemical reactions was revealed for the first time in 2016, through a collaborative work in which the Ebbesen and Moran research teams studied the very simple case of a deprotection reaction of an alkynyl silane, 1-phenyl-2-trimethylsilylacetylene (PTA), by tetra-*n*-butylammonium fluoride (TBAF) **(Figure 41)**. This system offers several practical advantages for the implementation of VSC. Firstly, PTA is a pure liquid and can therefore be injected directly into a microfluidic FP cavity in a homogeneous manner. Secondly, it is quite straightforward to selectively target a vibrational mode of the reagent, since there are relatively few of them that are well-defined and strongly absorbing. Lastly, the deprotection reaction occurs with pseudo first-order pseudo kinetics on a time scale of a few minutes, so that it can be monitored by FTIR spectroscopy at different time intervals.

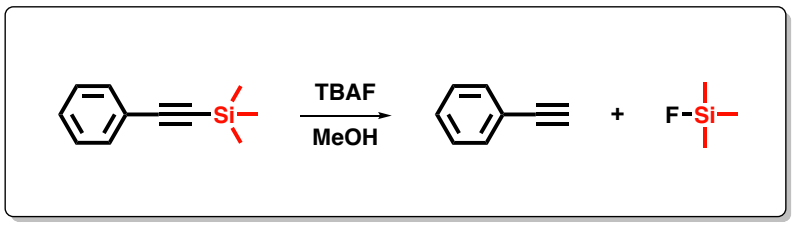

Figure 41. The silane deprotection reaction of 1-phenyl-2-trimethylsilylacetylene

Again, the mirrors that were used to build the FP cavity were parallel and made of ZnSe coated with Au, but this time, SiO_2 was sputtered on the Au layer in order to prevent any influence of the metal surface on the reaction. The distance between the mirrors was on the order of 6 µm and could be tuned precisely to be in resonance with any vibrational transitions of the reactant **(see IV.1.5. for a detailed procedure for cavity tuning)**. The FT-IR transmission spectrum of the reaction mixture in the confined field of an on-resonance cavity is shown in **Figure 42A**. The absorption band corresponding to the stretching modes of the Si-C bond at 860 cm^{-1} **(Figure 42B, intense signal on the blue curve)** splits into two new bands due to Rabi splitting **(Figure 42B, red curve)** when the cavity was tuned to be resonant with it. It can be noticed that another cavity mode coincided exactly with the stretching mode of the C≡C bond at 2160 cm^{-1}, but the interaction did not meet the criterion for strong coupling.

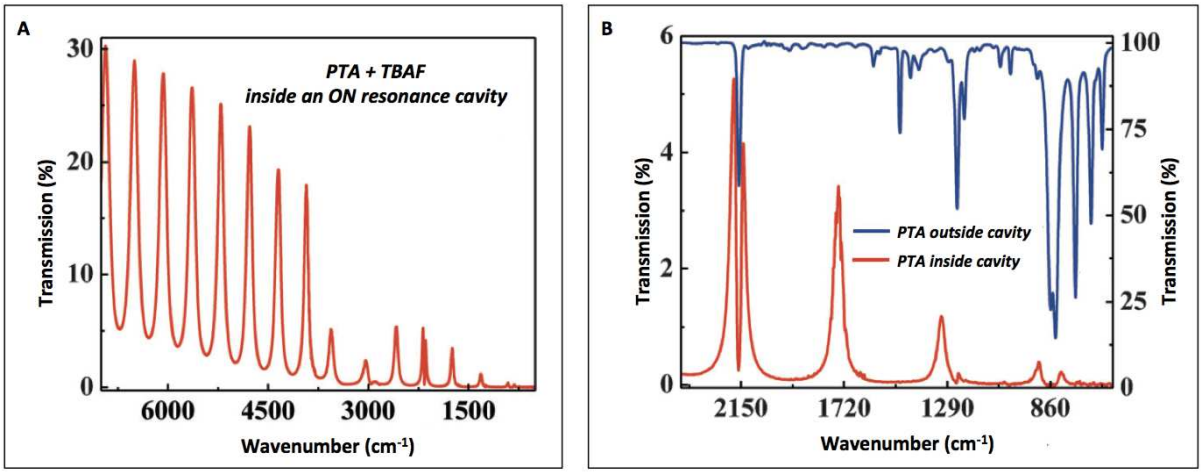

Figure 42. A. FT-IR transmission spectrum from 7000 to 500 cm^{-1} of the reaction mixture inside an on-resonance cavity immediately after injection. **B.** FT-IR transmission spectrum of PTA inside (red trace) and outside (blue trace) an on-resonance cavity. Taken with permission from reference [1].

The reaction was run inside a FP cavity that was either tuned to (on-resonance) or detuned from (off-resonance) the stretching mode of the C-Si bond. The detuned case served as a control experiment for the kinetics in the absence of VSC. An additional control experiment was carried out in an experimental setup where the mirrors of the cavity are replaced by bare ZnSe windows. The evolution of the system was followed by FTIR spectroscopy. In the next chapter, I will explain in detail how this can be done, but for now, the important result to be noted is that the rate constants in tuned and detuned cavity experiments were very different. In the resonant cavity, under VSC, the reaction rate constant decreased by a factor of 4.5 compared to the detuned cavity that gave roughly the same rate as a reaction outside the cavity. As expected from theory **(see sub-section I.3.2.2.3., Eq. 14)**, the authors demonstrated experimentally that the Rabi splitting energy depends on the square root of the PTA concentration ([PTA]). Thus, by varying [PTA], the authors were also able to show the non-linear dependence of the reaction rate on the Rabi splitting. The retardation of the reaction observed under VSC increased with the Rabi splitting. In addition, the change in reactivity was monitored qualitatively by gas-chromatography coupled with mass spectrometry (GC-MS) after 20 min. **Figure 43** shows the gas-chromatography (GC) chromatograms obtained by injection of the reaction mixture into the GC-MS column. The product/PTA ratios for the experiments in resonant cavities were totally different from those of the control experiments, reinforcing the evidence already provided by spectroscopic analysis that the observed changes in reaction rate were actually due to changes in the reactivity of PTA itself. Whereas product formation was clearly

retarded in the resonant cavity, the product distributions for the two control experiments were similar (the small variation in the reactant peak being within the experimental error of the measurement).

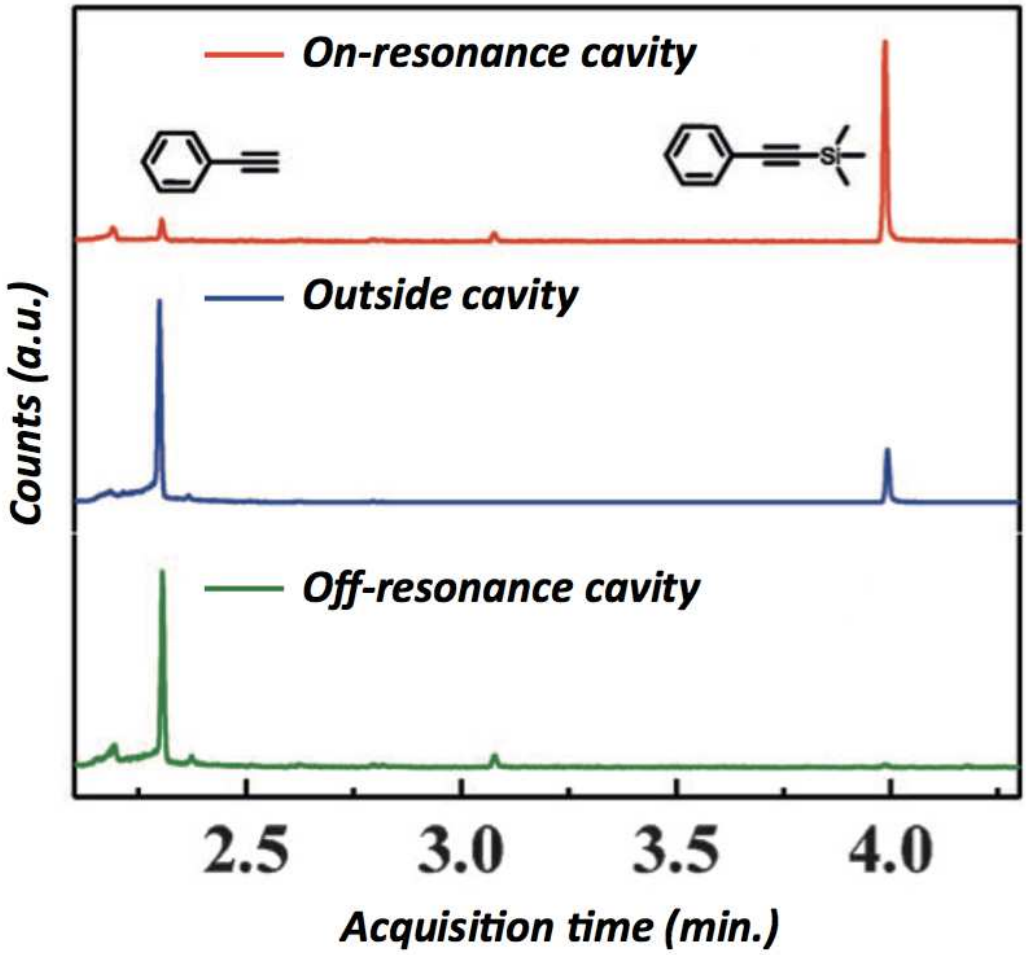

Figure 43. GC-MS chromatograms of silane deprotection reactions carried out inside an ON resonance cavity (red trace), an OFF resonance cavity (green trace), and outside the cavity (blue trace). Taken with permission from reference [1].

Finally, the reaction rate was also measured as a function of the temperature, allowing the extraction of the thermodynamic parameters associated with the transition state (TS): the enthalpy $\Delta H^{\ddagger}$ and entropy $\Delta S^{\ddagger}$. Under VSC, $\Delta H^{\ddagger}$ increased from 39 to 96 kJ.mol^{-1} while $\Delta S^{\ddagger}$ increased from -171 to 7.4 J.K^{-1}.mol^{-1}. These two very large and significant changes give insight about the changes in the chemical landscape induced by VSC. First of all, the reaction barrier increases under VSC as indicated by the increasingly positive enthalpy of activation. More importantly, the change in the sign of the entropy suggests a change in the nature of the TS.

The authors demonstrated here that VSC can be used as a tool, working in the dark and at room temperature, for the control of chemical reactions by significantly modifying energetic landscapes, providing a new approach for studying reaction mechanisms. The results are even more impressive because in the cavity, not all molecules are coupled simultaneously since they are randomly oriented in solution while the coupling depends on the alignment of their dipole transition moments with respect to the EM field. During my PhD, I have contributed to a study revealing that VSC could also be used to tilt the selectivity of a chemical reaction.[2] This work will be presented in detail in the following chapter.

CHAPTER II

II. TILTING A GROUND STATE REACTIVITY LANDSCAPE BY VSC

II.1. INTRODUCTION

In recent years, many methods have been developed by chemists for the implementation of chemo-, regio- or stereo-selective reactions. These methods generally involve reaction sequences based on protection-deprotection strategies and/or often tedious functionalization processes. Various catalysts and reagents have been developed for this purpose, but they only allow for the differentiation of functional groups with pronounced steric and electronic differences.

As mentioned in the general introduction, our team has shown that the ground-state reactivity landscape of a simple chemical reaction can be modified under VSC and can therefore change its properties, such as its rate. The desilylation of PTA, an alkynyl silane, was chosen as a model reaction during this previous work **(see sub-section I.5.2.2)**. In the work I will present now, we went one step further and used the light-matter hybridization between an organic molecule and quantum *vacuum* fluctuations within a flow cell FP cavity to influence the site-selectivity of a chemical reaction by the unique approach offered by VSC. To explore this possibility, we searched for a compound that would be structurally close to the PTA and that could be deprotected on two different sites in roughly similar rates, resulting in an approximately equal products distribution. Towards this goal, I initially synthesized two PTA analogues, **(A1)** and **(A2)**, with different silyl ether groups in *para* position to the trimethylsilyl (TMS)-protected alkyne **(Figure 44)**.

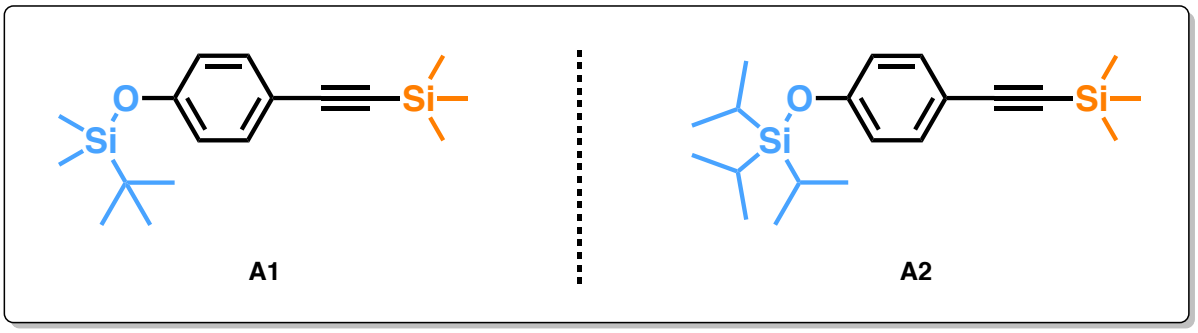

Figure 44. The structure of the two PTA analogue candidates, **(A1)** and **(A2)**, that were initially synthesized with the aim of being used as reactants to probe the influence of VSC on site-selectivity. *Tert*-butyldimethylsilyl (TBDMS) and triisopropylsilyl (TIPS) moieties were installed on iodophenol by reaction with their corresponding imidazole-activated silyl chloride, for the synthesis of **(A1)** and **(A2)** respectively. The TMS-alkynyl groups were installed subsequently by Sonogashira coupling.

The two PTA analogues, **(A1)** and **(A2)**, were both exposed to different TBAF concentrations (0.15, 0.5 and 1 equiv.) in MeOH for deprotection reaction tests. Unfortunately, in both cases, only O-deprotection was observed after 1 h of reaction. Considering the difference in pKa between phenol (pKa = 18.0)[132] and phenylacetylene (pKa ~ 26.5)[133], it was not really surprising that the O-deprotection was highly favored compared to the C-deprotection. Furthermore, complete conversion was reached with 0.5 and 1 equiv. of TBAF in the case of **(A1)**, but only with 1 equiv. of TBAF for **(A2)**. This was expected, given the relative stability of TBDMS (20 000) compared to TIPS (100 000)[134]. In light of these observations, I have synthesized the silane derivative, tert-butyldimethyl{[4-(trimethylsilyl)but-3-yn-1-yl]oxy]silane **(R)**[10,11], for which the pKa difference between the two distinct silyl groups should be less pronounced due to the absence of the phenyl ring. As the deprotection reaction did not occur in pure MeOH, tetrahydrofuran (THF), which is also employed in deprotection reactions of silyl ether,[134] was used as a co-solvent. Under these conditions, the nucleophilic attack of one of the two silicon atoms by a fluoride ion result in the formation of product **(1)** after breaking the Si-C bond or product **(2)** after breaking the Si-O bond **(Figure 45)**.

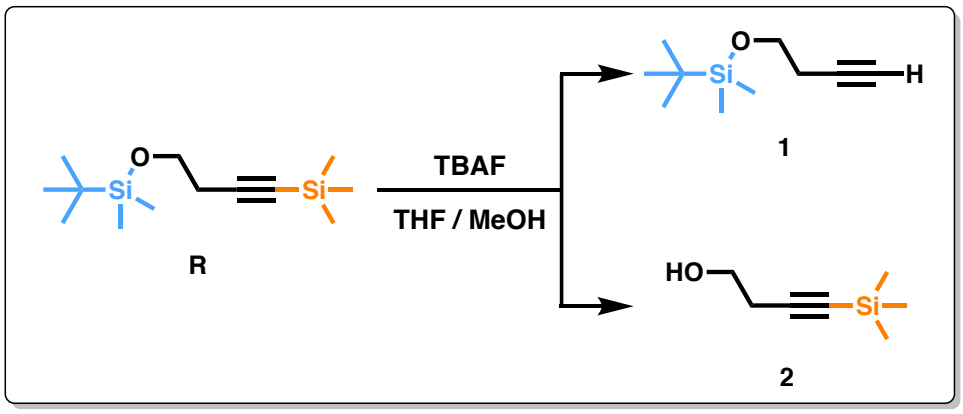

Figure 45. The reaction of deprotection of **(R)** with TBAF in a mixture of THF/MeOH at room temperature has been chosen as a model reaction to probe the influence of VSC on site selectivity.

The THF/MeOH ratio was optimized in order to get an approximately equal distribution between products **(1)** and **(2)** after 1h of reaction. Five different THF/MeOH ratios, varying from [3/7] to [7/3], were screened. As shown in **Table 4**, the best results were obtained in THF/MeOH [4/6] and [5/5], where the uncorrected GC-MS peak area ratio $\frac{\mathbf{1}}{\mathbf{2}}$ was equal to 2. The latter condition was maintained for the VSC experiments because it provided better solubility.

Table 4. $\frac{1}{2}$ ratios measured by GC-MS peak area integration after 1h reactions

THF / MeOH ratio	Uncorrected GC-MS peak area ratio $\frac{1}{2}$
3/7	3
4/6	2
5/5	2
5/6	4
3/7	10

The mechanism of fluoride-induced deprotection of a silane proceeds in two mechanistic steps **(Figure 46)**. In the first step, the fluoride anion attacks the silicon atom to produce a pentavalent intermediate. In the second step, the intermediate collapses expelling the leaving group. Usually, the first step is the rate-determining step. It should be noted that the herein described mechanism is associative and therefore has a negative entropy of activation.[135]

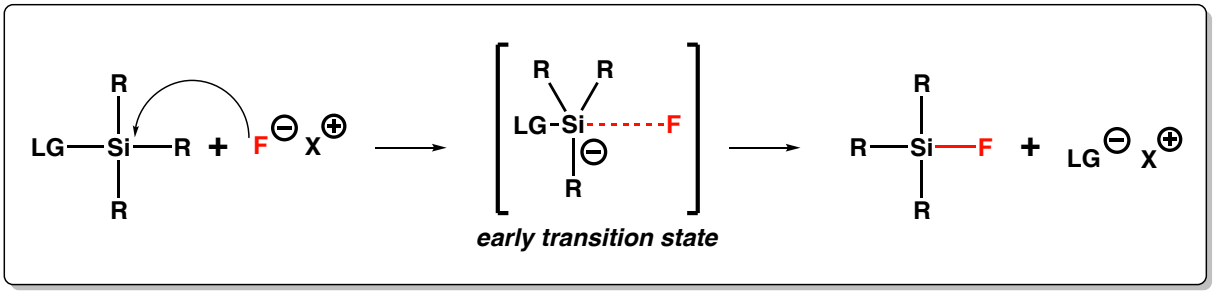

Figure 46. Mechanism of fluoride-induced deprotection of a silane.[135] The early TS resembles the reactant and is strained, therefore a large negative $\Delta S^{\ddagger}$ is expected.[136–138]

Because the formation of both products **(1)** and **(2)** occur through similar mechanistic pathways, we explored first whether the selective strong coupling of vibrational modes respectively associated with Si–C and Si–O has similar or different influences on the reactivity. The second and most important point of the present study was to ascertain whether changes in the reactivity landscape under VSC lead to site-selectivity and thereby changes to the branching ratio of the products as schematically presented in **Figure 47**.

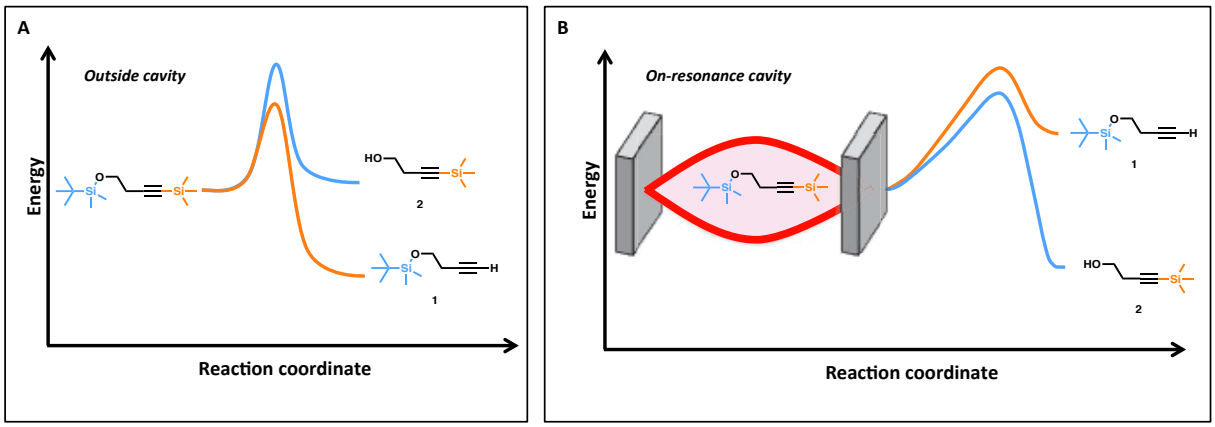

Figure 47. Schematic representation of the competing site-selective pathways outside cavity and upon VSC of the reactant in a resonant cavity.

The FP optical cavity used in the experiments performed here was assembled from two parallel metal mirrors made of Au (10 nm) sputtered on ZnSe IR-transmitting windows (2mm). To ensure that the reaction was not affected by the presence of both Au and ZnSe, a 200 nm layer of glass (SiO_2) was deposited on the inner surface of each mirror. The metallic mirrors were separated by a polyethylene terephthalate (PET - Mylar®) spacer of variable thickness with a hollow central channel designed for the injection of liquid samples **(see sub-section I.5.2.1, Figure 39)**. To prepare the different on- and off-resonance cavities in the present experiments, the thickness of the Mylar spacers used were varied in the range of 6 to 12 µm. The area of the cavity was 1 cm x 2.5 cm. The tuned part is typically 60% of this area because the four screws we are using to tune the cavity exert pressure on the flat windows, slightly deforming them. This aspect was systematically checked, by taking the spectrum of the cavity at different points using a small aperture of 2 mm in diameter. The reaction was monitored through a tuned area of the cavity using an aperture of 5 mm in diameter. The absolute yields of products that have been measured are corrected for the tuned area **(see section IV.1.10)**. For control experiments, described as “outside cavity“ experiments, the flow-cells were prepared in a similar manner as explained above but the metallic mirrors were replaced with bare glass coated ZnSe windows.

II.2. RESULTS AND DISCUSSION

II.2.1. IR CHARACTERIZATION OF THE SYSTEM UNDER STUDY

The reaction mixture consisted of a homogeneous solution of starting material **(R)** (0.90 M) and TBAF (0.86 M) in a 1:1 (v/v) mixture of MeOH and THF. These conditions have been optimized for strong coupling by maximizing the concentration of **(R)** to achieve the highest Rabi splitting value while maintaining a good solubility of **(R)** in the solvent system. The IR spectrum of **(R)** in the MeOH/THF mixture has been recorded outside the cavity and shows the characteristic intense bands of the Si-C (842 cm^{-1}), Si-O (1110 cm^{-1}) and Si-CH_3 (1250 cm^{-1}) bonds corresponding to their elongation (for Si-C and Si-O) and torsion (for Si-CH_3) modes **(Figure 48)**.

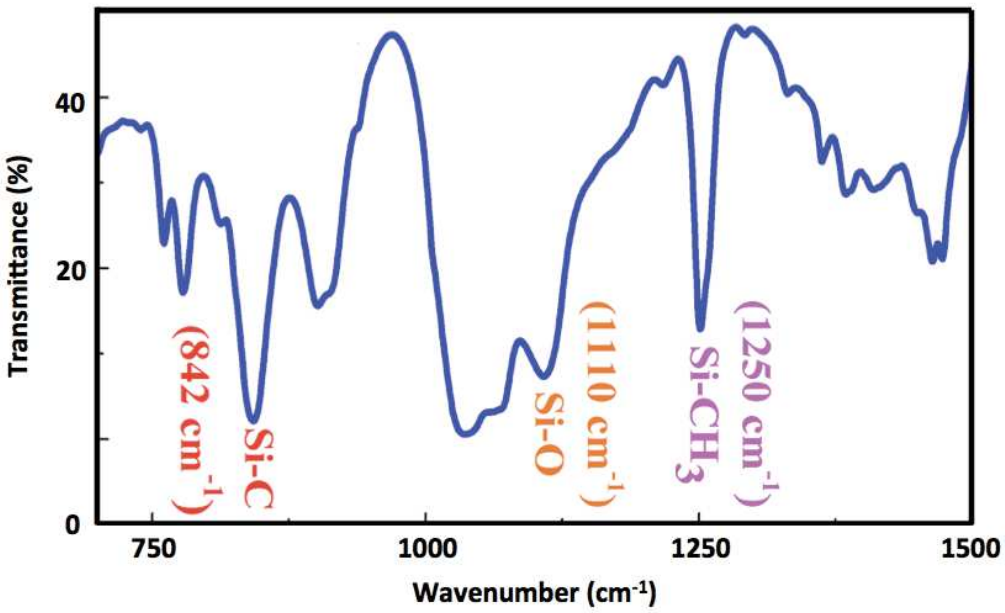

Figure 48. FT-IR transmission spectrum of the starting material **(R)** in the reaction mixture recorded in a flow-cell, with glass-coated ZnSe windows separated by the same spacer thickness as of the FP cavity.

To reach the VSC regime, it was necessary to tune the cavity modes so that one of them was resonant with a specific IR transition of **(R)**. This was achieved through careful adjustment of the spacer thickness by tightening or loosening the screws holding the mirrors assembly together in order to vary the applied pressure **(for a detailed procedure, see section IV.1.5.)**.

When the second mode of the flow-cell FP cavity was precisely tuned to 842 cm^{-1} and after injection of the homogeneous reaction mixture, two new bands corresponding to the polaritonic states P+ and P- appeared on the IR spectrum due to strong coupling of the Si-C stretching transition **(Figure 49A)**. The observed Rabi splitting $\hbar\Omega_R$ of 70 cm^{-1} showed that the system meets the strong coupling criteria **(see sub-section I.3.2.2.3)** as it was larger than the width of the cavity mode (30 cm^{-1}) and the Si–C vibrational band (30 cm^{-1}). Under these conditions, a largely detuned coupling between the bending mode of the CH_3 groups bonded to Si (Si–CH_3 at 1250 cm^{-1}) and the third mode of the cavity was also observed. The influence of the strongly coupled Si–CH_3 bending vibration on the reactivity was analyzed separately and will be described later in **section II.2.3.**.

In a different experiment, VSC of the Si–O stretching band was achieved by tuning the third mode of the cavity to 1110 cm^{-1} **(Figure 49B, solid line)**. The presence of the intense and broad vibrational modes of the solvents (1040 to 1060 cm^{-1}) splits and reduces the P- band intensity **(Figure 49B)** and complicates the spectrum analysis. In this case, we calculated the $\hbar\Omega_R$ using the standard optics technique **(transfer matrix simulation, as explained in IV.1.2.) (Figure 49B, dotted line)**. The extracted value of 85 cm^{-1} is well above the cavity and IR mode widths.

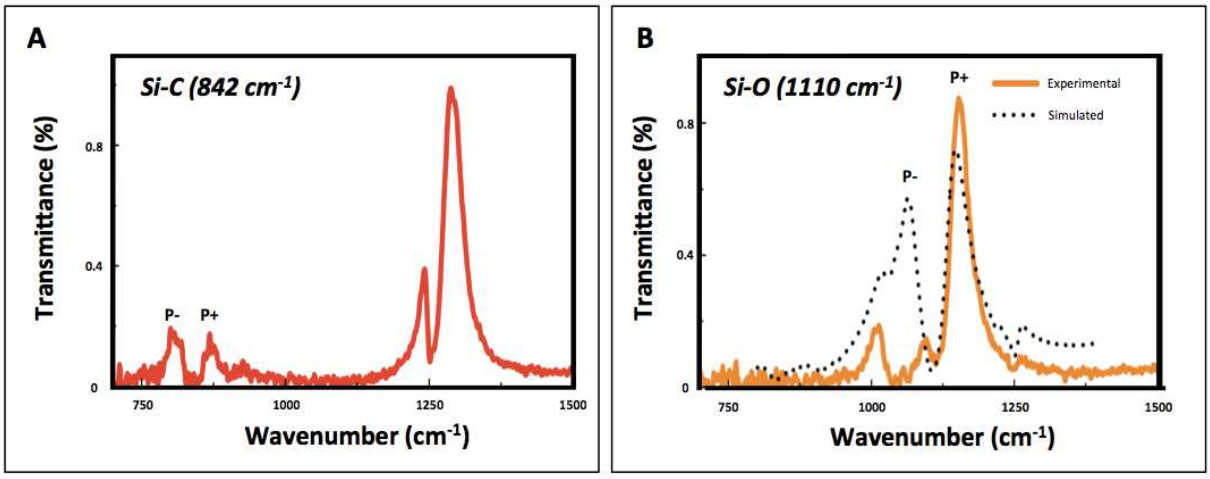

Figure 49. FT-IR transmission spectra showing P+ and P- splitting when two different modes are strongly coupled to the cavity. **A.** The coupling of the Si–C stretching mode **B.** The coupling of the Si–O stretching mode together with a transfer matrix simulated transmission spectrum (black dotted line).

II.2.2. INFLUENCE OF VSC ON VIBRATIONAL TRANSITIONS FROM BONDS THAT ARE BROKEN DURING THE REACTION MECHANISM

II.2.2.1. KINETIC MONITORING OF THE REACTION RATE BY IR SPECTROSCOPY

The kinetic evolution of the reaction was monitored by IR spectroscopy, using a small aperture in the central tuned area of the FP cavity. The overall bond-breaking reaction rate of the two different silyl groups was quantitatively determined from the ln plot of the temporal shit of a high-order cavity mode (from $\bar{\nu}_0$ to $\bar{\nu}_t$). Indeed, the reactant and the product have slightly different reactive indices (1.39 versus 1.43 for product **(1)** and 1.44 for product **(2)**) resulting in a change of the background refractive index (n) of the reactive medium as the reaction progresses. Because the product ratio is constant, monitoring this shift allows one to extract the rate of the reaction, as explained in **section IV.1.6.**.As for the experiment discussed in sub-section I.5.2.2, this analysis was aided by the slight change in the refractive indices of the reactant and products. The linearity of the ln plot **(Figure 50)** supported first-order kinetics, and from the slope, the rate constant corresponding to the disappearance of starting material was determined. When the stretching vibration of the Si-C bond was strongly coupled to a cavity mode **(Figure 50, red squares)**, the reaction rate decreased by a factor of 3.5 ± 0.2 compared with the control measurements done outside the cavity **(Figure 50, blue squares)** or in an off-resonance cavity that was not tuned to any of the selected vibration transitions of **(R) (Figure 50, green squares)**. Similarly, the strong coupling of the Si-O bond stretching vibration to a cavity mode **(Figure 50, orange squares)** slowed the overall reaction rate by a factor of 2.5 ± 0.1 compared to measurements done outside the cavity or in a non-resonant cavity.

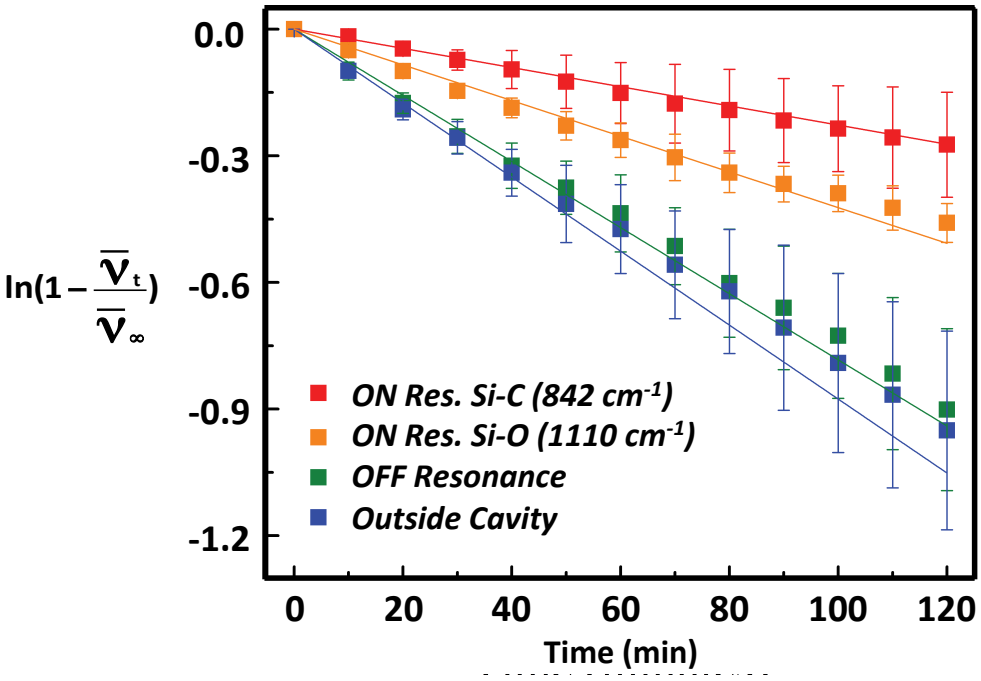

Figure 50. Kinetic data of the reaction carried out in cavities resonant with the vibrational modes of the Si-C bond stretching (red squares) and the Si-O bond stretching (orange squares) as well as in a non-resonant cavity (green squares) and outside the cavity (blue squares), as extracted from the temporal shifts in the higher-order cavity modes. The error bars show the standard deviation of at least five independent experiments.

II.2.2.2. DETERMINATION OF THE PRODUCT RATIOS BY GC-MS QUANTIFICATION

After each experiment, the reaction mixture was quantitatively analyzed by GC-MS in order to determine the ratio of product concentrations $\frac{[\mathbf{1}]}{[\mathbf{2}]}$ where [**1**] is the quantity of product **(1)** obtained by breaking of the Si-C bond and [**2**] the quantity of product **(2)** obtained by breaking of the Si-O bond **(Figure 51)**. The presence of unreacted starting material **(R)** in all the chromatograms showed that the reaction was far from completion in the 3-hour time period and that the ratio did not change over time within the limits of the experiments.

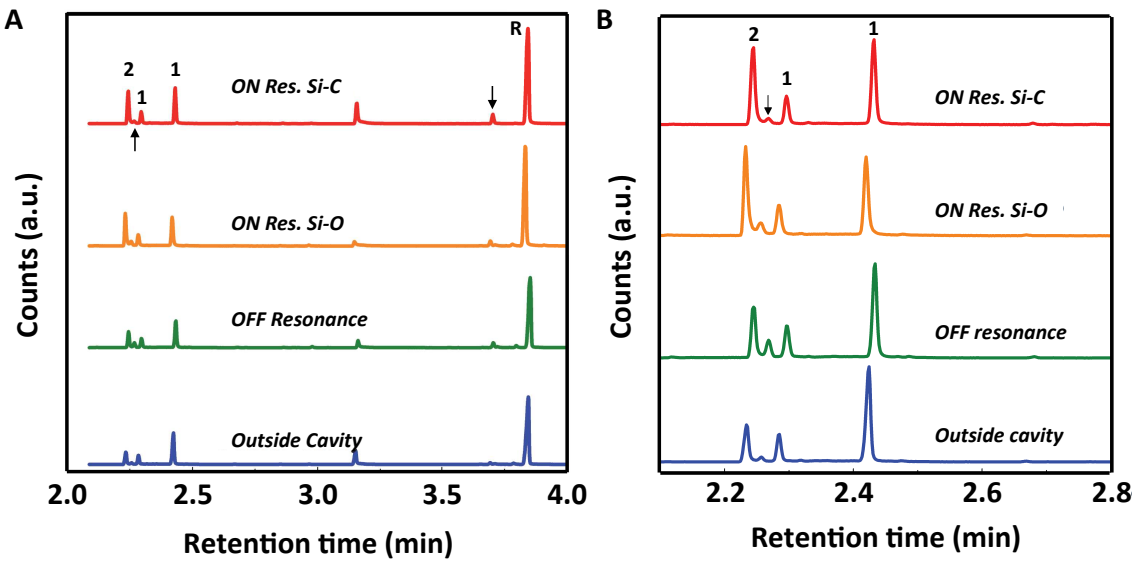

Figure 51. A. GC chromatograms of the reactions carried out in cavities tuned to be on-resonance with Si-C stretching (red) and Si-O stretching modes (orange), together with the data for an off-resonance cavity (green) and outside the cavity (blue). The unreacted starting material is marked as **(R).** The peaks corresponding to C- and O-deprotected products are marked as **(1)** and **(2)**, respectively. The peaks indicated by the arrows are impurities that come from the slow degradation of the GC-MS column and it is present in all the chromatograms that we measure. The peak at the retention time of 3.2 min corresponds to the TBAF, which is eluted as an ion pair in the GC column. **B.** For clarity, this is a zoomed version of the same GC chromatograms, focused on the products of the reaction.

For the reactions that were performed outside the cavity and in off-resonance cavities, the concentration ratios were equivalent within experimental error and indicated that product **(1)** was predominantly formed **(Table 5, entry 1 and 2)**. A significant increase in the formation of product **(2)** was observed when the stretching mode of the Si-C bond, appearing at 842 cm^{-1}, was strongly coupled to a cavity mode **(Figure 51B, red chromatogram)**, thus completely changing the distribution of the products **(Table 5, entry 3)**. A similar ratio was observed when the stretching vibration of the Si-O bond, appearing at 1110 cm^{-1}, was strongly coupled **(Table 5, entry 4)**. The values shown in **Table 5** take into account the fraction of the FP cavity under VSC, that is, as mentioned in part II.1., 60% of its total area. The remaining fraction is detuned beyond the width of the vibrational mode and, as a result, is in the off-resonance condition.

Table 5. Ratios of product concentrations $\frac{[1]}{[2]}$ extracted from GC-MS measurements.

Entry	Experiment	Product Ratio $\frac{[1]}{[2]}$
1	Outside cavity	1.5 ± 0.2
2	Off-resonance	1.4 ± 0.1
3	Si-C (842 cm^{-1})	0.3 ± 0.1
VSC		
4	Si-O (1110 cm^{-1})	0.3 ± 0.1

Thus, the VSC of any of the reaction sites directly involved in the scission of the Si-C or Si-O bonds modifies the reaction energy profile in such a way that it favors the breaking of the Si-O bond rather than the breaking of the Si-C bond which is normally kinetically preferred.

II.2.3. INFLUENCE OF VSC OF VIBRATIONAL TRANSITIONS OF A "SPECTATOR BOND"

Previous mode-selective chemistry experiments have shown that spectator modes - vibrations that are not directly linked to the reaction coordinate - also play a critical role in determining reaction outcomes.[13,14] In the present case, the strong IR band at 1250 cm^{-1} arising from the bending mode of the -CH_3 groups bonded to the Si atom[15], can be considered a spectator vibrational mode. If this -CH_3 group was isolated, one would expect to find this absorption band around 1460 cm^{-1}. The fact that it appears at 1250 cm^{-1} indicates that it actually interacts with other vibrations associated with the silicon atom.

The VSC of the Si-CH_3 bending mode was achieved without simultaneously coupling either the Si-C or Si-O stretching vibrations by varying the spacer thickness and with a $\hbar\Omega_R$ of 43 cm^{-1} **(Figure 52A)**. It had the effect of reducing the overall reaction rate by a factor of 3.5 ± 0.1 **(Figure 52B, magenta triangle)** and gave a product ratio $\frac{[1]}{[2]}$ of 0.3 ± 0.1 **(Figure 52C, magenta chromatogram)**, which is very close to the result obtained under VSC of the Si-C stretching transition.

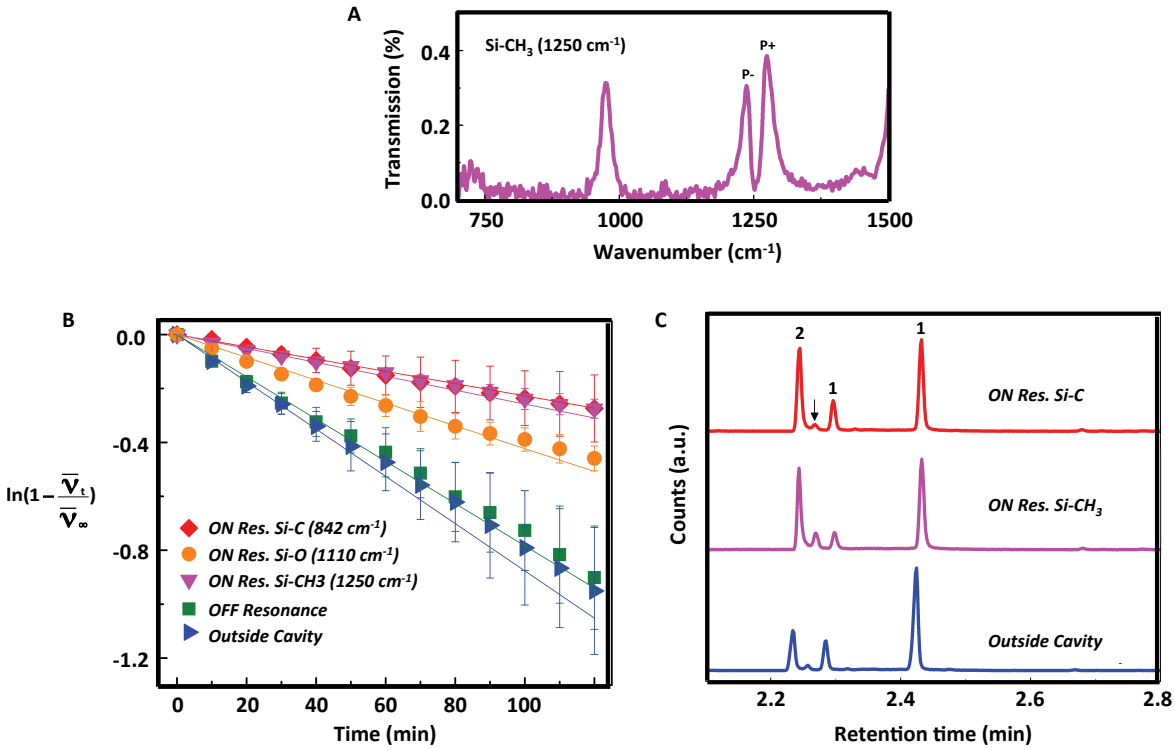

Figure 52. A. FT-IR transmission spectrum showing P+ and P- splitting when the Si–CH_3 bending mode is strongly coupled to the cavity. **B.** Kinetics of the reactions in cavities tuned to be on-resonance with the Si–CH_3 bending modes (magenta triangles). For a comparison, the data obtained in cavities on resonance with Si–C stretching (red diamonds) and Si–O stretching (orange circles) are shown together with the data for an off-resonance cavity (green squares) and outside the cavity (blue triangles). The error bars show the standard deviation of at least five independent experiments. **C.** The GC chromatograms of the reactions carried out in cavities tuned to be on-resonance with Si–CH_3 bending modes (magenta). For a comparison, GC chromatograms of the reactions carried out in cavities tuned to be on-resonance with Si–C stretching (red) is shown and together with the data for outside the cavity (blue).

In view of these results, we wanted to check whether the VSC of any vibrational mode of **(R)** would lead to similar effects or whether they are restricted to those vibrations that are associated with the reactive Si centers. To explore this question, we coupled the cavity to the C–O stretching transition (at 1045 cm^{-1}) of **(R)**, a vibration that should have little influence on the reaction from a mechanistic point of view. This mode is also embedded in

the broad region (1040 to 1060 cm^{-1}) **(Figure 48)** corresponding to the C–O vibrations of the solvents used (MeOH and THF) and so should also serve as a probe of whether coupling to a solvent vibration influences the outcome of the reaction. We observed that neither the rate nor the product ratio was affected by VSC of this C–O transition **(Figure 53)**.

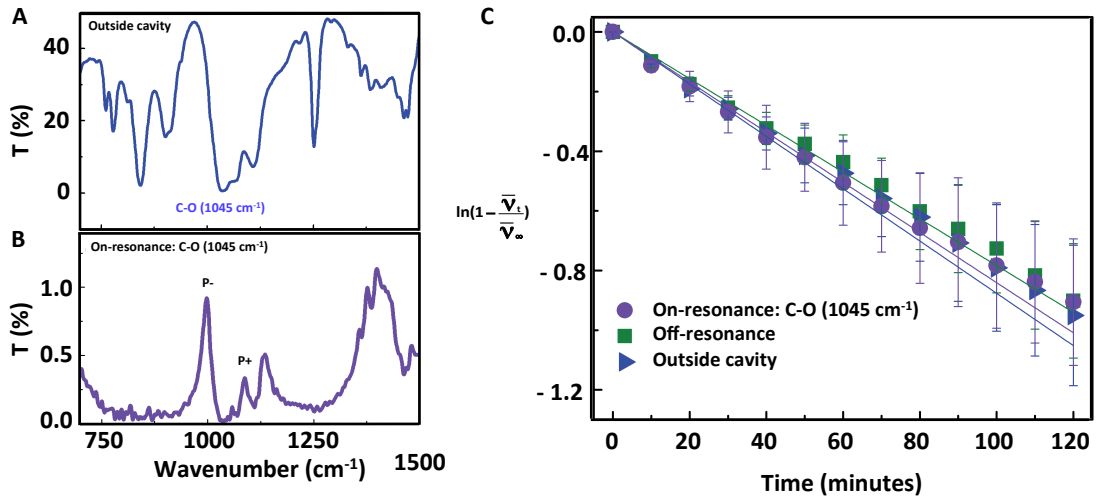

Figure 53. A. FT-IR transmission spectrum of the starting material **(R)** in the reaction mixture recorded outside cavity with the C-O stretching vibration noted in the plot. **B.** FT-IR transmission spectrum showing the vibrational strong coupling of the C-O stretching vibration of **(R)**, MeOH and THF. **C.** Kinetics of the reactions in cavities tuned to be on-resonance with the C-O stretching mode of **(R)** (violet circles) together with an off-resonance cavity (green squares) and outside the cavity (blue triangles). The error bars show the standard deviation of at least five independent experiments.

II.2.4. ACCESS TO THE INDIVIDUAL RATE CONSTANTS OF FORMATION OF PRODUCT (1) AND (2)

These experiments have been completed by measuring the overall observed reaction rate constant (k_{obs}) as a function of cavity tuning across the IR spectrum of **(R)** to obtain an action spectrum **(Figure 54)** that clearly confirms that only certain vibrational modes influence the reaction under VSC, namely: the Si-C (842 cm^{-1}) and Si-O (1110 cm^{-1}) stretching modes and the Si-CH_3 (1250 cm^{-1}) bending mode. This plot reflects the precise selectivity that can be achieved by this weak-field physical perturbation tool at room temperature.

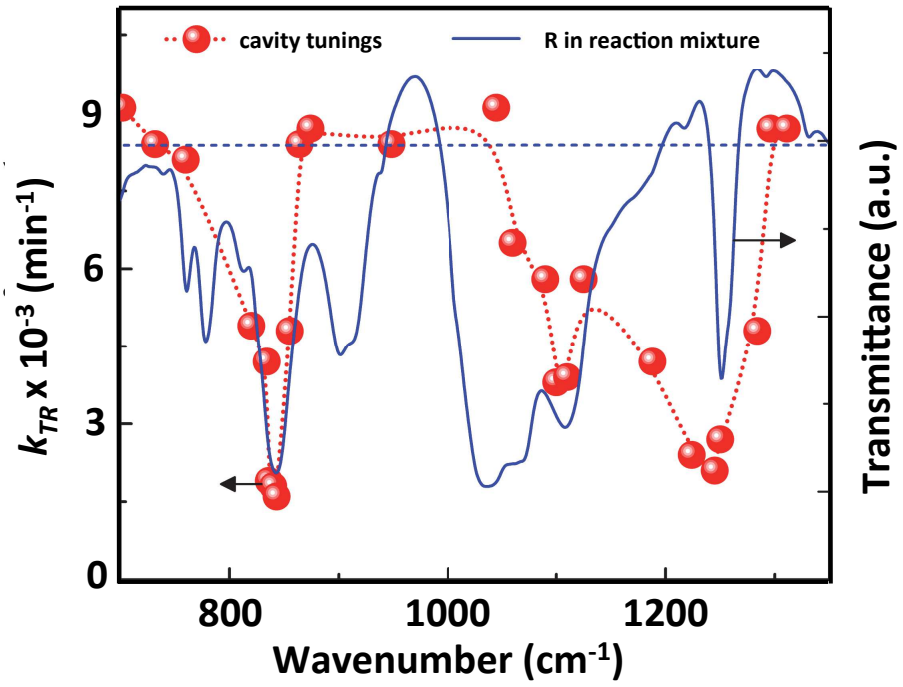

Figure 54. The overall reaction rate as a function of cavity tuning for reactions inside the cavity (red spheres). The red dotted line connecting the spheres is a guide for the eye. The blue solid line shows the IR absorption spectrum of **R** in the reaction medium. The blue dashed line represents the average rate of the reaction outside the cavity.

By combining the spectroscopically observed overall rate constant (k_{obs}) of the parallel reaction and the product distribution ratios $\frac{[\mathbf{1}]}{[\mathbf{2}]}$ obtained by GC-MS measurements, we were able to extract the individual rate constants k_1 and k_2 corresponding to the breaking of the Si-C and Si-O bonds, respectively. From these data, the respective yields (ϕ) of products **(1)** and **(2)** were calculated after various experiments in and out of the VSC regime for various coupling conditions **(Figure 55)**.

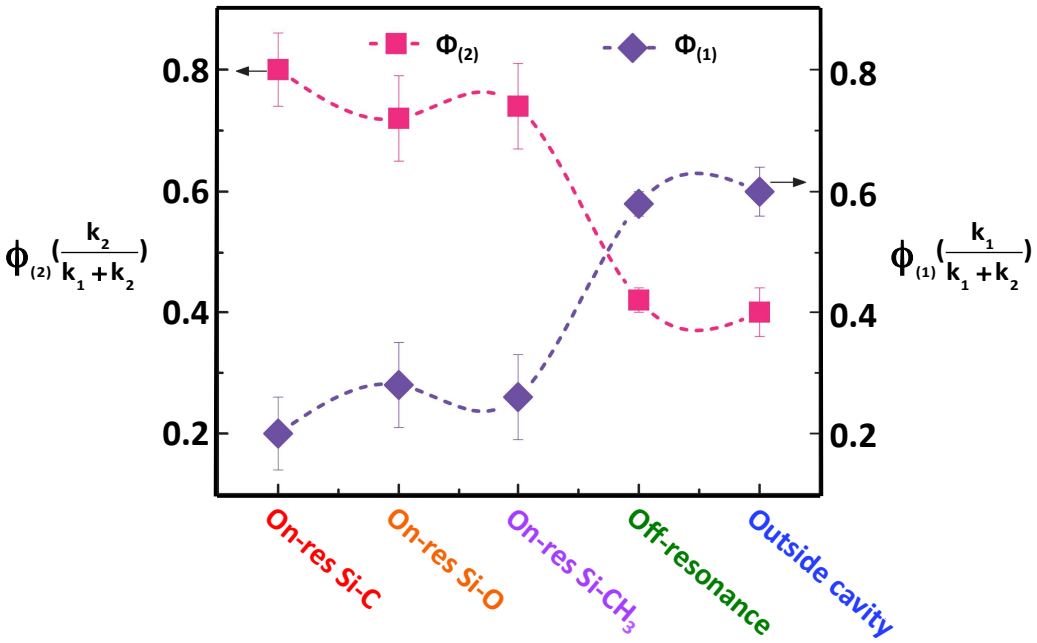

Figure 55. Plot showing the yields of product **(1)** (ϕ_1; violet diamonds) and **(2)** (ϕ_2; pink squares) under VSC of various vibrational modes of **(R)**, together with the off-resonance and outside cavity conditions. The error bars show the standard deviation of at least five independent experiments.

Outside the cavity and in off-resonance cavities, k_1 dominates over k_2, resulting in the preferential formation of product **(1) (Figure 55, purple diamonds)** while VSC reverses the selectivity of the reaction, leading to the prevalent formation of product **(2) (Figure 55, pink squares)**. This is again a direct proof of principle that the reaction energy profile of a chemical reaction can be tilted under the action of VSC by targeting the three vibrational modes associated with the reaction centers formed by the two silicon atoms. The values of both k_1 and k_2 under strong coupling conditions are lower than those observed outside the cavity, indicating that a higher activation energy is required for the reactions under VSC. Products **(1)** and **(2)** can undergo further silyl bond cleavage to give the bis-deprotected product shown in **Figure 56**.

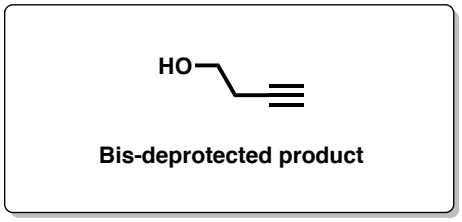

Figure 56. The structure of the bis-deprotected product that can be formed when product **(1)** and **(2)** undergo further silyl bond cleavage

Despite several attempts to detect commercially available samples of the bis-deprotected product by GC-MS, it has never been observed, due to the fact that its fragments are too volatile. Thus, it was not possible to quantify its formation in our experiments. However, given the low conversion observed in our experiments (average conversion of **(R)** is 25%), and the accumulation of **(1)** and **(2)** in the GC-MS analysis, the rate of this downstream reaction appear to be slow. This imparts a small error in the absolute yields but have no consequence on the overall results.

II.2.5. THERMODYNAMIC STUDY

The thermodynamic parameters were determined for each of the two bond-breaking reactions that lead to the formation of products **(1)** and **(2)** by measuring their rate as a function of the temperature under VSC of the Si-C and Si-O stretching vibrations as well as for outside cavity experiments. Using TS theory, the free activation energy ($\Delta H^{\ddagger}$) and activation entropy ($\Delta S^{\ddagger}$) were determined from the slope and intercept of the plot of ln(k) against the inverse of temperature **(Figure 57)**.

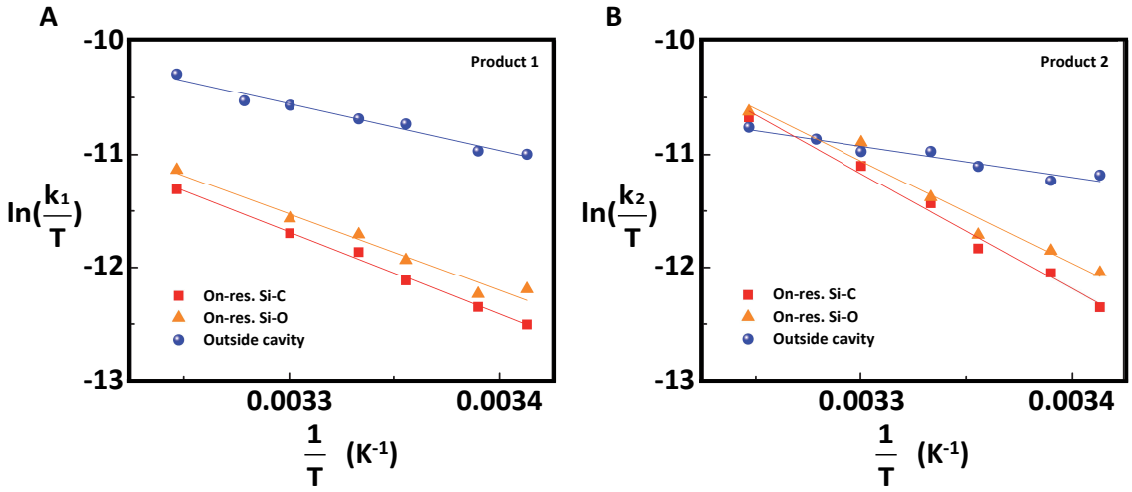

Figure 57. Eyring plots showing the reaction rate for the formation of products as a function of temperature between 20 and 35°C (298.15 and 308.15 K). **A.** Formation of product **1**. **B.** Formation of product **2**. Reactions inside the cavities tuned to be on-resonance with Si–C (red squares) or Si–O (orange triangles) stretching modes are compared with reactions outside the cavity (blue spheres). The data were fitted with a least-square method, and the quality of the fit can be assessed from coefficient of determination (R^2) values ≥0.95.

The results extracted from the plots of **Figure 57** are summarized in **Table 6**. They indicate that the values of the thermodynamic parameters were different for the formation of both product **(1)** and **(2)**, but they were significantly modified under VSC in both cases when compared to control reactions (off-resonance cavity and outside the cavity).

Table 6. Enthalpy and entropy of activation under strong coupling.

Products	Experiments	$\Delta H^{\ddagger}$ (kJ.mol-1)	$\Delta S^{\ddagger}$ (kJ.mol-1)
(1)	Outside cavity	34 ± 3	-173 ± 11
	On-resonance Si-C	60 ± 2	-95 ± 7
	On-resonance Si-O	57 ± 5	-106 ± 17
(2)	Outside cavity	23 ± 3	-214 ± 8
	On-resonance Si-C	85 ± 5	-6 ± 17
	On-resonance Si-O	76 ± 7	-39 ± 24

What was surprising was that the new values of $\Delta H^{\ddagger}$ and $\Delta S^{\ddagger}$ appeared to be very close regardless of whether one coupled the Si-C or the Si-O stretching vibrations. This could be totally fortuitous for the specific molecule chosen for this study. It has been shown in the literature that the presence of leaving groups far from each other can modify desilylation rates.[16]

The above results show that VSC can modify the chemical landscape, and the associated $\Delta H^{\ddagger}$ and $\Delta S^{\ddagger}$, in such a way that it tilts the landscape from one product to another. An interesting aspect of chemical reactions under VSC so far has been the elevation of the activation barrier for the breaking of Si-C and Si-O bonds. We knew that the departure of a fluoride-ion-induced silyl group occurred by an associative mechanism via a penta-coordinated intermediate[17] and we therefore expected to have a very strained TS with a large negative $\Delta S^{\ddagger}$, as it was the case for the reaction outside the cavity. The strong increase of $\Delta S^{\ddagger}$ from very negative values to values that are closer to positive $\Delta S^{\ddagger}$ values under VSC implies that the TS is modified, especially in the case of product **(2)**. A higher $\Delta H^{\ddagger}$ and a "less negative" $\Delta S^{\ddagger}$ suggest that the TS probably have a structure closer to products **(1)** and **(2)** than the starting reagent **(R)**, as in the case of late barrier reaction processes **(Figure 58)**.

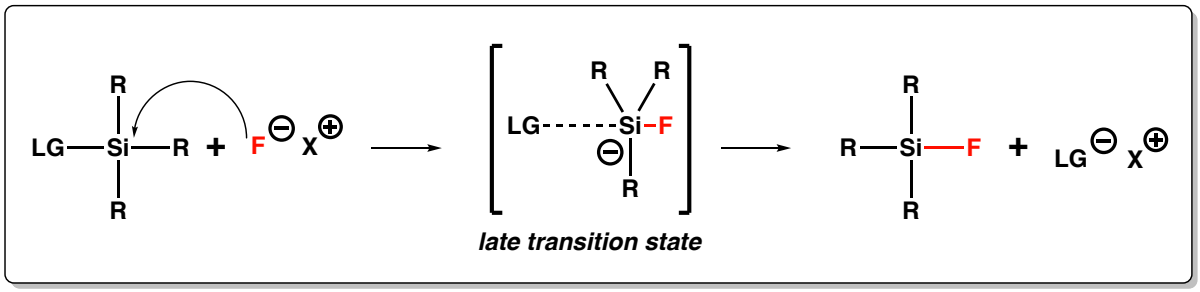

Figure 58. One potential explanation for the apparent change in reaction rate under VSC would be that the landscape is modified such that the TS is occurring at a much later stage of the mechanism described in **Figure 46**.

Barrier increases have also been seen in earlier experiments, whether occurring in the ground state **(see section I.5.2.2)**[1] or via the excited state under electronic strong coupling, such as in the photo-isomerization reaction of merocyanine **(see section I.4.1)**[5]. For the latter case, recent theoretical studies show that the collective response of molecules plays a role in widening the barrier at the conical intersection, preventing the isomerization[139,140]. However, such findings cannot yet be generalized; a recent study of hydrolysis reactions under VSC shows large rate accelerations (up to 10^4)[19]. More experimental and theoretical studies are required to be able to extract general features and understand the effects of VSC on different types of reactions.

II.2.6. CONCLUSION

This proof-of-principle study shows that it is possible to control reaction selectivity through VSC. Strong coupling is dependent on the orientation of the transition dipole moment relative to the electric field of the cavity mode. The molecules were randomly oriented, and the electric field was not uniform in the cavity; there were nodes where the field was essentially null. Hence, the fivefold increase in selectivity under VSC reported here is probably much larger if corrected for such features. For instance, experiments could be done in a tubular cavity to ensure a larger fraction of coupled molecules. Therefore, the selectivity displayed by VSC in the current experiment shows the remarkable potential of light-matter strong coupling for enhancing site selectivity of organic and inorganic chemical reactions. More reactions must be studied to evaluate the generality of this phenomenon and to see to what extent the selectivity can be enhanced at a given site.

CHAPTER III

III. CAVITY CATALYSIS BY VSC OF THE SOLVENT

This chapter describes an ongoing research project on which I will continue to work after my PhD. After an introduction, I will present some preliminary but promising observations that have been made and the difficulties encountered in this work. Finally, I will give perspective for the future.

III.1. INTRODUCTION

III.1.1. CONTEXT

Until now, I have presented different examples where the rates of chemical reactions were slowed down under VSC. During my PhD, I have used this ability of VSC to decrease reaction rates in order to influence site-selectivity, and thus to modify the branching ratio of a particular chemical reaction.[1,2] These studies provide solid proofs of concept and show that VSC can be a very interesting tool for chemistry. However, the fact remains that chemists are most of the time seeking to optimize reactions by accelerating their rates rather than slowing them down.

Depending on the chemical landscape, reaction rates could also be accelerated, as shown in a recent study on the solvolysis of *p*-nitrophenyl acetate where the reaction rate was increased by an order of magnitude.[18] In the latter case, catalysis was observed in a FP cavity in which VSC was generated by cooperative coupling of the C=O vibrational stretching mode of both the reactant and solvent molecules demonstrating that VSC could be transferred from the solvent to the solute as long as their vibrational resonances overlap. Furthermore, as already mentioned in the conclusion of **chapter II**, rate accelerations have been measured up to 10^4 in experiments where water (H_2O) acts both as a reagent and as a solvent for the hydrolysis of cyanate ions (OCN^-).[19] In this study, the OH stretching mode of H_2O was hybridized to a FP cavity mode, resulting in a Rabi splitting energy of 92 meV. Such an exceptionally high value corresponds to the vibrational ultra-strong coupling (V-USC) regime.

Nonetheless, considering the myriad of chemical reactions and their diverse nature, it is necessary to compare more examples of different types of reactions under VSC and/or V-USC in order to understand to what extent cavity catalysis could be achieved. In this context, it would be also very interesting to see whether rate acceleration could be achieved by VSC of the solvent alone rather than the reagent itself. With that in mind, and given the interest of the team of Prof. Joseph Moran for solvent effects observed with 1,1,1,3,3,3-hexafluoroisopropan-2-ol (HFIP), I have decided to study this versatile solvent under VSC.

III.1.2. HFIP, A VERSATILE SOLVENT

From the earliest reference that mentions HFIP, published in 1961[141], no less than six thousand references have cited the use of this highly volatile and toxic colorless liquid compound **(Figure 59)**.

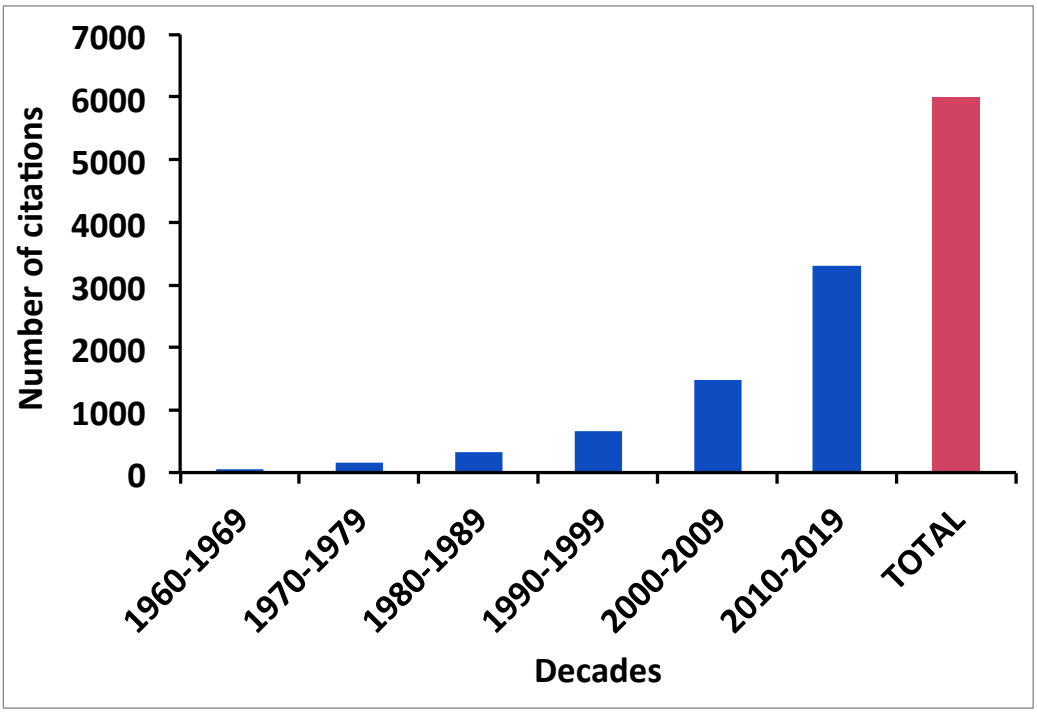

Figure 59. Number of citations mentioning HFIP per decade since its first synthesis in 1961 (blue bars). In total, six thousand citations mentioning HFIP are found in the Sci-Finder databse (red bar).

This extraordinary solvent has been widely used for many applications not only across the field of chemistry but also in biochemistry due to its interesting physical and chemical properties that facilitate unique modes of reactivity. The main physico-chemical properties of HFIP are reported and compared with those of both isopropanol (*i*-PrOH) and 2,2,2-trifluoroethanol (TFE) in **Table 7**.

Table 7. Key physico-chemical properties of *i*-PrOH, HFIP and TFE[142]

Property	HFIP	*i*-PrOH	TFE
Boiling point (°C)	59	82	74
Freezing point (°C)	-4	-88	-44
Density at 25°C (g.mL-1)	1.596	0.782	1.384
Relative dielectric constant ε_r at 20 °C	17.8	18.2	8.6
pK_a	9.3	17.1	12.8
Solvent nucleophilicity parameter N_{OTs}	-4.23	0.2	-2.78
Hydrogen bond donor parameter α	1.96	0.76	1.51
Hydrogen bond acceptor parameter β	0.00	0.95	0.00

HFIP does not absorb UV light, is thermally stable and is miscible with both water and most common polar organic solvents .[143] Compared to its non-fluorinated analog, *i*-PrOH, it has a lower boiling point and twice the density but their relative dielectric constants (ε_r) are quite similar. However, the ε_r of HFIP is twice as big as the ε_r of TFE. It is also a bad nucleophile as can be seen by looking at its negative solvent nucleophilicity parameter N_{OTs}. The high dielectric constant and low nucleophilicity of HFIP imply that it is an ideal solvent in which to generate and stabilize cations as demonstrated in studies that revealed strong effects of HFIP on the stabilization of allyl[144] and benzylic[145] cations for example, with nucleophiles including MeOH, H_2O and tetra-*n*-butylammonium bromide (Bu_4NBr). When comparing their acidity constant values, it can be seen that HFIP is 10^8 times more acidic

than *i*-PrOH. This is due to the negative inductive effect of the trifluoromethyl groups. Single-crystal X-ray structures of HFIP revealed infinite helices of hydrogen-bonded aggregates. These structures have been used as the basis to calculate its hydrogen-bonding properties in solution by use of density functional theory (DFT), demonstrating an aggregation-induced enhancement of the hydrogen-bonding ability (α) of HFIP, which has the highest α value among the majority of solvents (α = 1.96). The upper limit of this effect is a trimer of HFIP monomers **(Figure 60)**. However, HFIP is an extremely weak hydrogen bond acceptor (β = 0.00).[146]

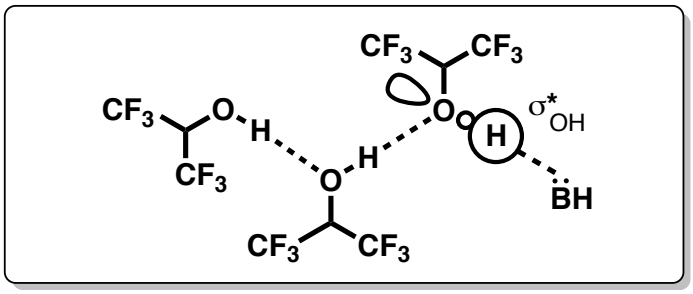

Figure 60. Trimer of HFIP monomers

The redox stability of HFIP make it suitable for use in electrochemistry[147,148] or in chemical reactions under highly oxidizing environments, such as the epoxidation of olefins with hydrogen peroxide (H_2O_2)[21] when other non-fluorinated alcohol solvents would be incompatible. Finally, it has been used as a solvent for metal-free[149,150] and metal-catalyzed[151–154] activation of C–H bonds and many other heteroatom-containing molecules such as carbonyl or acetals[155–157], imine[158,159], alcohols[160,161], halides[162,163] and sulfonates[164] for instance.

III.2. EPOXIDATION OF CIS-CYCLOOCTENE (R2) IN HFIP UNDER VSC

III.2.1. RESULTS AND DISCUSSION

As mentioned in the previous section **(see section III.1.2)**, HFIP has been extensively used as a solvent which enables the activation of H_2O_2 for the epoxidation of olefins with[20] or without[21] the presence of metal catalyst. This class of purely organo-catalytic reaction is well known since it has been thoroughly studied kinetically and theoretically by Berkessel *et al.*, who have elucidated its mechanism, thus pointing out the key catalytic role of HFIP aggregates.[22,23] Indeed, HFIP aggregates and H_2O_2 form clusters *via* a hydrogen-bond network that activates peroxides, thus facilitating the oxygen transfer to the olefin. Considering the reported mechanism, the absorption band corresponding to the O-H stretching mode ($(OH)_{str.}$) of the hydroxyl group in HFIP aggregates has been chosen as the target for VSC experiments, with the hope of demonstrating rate-acceleration in a system where only the solvent, which in this case have a catalytic activity, will be light-hybridized.

For several reasons, I decided to study the HFIP-catalyzed epoxidation of *cis*-cyclooctene to cyclooctene oxide with H_2O_2 **(Figure 61)** which has been reported in the literature by Berkessel *et al.*[22], as a model reaction to perform under VSC.

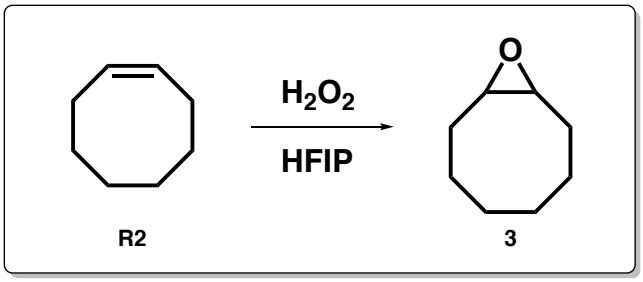

Figure 61. Epoxidation of *cis*-cyclooctene **(R2)** by H_2O_2 in HFIP

Firstly, the authors concluded from their study that the epoxidation reaction took place in a HFIP coordination sphere comprising about 12 HFIP molecules, thus explaining the considerable increase in the reaction rate at high concentration regime ($n_{HFIP}/n_{total} \geq 0.5$). In addition, a more recent work also indicates that the solvation pattern itself plays a crucial role in the reaction process.[24] These peculiar features seem particularly interesting given the

collective states property of the VSC **(see sub-section I.3.2.2.3)**. Secondly, the reaction should be convenient to study inside a FP cavity, as it occurs at room temperature. Finally, since *cis*-cyclooctene is commercially available, no tedious synthesis is required for the preparation of the starting material.

III.2.1.1. IR CHARACTERIZATION OF THE $(OH)_{STR.}$ OF HFIP

Before performing any HFIP-catalyzed reaction under VSC, the IR spectrum of HFIP **(Figure 62)** has to be elucidated. The discussion will be focused on the high frequency region (3000-3700 cm^{-1}) where the absorption band corresponding to the $(OH)_{str.}$ of HFIP is expected to be found.

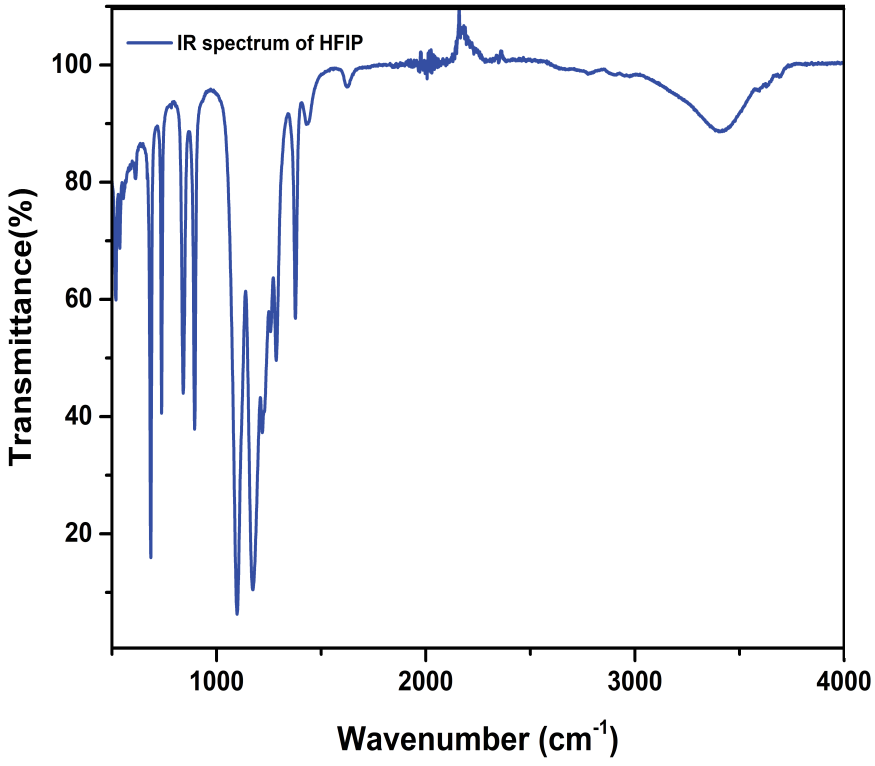

Figure 62. IR spectrum of neat HFIP measured with an attenuated total reflection (ATR)-IR spectrometer. The $(OH)_{str.}$ of HFIP aggregates appears around 3400 cm^{-1}.

It is interesting to point out here that the α angle between the two hydrogen atoms of the HFIP monomer defines its different conformations. The latter have an influence on its hydrogen bond donor ability **(Figure 63)**.[23]

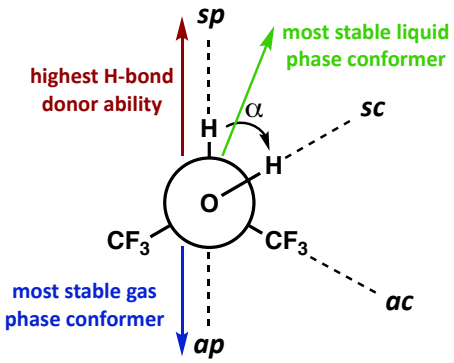

Figure 63. Dependence of the properties of monomeric HFIP on the α angle between the two hydrogen atoms. Adapted from reference [23].

Several studies revealed the presence of two well-separated absorption bands in the high frequency region of the IR spectrum of HFIP, when measured in the vapour phase or in carbon tetrachloride (CCl_4) solutions, which enable an analysis of the latter in its monomeric form. These two absorption bands correspond to the $(OH)_{str.}$ of the synclinal (±*sc*) and antiperiplanar (*ap*) conformers of HFIP. In solution in CCl_4, the band arising from the $(OH)_{str.}$ has a lower frequency and somewhat smaller IR intensity in the *ap* conformer than that in *sc* **(Figure 64)**.[25–27]

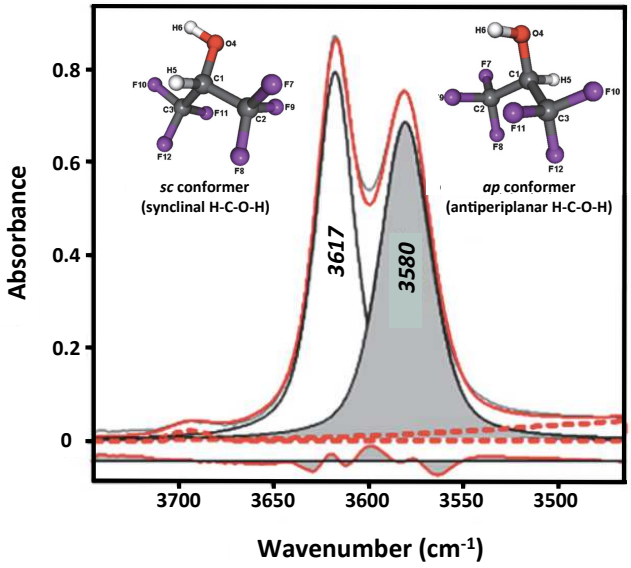

Figure 64. High frequency region of the IR spectrum of a 0.1M solution of HFIP in CCl_4, showing the $(OH)_{str.}$ of HFIP. The band assigned to the *ap* conformer is shadowed in grey. The optimized structures of the *ap* and *sc* conformers of HFIP are illustrated in the inset. Adapted from reference 25.

By measuring the IR spectrum of a 0.1M solution of HFIP in CCl_4 **(Figure 65A)** and comparing it with that obtained with neat HFIP **(Figure 65B)**, it can be seen that the two bands corresponding to the *ap* and *sc* HFIP conformers are clearly visible when recorded in solution in CCl_4, while in neat HFIP they appear as small shoulders that are barely visible. In the latter case, the lower frequency shifted broad absorption band is attributed to the $(OH)_{str.}$ of HFIP aggregates.

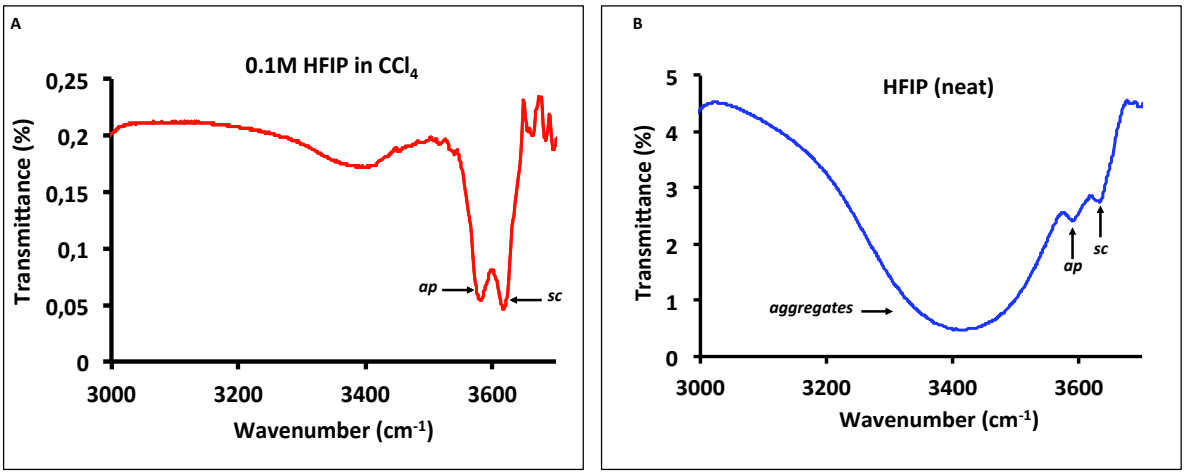

Figure 65. High frequency region of the IR spectrum of a 0.1M solution of HFIP in CCl_4 **(A)** and of a neat HFIP solution **(B)**.

III.2.1.2. EXPERIMENTS AND GC-MS QUANTITATIVE ANALYSIS

The $(OH)_{str.}$ of HFIP aggregates has been strongly coupled to a FP cavity mode **(Figure 66A)**. The two new bands corresponding to the polaritonic states P+ and P- are evidenced on the IR spectrum of HFIP inside a cavity tuned at 3389 cm^{-1} (**Figure 66B**). The observed Rabi splitting $\hbar\Omega_R$ of 225 cm^{-1} showed that HFIP meets the strong coupling criteria **(see sub-section I.3.2.2.3)** as it was larger than the FWHM of the cavity mode (34 cm^{-1}) and the vibrational band (206 cm^{-1}).

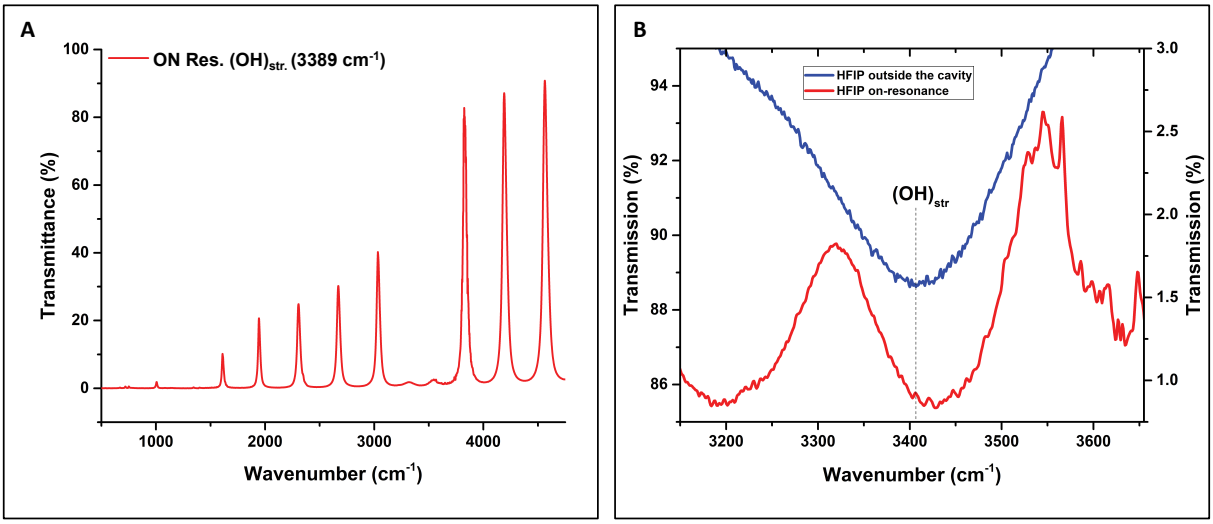

Figure 66. A. FT-IR transmission spectrum of an on-resonance FP cavity strongly coupled to the $(OH)_{str.}$ of HFIP aggregates **B.** Zoom on the spectral window where the new vibrational polaritonic bands P+ and P- appear under VSC (red) together with that of neat HFIP measured with an ATR-IR spectrometer (blue).

The FP optical cavity used in the following experiments was assembled from two parallel metal mirrors made of Au (10 nm) sputtered on ZnSe IR-transmitting windows (2mm). To ensure that the reaction was not affected by the presence of both Au and ZnSe, a 200 nm layer of glass (SiO_2) was deposited on the inner surface of each mirror. The metallic mirrors were separated by a polypropylene spacer of variable thickness with a hollow central channel designed for the injection of liquid samples **(see sub-section I.5.2.1, Figure 39)**. To prepare the different on- and off-resonance cavities in the present experiments, the thickness of the polypropylene spacers used were varied in the range of 4 to 12 µm. The area of the cavity was 1 cm x 2.5 cm. The tuned part was typically 40% of this area because the four screws we are using to tune the cavity put pressure on the flat windows, slightly deforming them. The reaction was monitored through a tuned area of the cavity using an aperture of 5 mm in diameter. For control experiments, described as "outside cavity" experiments, the flow-cells were prepared in a similar manner as explained above but the metallic mirrors were replaced with bare glass coated ZnSe windows. A homogeneous solution of the starting material **(R2)** (0.65 M), H_2O_2 (0.18 M) and the internal standard (I.S.) bromooctane (0.06 M) in HFIP (8.50 M; n_{HFIP}/n_{total} = 0.90) was used as the reaction medium throughout the experiments presented here. The reaction mixtures were quenched with manganese dioxide (MnO_2) and analyzed quantitatively by GC-MS after each experiment

(see sub-section IV.2.4.3), in order to determine the concentration ratio $\frac{[\mathbf{3}]}{[\mathbf{R2}]}$ where [**3**] is the quantity of product **(3)** obtained after epoxidation of the starting material **(R2)** whose remaining quantity is **[R2] (Table 8)**.

Table 8. $\frac{[3]}{[R2]}$ ratios measured by quantitative GC-MS analysis after each experiments

Entry	Experiment	Ratio $\frac{[\mathbf{3}]}{[\mathbf{R2}]}$
1	**Outside cavity**	**0.17** ± 0.09
2	**Off-resonance**	**0.12** ± 0.03
3	**On-resonance $(OH)_{str.}$**	**0.82** ± 0.17

The presence of unreacted starting material **(R2)** in all the chromatograms showed that the reaction was not complete after a 50 min time period **(Figure 67)**. For the reactions performed outside the cavity and in off-resonance cavities, the concentration ratios $\frac{[\mathbf{3}]}{[\mathbf{R2}]}$ were equivalent within experimental error **(Table 8, entry 1 and 2)**. As shown in the red chromatogram of **Figure 67**, a significant increase in the formation of product **(3)** was observed when the $(OH)_{str.}$ of the HFIP aggregates is strongly coupled to a cavity mode, thus indicating an acceleration of the product formation in resonant cavities by a factor of 4.8 **(Table 8, entry 3)**. The values shown in **Table 8** take into account the fraction of the FP cavity under VSC, that is 40% of its total area. The remaining fraction is detuned beyond the width of the vibrational mode and, as a result, is in the off-resonance condition.

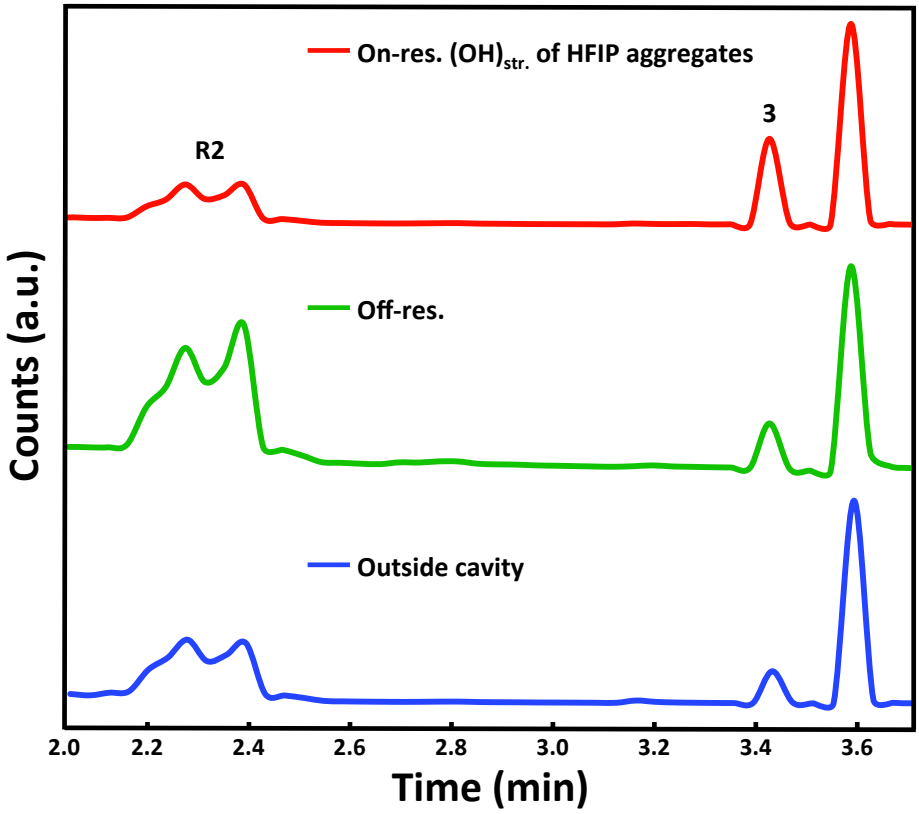

Figure 67. The GC chromatograms of the reactions carried out in cavities tuned to be on-resonance with $(OH)_{str.}$ of HFIP aggregates (red) together with the data for an off-resonance cavity (green) and outside the cavity (blue). The peaks corresponding to *cis*-cyclooctene and cyclooctene oxide are marked as **(R2)** and **(3)**, respectively. The peak at 3.6 min corresponds to bromooctane, which has been added in the reaction mixture as the I.S. for quantitative analysis. These chromatograms are zoomed-in on the compounds of interest for clarity; the complete ones can be found in **Figure 84 (see section IV.2.4.3)**.

In **Figure 68**, the concentration ratios $\frac{[3]}{[R2]}$ are plotted as a function of cavity tuning relative to the $(OH)_{str.}$ of HFIP aggregates (blue curve) for the mirrored cavity (red dots) with different spacing between the dielectric windows in order to obtain an action spectrum. The average ratio obtained for experiments performed outside the cavity is shown as a green dashed line. The largest effect is clearly seen under VSC at 3386 cm^{-1} where the ratio $\frac{[3]}{[R2]}$ was equal to 1.30, which is 7.6-fold higher than the average ratio of 0.17 measured outside the cavity.

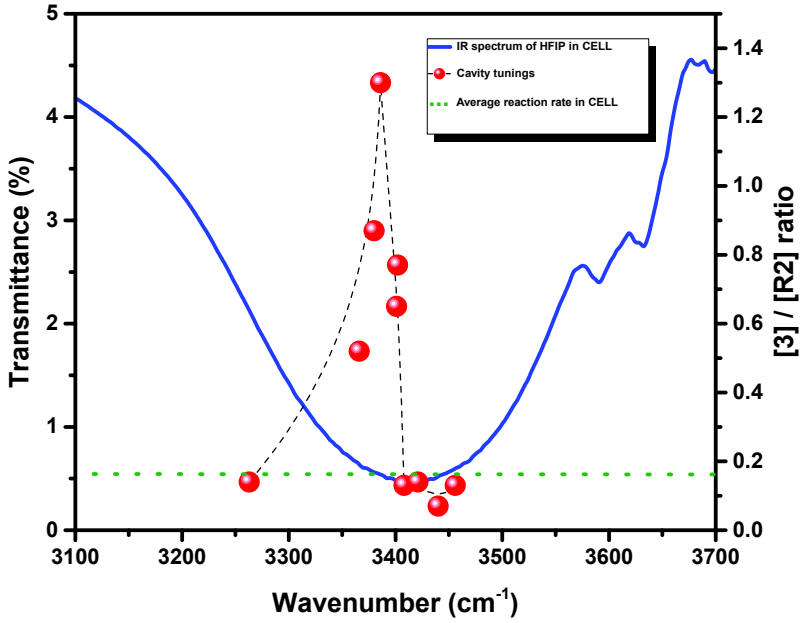

Figure 68. Relative influence of VSC in the region of the $(OH)_{str.}$ of HFIP aggregates. The blue solid line shows the IR absorption spectrum of HFIP, zoomed in the high frequency region where the absorption band corresponding to the $(OH)_{str.}$ of HFIP aggregates is found. The green dashed line represents the average rate of the reaction outside the cavity. The concentration ratios $\frac{[3]}{[R2]}$ are plotted as a function of cavity tunings for reactions inside the cavity (red spheres). The black dashed line connecting the spheres is a guide for the eye.

Surprisingly, the action spectrum does not fit the shape of the absorption band corresponding to the $(OH)_{str.}$ of HFIP aggregates **(Figure 68)**. As mentioned above, an important increase in the $\frac{[3]}{[R2]}$ ratio is observed in tuned cavities, thus indicating a faster reaction under VSC. However, if the ratio progressively increases between 3263 and 3386 cm^{-1}, it was not expected to decrease so abruptly at higher frequency. A possible explanation for this result could be related to the fact that, similarly to what is observed for monomeric HFIP **(see sub-section III.2.1.1)**, several HFIP aggregates can be distinguished depending on the conformation of the monomers that are involved in their formation. Thus, the observed broad absorption band corresponding to the $(OH)_{str.}$ of HFIP aggregates is probably the result of a combination of several components. Here, considering the shape of the action spectrum **(Figure 68)**, it is suggested that only one of them is sensitive to VSC. According to Berkessel et al., HFIP is likely to adopt an *sc* (most stable liquid phase conformer) or even *sp* (highest H-bond donor ability) conformation when it is to act as a H-bond donor **(Figure 63)**.[146] Therefore, as a hypothesis, it can be assumed that the aggregates formed by either of the two conformations are those which are VSC-sensitive and therefore involved in the catalytic activity.

III.2.1.3.KINETIC MONITORING OF THE REACTION RATE BY IR SPECTROSCOPY

I will discuss here the major issue that has been encountered in VSC experiments performed with HFIP. As in our previous studies, we wanted to follow the progress of the reaction by measuring the shifts in the high-order cavity resonances. Unfortunately, in most of the experiments in which the cavity was on- or off-resonance with the $(OH)_{str.}$ of HFIP aggregates, an unusual phenomenon was observed. As shown in **Figure 69**, the probed area of the cavity, where the reaction was followed through a small aperture, seemed to be empty after a time-period ranging from 15 to 30 min. The IR transmission spectrum of the reaction mixture right after injection inside the cavity was perfectly normal **(Figure 69A, blue spectrum)** and remained stable up to 10 min after injection **(Figure 69B, red spectrum)**. Then, a process that was initially not understood, led to an abnormal change in the IR spectrum **(Figure 69C, orange spectrum)** until the probed area of the cavity generated an "empty cavity" spectrum, indicating an absence of any molecular material in this region of the cavity **(Figure 69D, purple spectrum)**.

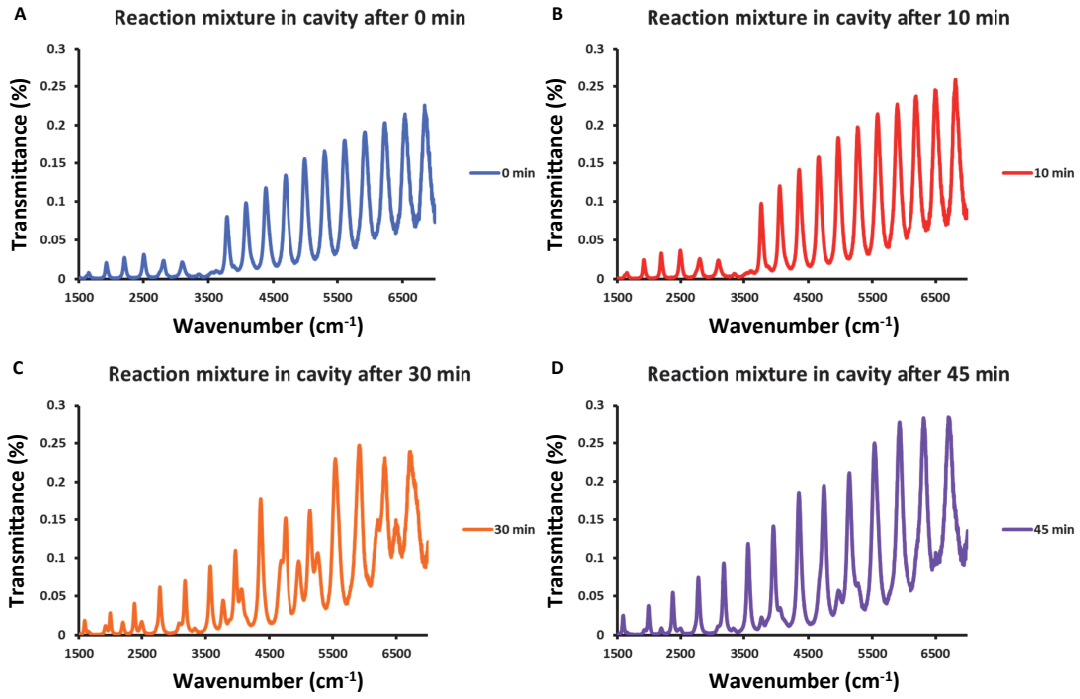

Figure 69. Evolution of the IR transmission spectrum of an on-resonance cavity in function of time. In this particular example, the cavity was tuned at 3386 cm^{-1}. The spectra shown here have been recorded immediately (A), 10 min (B), 30 min (C) and 45 min (D) after injection of the reaction mixture inside the cavity.

After examination of the cavity at the end of the experiments, I realized that this phenomenon was due to the formation of a bubble near the probed region of the cavity. One explanation to this could be that H_2O_2, one of the reagents in the reaction mixture, released dioxygen (O_2) and form bubbles inside the cavity. Surprisingly, this phenomenon never happened in control experiments, mentioned above as outside cavity experiments, in which the reaction mixture remained perfectly stable inside the microfluidic cell. It is worth emphasizing here that heterogeneous catalysis or any other interaction with Au can be ruled out, as the Au layer deposited on the mirrors of the cavity is coated with SiO_2 to avoid any contact with the reaction medium.

III.3. ACID-CATALYZED REARRANGEMENT OF 7,8,15,16-TETRAOXADISPIRO[5.2.5.2]HEXADECANE (R3) TO CAPROLACTONE (4) IN HFIP UNDER VSC

In order to try to overcome the formation of bubbles inside the cavity, we decided to switch to another system: the acid-catalyzed transformation of 7,8,15,16-tetraoxadispiro[5.2.5.2]hexadecane **(R3)** to *ε*-caprolactone **(4)** which requires the use of HFIP but where H_2O_2 is not necessary.[165] For these experiments, the reaction medium was prepared by dissolving the starting material **(R3)** (25 mg, 43.8 mM) in a 250 µL solution of *para*-toluenesulfonic acid (*p*-TsOH) in HFIP (4.38 mM). Unfortunately, the starting material **(R3)** decomposed on the GC column, rendering its quantification impossible by GC-MS. Thus, I have determined the $\frac{\mathbf{4}}{\mathbf{R3}}$ ratio by quantitative nuclear magnetic resonance (qNMR) using the ERETIC method, but no significant changes have been observed between on-resonance and outside cavity experiments.

Table 9. $\frac{4}{R2}$ ratio measured by qNMR after each experiments

Entry	Experiment	$\frac{4}{R3}$ ratio determined by qNMR
1	Outside cavity	0.21 ± 0.03
2	Off-resonance	0.22 ± 0.05
3	On-resonance OH	0.29 ± 0.11

Furthermore, as in the case of the epoxidation of *cis*-cyclooctene **(R2)**, the same phenomenon of bubbles formation has been observed with this system. Again, it occurred only in on- and off-resonance experiments. In view of the difficulties encountered here and given the very promising results obtained with the previous reaction **(see section** Erreur ! Source du renvoi introuvable.**.)**, it is planned to focus our efforts on the epoxidation reaction of *cis*-cyclooctene **(R2)** under VSC.

III.4. PERSPECTIVE: VSC AS A TOOL TO MIMIC KINETIC ISOTOPE EFFECT (KIE)

As shown by the preliminary results described above **(see part III.2.)**, it seems that VSC of the $(OH)_{str.}$ of HFIP aggregates leads to an acceleration of the rate of epoxidation of *cis*-cyclooctene by a factor of 4.8.

Interestingly, one of my co-worker observed an inverse KIE of 2.2 when deuterated HFIP was used as solvent in a Friedel-Crafts reaction **(see III.4.2., Figure 71)**. The deuterated hydroxyl group of HFIP has been identified as responsible for this KIE. This has been reported in his thesis manuscript.[43]

For a given reaction, if we could achieve similar rate-accelerations with deuterated HFIP (outside cavity) and protiated HFIP (under VSC), it would be a way to demonstrate the ability of the VSC to become a tool to mimic the KIE that would not require any chemical modification to the substrate.

III.4.1. DEFINITION

In organic molecules, the most common elements (C, H, N, O) are naturally found with a high proportion of a single isotope. Chemists are able to synthesize isotopologues[166] of a molecule of interest by the incorporation of different isotopes at specific positions.[167] Isotopic substitution has no effect on the potential energy and thus on the energy surfaces of the system.[168,169] However, it has a significant impact on molecular vibrations as they depend on the masses of the individual atoms in motion. Again, to describe the vibrational behavior of isotopomeric molecules, it is usual to use the harmonic oscillator model **(Figure 70)**. Let us consider the stretching vibration of molecules $M–m_L$ and $M–m_H$ where M >> m, and subscripts L and H refer to light and heavy isotopes of m. Their respective classical vibrational frequency, ν_L and ν_H are given by the expressions shown in **Figure 70**, where f is the bond strength constant of the bond under consideration. The difference in vibrational frequencies for the two isotopes is due to differences in their respective mass, m_L and m_H. This leads to differences in their reduced mass, μ_L and μ_H, to which the frequencies are inversely proportional. This applies equally to other vibrational modes.

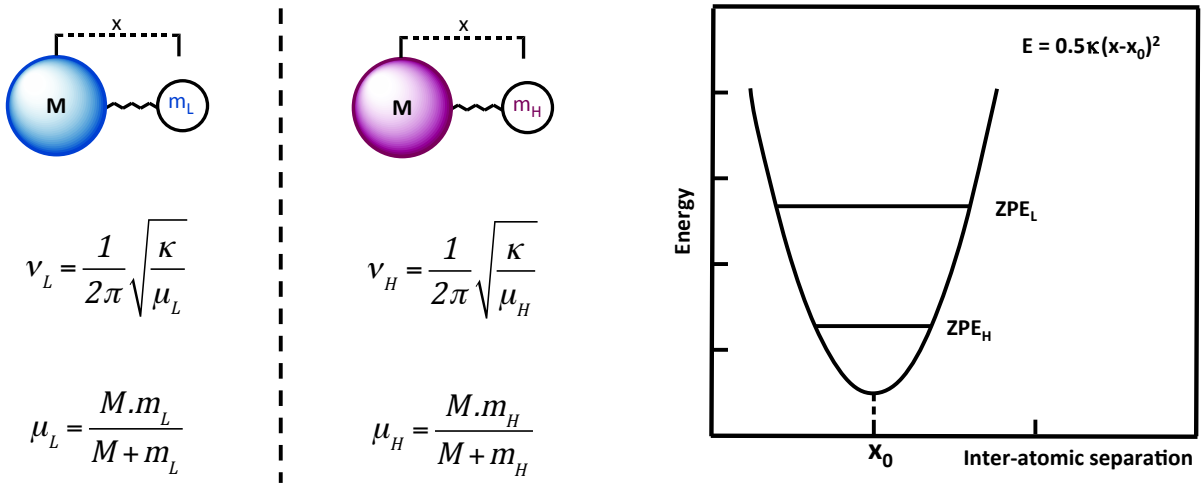

Figure 70. Vibrational behavior of a pair of isotopomeric molecules. Subscripts L and H refer to light and heavy isotopes, respectively. Their respective vibrational frequency, ν_L and ν_H, follow the simple harmonic oscillator model. f is the strength of the bond under consideration. μ_L and μ_H, and m_L and m_H, are the respective reduced mass and mass of the two isotopes.

Molecular oscillators are quantized microscopic systems and therefore have a ZPE of $\frac{1}{2}h\nu$ **(see section I.2.1.)**. The difference in ZPE for a particular vibration in isotopomers depends upon their respective vibrational frequencies. These, in turn, depend on the bond strength constant f (which is the same for both isotopes), and on the reduced masses μ_H and μ_L:

$$\Delta ZPE = ZPE_L - ZPE_H = \frac{1}{2}h(\nu_L - \nu_H) = \frac{1}{2}h\nu_L\left(1 - \sqrt{\frac{\mu_L}{\mu_H}}\right)$$

In theory, the global effect of isotopic substitution is the sum of all contributing terms from vibrations involving distinct motion of the isotopically substituted atom, although, in practice, there is usually only one major contributor. For example, in the case of isotopic substitution of hydrogen at tetracoordinate carbon by deuterium and tritium, contributions from the bonds stretching (ν_L = 2850 cm^{-1}) are 4.54 and 6.48 $kJ.mol^{-1}$, respectively, and 2.15 and 3.15 $kJ.mol^{-1}$ for angle bending (ν_L = 1350 cm^{-1}).[170]

Isotopomers are generally used in order to detect and characterize the TS of a rate-determining step, thus providing a powerful and very sensitive tool for the study of the mechanisms of chemical reactions in which covalent bonds are broken or formed.[171] For example, the KIE is used to determine whether a nucleophilic substitution reaction follows a unimolecular (S_N1) or bimolecular (S_N2) pathway.[172] Most of the time, the isotopic

substitution is done on a protium atom which is replaced by a deuterium atom. As its atomic mass is twice that of protium, the difference in the reduced mass is particularly important in this case. Thus, the vibrational frequency and, consequently, the ZPE will be lower for deuterium than for protium resulting in a greater dissociation enthalpy for C-D bonds than for C-H bonds.[173]

According to the IUPAC Gold Book, a kinetic isotope effect (KIE) occurs when the rate constant of a reaction varies due to isotopic substitution in one of the reactants. Let us consider the following reaction:

$$A + B \rightarrow C$$

The KIE is defined as the ratio of reaction rate constants:

$$KIE = \frac{k^L}{k^H}$$

where k^L is the reaction rate constant with molecule A containing a light isotope and k^H is the rate constant of the same reaction in which the light isotope in A is replaced by a heavier one. Within the framework of TS theory, the reaction is rewritten as:

$$A + B \rightleftarrows [TS]^{\ddagger} \rightarrow C$$

$\frac{k^L}{k^H}$ can be considered as the equilibrium constant for an isotope exchange reaction between the isotopically substituted reactant A and the TS, $[TS]^{\ddagger}$, calculated from their vibrational mode involving motion of isotopically different atom.[174] The theory governing the effects of isotopic substitution on equilibria and reaction rates of isotopomeric species is well understood.[175]

KIEs are often divided into two categories:

- Primary KIEs: occur when the bonds that are broken or formed in the rate-determining step of a reaction are those of the isotopic atom.[176] Primary KIEs have been widely employed as a tool for the mechanistic understanding of chemical reactions through corroborating their rate-limiting steps,[171] but also to study tunneling phenomenon, which have been found to increase the isotope effect beyond what would normally be expected.[177]
- Secondary KIEs: occur when the reaction rate is affected upon the isotopic substitution, even though no bonds involving the isotope-substituted atom(s) are broken or made in the rate-limiting step. Their origin is often attributed to electronic effects dependent on bond geometry (lengths and angles, which may be affected by isotopic substitution). These electronic effects include e.g. hyperconjugation or hybridization. Secondary isotope effects can be inverse ($\frac{k_L}{k_H} < 1$) or normal ($\frac{k_L}{k_H} < 1$).[171]

III.4.2. VSC AS A TOOL TO MIMIC KIE

A distinction is made when isotopic substitution is done on the solvent instead of the reactant and causes changes in reaction rates or equilibria. In this case we speak about kinetic solvent isotope effect (KSIE). Solvent is often essential for a reaction to proceed, as it can be involved in its mechanism, e.g. by being one of the reactants or by stabilizing the TS. KSIE has been the most thoroughly studied in water due to the vital role of aqueous environments in biological processes.[178] Heavy water (D_2O) is known to slow down a wide range of reactions, including enzymatic reactions.[173] However, D_2O has shown the ability to accelerate many processes (inverse KSIE), like for example, acid-catalysed or hydroxyl ion-catalysed reactions, the esterification of benzoic acid, and enzymatic reactions where the substrate has a low affinity for the enzyme.[173]

As already mentioned in the introduction of **part III.4.**, the idea of using the VSC as a tool for mimicking KIE arose when a former PhD student of our lab, performed a series of kinetic experiments in an attempt to get deeper insight into details of the mechanism of

catalytic dehydroarylative reactions of deactivated benzylic alcohols.[43] One of these experiment consisted in carrying out the Friedel-Crafts reaction shown in **Figure 71**, in deuterated HFIP.

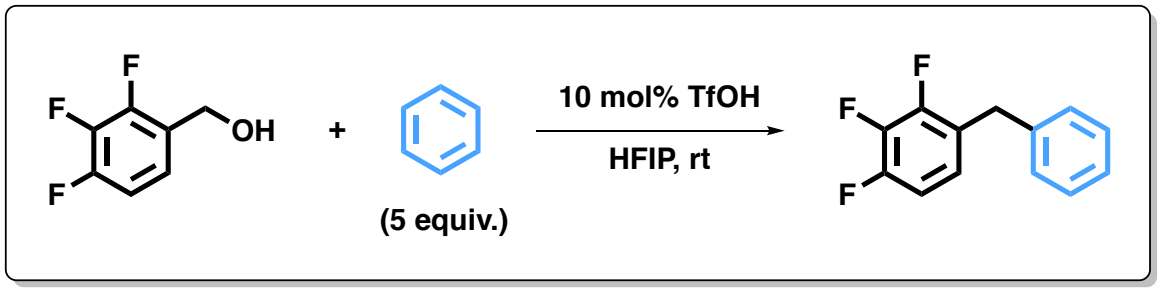

Figure 71. Friedel-Craft reaction between a deactivated benzylic alcohol and a nucleophile (benzene, in blue) in which KSIE has been observed by one of my co-worker, Vuk Vuković, during his PhD.[43]

The reaction was first followed in HFIP-d_2 and the following KSIE was observed:

$$KSIE_{d2} = \frac{v_H}{v_D} = \frac{1.42 \times 10^{-5}\ mol.L^{-1}.s^{-1}}{3.10 \times 10^{-5}\ mol.L^{-1}.s^{-1}} = 0.46$$

This result indicates that the reaction is slower in protonated HFIP than in HFIP-d_2. More precisely, the reaction is 2.2 times faster in HFIP-d_2 ($KSIE_{d2}^{-1}$ = 2.2), therefore indicating an inverse KSIE. To further understand the effect of isotopic substitution of the respective hydroxyl group and methine protons of HFIP, the same reaction was carried out in HFIP-d_1(O-D) under identical conditions. The KSIE in this case was quasi similar to the previous value obtained with HFIP-d_2 (0.46):

$$KSIE_{d1} = \frac{v_H}{v_D} = \frac{1.42 \times 10^{-5}\ mol.L^{-1}.s^{-1}}{3.01 \times 10^{-5}\ mol.L^{-1}.s^{-1}} = 0.47$$

Thus confirming that its origin is found at the deuterated hydroxyl group of HFIP. Interestingly, the observed value of the KSIE is in the range of KSIE for acid-catalyzed reactions in H_2O and D_2O.[179] The following hypotheses have been proposed as a potential explanation of the observed KSIE.

The mechanism of the reaction proceeds *via* protonation of the benzylic alcohol substrate, followed by C-O bond cleavage, which is the rate determining step:

$$\text{(step 1)}\ ROH + H^+ \leftrightharpoons ROH_2^+ \quad and \quad \text{(step 1')}\ ROD + D^+ \leftrightharpoons ROD_2^+$$
$$\text{(step 2)}\ ROH_2^+ \rightarrow R^+ + H_2O \quad and \quad \text{(step 2')}\ ROD_2^+ \rightarrow R^+ + D_2O$$

Thus, the overall rate constant is $k = K_1 k_2$, where K_1 is the equilibrium constant of the first step (step 1), and k_2 is the rate constant of the second step (step 2). Since heteroatom-deuterium bonds are stronger than corresponding heteroatom-proton bonds, the equilibrium (step 1') is shifted more towards the right than the equilibrium (step 1), and therefore: $K1' > K1$. The resulting effect is: $k' > k$.

Another possibility would be that deuterated HFIP stabilizes the TS of the step (step 2') more than protiated HFIP for step (step 2), since the deuterium bonds are stronger than corresponding hydrogen bonds, especially in dimers and trimers.[180] However, the stabilization might also be due to a change of the hydrogen bond geometry due to deuteration.[181]

In light of these results, I think that studying HFIP catalyzed Friedel-Crafts reactions in the framework of VSC, could help to demonstrate its ability to mimic KSIE and therefore to become a tool for mechanistic studies where chemical modification of the substrate is not required.

III.5. CONCLUSION

In this chapter, I have presented one of the ongoing research projects on which I will continue to work after my PhD. The preliminary results obtained in the case of the epoxidation reaction of *cis*-cyclooctene are quite promising. However, additional work will be necessary to fully characterize this system under VSC. Firstly, an optimization of the reaction conditions is necessary in order to avoid any perturbation due to the formation of bubbles inside the cavity. In order to collect the kinetic data by IR spectroscopy, I will monitor the first 15 minutes of the reaction, for which the reaction mixture showed better stability in cavity experiments. Secondly, as I suggested in **sub-section III.2.1.2** that the strong coupling of only a specific type of HFIP aggregate (based on the conformation of the HFIP monomers that constitute it) has an influence on the epoxidation rate of *cis*-cyclooctene, it would be worthwhile to perform simulations to be able to decipher the IR spectrum of the $(OH)_{str.}$ of HFIP aggregates. This should allow supporting or overriding the hypothesis concerning the ability of VSC to differentiate between different conformers.

Furthermore, the VSC could potentially be used as a mimic of KIE for mechanistic studies. For instance, VSC experiments on a good Friedel-Crafts model reaction could be conducted to demonstrate this possibility.

CHAPTER IV

IV. EXPERIMENTAL PART

IV.1. TILTING A GROUND-STATE REACTIVITY LANDSCAPE BY VSC

IV.1.1. MATERIAL AND METHODS

Unless otherwise noted, all reagents and solvents were purchased from commercial suppliers and used without further purification.

The FT-IR transmission spectra of the FP cavities and the "outside the cavity" cells were acquired by standard FT-IR spectrometer (Bruker Vertex70) in transmission mode. The transmission was recorded by DTGS (deuterated triglycine sulfate) detector with 2 cm^{-1} resolution over 64 scans.

GC-MS analysis was performed on a GC System 7820A (G4320) connected to a MSD block 5977E (G7036A), using Agilent High Resolution GC Column: PN 19091S 10 – 433UI, HP – 5MS UI, 28m×0.250 mm, 0.25 Micron, SN USD 489634H. All samples were prepared in 2-propanol (200 µL sample volume). The analysis was carried out on a splitless 1 µL injection volume with an injection port temperature 250 °C. Column oven temperature program was as follows: 60 °C for 1 min, ramped at 30 °C min^{-1} to 310 °C with 3min hold, with a total running time of 12.33 min. The mass spectrometer was turned on after 2 min and was operated at the electron ionization mode with quadrupole temperature of 150 °C. Data acquisition was performed in the full-scan mode (50-500). Hydrogen (99.999 % purity) was used as carrier gas at a constant flow rate of 1.5 $mL.min^{-1}$.

^{1}H NMR spectrum of starting material **(R)** in deuterated chloroform ($CDCl_3$) was recorded on a Bruker Avance 400 (400 megahertz (MHz)) spectrometer at ambient temperature and is reported in parts per million (ppm) scale using the residual solvent resonance as the I.S. ($CDCl_3$ at 7.26 ppm).

IV.1.2. TRANSFER-MATRIX SIMULATION

The fitting of experimental data has been done thanks to a Matlab code based on the T-Matrix method, that allows to simulate the transmission spectra of multilayered samples. To do this calculation, one needs to define precisely the refractive index for each layer. For the ZnSe windows of the cell and the protective SiO_2 layers, the refractive indexes were both calculated from experimental transmission data of those materials. The refractive index of the gold mirrors was calculated from the reported polynomial expression[182], with a correction in the damping factor to take into account their very small thickness. Finally, the refractive index of the material itself was determined by fitting the experimental absorption of the material measured in ATR and measured in a cell, to define it as rigorously as possible, in particular because the presence of solvents in the cell affects the Si-O bond absorption region.

IV.1.3. SYNTHESIS OF *TERT*-BUTYLDIMETHYL((4-TRIMETHYLSILYL)BUT-3-YN-1-YL)OXY)SILANE (R)

A reported procedure was followed to prepare the starting material **(R)**.[10,11] To a stirred solution of 4-(trimethylsilyl)but-3-yn-1-ol (3.50 mmol, 0.585 mL) in dimethylformamide (DMF) (5 mL) at 0 °C were added imidazole (8.75 mmol, 0.596 g) and *tert*-butylchlorodimethylsilane (4.38 mmol, 0.658 mg). The reaction was quenched by the addition of aq. Saturated ammonium chloride (NH_4Cl) (15 mL). The organic layer was collected and extracted with diethyl ether through repeated washings. The combined organic fractions were then washed with water, dried over sodium sulfate (Na_2SO_4) and concentrated under reduced pressure to give the crude product as a pale yellow liquid. The crude product was purified by column chromatography on silica using a mixture of ethyl acetate (EtOAc) and petroleum ether (1:9 ; v/v) as the eluent to give the pure product **(R)** (0.754 g ; 84%) as a colorless liquid.

^{1}H NMR (400 MHz, $CDCl_3$) δ 3.72 (t, *J* = 7.0 Hz, 2H, **3**), 2.44 (t, J = 7.0 Hz, 2H, **4**), 0.90 (s, 9H, **1**), 0.14 (s, 9H, **5**), 0.08 (s, 6H, **2**)

^{13}C NMR (101 MHz, $CDCl_3$) δ 104.29 (**F**), 85.61 (**G**), 61.86 (**D**), 25.93 (**A**), 24.31 (**B**), 18.40 (**E**), 0.12 (**H**), -5,22 (**C**)

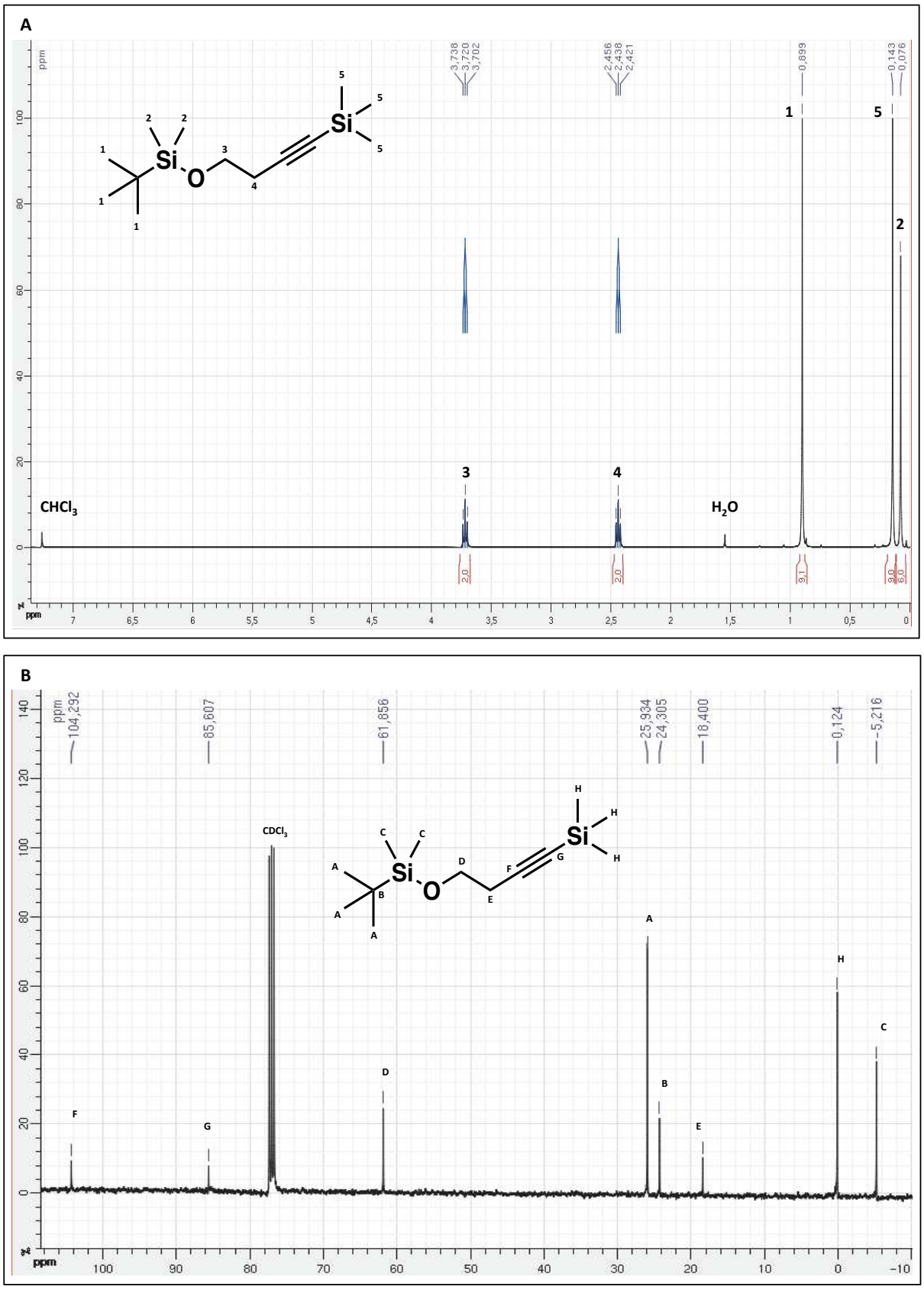

Figure 72. ^{1}H NMR spectrum of the reactant **(R)** with its various ^{1}H signals labeled from 1 to 5 on the schematic structure of **(R)** given in the inset. **B.** 13C NMR spectrum with its various ^{13}C signals marked from A to H.

IV.1.4. FT-IR CHARACTERIZATION OF STARTING MATERIAL (R), SOLVENTS AND PRODUCTS (1) AND (2)

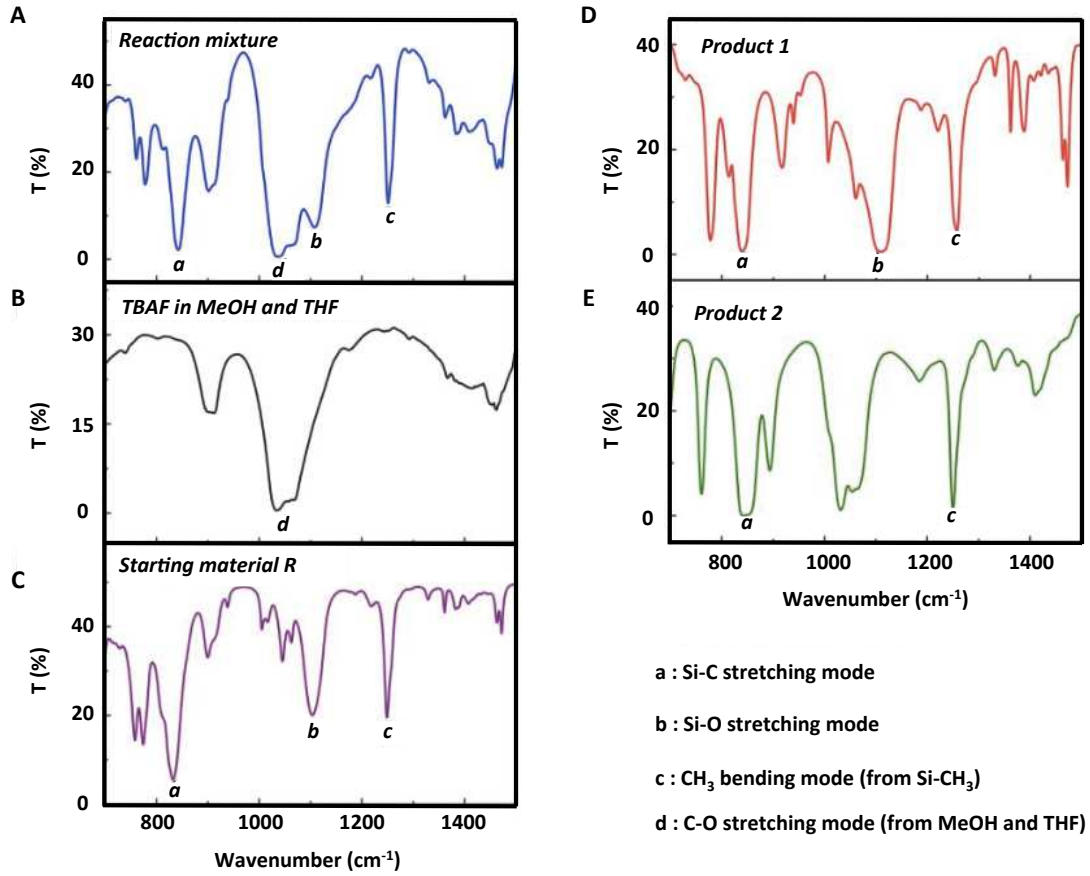

Figure 73. FT-IR transmission spectrum of: **A.** The reaction mixture containing the starting materiel **(R) B.** A solution of TBAF in methanol (MeOH) and THF **C.** Neat starting material **(R) D.** Neat product **(1) E.** Neat product **(2)**. The spectral window is limited to the region of interest of the present study. The vibrational modes of interest in the present study are marked from a-d. Neat products **(1)** and **(2)** were obtained from commercial sources.

IV.1.5. TUNING OF TH FP CAVITIES

An air-filled FP cavity (hereafter referred to as "empty" cavity) of length L exhibits a transmission spectrum with a series of resonances. The frequency of these modes, which are multiples of the fundamental cavity mode, in wavenumber units is given by the equation

$$\bar{\nu}_{(cm^{-1})} = \frac{10^4 m}{2nL} \quad \textbf{(Equation 16)}$$

where m is the mode order, n is the refractive index of the medium and L is the thickness of the cavity in micrometers. The spacing between each mode, called the free spectral range (FSR), gives the frequency corresponding to the fundamental mode. For a given spacer and metal mirror thickness, the FSR of such an "empty" cavity is a constant. The injection of a sample further changes the cavity mode spacing as a function of its refractive index n. As a general procedure, to prepare an on-resonance cavity with respect to a given vibrational transition, the refractive index n of the medium to be injected is calculated first. Subsequently, the "empty" cavity is tuned to get the required FSR, such that when the sample is injected, one of the cavity modes is in resonance with the chosen vibrational transition. For example, in the present experiments, to make an on-resonance cavity with Si-C stretching transition at 842 cm^{-1}, we first tuned our "empty" cavity to attain the FSR of 586 cm^{-1} as shown in **Figure 74A**. Therefore, the injection of our reaction mixture, whose n is 1.395, will modify the FSR to 420 cm^{-1} and result in the strong coupling of the Si-C stretching transition with the second mode of the cavity as shown in **Figure 74B**.

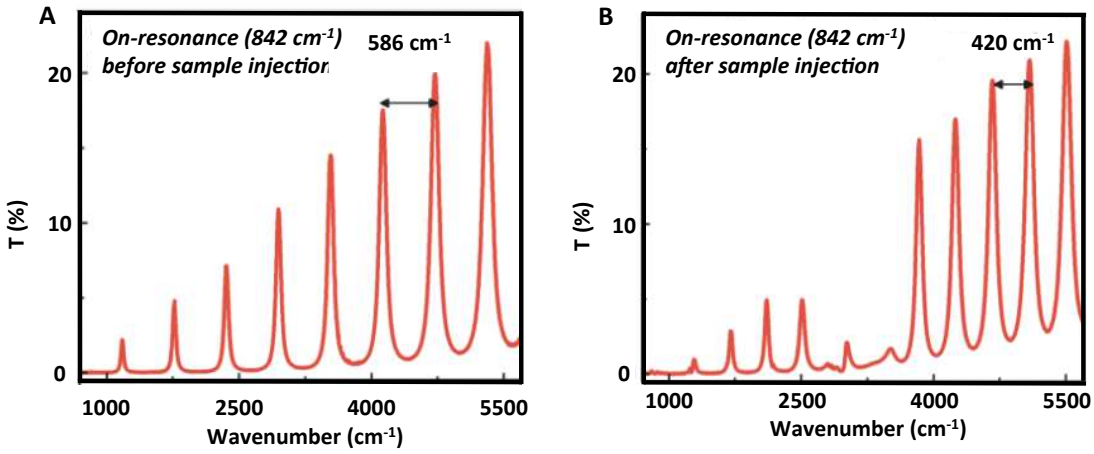

Figure 74. Measured optical resonances of a flow-cell FP cavity of length 8.5 mm: before **(A)** and after **(B)** the injection of reaction mixture.

IV.1.6. PREPARATION OF THE REACTION MIXTURE AND INJECTION INTO THE FP CAVITIES

Once the desired "empty" cavity was obtained, the liquid sample cell was inserted in the variable temperature mount and was kept for 2 hours to stabilize and equilibrate to the experimental temperature (25 °C, except if otherwise noted).

The sample injection into the cavities and flow-cells was done as follows. A stock solution of TBAF (3 M) was prepared using a mixture of MeOH and THF in 1:1 ratio (v/v). For the reaction medium, the starting material **(R)** (0.31 mmol, 100 µL) was mixed MeOH (75 µL) and THF (75 µL) in a 5 mL glass vial followed by the addition of TBAF stock solution (100 µL). The mixture was shaken to obtain a homogeneous solution and was then directly injected into the flow-cell FP cavity making sure that the cavity is filled without any air-bubbles.

IV.1.7. RATE OF THE REACTION

The rate of the reaction was calculated from the shift in the higher order cavity mode due to a change in the refractive index during the reaction **(see Eq. 16)**. The reactant and the products have slightly different reactive indices (1.39 versus 1.43 for product **(1)** and 1.44 for product **(2)**) resulting in a change of the background refractive index (n) of the reactive medium as the reaction progresses. Because the product ratio is constant, monitoring this shift allows one to extract the rate of the reaction as explained below. The use of ZnSe windows for making the sample cells for outside the cavity experiments resulted in a very weak interference fringes as shown in **Figure 75C**. This is because of the relatively large difference between the n of ZnSe and the reactive medium. These weak interference fringes also shifted in the same way as those of the cavity mode, indicating the progress of the reaction. To calculate the rate of the reaction, the temporal shift ($\Delta\bar{\nu}_t$) of a higher order cavity mode peak for all on- as well as off-resonance experiments with respect to the starting value ($\bar{\nu}_0$) was recorded. For experiments outside the cavity, the peak of a weak interference fringe was considered. For all these experiments, a mode at ~5000 cm^{-1}, well isolated from the molecular vibrational modes, was monitored as shown in **Figure 75**.

The maximum shift ($\Delta\bar{\nu}_{\infty}$) corresponding to the completion of the reaction was determined separately from an outside the cavity experiment. The ln plot of the temporal shift ($\ln(1-\frac{\Delta\bar{\nu}_t}{\Delta\bar{\nu}_{\infty}})$) gave a straight line, indicating a pseudo first-order reaction and from the slope the rate constant for the total reaction (k_{TR}) was calculated.

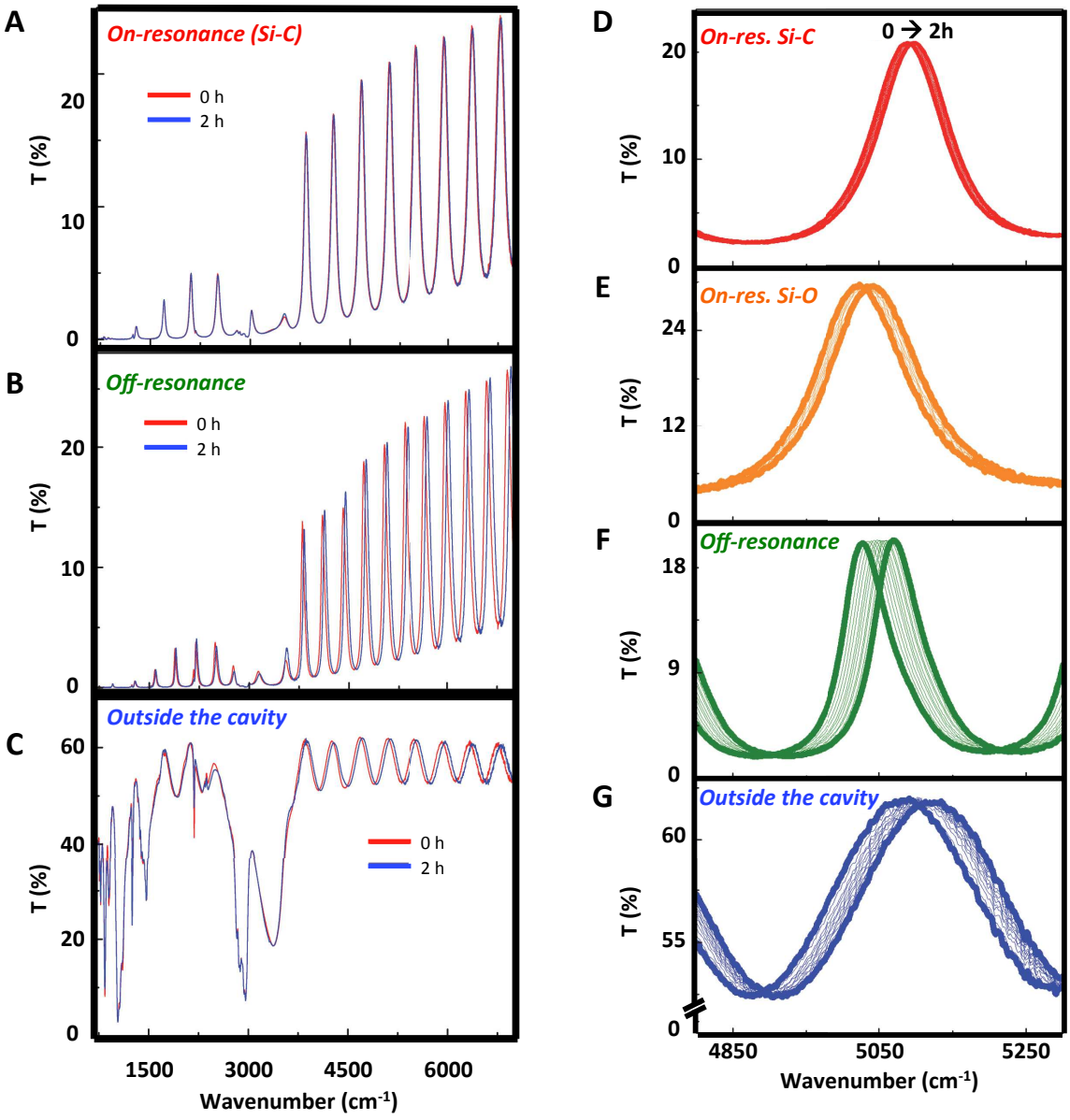

Figure 75. FT-IR transmission spectrum of the on-resonance cavity **(A)**, off-resonance cavity **(B)**, and outside the cavity **(C)** immediately after injection of the reaction mixture (red curve) and after 2h (blue curve). (**D-G)** Shows the temporal shift of the higher cavity order mode during the reaction (0 to 2h) for cavities on-resonance with the Si-C **(D)** and the Si-O stretching mode **(E)**, off- resonance cavity **(F)** and outside the cavity **(G)**.

IV.1.8. STABILITY CHECK OF THE STRONGLY COUPLED STARTING MATERIAL (R)

To check if the starting material alone could induce a temporal shift of a higher order mode cavity, a control experiment was carried out. The staring material **(R)** was injected to a cavity tuned to be in resonance with the Si-CH_3 vibrational transition (1250 cm^{-1}) and the transmission spectrum was recorded at different time intervals **(Figure 76)**. No shift of the cavity modes was observed even after 5 h.

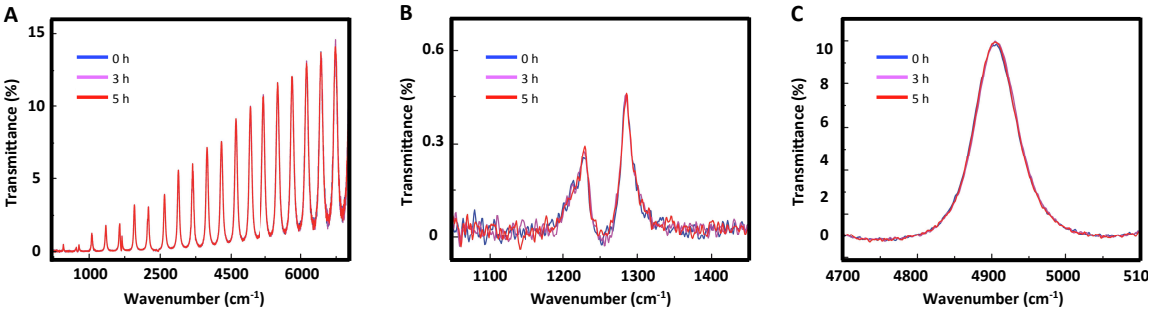

Figure 76. FT-IR transmission spectrum of strongly coupled **(R)** in the total spectral range of 500-7000 cm^{-1} **(A)**, the zoomed region of the strongly coupled vibrational mode **(B)**, and the higher order cavity mode **(C)**. The spectrum was recorded immediately after injection of **(R)** (blue curve), after 3h (magenta curve) and after 5 h (red curve).

IV.1.9. FT-IR TRANSMISSION SPECTRUM OF AN OFF-RESONANCE CAVITY

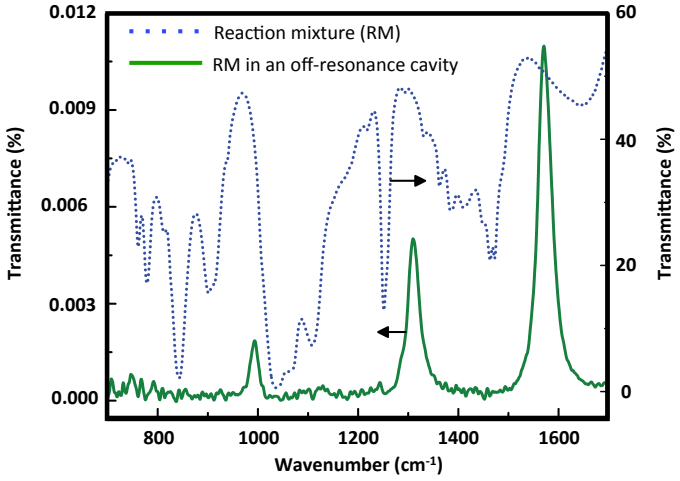

Figure 77. FT-IR transmission spectrum of the reaction mixture injected into an off-resonance cavity (green curve), and the spectrum recorded outside the cavity (blue dotted line). No vibrational modes of interest are strongly coupled.

IV.1.10. IDENTIFICATION OF PRODUCTS (1) AND (2)

Reaction products **(1)** and **(2)** were identified by comparing the mass spectra and retention times against commercially available samples of **(1)** and **(2)** **(Figure 78)**. The GC chromatograms are given in the top panel of **Figure 78A-B** and the respective mass fragments are given in bottom panels. The mass spectrum given in magenta colour in **Figure 78A** corresponds to the second peak of the chromatogram (retention time 2.42 min) and the mass spectra given in orange color corresponds to the first peak (retention time 2.29 min). The first peak in GC chromatogram of **Figure 78A** is coming from the decomposition of **(1)** on the GC column. The GC chromatogram and the corresponding mass fragments of **(2)** are shown in **Figure 78B**.

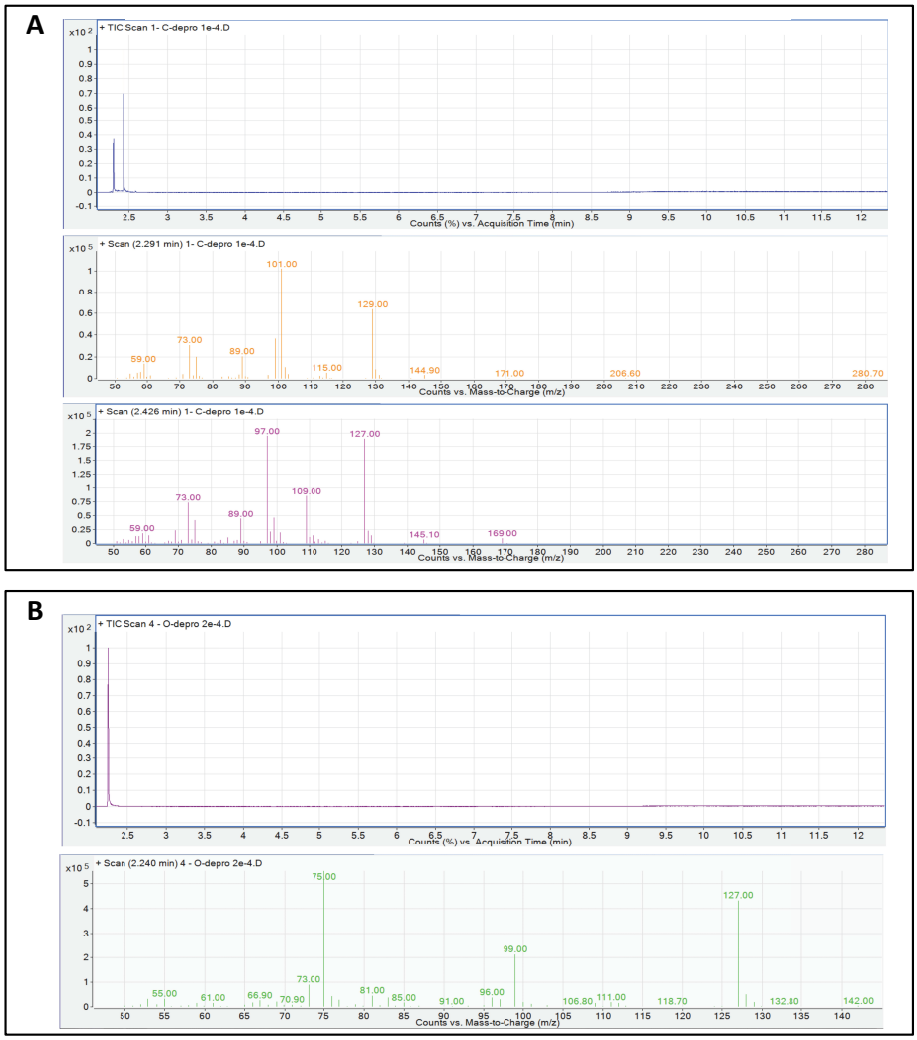

Figure 78. GC chromatogram (top panels) and mass spectra (bottom panels) of commercially available product **(1) (A)** and product **(2) (B)**. The concentration of products **(1)** and **(2)** in the samples used for this analysis was 0.1 mM and 0.2 mM, respectively.

IV.1.11. QUANTITATIVE ANALYSIS OF PRODUCTS (1) AND (2)

200 µL solutions of compound **(1)** and **(2)** at different concentrations (0.1 to 10 mM) were prepared by diluting stock solutions of these compounds in isopropanol. For each compound, a six-point graph was plotted; correlating the characteristic GC peaks (as integrated automatically by the *Agilent MassHunter Workstation v.B.06.00* software) with substrate concentration **(Figure 79)**. Each data point was the mean of three independent measurements and the correlation line was obtained from the least-squares fitting (intercept = 0). Error bars on graphs are shown as ± standard deviation for each data point.

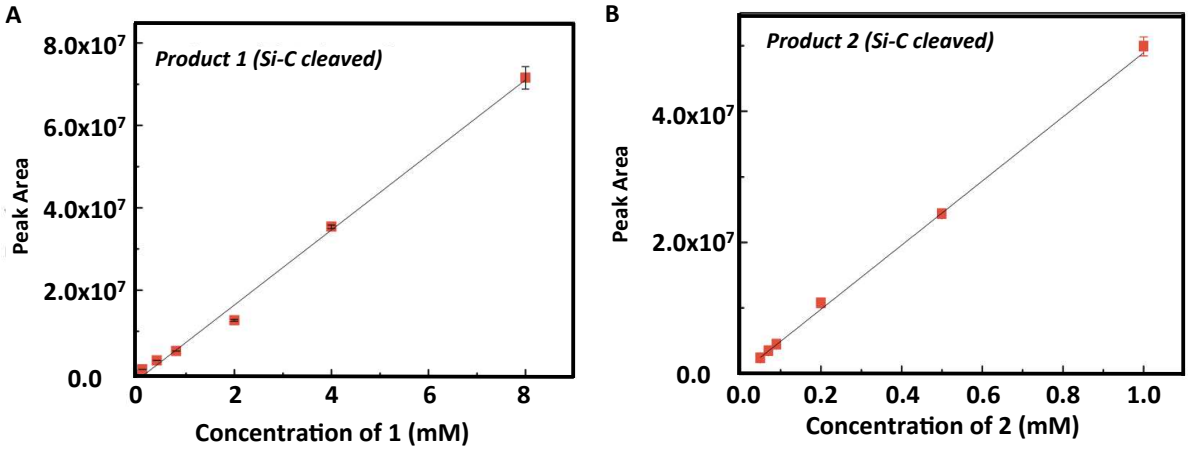

Figure 79. Correlation between the concentration of the products in *i*-PrOH and the measured GC peak areas. The calibration curves for C- and O-deprotected products are shown in **(A)** and **(B)** respectively.

After 3 h of reaction, the flow-cell FP cavity (for on- and off-resonance measurements, or the liquid cell, in the case of the "outside cavity" experiments) was opened and the reaction mixture was extracted with isopropanol (1 mL). 200 µL of this solution were directly injected into the GC-MS. The concentrations of products **(1)** and **(2)** in the reaction mixture were calculated by comparing the product peak area with the calibration line and the ratio between the two products (**(1)** over **(2)**) was determined. The reported ratios are an average of multiple runs, with an error corresponding to the mean (±) absolute deviation.

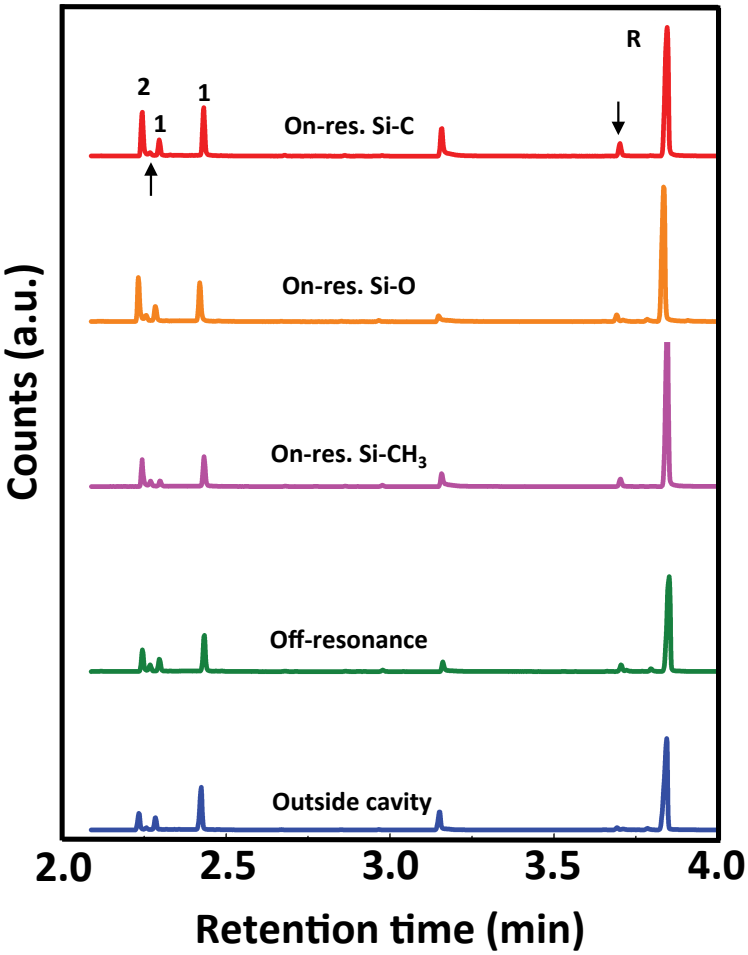

Figure 80. The GC-MS chromatograms of the reactions carried out in cavities tuned to be on- resonance with Si-C stretching (red), Si-O stretching (orange) and Si-CH_3 bending modes (magenta), together with the data for an off-resonance cavity (green) and outside the cavity (blue). The unreacted starting material is marked as **(R).** The peaks corresponding to C- and O-deprotected products are marked as **(1)** and **(2)**, respectively. The peaks indicated by the arrows are impurities that come from the slow degradation of the GC-MS column and it is present in all the chromatograms that we measure. The peak at the retention time of 3.2 min corresponds to the TBAF, which is eluted as an ion pair in the GC column.

As mentioned in chapter II, the GC-MS ratio of the two products under on-resonance conditions has to be corrected for the tuned area under VSC using the following formula:

$$Ratio_{corrected} = \frac{Ratio_{obs.} - (Ratio_{outside\ cav.} \times (1 - \%\ coupled\ area))}{\%\ coupled\ area}$$

where $Ratio_{corrected}$ is the corrected GC-MS ratio, $Ratio_{obs.}$ is the GC-MS ratio observed in the on-resonance experiments, $Ratio_{outside\ cav.}$ is the average ratio measured outside the cavity and $\%\ coupled\ area$ is the pourcentage area of the cavity under VSC.

In the experiments reported herein, the area under VSC corresponds to ca. 60% of the FP microfluidic cell. The other 40% is detuned beyond the width of the vibrational mode being coupled and hence is in the off-resonance condition. **Table 10** below shows the uncorrected and corrected ratios of products **(1)** and **(2).**

Table 10. Observed product ratios ([**1**]/[**2**]) extracted from GC-MS measurements and the corresponding corrected values under VSC for the tuned area.

Experiment		Product Ratio [1]/[2]	
		Observed	Corrected for tuned area under VSC
Outside cavity		1.5 ± 0.2	-
Off-resonance		1.4 ± 0.1	-
VSC	Si-C	0.8 ± 0.1	0.3 ± 0.1
	Si-O	0.9 ± 0.1	0.4 ± 0.1
	$Si-CH_3$	0.8 ± 0.1	0.3 ± 0.1

IV.2. CAVITY CATALYSIS BY VSC OF THE SOLVENT

IV.2.1. MATERIAL AND METHODS

Unless otherwise noted, all reagents and solvents were purchased from commercial suppliers and used without further purification.

The FT-IR transmission spectra of the FP cavities and the "outside the cavity" cells were acquired by standard FT-IR spectrometer (Bruker Vertex70) in transmission mode. The transmission was recorded by DTGS (deuterated triglycine sulfate) detector with 2 cm^{-1} resolution over 64 scans, except for the case of HFIP alone in the on-resonance cavity shown in **Figure 66 (see sub-section III.2.1.2.)** where it has been recorded by MCT (mercury cadmium telluride) detector with 1 cm^{-1} resolution over 128 scans.

GC-MS analysis was performed on a GC System 7820A (G4320) connected to a MSD block 5977E (G7036A), using Agilent High Resolution Gas Chromatography Column: PN 19091S 10 – 433UI, HP – 5MS UI, 28m×0.250 mm, 0.25 Micron, SN USD 489634H. All samples were prepared in 2-propanol (200 µL sample volume). The analysis was carried out on a splitless 1 µL injection volume with an injection port temperature 250 °C. Column oven temperature program was as follows: 60 °C for 1 min, ramped at 30 °C min^{-1} to 310 °C with 3min hold, with a total running time of 12.33 min. The mass spectrometer was turned on after 2 min and was operated at the electron ionization mode with quadrupole temperature of 150 °C. Data acquisition was performed in the SIM mode (selected ion monitoring) based on the ions detected for the commercial compounds. Hydrogen (99.999 % purity) was used as carrier gas at a constant flow rate of 1.5 $mL.min^{-1}$.

^{1}H NMR spectrum of starting material **(R3)** and *ε*-caprolactone **(4)** in $CDCl_3$ were recorded on a Bruker Avance 400 (400 MHz) spectrometer at ambient temperature and is reported in ppm scale using the residual solvent resonance as the I.S. ($CDCl_3$ at 7.26 ppm).

IV.2.2. PREPARATION OF THE REACTION MIXTURE FOR THE *CIS*-CYCLOOCTENE (R2) EPOXIDATION AND INJECTION INTO THE FP CAVITIES

Once the desired “empty” cavity was obtained, the liquid sample cell was inserted in the variable temperature mount and was kept for 2 hours to stabilize and equilibrate to the experimental temperature (15 °C).

The sample injection into the cavities and flow-cells were done as follows. For the reaction medium, the starting material **(R2)** (0.61 mmol, 80 µL), H_2O_2 (0.17 mmol, 10 µL) and bromooctane (0.06 mmol, 10 µL) were mixed in 850 µL of HFIP. The mixture was shaken to obtain a homogeneous solution and was then directly injected into the flow-cell FP cavity making sure that the cavity is filled without any air-bubbles. After 50 minutes, the reaction mixtures were extracted from the cavities, quenched with a scoop of MnO_2 and analyzed qualitatively by GC-MS.

IV.2.3. IDENTIFICATION OF *CIS*-CYCLOOCTENE (R2) AND CYCLOOCTENE OXIDE (3)

The starting material, *cis*-cyclooctene **(R2)**, and the product of its epoxidation, cyclooctene oxide **(3)**, were identified by comparing the mass spectra and retention times against commercially available samples of **(R2)** (retention time = 2.43 min) and **(3)** (retention time = 3.46 min) **(Figure 81)**. The GC chromatograms are given in the top panel of **Figure 81A-B** and the respective mass fragments are given in bottom panels. The GC chromatogram of bromoocotane (retention time = 3.61 min) is shown in the top panel of **Figure 81C** together with its mass fragment in the bottom panel.

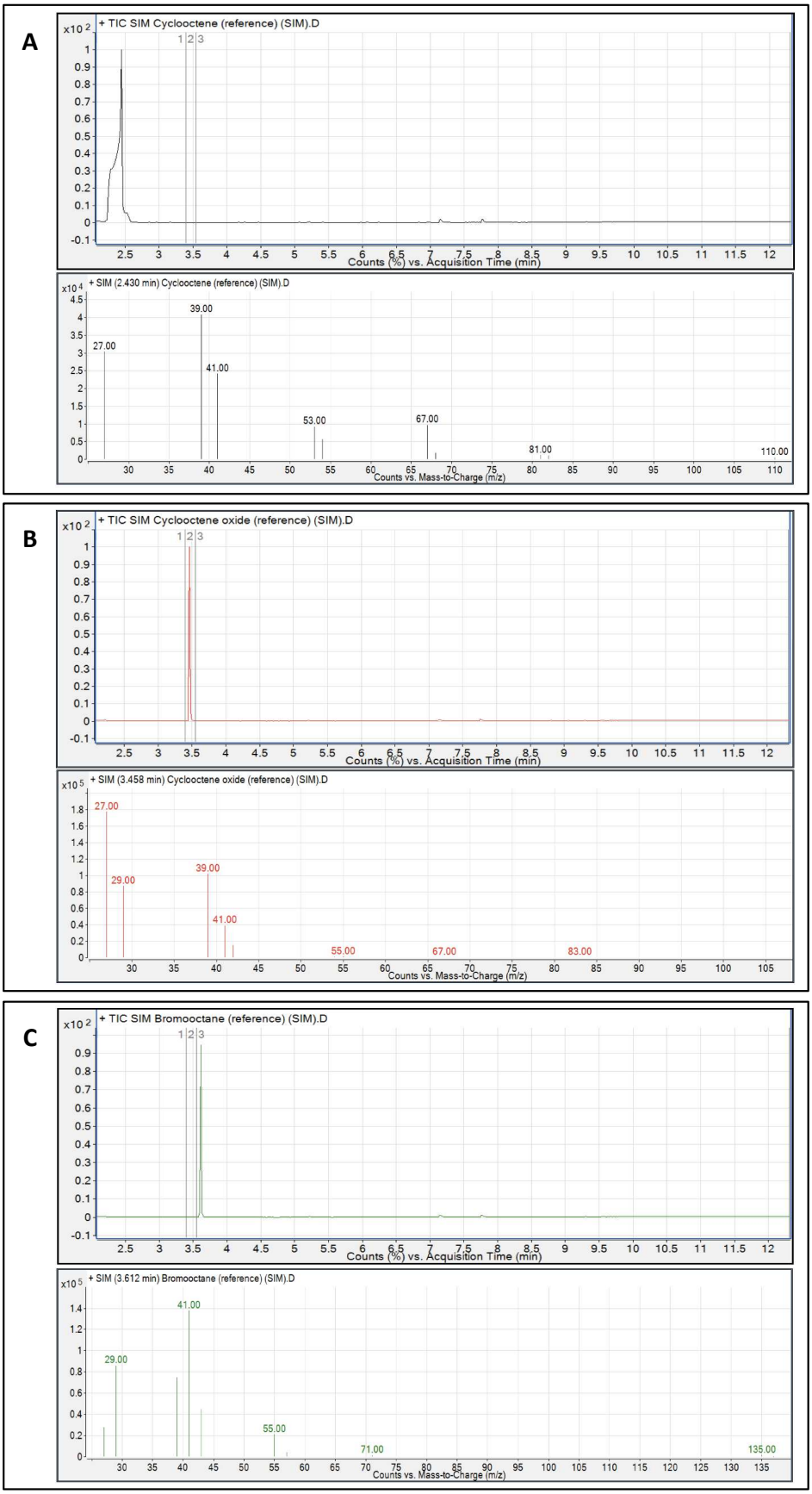

Figure 81. GC chromatogram (top panels) and mass spectra (bottom panels) of commercially available *cis*-cyclooctene **(R2)**, cyclooctene oxide **(B)** and bromoocotane.

IV.2.4.QUANTITATIVE ANALYSIS OF *CIS*-CYCLOOCTENE (R2) AND CYCLOOCTENE OXIDE (3)

IV.2.4.1.DETERMINATION OF THE RELATIVE RESPONSE FACTORS

The relative response factor (RRF) of both compounds, $RRF_{(R2)}$ and $RRF_{(3)}$, relatively to the I.S., bromoocotane, has been determined. 250 µL solutions of **(R2)** and **(3)** at different concentrations (0.013 mM to 1.3 mM) were prepared by diluting stock solutions of these compounds in *i*-PrOH. A fixed quantity of the I.S. (0.12 mM) was added in each solution. For both compound, a five-points graph was plotted as a calibration curve. It correlates the ratio of the GC peak areas ($A_{(R2)}$ or $A_{(3)}$) to that of the I.S. ($A_{I.S.}$) with the ratio of their concentrations ([R2] or [3]) to that of the I.S. ([I.S.]) **(Figure 82)**. The GC peak areas were integrated automatically by the *Agilent MassHunter Workstation v.B.06.00* software. The equations of the calibration lines shown in **Figure 82A** and **B** are respectively:

$$\frac{A_{(R2)}}{A_{I.S.}} = \frac{[R2]}{[I.S.]} \times slope \quad \textbf{(Equation 17)} \quad \text{and} \quad \frac{A_{(3)}}{A_{I.S.}} = \frac{[3]}{[I.S.]} \times slope \quad \textbf{(Equation 18)}$$

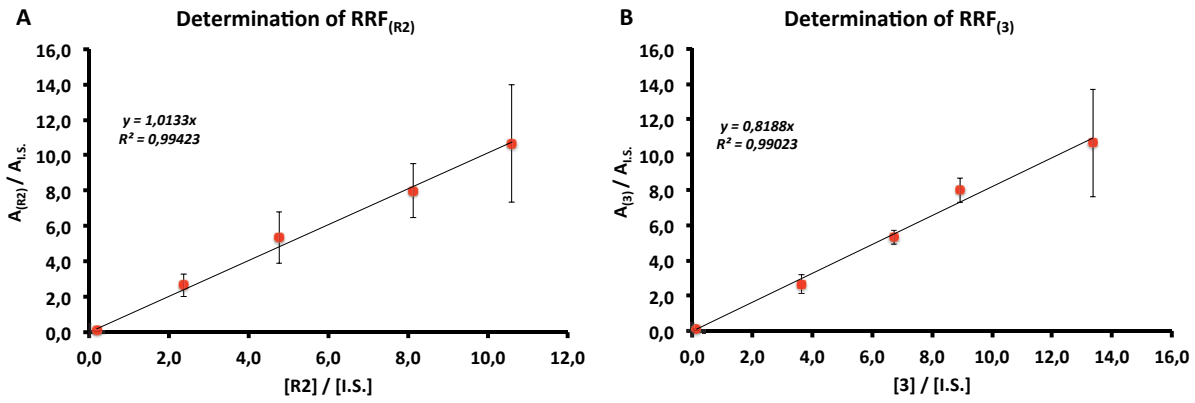

Figure 82. A. Correlation between the concentration ratio [R2]/[I.S.] and the ratio $A_{(R2)}/A_{I.S.}$, obtained by respective integration of the GC peak area of **(R2)** and the I.S. respectively. $RRF_{(R2)}$ (1.01) is given by the slope of the calibration curve. **B.** Correlation between the concentration ratio [3]/[I.S.] and the ratio $A_{(3)}/A_{I.S.}$, obtained by respective integration of the GC peak area of **(3)** and the I.S. respectively. $RRF_{(3)}$ (0.82) is given by the slope of the calibration curve.

Each data point was the mean of two independent measurements and the correlation line was obtained from the least-squares fitting (intercept = 0). Error bars on graphs are shown as ± standard deviation for each data point.

IV.2.4.2. QUANTIFICATION OF THE I.S. INSIDE FP MICROFLUIDIC CELL

The volume of the reaction mixture that is injected into the flow-cell FP cavity can vary between experiments. Therefore, the [I.S.] may also vary after the dilution that occurs when extracting the reaction mixture from FP microfluidic cavity to prepare the GC-MS sample. However, it is required to know the exact [I.S.] to be able to use the calibration curves shown in the previous **sub-section IV.2.4.1.** for quantification of **(R2)** and **(R3)**. For an accurate determination of [I.S.] in reaction mixtures, a five-points graph was plotted as a calibration curve; correlating the GC peak area (as integrated automatically by the *Agilent MassHunter Workstation v.B.06.00* software) with the concentration of the I.S. **(Figure 83)**. Each data point was the mean of three independent measurements and the correlation line was obtained from the least-squares fitting (intercept = 0). Error bars on graphs are shown as ± standard deviation for each data point.

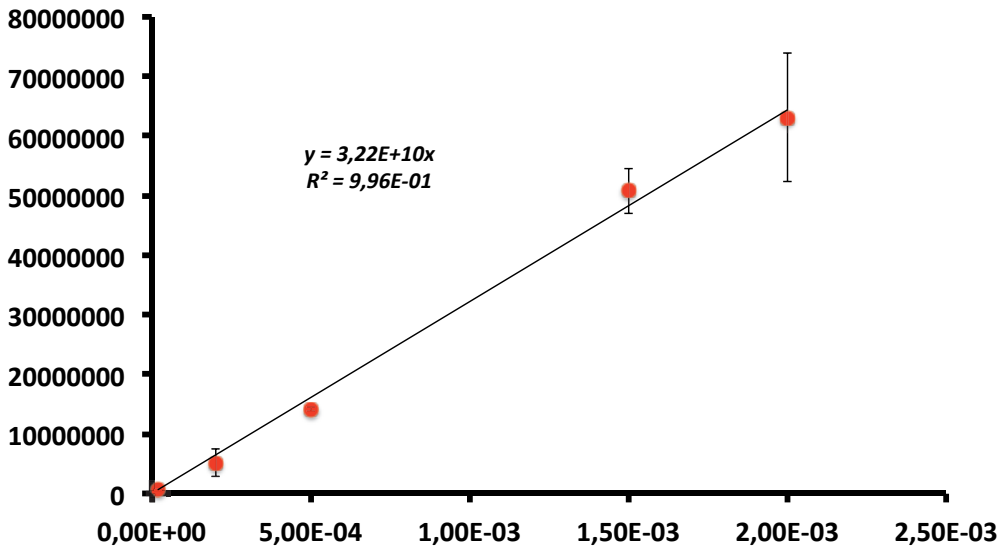

Figure 83. Correlation between the concentration of the I.S. in *i*-PrOH and the measured GC peak areas.

IV.2.4.3. QUANTIFICATION OF **(R2)** AND **(3)**

After 50 min of reaction, the flow-cell FP cavity (for on- and off-resonance measurements) as well as the liquid cells (for the "outside cavity" experiments) was opened and the reaction mixture was extracted with *i*-PrOH (1mL). A scoop of MnO_2 was added to quench the reaction mixture. After centrifugation, 200 µL of this solution were injected into the GC-MS.

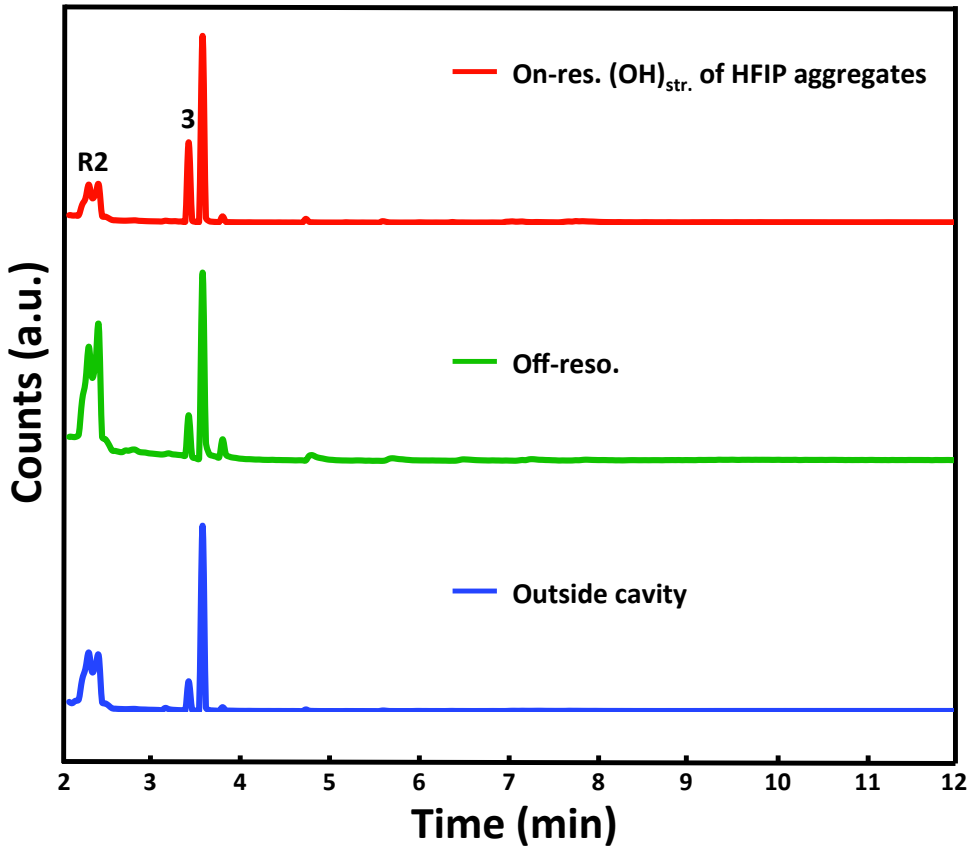

Figure 84. The GC chromatograms of the reactions carried out in cavities tuned to be on-resonance with O-H stretching mode (red) together with the data for an off-resonance cavity (green) and outside the cavity (blue). The peaks corresponding to *cis*-cyclooctene and cyclooctene oxide are marked as **(R2)** and **(3)**, respectively. The peak at 3.6 min corresponds to bromooctane, which has been added in the reaction mixture to be used as the I.S. for quantitative analysis.

The concentrations of **(R2)** and **(3)** in the reaction mixture were calculated using the calibration line of the I.S. and the **eq. 17** and **18**. The ratio $\frac{[3]}{[R2]}$ was than determined. The reported ratios are an average of multiple runs, with an error corresponding to the mean (±) absolute deviation. The GC-MS ratio of **(3)** and **(R2)** under on-resonance conditions has been corrected for the tuned area under VSC (as explained in **section IV.1.11.**). In the experiments

reported herein, the area under VSC corresponds to ca. 40% of the FP microfluidic cell. The other 60% is detuned beyond the width of the vibrational mode being coupled and hence is in the off-resonance condition. **Table 11** below shows the uncorrected and corrected $\frac{[3]}{[R2]}$ ratios.

Table 11. Observed $\frac{[3]}{[R2]}$ ratios extracted from GC-MS measurements and the corresponding corrected values under VSC for the tuned area.

Experiment	**Ratio $\frac{[3]}{[R2]}$**	
	Observed	Corrected for tuned area under VSC
Outside cavity	**0.17** ± 0.09	-
Off-resonance	**0.12** ± 0.03	-
On-resonance	**0.43** ± 0.12	**0.82** ± 0.17

IV.2.5. SYNTHESIS OF 7,8,15,16-TETRAOXADISPIRO[5.2.5.2]HEXADECANE (R3)

In a 100 mL flask, methyltrioxorhenium (0.024 mmol; 6.0 mg), a 54% HBF_4 solution in Et_2O (24.0 mmol; 3.24 mL) and 50% H_2O_2 solution in H_2O (34.8 mmol; 1.98 mL) were mixed in TFE (24 mL). Then, cyclohexanone (24.0 mmol; 2.48 mL) was added at 0 °C and the reaction mixture was stirred for 3 minutes at RT. After precipitation, the product **(R3)** was immediately filtered to avoid re-dissolution. Finally, the crude was recrystallized in MeOH (≃25 mL) to give the pure compound **(R3)** (8.23 mmol; 1.88 g)

^{1}H NMR (400 MHz, $CDCl_3$) δ 2.29 (bs, 4H), 1.51-1.86 (bs, 12H), 1.37-1.51 (bs, 4H)

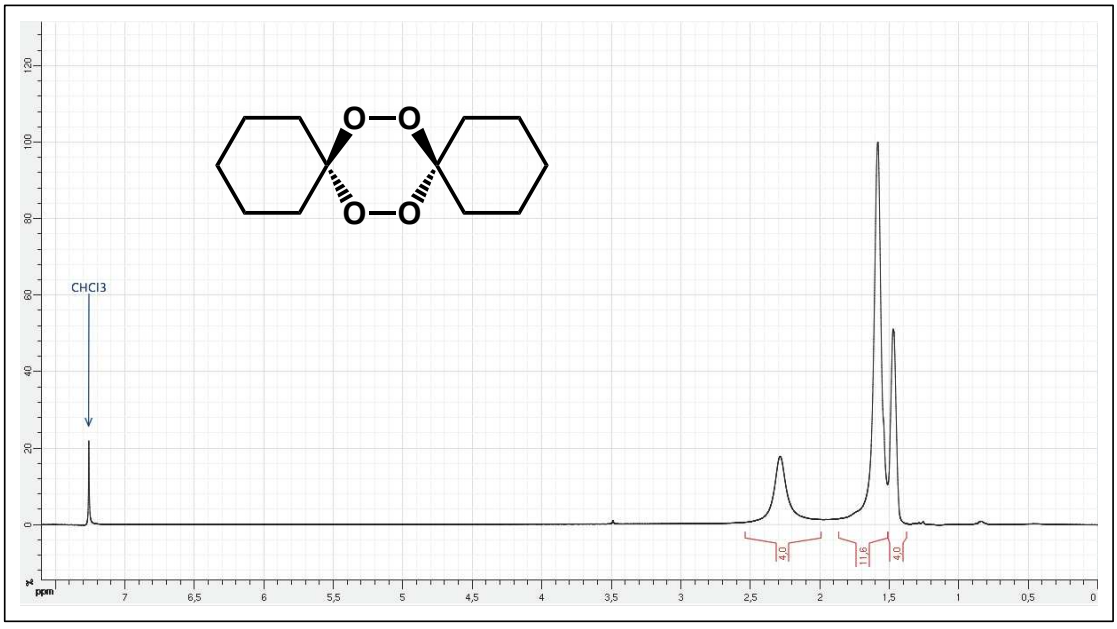

Figure 85. ^{1}H NMR spectrum of the reactant **(R3)** with its schematic structure given in the inset.

IV.2.6. PREPARATION OF THE REACTION MIXTURE FOR THE ACID-CATALYZED REARRANGEMENT OF 7,8,15,167,8,15,16-TETRAOXADISPIRO[5.2.5.2]HEXADECANE (R3) TO CAPROLACTIONE (4) AND INJECTION INTO THE FP CAVITIES

Once the desired “empty” cavity was obtained, the liquid sample cell was inserted in the variable temperature mount and was kept for 2 hours to stabilize and equilibrate to the experimental temperature (25 °C).

The sample injection into the cavities and flow-cells were done as follows. A stock solution of *p*-TsOH (0.046 mM) in pure HFIP was prepared. For the reaction medium, the starting material **(R3)** (0.22 mmol, 50 mg) was dissolved in 250 µL of the stock solution of *p*-TsOH (0.0115 mmol; 5 mol %) in HFIP. The mixture was shaken to obtain a homogeneous solution and was then directly injected into the flow-cell FP cavity making sure that the cavity is filled without any air-bubbles. After 30 minutes, the reaction mixtures were extracted from the cavities with $CDCl_3$ and analyzed quantitatively by qNMR (ERETIC) with dichloromethane (DCM) as the I.S..

IV.2.7. NMR IDENTIFICATION OF CAPROLACTONE (4)

The NMR spectrum of commercially purchased *ε*-caprolactone **(4)** has been recorded.

^{1}H NMR (400 MHz, $CDCl_3$) δ 4.22 (t, *J* = 4.6, 2H, **1**), 2.63 (t, *J* = 4.6 Hz, 2H, **5**), 1.85 (bs, 2H, **2**), 1.76 (bs, 4H, **3** and **4**)

It contains 9% of its hydrolyzed form, the 6-hydrohyhexanoic acid.

^{1}H NMR (400 MHz, $CDCl_3$) δ 4.05 (t, *J* = 6.5, 2H, **10**), 2.30 (t, *J* = 7.5 Hz, 2H, **1**), 1.52-1.69 (m, 5H, **7, 9 and 11**), 1.29-1.47 (m, 4H, **8**)

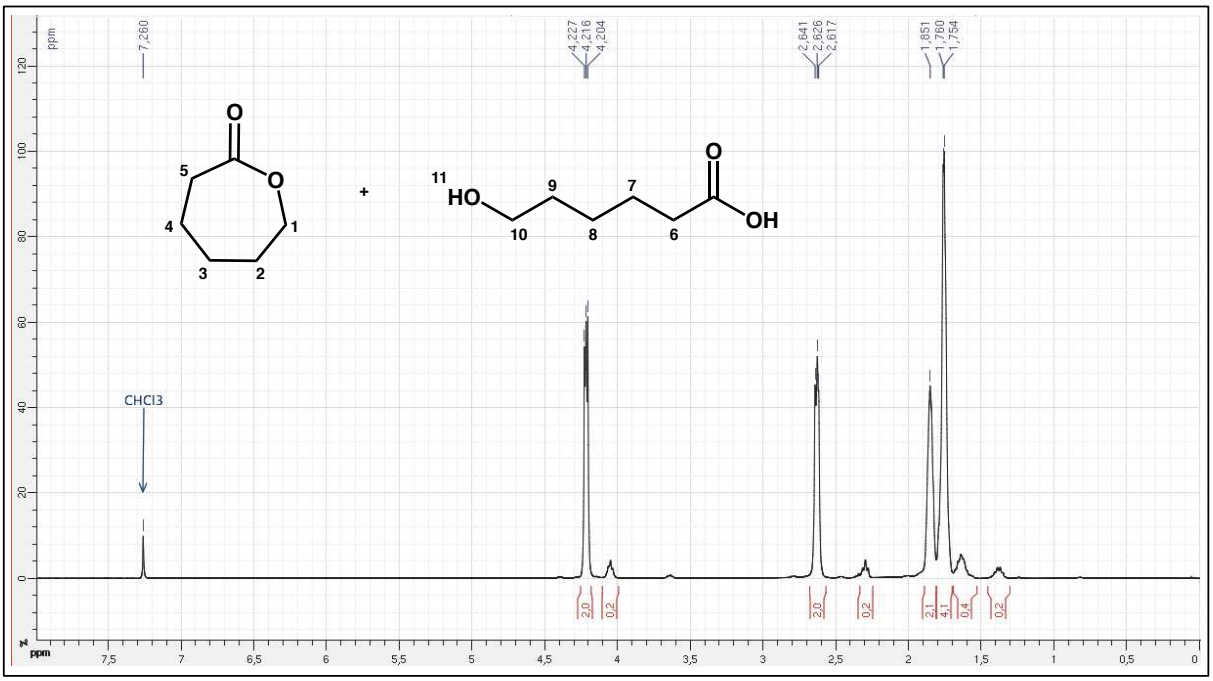

Figure 86. ^{1}H NMR spectrum of the product **(4)** with its various ^{1}H signals labeled from 1 to 5 on the schematic structure of **(4)** given in the inset (molecule on the left). The hydrolyzed form of product **(4)** is also visible on the spectrum, with its various ^{1}H signals labeled from 6 to 11 on the schematic structure given in the inset (molecule on the right).

CHAPTER V

V. GENERAL CONCLUSION

This thesis manuscript was written by and for chemists discovering the world of light-matter interactions. The general introduction begins with an historical and chronological description of Man's understanding of light, from ancient times to the advent of quantum physics. It can be noticed that very early on, the conception of light was associated with the environment in which it propagates. Later, when it was realized through quantum physics that even the *vacuum* was not "nothing", modifications of several properties of matter were achieved simply by controlling its environment. I have cited the case of early cQED experiments where the EM vacuum field surrounding single atoms was structured to study and regulate quantum properties of matter.[28–32] Fundamental research in this field led to major advances in the understanding of light-matter interactions and to important societal applications such as optical communication[33–35], optical imaging[36–38] and lasers[39–41]. In line with this pioneering works, it was subsequently shown that various properties of molecular systems could be regulated by strong coupling with cavity modes. The core of this thesis manuscript focuses on VSC since it is used as a new approach to control chemical reaction landscapes. For instance, in 2016, collaboration between the teams of Prof. Ebbesen and Prof. Moran demonstrated the ability of VSC to reduce the rate of a chemical reaction.[42]

For most of my thesis, I contributed significantly to the study of a slightly more complex reaction system that was designed to demonstrate the ability of VSC to drive the formation of one product relative to another. Indeed, the reagent used for the experiments had two distinct silyl (Si-CR_3) and silyl ether (Si-OR_3) groups that could be competitively deprotected by TBAF. Kinetic analysis has shown that the VSC of either site (Si-C or Si-O) favored the cleavage of the Si-O bond over the cleavage of the otherwise kinetically favored Si-C bond. Thermodynamic analysis revealed that the activation barrier and entropy activation of the system increased under VSC, suggesting a "product-like" transition state that is slightly less strained than the standard transition state known for this type of deprotection reaction. This work has been discussed in chapter II and published in Science. It constitutes a proof-of-concept showing that it is possible to control reaction selectivity through VSC.[2]

In an effort to discover new features of VSC, we wanted to evaluate its ability to enhance chemical reactions rates. I chose to work on a well-known reaction from the literature: the epoxidation of an olefin with H_2O_2 in HFIP. A kinetic study of this reaction by Berkessel *et al.* revealed a crucial catalytic role of the solvent (HFIP) at high concentration, which is brought by clusters assembly.[22] The preliminary results presented in chapter III seem to indicate a 4.8-fold increase in the reaction rate under VSC. However, an optimization of the experimental conditions is required to confirm this interesting result. Moreover, in view of the response obtained by coupling the $(OH)_{str.}$ of HFIP aggregates in preliminary experiments, it is suspected that only one type of HFIP aggregates, depending on the conformers inside the aggregate itself, is sensitive to VSC and therefore catalytically relevant.

An inverse KSIE was observed when HFIP-d_1(O-D) was used as a solvent in a Friedel-Crafts reaction studied by one of my colleagues[43]. In the future, such a model reaction could be used to explore the possibility of using VSC as a mimic of the KIE where no chemical modification would be required on the substrate.

All these results contribute to show that VSC provides a weak-field room-temperature method that has the potential to become an everyday tool for chemists to physically control chemical reactivity without catalysts, pre-functionalization, or chemical changes to the reaction conditions and could also provide a new tool for mechanistic studies.

ANNEX

ANNEX – METALS PROMOTE SEQUENCES OF THE REVERSE KREBS CYCLE

During the first months of my thesis, I participated in the main project of Prof. Joseph Moran's team, namely: the understanding of the origin of life. As part of this project, I co-authored an article published in Nature Ecology & Evolution.

In this article, we successfully reproduced, non-enzymatically and in a pre-biotic environment, 6 of the 11 steps of the inverse Krebs cycle. This cycle, at the heart of the metabolism of certain primitive organisms, allows the synthesis of the five precursors at the origin of sugars, amino acids or other molecules essential to the metabolism of living beings' cells. Thanks to biology, it is now well established that the enzymes present in living organisms make this chemistry possible. To reproduce this cycle in a pre-biotic environment and without enzymes, would give insight into the conditions under which life emerged.

This complex and fascinating project would deserve to be developed in several chapters, but since it is very different from the VSC project on which I have worked for the most part of my thesis, I have decided to enclose this article as an annex.

nature ecology & evolution

ARTICLES

DOI: 10.1038/s41559-017-0311-7

Metals promote sequences of the reverse Krebs cycle

Kamila B. Muchowska, Sreejith J. Varma, Elodie Chevallot-Beroux, Lucas Lethuillier-Karl, Guang Li and Joseph Moran*

The reverse tricarboxylic acid (rTCA) cycle (also known as the reverse Krebs cycle) is a central anabolic biochemical pathway whose origins are proposed to trace back to geochemistry, long before the advent of enzymes, RNA or cells, and whose imprint remains intimately embedded in the structure of core metabolism. If it existed, a primordial version of the rTCA cycle would necessarily have been catalysed by naturally occurring minerals at the earliest stage of the transition from geochemistry to biochemistry. Here, we report non-enzymatic promotion of multiple reactions of the rTCA cycle in consecutive sequence, whereby 6 of its 11 reactions were promoted by Zn^{2+}, Cr^{3+} and Fe^0 in an acidic aqueous solution. Two distinct three-reaction sequences were achieved under a common set of conditions. Selectivity was observed for reduction reactions producing rTCA cycle intermediates compared with those leading off-cycle. Reductive amination of ketoacids to furnish amino acids was observed under similar conditions. The emerging reaction network supports the feasibility of primitive anabolism in an acidic, metal-rich reducing environment.

Life is inextricably linked to metabolism—a complex web of chemical reactions that build up (anabolize) and break down (catabolize) biomolecules. At the earliest stages of prebiotic chemistry at the origin of life, before the advent of enzymes or cells, synthetic chemical pathways must have acted to build molecular complexity from simpler starting materials[1,2]. However, debate exists over whether such a proto-anabolism "must generally be different from the underlying chemistry used in biology"[3] or whether it is recapitulated in extant anabolic pathways[4–9]. The former philosophy has inspired masterful syntheses of crucial biological molecules using chemical building blocks and custom-made synthetic routes that bear little resemblance to those used by life's anabolic pathways. Although this approach is important, it inevitably leaves a vast gulf between the purported prebiotic chemistry and the biochemistry it ultimately aims to explain[10]. An alternative view is that primitive forms of certain existing biological anabolic pathways could have originated spontaneously from geochemistry through naturally occurring catalysts before the existence of enzymes, RNA or cells—a parsimonious explanation for the emergence and organization of biochemistry. Indeed, Ralser et al. demonstrated that several catabolic pathways, including most of the oxidative TCA cycle, are promoted without enzymes simply by using Fe^{2+} as a catalyst and/or peroxydisulfate ions as an oxidizing agent[11–13]. In contrast, non-enzymatic catalysis of extant anabolic pathways—reaction sequences that build up the complexity of biomolecules—remains rare. The anabolic pathways of greatest interest for proto-anabolism are specific reductive CO_2-fixing pathways used by chemoautotrophs[14]: the acetyl-CoA (AcCoA) pathway (also known as the Wood–Ljungdahl pathway)[5–9,15], complete or incomplete versions of the reverse tricarboxylic acid (rTCA) cycle (also know as the reverse Krebs cycle)[16–19] or hypothetical combinations thereof[20,21]. These synthetic pathways are proposed to have been spontaneously driven into existence as a mechanism to dissipate geochemical redox gradients built up between the Earth's reduced core (mostly Fe^0) and its relatively oxidized atmosphere[22], providing an origins scenario that is continuous from geochemistry to the reductive thermophilic carbon-fixing organisms found at the root of the tree of life[19,23,24]. The rTCA cycle exhibits further appeal as a prebiotic pathway since it contains all five universal metabolic precursors for biosynthesis, consists of only five mechanistically distinct reactions, does not use bimolecular reactions between intermediates and possesses an autocatalytic feedback loop that could allow it to persist and self-amplify under the right conditions[18,25]. Hypothetical proto-anabolic networks consisting of the AcCoA pathway together with the complete rTCA cycle[20], or the AcCoA pathway together with an incomplete linear version of the rTCA that stops after step F in Fig. 1 (see also refs [6,21]), have also been suggested as primordial synthetic pathways. The 'complete' hybrid pathway constitutes a stabilized autocatalytic network that, once realized, could display robustness in the face of low synthetic efficiencies or parasitic reactions, providing a compelling reason for why its molecules were preserved in metabolism. On the other hand, an incomplete linear hybrid network is shorter and more plausible under non-enzymatic catalysis due to the challenge of diminishing yields faced in any sequence of chemical reactions[26].

The reductive coupling of two molecules of CO_2 to acetate (**1**), equivalent to the AcCoA pathway, has been observed under aqueous conditions either by using Fe^0 nanoparticles as reducing agents or through electrochemistry on greigite electrodes, albeit in small quantities and with poor selectivity[27–29]. Production of **1** from CO and MeSH in the presence of (Fe,Ni)S has also been reported[30]. Experimental efforts to test the plausibility of a prebiotic rTCA cycle have not been as encouraging[31,32]. Thus far, only two non-consecutive steps of the rTCA cycle (steps C and E in Fig. 1) have been reported with a greater than 5% yield under plausibly prebiotic conditions using mineral photocatalysis[32]. Notably, pyruvate (**2**) has been observed in low yields under electrochemical[28] and CO-rich hydrothermal conditions[33]. Further efforts are needed to test the plausibility of an abiotic (complete or incomplete) rTCA cycle which, when viewed together with an abiotic AcCoA pathway, would provide a satisfying theory for the origin and organization of modern biochemistry. Here, we describe our efforts to assess the prebiotic viability of the six

Institute of Supramolecular Science and Engineering (ISIS UMR 7006), University of Strasbourg, National Center for Scientific Research (CNRS), F-67000 Strasbourg, France. *e-mail: moran@unistra.fr

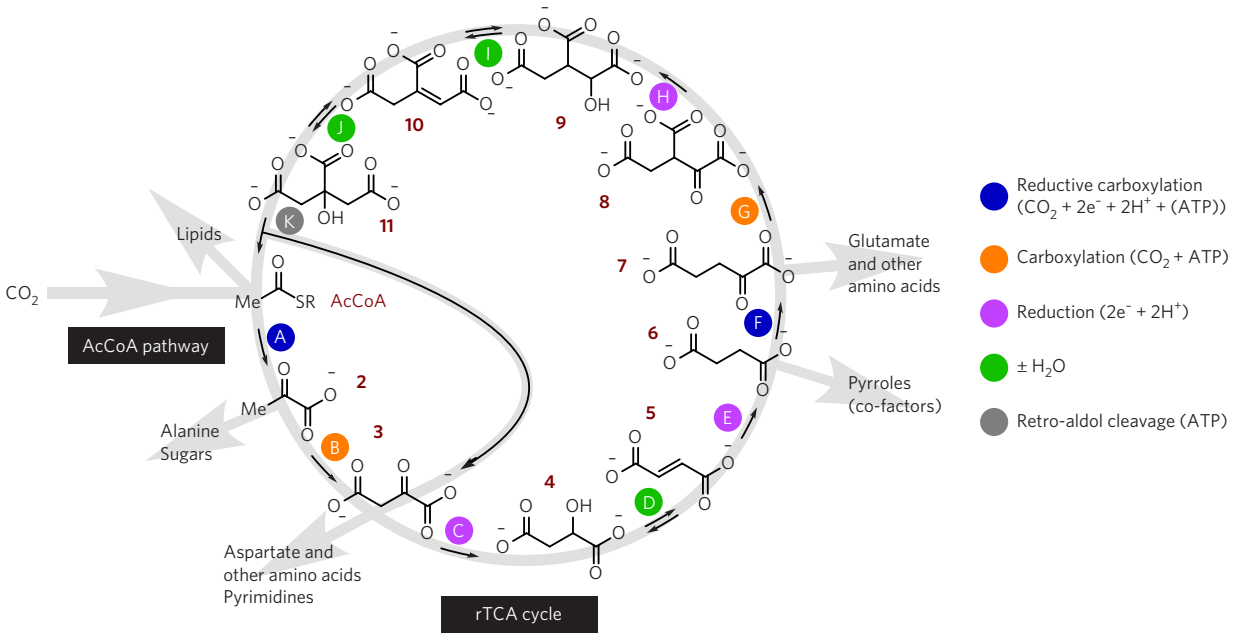

Fig. 1 | Hypothetical proto-anabolic network consisting of the AcCoA pathway (CO_2 to AcCoA) and the rTCA cycle. This pathway includes the epicycle for synthesis of **3**, showing the role of its intermediates as universal biosynthetic precursors[19,20]. The steps of the cycle are labelled alphabetically. Variants with an incomplete rTCA cycle that stops after step F have also been proposed[6,21]. ATP, adenosine triphosphate.

reduction and (de)hydration steps of the rTCA cycle under the influence of metals and metal ions[34].

Results and discussion

Of initial consideration was a search for a viable reducing agent for the two ketone reductions (steps C and H) and one alkene reduction (step E). In biological systems, steps C and H use nicotinamide adenine dinucleotide phosphate as reducing agent and are catalysed by malate dehydrogenase and isocitrate dehydrogenase, respectively. Step E uses flavin adenine dinucleotide as a reducing agent and is catalysed by fumarate reductase. The ketone reductions are thought to be challenging as prebiotic processes due to the rapid spontaneous decarboxylation of oxaloacetate (**3**) and oxalosuccinate (**8**)[35]. In aqueous solution, **3** has indeed only been observed to be reduced photochemically[32]. A preliminary screen of simple chemical reducing agents (Fe^0, Ni^0, Zn^0, Mn^0, Mo^0 and $Na_2S_2O_4$) at various temperatures and across pH ranges revealed several that were capable of some or all of the reductions, but Fe^0 under acidic aqueous conditions stood out for its unique ability to accomplish all three desired individual reductions (Table 1, entries 1–3) while minimizing undesired parasitic reactions and promoting sequences (see below). These observations, in addition to the geological relevance of iron as the major constituent of the Earth's core and the widespread occurrence of its salts in native element minerals, prompted us to select Fe^0 as the reducing agent for further experiments.

In biological systems, the dehydrations of malate (**4**) to fumarate (**5**) and of isocitrate (**9**) to *cis*-aconitate (**10**) (steps D and I) are carried out by the enzymes malate dehydratase and aconitase, respectively. We surmised that these steps should be particularly prone to metal ion catalysis as some dehydratases are Fe^{2+} dependent and aconitase makes use of a Lewis acidic Fe–S cluster to facilitate isocitrate dehydration[36]. The dehydrations of **4** and **9** are both slightly endergonic (+2.3 kJ mol^{-1}) at neutral pH[18]. Perhaps not surprisingly given these unfavourable thermodynamics, in both cases, no more than trace dehydration products were detected upon heating to 140 °C in acidic or basic solution, even in the presence of a wide selection of metal ions. In contrast, the thermodynamically favoured hydration of **5** to **4** occurred even in the absence of metal ions (Table 1, entry 4). We therefore sought to push the dehydration forward by coupling the small amounts of **5** generated at chemical equilibrium to the subsequent irreversible reduction step (steps D and E). A screen of various metal ions in the presence of Fe^0 revealed that Zn^{2+} ions in acidic solution at 140 °C were effective in mediating the dehydration of **4** to **5** and putative reduction to **6** in a single operation, albeit in low yield (Table 1, entry 5; see also Supplementary Table 2). Next, we carried out the same reaction in the presence of a 1% w/w aqueous micellar solution of α-tocopherol methoxypolyethylene glycol succinate, a popular non-ionic surfactant that self-assembles into nano-sized reaction compartments[37], and found that it promoted the two-step sequence even at ambient temperature (Table 1, entry 6). Although this micelle has no direct prebiotic relevance, the experiment supports existing ideas that compartmentalization can enhance the efficiency of prebiotic metabolic processes[1]. A similar screen of metal ions at various temperatures and pH values revealed that the dehydration of **9** to **10** was also promoted by Zn^{2+} ions under hot acidic aqueous conditions (Table 1, entry 7; see also Supplementary Table 3). As with the enzymatic system, step I was reversible under these conditions (Table 1, entry 8).

The sole hydration reaction of the rTCA cycle is the hydration of **10** to citrate (**11**) (step J), a reaction that is also carried out in biological systems by the Fe–S cluster enzyme aconitase. All attempts to observe this reaction under simple acid or base catalysis failed. To our delight, a screen of more than 20 different metal ions at various temperatures and pH values revealed that Cr^{3+} was uniquely effective at enabling hydration to yield substantial amounts of citrate in acidic solution at 140 °C (Table 1, entry 9)[38]. Much smaller amounts of citrate were observed in the presence of other metal ions or at lower temperatures (Supplementary Table 4). Again, as in the enzymatic system, step J was found to be reversible under these conditions (Table 1, entry 10). The observation that Zn^{2+} and Cr^{3+} promoted hydration and dehydration only under acidic conditions can be ascribed to the tendency of metal cations to become aquated at low pH, where they may form structurally diverse polynuclear species that can complex the rTCA acids. In contrast, under alkaline

Table 1 | Non-enzymatic reactions of the rTCA cycle

Entry	Substrate (0.1 mmol)	Conditions[a]				Species detected in the mixture post-reaction (%)[b]											
						On-cycle								Off-cycle			
		Fe^0 (equiv)	Zn^{2+} (equiv)	Cr^{3+} (equiv)	Micelles	2	4	5	6	7	9	10	11	12	13	14	15
Reduction																	
1	**3**	10	–	–	–		90	10									
2[c]	**5**	10	–	–	–		15	20	65								
3[d]	**8**	10	–	–	–				2		98						
Hydration–dehydration																	
4[e]	**5**	–	–	–	–		77	23									
5[e]	**4**	10	10	–	–		94	4	2								
6[f]	**4**	10	10	–	Yes		82	7	11								
7[e,g]	**9**	–	1	–	–						51	49					
8[e,g]	**10**	–	1	–	–						12	88					
9[h]	**10**	–	–	6	–							67	33				
10[h]	**11**	–	–	6	–							23	77				
Three-step sequences																	
11[f]	**3**	10	15	4	Yes		52	3	41					4			
12[i]	**8**	5	10	6	–						65	30	2		3		
13[i]	**8**	5	10	6	Yes				5		72	21	2				
Competitive reduction																	
14[d]	**2 + 3 + 5 + 7 + 10**	10	15	6	Yes	20	6	18	4	20		28		2	2	<1	
Reductive amination																	
15[j]	**2**	10	–	3	–									3			97

[a]Unless otherwise specified: 1 M HCl in H_2O for 16 h at 140 °C. [b]Reported values were determined by gas chromatography–mass spectrometry after a derivatization procedure and represent the average of at least two runs. **3** and **8** were not detected by this method and have thus been omitted. [c]3 h at 140 °C. [d]3 h at 40 °C. [e]48 h at 140 °C. [f]20 °C at 24 h. [g]Reaction in 1 M H_2SO_4 in H_2O for 16 h at 140 °C. [h]1 h at 20 °C and 24 h at 140 °C. [i]Thermal cycling: 16 h at 140 °C, then 10 h at 20 °C, then 16 h at 140 °C. [j]Reaction with hydrazine hydrate (2 equiv); 1 M HCl in H_2O at 80 °C for 16 h. See the Supplementary Information for additional control experiments, mean absolute deviations and the crude ^{1}H NMR spectra of selected reactions.

aqueous conditions, many transition metal ions form hydroxides that do not efficiently bind carboxylic acids. By analogy with previous studies on metal ion promoted hydration[38], we propose that upon binding of the carboxylic acid to the aquated metal ion, the dehydration (Fig. 2a) or hydration (Fig. 2b) occurs with the assistance of water molecules present in the second coordination sphere of the metal complex. This proposed mechanism is also similar to the well-studied mechanism of enzymatic hydration–dehydration catalysed by aconitase, in the sense that Zn^{2+} performs the function of the Fe–S cluster's 'isocitrate mode' and Cr^{3+} performs the function of its 'citrate mode'[39].

The realization that various combinations of Fe^0, Zn^{2+}, Cr^{3+} and micelles can mediate the individual reduction, dehydration and hydration reactions of the rTCA cycle prompted us to assess their mutual compatibility for three-step reduction–(de)hydration sequences. The reduction–dehydration–reduction sequence starting from **3** (steps C, D and E) works in the presence of all promoting components to deliver **6** even at ambient temperature (Table 1, entry 11; see Supplementary Table 1 for control experiments). Next, we evaluated the three-step reduction–dehydration–hydration sequence spanning steps H, I and J. When an acidic aqueous solution containing **8**, Fe^0, Zn^{2+} and Cr^{3+} was heated to140 °C, **11** was formed (Table 1, entry 12). The presence of micelles had little effect on the outcome of this sequence (Table 1, entry 13). These results demonstrate that sequences of non-enzymatic reactions of the rTCA cycle are possible with the help of simple, mutually compatible reagents.

A notable criticism by Orgel[26] concerning the hypothesis of a prebiotic complete rTCA cycle is the difficulty for simple non-enzymatic catalysts to promote the reactions of the cycle over parasitic reactions with sufficient selectivity to achieve the theoretical 50% efficiency threshold such that autocatalysis could self-sustain or self-amplify. Although this criticism does not take into account the possibility that the rTCA cycle might be sustained at lower efficiency thresholds with the help of feeder pathways such as the AcCoA pathway[20], it nonetheless correctly points out that on-cycle versus off-cycle selectivity imposes important kinetic constraints on the sustainability of an autocatalytic reaction network. We therefore set out to assess the level of selectivity for on-cycle (steps C, E and H) over off-cycle reduction reactions (mauve arrows, Fig. 3). Several potential 'dead-end' reduction reactions may lead off-cycle, such as the reduction of **2** to give lactate (**12**), the reduction of α-ketoglutarate (**7**) to give α-hydroxyglutarate (**13**) and the reduction of **10** to give tricarballylate (**14**). A competitive reduction experiment on a mixture of five rTCA cycle intermediates (**2**, **3**, **5**, **7** and **10**) in the presence of all identified reaction promoters (10 equiv Fe^0, Zn^{2+}, Cr^{3+} and micelles) revealed that less than 5% of the compounds observed in the mixture after 3 h at 40 °C were derived from off-cycle reduction (Table 1, entry 14). Notably, a similar competitive reduction experiment using Ni^0 as the reducing agent gave even higher levels of selectivity, but Ni^0 was less effective at promoting reaction sequences (Supplementary Tables 5 and 7). Since the most sensitive compounds, such as **3** and **8**, were both reduced at temperatures below 40 °C, the survival of a complete reaction network

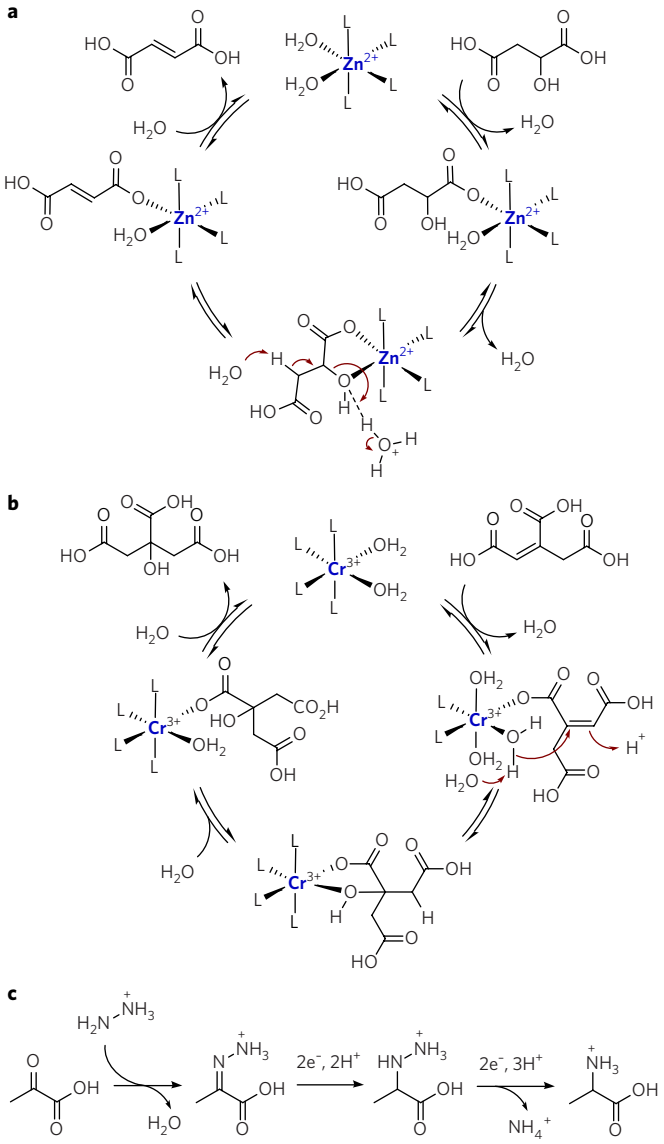

Fig. 2 | Plausible chemical mechanisms. a, Reversible Zn^{2+} promoted dehydration of **4** or **9**. **b**, Reversible Cr^{3+} promoted hydration of aconitate. **c**, Reductive amination of **2** with hydrazine and subsequent reductive N–N bond cleavage to generate **15**. Metal complexes are depicted as mononuclear species for clarity. L, undefined ligand.

shown in Fig. 1 may be feasible in the presence of Zn^{2+} and Cr^{3+} in a reaction environment that cycles over a temperature gradient of approximately 20–140 °C and where **3** and **8** are produced and reduced at the cooler end of the temperature range. It is not clear whether such thermal cycling could be achieved in a natural environment under acidic conditions. However, since steps C to E occur at 20 °C in the presence of Zn^{2+} and micelles, the observed selectivity is also compatible with a linear reaction network incorporating the AcCoA pathway and an incomplete rTCA cycle that stops after step F, without invoking thermal cycling[6,21].

A crucial aspect of any prebiotic reaction network is the ability to branch out into productive synthetic pathways that might eventually contribute to the stability of the network. We therefore became interested in the production of α-amino acids by reductive amination of the α-ketoacids of the rTCA cycle, in analogy with biosynthesis (Fig. 3, light blue arrow). Although reductive amination of α-ketoacids with NH_3 in aqueous solution is known[40,41], it is challenging under the highly acidic conditions required for metal ion promotion of the rTCA cycle since all NH_3 is trapped as NH_4^+. We speculated that NH_2NH_2, which is an intermediate and product of biological and abiological N_2 reduction[42,43], could be an effective surrogate for NH_3 under acidic conditions, since it should retain one free amino group and thus remain available for reaction with α-ketoacids. The initial product of reductive amination of the α-ketoacid with hydrazine is presumably a hydrazinium acid, which possesses a weak N–N bond and which we suspected could be subsequently cleaved under the same reducing conditions to yield amino acids (Fig. 2c). Indeed, exposure of **2** to just 2 equiv of NH_2NH_2 and excess Fe^0 under typical acidic conditions at 80 °C resulted in the formation of alanine (**15**) as the major product (Table 1, entry 15). This reactivity was maintained with Fe^0 across a wide temperature range (25–140 °C), while the use of Ni^0 as a reducing agent furnished **15** only at 140 °C (Supplementary Table 6). The requisite amount of NH_2NH_2 is notably far less than the greater than 100-fold excess of NH_3 required in other reductive aminations under aqueous conditions[40], allowing reduced nitrogen to be viewed as a limiting feedstock for prebiotic chemistry, rather than one required in large excess.

Conclusion

We have demonstrated that more than half of the rTCA cycle—an anabolic pathway central to biochemistry—can be promoted under a common set of conditions by just two metal ions and driven by Fe^0 with on-cycle selectivity, a feat normally carried out by the action of five different enzymes. Amino acid synthesis via reductive amination using Fe^0 and NH_2NH_2 also occurs under typical conditions. These observations bolster the plausibility of a non-enzymatic rTCA cycle or an incomplete variant thereof as a prebiotic pathway and should be taken into account in future attempts to model prebiotic metabolism[44]. They also demonstrate that metal ions such as Zn^{2+} and Cr^{3+} can promote reactions typically associated with Fe–S cluster enzymes. Indeed, several authors have argued for an important role for Zn^{2+} in prebiotic chemistry or early life[45,46]. The conditions described here are remarkably similar to those reported for the generation of **1** from CO_2 and Fe^0 nanoparticles,[27] providing hope that a prebiotic reaction network containing both the AcCoA pathway and (at least parts of) the rTCA cycle may eventually be identified. The acidic conditions identified for metal ion promotion of the rTCA cycle seem more compatible with acidic or locally acidic metal-rich environments such as those found in some hydrothermal fields and hydrothermal vents[47,48]. This is in agreement with previous observations of enhanced stability of peptide, RNA phosphodiester and aminoacyl–(t)RNA bonds at acidic pH (ref. [49]). Although Fe^0 and Ni^0 are themselves generally considered to be rare near the Earth's surface, we note that electric currents with negative potentials have recently been observed across the surfaces of acidic hydrothermal vents[50]. An electric current with a potential between those of Fe^0 and Ni^0 could provide a continuous supply of electrons with similar reactivity and selectivity to that observed in our study. Ongoing investigations in our laboratories are focused on identifying catalysts and conditions for the C–C bond-forming reactions of the rTCA cycle and the AcCoA pathway, as well as interfacing with other productive off-cycle anabolic pathways including gluconeogenesis.

Methods

Analytical methods. Gas chromatography–mass spectrometry analysis was performed on a GC System 7820 A (G4320) connected to an MSD block 5977E (G7036A) using an Agilent high resolution gas chromatography column (PN 19091 S – 433UI, HP – 5MS UI; 28 m × 0.250 mm; 0.25 Micron, SN USD 489634 H). All samples were prepared in ethyl acetate (200 µl sample volume). The analysis was carried out on a splitless 1 µl injection volume with an injection port temperature of 250 °C. The column oven temperature programme was as

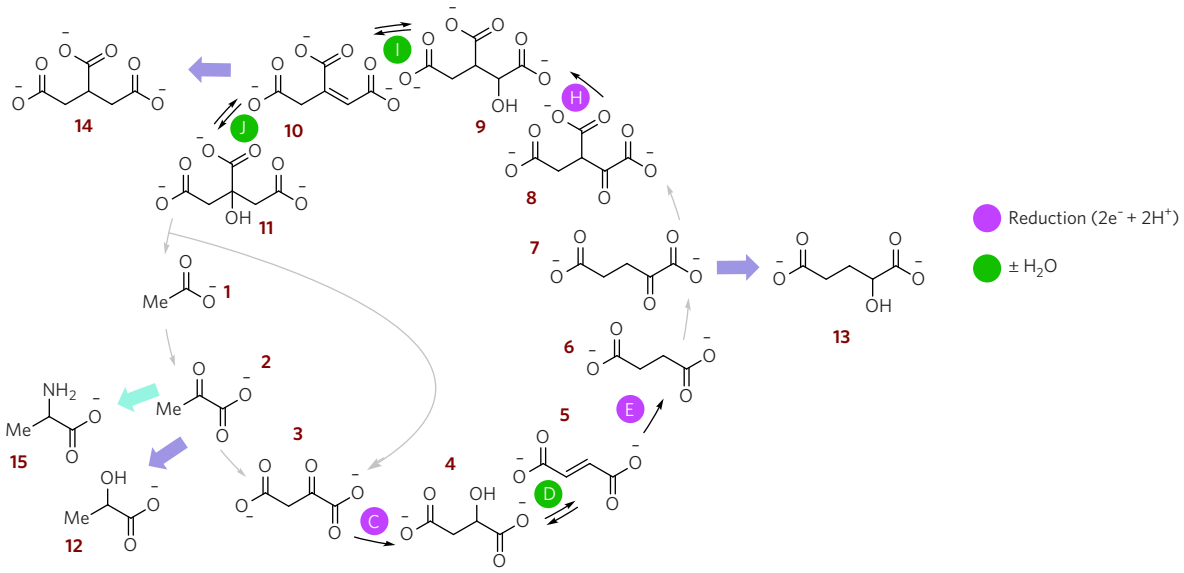

Fig. 3 | Prebiotic reaction network. The rTCA cycle, reductive amination (light blue arrow) and potential off-cycle reductions (mauve arrows) are shown. For consistency with Fig. 1, the compounds have been drawn in their anionic forms; however, under the acidic experimental conditions the compounds existed in their protonated forms.

follows: 60 °C for 1 min, ramped at 30 °C min^{-1} to 310 °C with a 3 min hold, with a total running time of 12.33 min. The mass spectrometer was turned on after 2 min and operated at the electron ionization mode with a quadrupole temperature of 150 °C. Data acquisition was performed in the full-scan mode (50–500). Hydrogen (99.999% purity) was used as the carrier gas at a constant flow rate of 1.5 ml min^{-1}.

Derivatization and product identification. For optimal gas chromatography resolution, the carboxylic acids used in this study were converted to ethyl esters using a mixture of ethanol and ethyl chloroformate or to methyl esters using a mixture of methanol and methyl chloroformate, as described in the Supplementary Information. Reaction products were identified by comparing the mass spectra and retention times of derivatized authentic samples (Supplementary Figs. 1–15) against analogously derivatized samples obtained from the reaction (Supplementary Figs. 16–54). Ethyl chloroformate derivatization was preferred for small molecule substrates (**2**, **12**, **4**, **5**, **6**, **7**, **13** and **15**), while methyl chloroformate derivatization gave clearer results (fewer elimination by-products and better resolution) for **10**, **14**, **9** and **11**.

Quantification and error analysis. For the purposes of this study, we have not reported the absolute percentage yields based on the number of moles of the starting materials, but rather the percentage contributions to the total composition of the final reaction mixture. This allowed us to account for potential concentration changes due to solvent loss (since many reactions were carried out in sealed tubes at temperatures above the boiling point of water), as well as potentially incomplete extraction during the derivatization procedure. The compound distributions were calculated by comparing the product peak area with the gas chromatography–mass spectrometry calibration lines (Supplementary Figs. 55–67). Each reaction was performed at least twice and the reported percentage compositions are an average of these runs. Mean absolute deviations associated with the mean values shown in Table 1 can be found in Supplementary Table 1.

General procedure for Fe^0, Zn^{2+} and Cr^{3+}, and Ni^0, Zn^{2+} and Cr^{3+} promoted reactions. To a 10 ml Pyrex pressure tube containing a Teflon-coated magnetic stir bar was added (unless otherwise specified) carboxylic acid substrate(s) (1 equiv, 0.100 mmol of each acid), Fe^0 or Ni^0 powder (10 equiv, 1.0 mmol, 56 mg Fe^0 or 59 mg Ni^0) and/or $ZnCl_2$ (15 equiv, 1.50 mmol, 204 mg) and/or $Cr_2(SO_4)_3{\cdot}12H_2O$ (3 equiv, 0.300 mmol, 183 mg). This was followed by the addition of 3 ml of solvent (unless otherwise specified: 1 M HCl in H_2O). The contents of the tube were flushed with argon for ≈ 30 s. The tube was then quickly sealed and the reaction mixture magnetically stirred for 16 h in a 12 tube metal heating block that was maintained at an internal temperature of 140 °C using an electronic thermocouple. The reaction tube was then removed from the heating block and allowed to cool to room temperature before derivatization and gas chromatography–mass spectrometry analysis.

General procedure for reductive amination. A solution of sodium pyruvate (1 equiv, 0.100 mmol, 11.0 mg) and $Cr_2(SO_4)_3{\cdot}12H_2O$ (3 equiv, 0.300 mmol, 183 mg) in 1 M HCl in H_2O (3 ml) was added to a 10 ml Pyrex pressure tube containing a Teflon-coated magnetic stir bar. Hydrazine monohydrate (2 equiv, 0.20 mmol, ~10 µl) was then added, followed by Fe^0 or Ni^0 powder (10 equiv, 1.0 mmol, 56 mg Fe^0 or 59 mg Ni^0). The tube was then quickly sealed and the reaction mixture magnetically stirred for 16 h in a 12 tube metal heating block that was maintained at the specified internal temperature (20–140 °C) using an electronic thermocouple. The reaction tube was then removed from the heating block and allowed to cool to room temperature before derivatization and gas chromatography–mass spectrometry analysis.

Metal screens for malate dehydration. Inorganic salts containing the following metals were used in the reaction screen: Zn^{2+}, Cu^{2+}, Ni^{2+}, Co^{2+}, Fe^{2+}, Mn^{2+}, Cr^{2+} and V^{2+}. Zn^{2+} gave the best yields when used together with Fe^0 (two-step reaction). For detailed metal screens, see Supplementary Table 2.

Metal screens for isocitrate dehydration. Inorganic salts containing the following metals were used in the reaction screen: Zn^{2+}, Cu^{2+}, Ni^{2+}, Co^{2+}, Fe^{2+}, Mn^{2+}, Cr^{2+}, V^{2+}, Pd^{2+}, Cd^{2+}, Fe^{3+}, Mn^{3+}, Cr^{3+}, As^{3+}, Ru^{3+}, Ir^{3+}, Rh^{3+} and Ti^{3+}. Zn^{2+} was selected for further experiments due to high yields and geochemical accessibility, although substantial reactivity was also observed for Cr^{2+}, Pd^{2+}, Fe^{3+}, Mn^{3+}, As^{3+}, Ru^{3+}, Ir^{3+} and Rh^{3+}. For detailed metal screens, see Supplementary Table 3.

Metal screens for aconitate hydration. Inorganic salts containing the following metals were used in the reaction screen: Cu^{+}, Zn^{2+}, Cu^{2+}, Ni^{2+}, Co^{2+}, Fe^{2+}, Mn^{2+}, Cr^{2+}, Cd^{2+}, Hg^{2+}, Fe^{3+}, Co^{3+}, Mn^{3+}, Cr^{3+}, Ti^{3+}, Ru^{3+}, Mo^{4+}, W^{4+}, Mo^{6+} and W^{6+}. Only Cr^{3+} returned a substantial positive result. For detailed metal screens, see Supplementary Table 4.

Data availability. The data that support the findings of this study are available in the Supplementary Information.

Received: 22 March 2017; Accepted: 10 August 2017;
Published online: 02 October 2017

References

1. Ruiz-Mirazo, K., Briones, C. & de la Escosura, A. Prebiotic systems chemistry: new perspectives for the origins of life. *Chem. Rev.* **114**, 285–366 (2014).
2. Peretó, J. Out of fuzzy chemistry: from prebiotic chemistry to metabolic networks. *Chem. Soc. Rev.* **41**, 5394–5403 (2012).
3. Sutherland, J. D. Studies on the origin of life—the end of the beginning. *Nat. Rev. Chem.* **1**, 0012 (2017).
4. Morowitz, H. J. *Beginnings of Cellular Life: Metabolism Recapitulates Biogenesis* (Yale Univ. Press, London, 1992).
5. Wächtershäuser, G. Before enzymes and templates: theory of surface metabolism. *Microbiol. Rev.* **52**, 452–484 (1988).

6. Martin, W. & Russell, M. J. On the origin of biochemistry at an alkaline hydrothermal vent. *Phil. Trans. R. Soc. B* **362**, 1887–1926 (2007).
7. Peretó, J. G., Velasco, A. M., Becerra, A. & Lazcano, A. Comparative biochemistry of CO_2 fixation and the evolution of autotrophy. *Int. Microbiol.* **2**, 3–10 (1999).
8. Lane, N., Allen, J. F. & Martin, W. How did LUCA make a living? Chemiosmosis in the origin of life. *Bioessays* **32**, 271–280 (2010).
9. Russell, M. J., Nitschke, W. & Branscomb, E. The inevitable journey to being. *Phil. Trans. R. Soc. B* **368**, 20120254 (2013).
10. Sutherland, J. D. The origin of life—out of the blue. *Angew. Chem. Int. Ed.* **55**, 104–121 (2015).
11. Keller, M. A., Turchyn, A. V. & Ralser, M. Non-enzymatic glycolysis and pentose phosphate pathway-like reactions in a plausible Archean ocean. *Mol. Syst. Biol.* **10**, 725 (2014).
12. Keller, M. A. et al. Conditional iron and pH-dependent activity of a non-enzymatic glycolysis and pentose phosphate pathway. *Sci. Advances* **2**, e1501235 (2016).
13. Keller, M. A., Kampjut, D., Harrison, S. A. & Ralser, M. Sulfate radicals enable a non-enzymatic Krebs cycle precursor. *Nat. Ecol. Evol.* **1**, 0083 (2017).
14. Berg, I. A. et al. Autotrophic carbon fixation in archaea. *Nat. Rev. Microbiol.* **8**, 447–460 (2010).
15. Ljundahl, L. G., Irion, E. & Wood, H. G. Total synthesis of acetate from CO_2. I. Co-methylcobyric acid and co-(methyl)-5-methoxy-benzimidizolycobamide as intermediates with *Clostridium thermoaceticum*. *Biochemistry* **4**, 2771–2779 (1965).
16. Evans, M. C. W., Buchanan, B. B. & Arnon, D. I. A new ferredoxin-dependent carbon reduction cycle in a photosynthetic bacterium. *Proc. Natl Acad. Sci. USA* **55**, 928–934 (1966).
17. Morowitz, H. J., Kostelnik, J. D., Yang, J. & Cody, G. D. The origin of intermediary metabolism. *Proc. Natl Acad. Sci. USA* **97**, 7704–7708 (2000).
18. Smith, E. & Morowitz, H. J. Universality in intermediary metabolism. *Proc. Natl Acad. Sci. USA* **101**, 13168–13173 (2004).
19. Smith, E. & Morowitz, H. J. *The Origin and Nature of Life on Earth: The Emergence of the Fourth Geosphere* (Cambridge Univ. Press, Cambridge, 2016).
20. Braakman, R. & Smith, E. The emergence and early evolution of biological carbon-fixation. *PLoS Comp. Biol.* **8**, e1002455 (2012).
21. Camprubi, E., Jordan, S. F., Vasiliadou, R. & Lane, N. Iron catalysis at the origin of life. *IUBMB Life* **69**, 373–381 (2017).
22. Russell, M. J., Hall, A. J. & Mellersh, A. R. in *Natural and Laboratory Simulated Thermal Geochemical Processes* 325–388 (Springer Netherlands, Dordrecht, 2003).
23. Reysenbach, A.-L. & Shock, E. Merging genomes with geochemistry in hydrothermal ecosystems. *Science* **296**, 1077–1082 (2002).
24. Weiss, M. C. et al. The physiology and habitat of the last universal common ancestor. *Nat. Microbiol.* **1**, 16116 (2016).
25. Plasson, R., Brandenburg, A., Jullien, L. & Bersini, H. Autocatalyses. *J. Phys. Chem. A* **115**, 8073–8085 (2011).
26. Orgel, L. E. The implausibility of metabolic cycles on the prebiotic Earth. *PLoS Biol.* **6**, e18 (2008).
27. He, C., Tian, G., Liu, Z. & Feng, S. A mild hydrothermal route to fix carbon dioxide to simple carboxylic acids. *Org. Lett.* **12**, 649–651 (2010).
28. Roldan, A. et al. Bio-inspired CO_2 conversion by iron sulfide catalysts under sustainable conditions. *Chem. Commun.* **51**, 7501–7504 (2015).
29. Herschy, B. et al. An origin-of-life reactor to simulate alkaline hydrothermal vents. *J. Mol. Evol.* **79**, 213–227 (2014).
30. Huber, C. & Wächtershauser, G. Activated acetic acid by carbon fixation on (Fe,Ni)S under primordial conditions. *Science* **276**, 245–247 (1997).
31. Cody, G. D. et al. Geochemical roots of autotrophic carbon fixation: hydrothermal experiments in the system citric acid, H_2O-(±FeS)–(±NiS). *Geochim. Cosmochim. Acta* **65**, 3557–3576 (2001).
32. Zhang, X. V. & Martin, S. T. Driving parts of Krebs cycle in reverse through mineral photochemistry. *J. Am. Chem. Soc.* **128**, 16032–16033 (2006).
33. Cody, G. D. et al. Primordial carbonylated iron-sulfur compounds and the synthesis of pyruvate. *Science* **289**, 1337–1340 (2000).
34. Morowitz, H. J., Srinivasan, V. & Smith, E. Ligand field theory and the origin of life as an emergent feature of the periodic table of elements. *Biol. Bull.* **219**, 1–6 (2010).
35. Ross, D. S. The viability of a nonenzymatic reductive citric acid cycle—kinetics and thermochemistry. *Orig. Life Evol. Biosph.* **37**, 61–65 (2007).
36. Flint, D. H. & Allen, R. M. Iron–sulfur proteins with nonredox functions. *Chem. Rev.* **96**, 2315–2334 (1996).
37. Lipshutz, B. H. et al. TPGS-750-M: a second-generation amphiphile for metal-catalyzed cross-couplings in water at room temperature. *J. Org. Chem.* **76**, 4379–4391 (2011).
38. Olson, M. V. & Taube, H. Hydration and isomerization of coordinated maleate. *J. Am. Chem. Soc.* **92**, 3236–3237 (1970).
39. Nicolet, Y. & Fontecilla-Camps, J. C. in *Bioinspired Catalysis* 21–48 (Wiley, Weinheim, Germany, 2014).
40. Huber, C. & Wächtershäuser, G. Primordial reductive amination revisited. *Tetrahedron Lett.* **44**, 1695–1697 (2003).
41. Wang, W. et al. Photocatalytic reversible amination of α-keto acids on a ZnS surface: implications for the prebiotic metabolism. *Chem. Commun.* **48**, 2146–2148 (2012).
42. Dietl, A. et al. The inner workings of the hydrazine synthase multiprotein complex. *Nature* **527**, 394–297 (2015).
43. Barney, B. M. et al. Trapping a hydrazine reduction intermediate on the nitrogenase active site. *Biochemistry* **44**, 8030–8037 (2005).
44. Zubarev, D. Y., Rappoport, D. & Aspuru-Guzik, A. Uncertainty of prebiotic scenarios: the case of the non-enzymatic reverse tricarboxylic acid cycle. *Sci. Rep.* **5**, 8009 (2015).
45. Zerkle, A. L., House, C. H. & Brantley, S. L. Biogeochemical signatures through time as inferred from whole microbial genomes. *Am. J. Sci.* **305**, 467–502 (2005).
46. Mulkidjanian, A. Y. & Galperin, M. Y. On the origin of life in the zinc world. 2. Validation of the hypothesis on the photosynthesizing zinc sulfide edifices as cradles of life on Earth. *Biol. Direct* **4**, 27 (2009).
47. Martin, W., Baross, J., Kelley, D. & Russell, M. J. Hydrothermal vents and the origin of life. *Nat. Rev. Microbiol.* **6**, 805–814 (2008).
48. Ross, D. S. & Deamer, D. Dry/wet cycling and the thermodynamics and kinetics of prebiotic polymer synthesis. *Life* **6**, 28 (2016).
49. Bernhardt, H. S. & Tate, W. P. Primordial soup or vinaigrette: did the RNA world evolve at acidic pH? *Biol. Direct* **7**, 4 (2012).
50. Nakamura, R. et al. Electrical current generation across a black smoker chimney. *Angew. Chem. Int. Ed.* **49**, 7692–7694 (2010).

Acknowledgements

This study received funding from the European Research Council under the European Union's Horizon 2020 research and innovation programme (grant agreement 639170). Further funding was provided by a grant from LabEx 'Chemistry of Complex Systems'. We thank the ELSI Origins Network, which is supported by a grant from the John Templeton Foundation provided through the Earth-Life Science Institute of the Tokyo Institute of Technology. We thank E. Smith for stimulating discussions. This paper is dedicated to the memory of H. J. Morowitz.

Author contributions

J.M. supervised the research and the other authors performed the experiments. All authors contributed intellectually throughout the study. J.M. wrote the paper and K.B.M. assembled the Supplementary Information, incorporating data from S.J.V., E.C.-B. and L.L.-K. Important preliminary experiments were carried out by G.L.

Competing interests

The authors declare no competing financial interests.

Additional information

Supplementary information is available for this paper at doi:10.1038/s41559-017-0311-7.

Reprints and permissions information is available at www.nature.com/reprints.

Correspondence and requests for materials should be addressed to J.M.

Publisher's note: Springer Nature remains neutral with regard to jurisdictional claims in published maps and institutional affiliations.

BIBLIOGRAPHY

1. Thomas, A. *et al.* Ground-State Chemical Reactivity under Vibrational Coupling to the Vacuum Electromagnetic Field. *Angew. Chem. Int. Ed.* **55**, 11462–11466 (2016).
2. Thomas, A. *et al.* Tilting a ground-state reactivity landscape by vibrational strong coupling. *Science* **363**, 615–619 (2019).
3. Kaluzny, Y., Goy, P., Gross, M., Raimond, J. M. & Haroche, S. Observation of Self-Induced Rabi Oscillations in Two-Level Atoms Excited Inside a Resonant Cavity: The Ringing Regime of Superradiance. *Phys. Rev. Lett.* **51**, 1175–1178 (1983).
4. Haroche, S. & Raimond, J.-M. *Exploring the quantum: atoms, cavities and photons*. (Oxford University Press, 2006).
5. Hutchison, J. A., Schwartz, T., Genet, C., Devaux, E. & Ebbesen, T. W. Modifying Chemical Landscapes by Coupling to Vacuum Fields. *Angew. Chem. Int. Ed.* **51**, 1592–1596 (2012).
6. Shalabney, A. *et al.* Coherent coupling of molecular resonators with a microcavity mode. *Nat. Commun.* **6**, 5981 (2015).
7. Long, J. P. & Simpkins, B. S. Coherent Coupling between a Molecular Vibration and Fabry–Perot Optical Cavity to Give Hybridized States in the Strong Coupling Limit. *ACS Photonics* **2**, 130–136 (2015).
8. George, J. *et al.* Multiple Rabi Splittings under Ultrastrong Vibrational Coupling. *Phys. Rev. Lett.* **117**, (2016).
9. Vergauwe, R. M. A. *et al.* Quantum Strong Coupling with Protein Vibrational Modes. *J. Phys. Chem. Lett.* **7**, 4159–4164 (2016).
10. Rahaim, R. J. & Shaw, J. T. Zinc-Catalyzed Silylation of Terminal Alkynes. *J. Org. Chem.* **73**, 2912–2915 (2008).
11. Shelke, S. V. *et al.* A Fragment-Based In Situ Combinatorial Approach To Identify High-Affinity Ligands for Unknown Binding Sites. *Angew. Chem. Int. Ed.* **49**, 5721–5725 (2010).
12. George, J., Shalabney, A., Hutchison, J. A., Genet, C. & Ebbesen, T. W. Liquid-Phase Vibrational Strong Coupling. *J. Phys. Chem. Lett.* **6**, 1027–1031 (2015).
13. Zhang, W., Kawamata, H. & Liu, K. CH Stretching Excitation in the Early Barrier F + CHD3 Reaction Inhibits CH Bond Cleavage. *Science* **325**, 303–306 (2009).
14. Schatz, G. C., Colton, M. C. & Grant, J. L. A quasiclassical trajectory study of the state-to-state dynamics of atomic hydrogen + water .fwdarw. hydroxyl + molecular hydrogen. *J. Phys. Chem.* **88**, 2971–2977 (1984).

15. Grill, A. & Neumayer, D. A. Structure of low dielectric constant to extreme low dielectric constant SiCOH films: Fourier transform infrared spectroscopy characterization. *J. Appl. Phys.* **94**, 6697–6707 (2003).

16. Bastiaansen, P. M. F. M., Orru, R. V. A., Wijnberg, J. B. P. A. & de Groot, A. Long-Range Effects of Through-Bond Orbital Interactions on the Desilylation Rate of Silyl Ethers. *J. Org. Chem.* **60**, 6154–6158 (1995).

17. *The chemistry of organic silicon compounds*. (Wiley, 1989).

18. Lather, J., Bhatt, P., Thomas, A., Ebbesen, T. W. & George, J. Cavity Catalysis by Cooperative Vibrational Strong Coupling of Reactant and Solvent Molecules. *Angew. Chem. Int. Ed.* (2019) doi:10.1002/anie.201905407.

19. Hiura, H., Shalabney, A. & George, J. Cavity Catalysis –Accelerating Reactions under Vibrational Strong Coupling–. doi:10.26434/chemrxiv.7234721.v3.

20. Shryne, T. M. & Kim, L. Process For The Epoxidation of Olefins. (1977).

21. Neimann, K. & Neumann, R. Electrophilic Activation of Hydrogen Peroxide: Selective Oxidation Reactions in Perfluorinated Alcohol Solvents. *Org. Lett.* **2**, 2861–2863 (2000).

22. Berkessel, A. & Adrio, J. A. Kinetic Studies of Olefin Epoxidation with Hydrogen Peroxide in 1,1,1,3,3,3-Hexafluoro-2-propanol Reveal a Crucial Catalytic Role for Solvent Clusters. *Adv. Synth. Catal.* **346**, 275–280 (2004).

23. Berkessel, A. & Adrio, J. A. Dramatic Acceleration of Olefin Epoxidation in Fluorinated Alcohols: Activation of Hydrogen Peroxide by Multiple H-Bond Networks. *J. Am. Chem. Soc.* **128**, 13412–13420 (2006).

24. Hollóczki, O. *et al.* The Catalytic Effect of Fluoroalcohol Mixtures Depends on Domain Formation. *ACS Catal.* **7**, 1846–1852 (2017).

25. Czarnik-Matusewicz, B., Pilorz, S., Bieńko, D. & Michalska, D. Molecular and electronic structures, infrared spectra, and vibrational assignment for ap and sc conformers of hexafluoro-iso-propanol. *Vib. Spectrosc.* **47**, 44–52 (2008).

26. Barnes, A. J. & Murto, J. Infra-red cryogenic studies. Part 10.—Conformational isomerism of 1,1,1,3,3,3-hexafluoropropan-2-ol. *J Chem Soc Faraday Trans 2* **68**, 1642–1651 (1972).

27. Murto, J. *et al.* Fluoroalcohols. Part 18. Infrared and Raman Spectra of the Perfluorinated t-Butyl Alcohols (CF3)3COH and (CF3)3COD. *Acta Chem. Scand.* **27**, 107–120 (1973).

28. Goy, P., Raimond, J. M., Gross, M. & Haroche, S. Observation of Cavity-Enhanced Single-Atom Spontaneous Emission. *Phys. Rev. Lett.* **50**, 1903–1906 (1983).

29. Hulet, R. G., Hilfer, E. S. & Kleppner, D. Inhibited Spontaneous Emission by a Rydberg Atom. *Phys. Rev. Lett.* **55**, 2137–2140 (1985).

30. Jhe, W. *et al.* Suppression of spontaneous decay at optical frequencies: Test of vacuum-field anisotropy in confined space. *Phys. Rev. Lett.* **58**, 666–669 (1987).

31. Martini, F. D., Innocenti, G., Jacobovitz, G. R. & Mataloni, P. Anomalous Spontaneous Emission Time in a Microscopic Optical Cavity. *Phys. Rev. Lett.* **59**, 2955–2958 (1987).

32. Haroche, S. & Kleppner, D. Cavity Quantum Electrodynamics. *Phys. Today* **42**, 24–30 (1989).

33. Lee, J. *et al.* Monolayer optical memory cells based on artificial trap-mediated charge storage and release. *Nat. Commun.* **8**, (2017).

34. Kollár, A. J. *et al.* Supermode-density-wave-polariton condensation with a Bose–Einstein condensate in a multimode cavity. *Nat. Commun.* **8**, (2017).

35. Herrera, F. & Spano, F. C. Absorption and photoluminescence in organic cavity QED. *Phys. Rev. A* **95**, (2017).

36. Kryuchkyan, G. Yu., Shahnazaryan, V., Kibis, O. V. & Shelykh, I. A. Resonance fluorescence from an asymmetric quantum dot dressed by a bichromatic electromagnetic field. *Phys. Rev. A* **95**, (2017).

37. Chen, N. *et al.* Surface-enhanced Raman spectroscopy of serum accurately detects prostate cancer in patients with prostate-specific antigen levels of 4–10 ng/mL. *Int. J. Nanomedicine* **Volume 12**, 5399–5407 (2017).

38. Hansen, M., Truong, J., Xie, T. & Hahm, J. Spatially distinct Raman scattering characteristics of individual ZnO nanorods under controlled polarization: intense end scattering from forbidden modes. *Nanoscale* **9**, 8470–8480 (2017).

39. Strauf, S. *et al.* Self-Tuned Quantum Dot Gain in Photonic Crystal Lasers. *Phys. Rev. Lett.* **96**, (2006).

40. Palatnik, A., Aviv, H. & Tischler, Y. R. Microcavity Laser Based on a Single Molecule Thick High Gain Layer. *ACS Nano* **11**, 4514–4520 (2017).

41. Hakala, T. K. *et al.* Lasing in dark and bright modes of a finite-sized plasmonic lattice. *Nat. Commun.* **8**, (2017).

42. Ebbesen, T. W. Hybrid Light–Matter States in a Molecular and Material Science Perspective. *Acc. Chem. Res.* **49**, 2403–2412 (2016).

43. Vuković, V. Synergistic Effect of Acids and HFIP on Friedel-Crafts Reaction of Alcohols and Cyclopropanes. (Université de Strasbourg, 2018).

44. Burton, H. E. The Optics of Euclid. *J. Opt. Soc. Am.* **35**, 357 (1945).

45. Alhazen & Sabra, A. I. *The Optics of Ibn al-Haytham. Books I-III: On direct vision*. (Warburg Institute, University of London, 1989).

46. Aristoteles. *The complete works of Aristotle: the revised Oxford translation. 1: ...* (Princeton Univ. Press, 1995).

47. Platon. *Oeuvres complètes*. (Flammarion, 2008).

48. da C. Andrade, E. N. The history of the vacuum pump. *Vacuum* **9**, 41–47 (1959).

49. Sparnaay, M. J. *Adventures in vacuums*. (Elsevier Science Publ, 1992).

50. Hablanian, M. H. Comments on the history of vacuum pumps. *J. Vac. Sci. Technol. Vac. Surf. Films* **2**, 118–125 (1984).

51. Madey, T. E. Early applications of vacuum, from Aristotle to Langmuir. *J. Vac. Sci. Technol. Vac. Surf. Films* **2**, 110–117 (1984).

52. Redhead, P. A. The ultimate vacuum. *Vacuum* **53**, 137–149 (1999).

53. Descartes, R. *Discours de la méthode*. (1991).

54. Hooke, R. *Micrographia*. (General Books, 2010).

55. Grimaldi, F. M. *Physico-mathesis de lumine, coloribus et iride ...* (ex typographia haeredis Victorii Benatii. Impensis Hieronymi Berniae, 1665). doi:10.3931/e-rara-9459.

56. Huygens, C. *Treatise on Light*. (tredition, 2011).

57. Newton, I. & Roller, D. H. D. *Opticks: or, a treatise of the reflections, refractions, inflections, & colours of light*. (Dover Publications, Inc, 2012).

58. Young, T. II. The Bakerian Lecture. On the theory of light and colours. *Philos. Trans. R. Soc. Lond.* **92**, 12–48 (1802).

59. Maxwell, J. C. VIII. A dynamical theory of the electromagnetic field. *Philos. Trans. R. Soc. Lond.* **155**, 459–512 (1865).

60. Röntgen, W. C. Ueber eine neue Art von Strahlen. *Ann. Phys.* **300**, 12–17 (1898).

61. Becquerel, H. Sur les radiations émises par les corps phosphorescents. *Comptes Rendus Hebdomadaires des Séances de l'Académie des Sciences* **122**, 501–503 (1896).

62. Mulligan, J. F. Heinrich Hertz and the Development of Physics. *Phys. Today* **42**, 50–57 (1989).

63. Herschel, W. XIX. Experiments on the solar, and on the terrestrial rays that occasion heat; with a comparative view of the laws to which light and heat, or rather the rays which occasion them, are subject, in order to determine whether they are the same, or different. *Philos. Trans. R. Soc. Lond.* **90**, 437–538 (1800).

64. Ritter, J. W. Versuche über das Sonnenlicht. *Ann. Phys.* **12**, 409–415 (1803).

65. Michelson, A. A. & Morley, E. W. LVIII. *On the relative motion of the earth and the*

luminiferous Æther. *Lond. Edinb. Dublin Philos. Mag. J. Sci.* **24**, 449–463 (1887).

66. Cahill, R. T. The Michelson and Morley 1887 Experiment and the Discovery of Absolute Motion. *arXiv:physics/0508174* (2005).

67. Einstein, A. Zur Elektrodynamik bewegter Körper. *Ann. Phys.* **322**, 891–921 (1905).

68. Planck, M. *The theory of heat radiation*. (Dover Publications, 1991).

69. Einstein, A. Concerning an Heuristic Point of View Toward the Emission and Transformation of Light. *Ann. Phys.* **17**, 164–181 (1905).

70. Bohr, N. I. *On the constitution of atoms and molecules*. *Lond. Edinb. Dublin Philos. Mag. J. Sci.* **26**, 1–25 (1913).

71. Broglie, L. de. XXXV. *A tentative theory of light quanta*. *Lond. Edinb. Dublin Philos. Mag. J. Sci.* **47**, 446–458 (1924).

72. Dirac, P. A. M. The Quantum Theory of the Emission and Absorption of Radiation. *Proc. R. Soc. Math. Phys. Eng. Sci.* **114**, 243–265 (1927).

73. Schweber, S. S. *QED and the men who made it: Dyson, Feynman, Schwinger, and Tomonaga*. (Princeton University Press, 1994).

74. Milonni, P. W. Why spontaneous emission? *Am. J. Phys.* **52**, 340–343 (1984).

75. Shifman, M. A. *Advanced topics in quantum field theory: a lecture course*. (Cambridge University Press, 2012).

76. Boyer, T. H. Random electrodynamics: The theory of classical electrodynamics with classical electromagnetic zero-point radiation. *Phys. Rev. D* **11**, 790–808 (1975).

77. Cohen-Tannoudji, C., Diu, B., Laloë, F. & CNRS éditions. *Mécanique quantique. Tome III, Tome III,*. (EDP Sciences, 2017).

78. Feynman, R. P. *QED: the strange theory of light and matter*. (Princeton University Press, 1988).

79. Silk, J. *A short history of the universe*. (Scientific American Library : Distributed by W.H. Freeman, 1994).

80. Lamb, W. E. & Retherford, R. C. Fine Structure of the Hydrogen Atom by a Microwave Method. *Phys. Rev.* **72**, 241–243 (1947).

81. Bethe, H. A. The Electromagnetic Shift of Energy Levels. *Phys. Rev.* **72**, 339–341 (1947).

82. CASIMIR - 1948 - KNAW.pdf.

83. Lamoreaux, S. K. Demonstration of the Casimir Force in the 0.6 to 6 μ m Range. *Phys. Rev. Lett.* **78**, 5–8 (1997).

84. Riek, C. *et al.* Direct sampling of electric-field vacuum fluctuations. *Science* **350**, 420–

423 (2015).

85. Purcell, E. M., Torrey, H. C. & Pound, R. V. Resonance Absorption by Nuclear Magnetic Moments in a Solid. *Phys. Rev.* **69**, 37–38 (1946).

86. Paschotta, R. *Field guide to lasers*. (SPIE Press, 2008).

87. Lakowicz, J. R. *Principles of fluorescence spectroscopy*. (Springer, 2010).

88. Fort, E. & Grésillon, S. Surface enhanced fluorescence. *J. Phys. Appl. Phys.* **41**, 013001 (2008).

89. Drexhage, K. H. Monomolecular Layers and Light. *Sci. Am.* **222**, 108–119 (1970).

90. Czolczynski, K., Perlikowski, P., Stefanski, A. & Kapitaniak, T. HUYGENS' ODD SYMPATHY EXPERIMENT REVISITED. *Int. J. Bifurc. Chaos* **21**, 2047–2056 (2011).

91. Ebbesen, T. W. *L'alchimie du vide: interactions lumière-matière en chimie physique*. (2019).

92. Rempe, G., Walther, H. & Klein, N. Observation of quantum collapse and revival in a one-atom maser. *Phys. Rev. Lett.* **58**, 353–356 (1987).

93. Törmä, P. & Barnes, W. L. Strong coupling between surface plasmon polaritons and emitters: a review. *Rep. Prog. Phys.* **78**, 013901 (2015).

94. Bellessa, J. *et al.* Strong Coupling between Plasmons and Organic Semiconductors. *Electronics* **3**, 303–313 (2014).

95. Ballarini, D. *et al.* Polariton-Induced Enhanced Emission from an Organic Dye under the Strong Coupling Regime. *Adv. Opt. Mater.* **2**, 1076–1081 (2014).

96. Wang, S. *et al.* Quantum Yield of Polariton Emission from Hybrid Light-Matter States. *J. Phys. Chem. Lett.* **5**, 1433–1439 (2014).

97. Tanyi, E. K. *et al.* Control of the Stokes Shift with Strong Coupling. *Adv. Opt. Mater.* **5**, 1600941 (2017).

98. Wersäll, M., Cuadra, J., Antosiewicz, T. J., Balci, S. & Shegai, T. Observation of Mode Splitting in Photoluminescence of Individual Plasmonic Nanoparticles Strongly Coupled to Molecular Excitons. *Nano Lett.* **17**, 551–558 (2017).

99. Baieva, S., Hakamaa, O., Groenhof, G., Heikkilä, T. T. & Toppari, J. J. Dynamics of Strongly Coupled Modes between Surface Plasmon Polaritons and Photoactive Molecules: The Effect of the Stokes Shift. *ACS Photonics* **4**, 28–37 (2017).

100. Wang, H. *et al.* The role of Rabi splitting tuning in the dynamics of strongly coupled J-aggregates and surface plasmon polaritons in nanohole arrays. *Nanoscale* **8**, 13445–13453 (2016).

101. Grant, R. T. *et al.* Efficient Radiative Pumping of Polaritons in a Strongly Coupled

Microcavity by a Fluorescent Molecular Dye. *Adv. Opt. Mater.* **4**, 1615–1623 (2016).

102. Zengin, G. *et al.* Approaching the strong coupling limit in single plasmonic nanorods interacting with J-aggregates. *Sci. Rep.* **3**, (2013).

103. Muallem, M., Palatnik, A., Nessim, G. D. & Tischler, Y. R. Strong Light-Matter Coupling and Hybridization of Molecular Vibrations in a Low-Loss Infrared Microcavity. *J. Phys. Chem. Lett.* **7**, 2002–2008 (2016).

104. Schwartz, T. *et al.* Polariton Dynamics under Strong Light-Molecule Coupling. *ChemPhysChem* **14**, 125–131 (2013).

105. Vasa, P. *et al.* Ultrafast Manipulation of Strong Coupling in Metal−Molecular Aggregate Hybrid Nanostructures. *ACS Nano* **4**, 7559–7565 (2010).

106. George, J. *et al.* Ultra-strong coupling of molecular materials: spectroscopy and dynamics. *Faraday Discuss.* **178**, 281–294 (2015).

107. Schachenmayer, J., Genes, C., Tignone, E. & Pupillo, G. Cavity-Enhanced Transport of Excitons. *Phys. Rev. Lett.* **114**, (2015).

108. Flick, J., Ruggenthaler, M., Appel, H. & Rubio, A. Atoms and molecules in cavities, from weak to strong coupling in quantum-electrodynamics (QED) chemistry. *Proc. Natl. Acad. Sci.* **114**, 3026–3034 (2017).

109. Herrera, F. & Spano, F. C. Cavity-Controlled Chemistry in Molecular Ensembles. *Phys. Rev. Lett.* **116**, (2016).

110. Litinskaya, M., Tignone, E. & Pupillo, G. Cavity polaritons with Rydberg blockade and long-range interactions. *J. Phys. B At. Mol. Opt. Phys.* **49**, 164006 (2016).

111. Kowalewski, M., Bennett, K. & Mukamel, S. Non-adiabatic dynamics of molecules in optical cavities. *J. Chem. Phys.* **144**, 054309 (2016).

112. Gentile, M. J., Horsley, S. A. R. & Barnes, W. L. Localized exciton–polariton modes in dye-doped nanospheres: a quantum approach. *J. Opt.* **18**, 015001 (2016).

113. González-Tudela, A., Huidobro, P. A., Martín-Moreno, L., Tejedor, C. & García-Vidal, F. J. Theory of Strong Coupling between Quantum Emitters and Propagating Surface Plasmons. *Phys. Rev. Lett.* **110**, (2013).

114. Khitrova, G., Gibbs, H. M., Kira, M., Koch, S. W. & Scherer, A. Vacuum Rabi splitting in semiconductors. *Nat. Phys.* **2**, 81–90 (2006).

115. Raimond, J. M., Brune, M. & Haroche, S. Manipulating quantum entanglement with atoms and photons in a cavity. *Rev. Mod. Phys.* **73**, 565–582 (2001).

116. Houdré, R., Stanley, R. P. & Ilegems, M. Vacuum-field Rabi splitting in the presence of inhomogeneous broadening: Resolution of a homogeneous linewidth in an

inhomogeneously broadened system. *Phys. Rev. A* **53**, 2711–2715 (1996).

117. Skolnick, M. S., Fisher, T. A. & Whittaker, D. M. Strong coupling phenomena in quantum microcavity structures. *Semicond. Sci. Technol.* **13**, 645–669 (1998).

118. Pino, J. del, Feist, J. & Garcia-Vidal, F. J. Quantum theory of collective strong coupling of molecular vibrations with a microcavity mode. *New J. Phys.* **17**, 053040 (2015).

119. Zhong, X. *et al.* Non-Radiative Energy Transfer Mediated by Hybrid Light-Matter States. *Angew. Chem. Int. Ed.* **55**, 6202–6206 (2016).

120. Orgiu, E. *et al.* Conductivity in organic semiconductors hybridized with the vacuum field. *Nat. Mater.* **14**, 1123–1129 (2015).

121. Hutchison, J. A. *et al.* Tuning the Work-Function Via Strong Coupling. *Adv. Mater.* **25**, 2481–2485 (2013).

122. Chervy, T. *et al.* High-Efficiency Second-Harmonic Generation from Hybrid Light-Matter States. *Nano Lett.* **16**, 7352–7356 (2016).

123. Plumhof, J. D., Stöferle, T., Mai, L., Scherf, U. & Mahrt, R. F. Room-temperature Bose–Einstein condensation of cavity exciton–polaritons in a polymer. *Nat. Mater.* **13**, 247–252 (2014).

124. Daskalakis, K. S., Maier, S. A., Murray, R. & Kéna-Cohen, S. Nonlinear interactions in an organic polariton condensate. *Nat. Mater.* **13**, 271–278 (2014).

125. Bouas-Laurent, H. & Dürr, H. Organic photochromism (IUPAC Technical Report). *Pure Appl. Chem.* **73**, 639–665 (2001).

126. Photostationary State. *IUPAC Compendium of Chemical Terminology* (eds. Nič, M., Jirát, J., Košata, B., Jenkins, A. & McNaught, A.) (IUPAC, 2009). doi:10.1351/goldbook.P04654.

127. Winchell, A. N. *THE OPTICAL PROPERTIES OF ORGANIC COMPOUNDS*. (Academic Press, 1954).

128. Fontcuberta i Morral, A. & Stellacci, F. Ultrastrong routes to new chemistry. *Nat. Mater.* **11**, 272–273 (2012).

129. Wang, S. *et al.* Phase transition of a perovskite strongly coupled to the vacuum field. *Nanoscale* **6**, 7243–7248 (2014).

130. Frei, H., Fredin, L. & Pimentel, G. C. Vibrational excitation of ozone and molecular fluorine reactions in cryogenic matrices. *J. Chem. Phys.* **74**, 397–411 (1981).

131. Frei, H. & Pimentel, G. C. Selective vibrational excitation of the ethylene–fluorine reaction in a nitrogen matrix. I. *J. Chem. Phys.* **78**, 3698–3712 (1983).

132. Ripin, D. H. & Evans, D. A. Evans pKa Table. (2016).

133. Bordwell, F. G. & Matthews, W. S. Equilibrium acidities of carbon acids. II. Hydrocarbon indicators, phenylacetylene, and other carbon acids in the 20-27 pK region. *J. Am. Chem. Soc.* **96**, 1214–1216 (1974).

134. Greene, T. W. & Wuts, P. G. M. *Protective groups in organic synthesis*. (Wiley, 1999).

135. Bassindale, A. R., Glynn, S. J. & Taylor, P. G. Reaction Mechanisms of Nucleophilic Attack at Silicon. in *PATAI'S Chemistry of Functional Groups* (ed. Rappoport, Z.) (John Wiley & Sons, Ltd, 2009). doi:10.1002/9780470682531.pat0171.

136. Hammond, G. S. A Correlation of Reaction Rates. *J. Am. Chem. Soc.* **77**, 334–338 (1955).

137. Leffler, J. E. Parameters for the Description of Transition States. *Science* **117**, 340–341 (1953).

138. Haddon, R. C., Tian, Z. & Jiang, D. Comparative Reaction Diagrams for the S_N2 Reaction Formulated According to the Leffler Analysis and the Hammond Postulate. *J. Org. Chem.* **81**, 3648–3653 (2016).

139. Galego, J., Garcia-Vidal, F. J. & Feist, J. Suppressing photochemical reactions with quantized light fields. *Nat. Commun.* **7**, (2016).

140. Galego, J., Garcia-Vidal, F. J. & Feist, J. Many-Molecule Reaction Triggered by a Single Photon in Polaritonic Chemistry. *Phys. Rev. Lett.* **119**, (2017).

141. Knunyants, I. L. & Krasuskaya, M. P. Hexafluoroisopropyl alcohol. 25 (1960).

142. Bégué, J.-P., Bonnet-Delpon, D. & Crousse, B. Fluorinated Alcohols: A New Medium for Selective and Clean Reaction. *Synlett* 18–29 (2004) doi:10.1055/s-2003-44973.

143. Phillips, A. J. 1,1,1,3,3,3-Hexafluoro-2-propanol. in *Encyclopedia of Reagents for Organic Synthesis* (ed. John Wiley & Sons, Ltd) (John Wiley & Sons, Ltd, 2010). doi:10.1002/047084289X.rn01164.

144. Hallett-Tapley, G., Cozens, F. L. & Schepp, N. P. Absolute reactivity of arylallyl carbocations. *J. Phys. Org. Chem.* **22**, 343–348 (2009).

145. Ammer, J. & Mayr, H. Solvent nucleophilicities of hexafluoroisopropanol/water mixtures. *J. Phys. Org. Chem.* **26**, 59–63 (2013).

146. Berkessel, A., Adrio, J. A., Hüttenhain, D. & Neudörfl, J. M. Unveiling the "Booster Effect" of Fluorinated Alcohol Solvents: Aggregation-Induced Conformational Changes and Cooperatively Enhanced H-Bonding. *J. Am. Chem. Soc.* **128**, 8421–8426 (2006).

147. Sawyer, D. T., Sobkowiak, A., Roberts, J. L. & Sawyer, D. T. *Electrochemistry for chemists*. (Wiley, 1995).

148. Ayata, S., Stefanova, A., Ernst, S. & Baltruschat, H. The electro-oxidation of water and

alcohols at BDD in hexafluoroisopropanol. *J. Electroanal. Chem.* **701**, 1–6 (2013).

149. Adams, A. M. & Du Bois, J. Organocatalytic C–H hydroxylation with Oxone® enabled by an aqueous fluoroalcohol solvent system. *Chem Sci* **5**, 656–659 (2014).

150. Mfuh, A. M., Doyle, J. D., Chhetri, B., Arman, H. D. & Larionov, O. V. Scalable, Metal- and Additive-Free, Photoinduced Borylation of Haloarenes and Quaternary Arylammonium Salts. *J. Am. Chem. Soc.* **138**, 2985–2988 (2016).

151. Wencel-Delord, J. & Colobert, F. A remarkable solvent effect of fluorinated alcohols on transition metal catalysed C–H functionalizations. *Org. Chem. Front.* **3**, 394–400 (2016).

152. Dherbassy, Q. *et al.* 1,1,1,3,3,3-Hexafluoroisopropanol as a Remarkable Medium for Atroposelective Sulfoxide-Directed Fujiwara-Moritani Reaction with Acrylates and Styrenes. *Chem. - Eur. J.* **22**, 1735–1743 (2016).

153. Jerhaoui, S., Djukic, J.-P., Wencel-Delord, J. & Colobert, F. Stereoselective Sulfinyl Aniline-Promoted Pd-Catalyzed C−H Arylation and Acetoxylation of Aliphatic Amides. *Chem. - Eur. J.* **23**, 15594–15600 (2017).

154. Jerhaoui, S., Poutrel, P., Djukic, J.-P., Wencel-Delord, J. & Colobert, F. Stereospecific C–H activation as a key step for the asymmetric synthesis of various biologically active cyclopropanes. *Org. Chem. Front.* **5**, 409–414 (2018).

155. Motiwala, H. F. *et al.* Overcoming Product Inhibition in Catalysis of the Intramolecular Schmidt Reaction. *J. Am. Chem. Soc.* **135**, 9000–9009 (2013).

156. Motiwala, H. F., Vekariya, R. H. & Aubé, J. Intramolecular Friedel–Crafts Acylation Reaction Promoted by 1,1,1,3,3,3-Hexafluoro-2-propanol. *Org. Lett.* **17**, 5484–5487 (2015).

157. Ratnikov, M. O., Tumanov, V. V. & Smit, W. A. Lewis Acid Catalyst Free Electrophilic Alkylation of Silicon-Capped π Donors in 1,1,1,3,3,3-Hexafluoro-2-propanol. *Angew. Chem. Int. Ed.* **47**, 9739–9742 (2008).

158. Malakar, C. C., Stas, S., Herrebout, W. & Abbaspour Tehrani, K. Lewis Acid Mediated Vinyl-Transfer Reaction of Alkynes to *N* -Alkylimines by Using the *N* -Alkyl Residue as a Sacrificial Hydrogen Donor. *Chem. - Eur. J.* **19**, 14263–14270 (2013).

159. Kushwaha, K. *et al.* Metal-Free Synthesis of Chlorinated β-Amino Ketones *via* an Unexpected Reaction of Imines with Arylacetylenes in 1,1,1,3,3,3-Hexafluoro-2-propanol. *Adv. Synth. Catal.* **358**, 41–49 (2016).

160. Trillo, P., Baeza, A. & Nájera, C. Fluorinated Alcohols As Promoters for the Metal-Free Direct Substitution Reaction of Allylic Alcohols with Nitrogenated, Silylated, and Carbon Nucleophiles. *J. Org. Chem.* **77**, 7344–7354 (2012).

161. Vuković, V. D., Richmond, E., Wolf, E. & Moran, J. Catalytic Friedel-Crafts Reactions of

Highly Electronically Deactivated Benzylic Alcohols. *Angew. Chem. Int. Ed.* **56**, 3085–3089 (2017).

162. Champagne, P. A., Benhassine, Y., Desroches, J. & Paquin, J.-F. Friedel-Crafts Reaction of Benzyl Fluorides: Selective Activation of C F Bonds as Enabled by Hydrogen Bonding. *Angew. Chem. Int. Ed.* **53**, 13835–13839 (2014).

163. Ratnikov, M. O., Tumanov, V. V. & Smit, W. A. Elaboration of a Lewis acid-free protocol for the alkylation of silicon-containing π-donors by β-arylthioalkyl chlorides. *Tetrahedron* **66**, 1832–1836 (2010).

164. Denmark, S. E., Burk, M. T. & Hoover, A. J. On the Absolute Configurational Stability of Bromonium and Chloronium Ions. *J. Am. Chem. Soc.* **132**, 1232–1233 (2010).

165. Berkessel, A., Andreae, M. R. M., Schmickler, H. & Lex, J. Baeyer–Villiger Oxidations with Hydrogen Peroxide in Fluorinated Alcohols: Lactone Formation by a Nonclassical Mechanism. *Angew. Chem. Int. Ed.* **41**, 4481–4484 (2002).

166. isotopologue. in *IUPAC Compendium of Chemical Terminology* (eds. Nič, M., Jirát, J., Košata, B., Jenkins, A. & McNaught, A.) (IUPAC, 2009). doi:10.1351/goldbook.I03351.

167. *Isotopes in organic chemistry*. (Elsevier Scientific Pub. Co. ; distributors for the U.S. and Canada, Elsevier North-Holland, 1978).

168. Anslyn, E. V. & Dougherty, D. A. *Modern physical organic chemistry*. (University Science, 2006).

169. Turowski, M. *et al.* Deuterium Isotope Effects on Hydrophobic Interactions: The Importance of Dispersion Interactions in the Hydrophobic Phase. *J. Am. Chem. Soc.* **125**, 13836–13849 (2003).

170. *The investigation of organic reactions and their mechanisms*. (Blackwell Pub, 2006).

171. Giagou, T. & Meyer, M. P. Kinetic Isotope Effects in Asymmetric Reactions. *Chem. - Eur. J.* **16**, 10616–10628 (2010).

172. Westaway, K. C. Using kinetic isotope effects to determine the structure of the transition states of SN2 reactions. in *Advances in Physical Organic Chemistry* vol. 41 217–273 (Elsevier, 2006).

173. Wiberg, K. B. The Deuterium Isotope Effect. *Chem. Rev.* **55**, 713–743 (1955).

174. kinetic isotope effect. in *IUPAC Compendium of Chemical Terminology* (eds. Nič, M., Jirát, J., Košata, B., Jenkins, A. & McNaught, A.) (IUPAC, 2009). doi:10.1351/goldbook.K03405.

175. Melander, L. C. S. & Saunders, W. H. *Reaction rates of isotopic molecules*. (Wiley, 1980).

176. Muller, P. Glossary of terms used in physical organic chemistry (IUPAC Recommendations 1994). *Pure Appl. Chem.* **66**, 1077–1184 (1994).

177. Truhlar, D. G. *et al.* The Incorporation of Quantum Effects in Enzyme Kinetics Modeling. *Acc. Chem. Res.* **35**, 341–349 (2002).

178. Van Hook, W. A. Isotope Effect in Chemistry. *Nukleonika* **56**, 217–240 (2011).

179. Laidler, K. J. *Chemical kinetics*. (Harper & Row, 1987).

180. Scheiner, S. & Čuma, M. Relative Stability of Hydrogen and Deuterium Bonds. *J. Am. Chem. Soc.* **118**, 1511–1521 (1996).

181. Shi, C., Zhang, X., Yu, C.-H., Yao, Y.-F. & Zhang, W. Geometric isotope effect of deuteration in a hydrogen-bonded host–guest crystal. *Nat. Commun.* **9**, (2018).

182. Rakić, A. D., Djurišić, A. B., Elazar, J. M. & Majewski, M. L. Optical properties of metallic films for vertical-cavity optoelectronic devices. *Appl. Opt.* **37**, 5271 (1998).

Lucas LETHUILLIER-KARL

TILTING A GROUND-STATE REACTIVITY LANDSCAPE BY VIBRATIONAL STRONG COUPLING

Résumé

La nature de la lumière et des phénomènes qui lui sont associés est l'objet de réflexions intellectuelles et scientifiques depuis l'Antiquité. Très tôt, notre compréhension de la lumière a été associée à l'environnement dans lequel elle se propage. Lorsque l'on s'est rendu compte grâce à la physique quantique que même le vide n'était pas "rien", des modifications de plusieurs propriétés de la matière ont été réalisées simplement en contrôlant son environnement. Le cœur de ce manuscrit de thèse porte sur le couplage vibrationnel fort (VSC). Il s'agit d'une nouvelle approche exploitant les interactions lumière-matière, que nous avons utilisée pour contrôler le déroulement et l'issue de réactions chimiques, en structurant le champ EM à l'intérieur de cavités optiques. Plus particulièrement, un système réactionnel a été élaboré pour démontrer la capacité du VSC à favoriser la formation d'un produit relativement à un autre. De récents résultats préliminaires, obtenus avec un autre système réactionnel, ont également montré que le VSC pourrait être utilisé pour faire de la catalyse en cavité. Ainsi, cette méthode à température ambiante et à champ faible a le potentiel de devenir un outil quotidien pour les chimistes, leur permettant de contrôler physiquement la réactivité chimique sans catalyseurs, sans pré-fonctionnalisation ou changements chimiques dans les conditions de réaction et pourrait également fournir un nouvel outil pour les études mécanistiques.

Mots-clés : Interactions lumière-matière, Couplage vibrationnel fort, Séléctivité de site

Summary

The nature of light has been the subject of intellectual and scientific inquiry since antiquity. Very early on, the conception of light was associated with the environment in which it propagates. When it was realized through quantum physics that even *vacuum* was not "nothing", modifications of several properties of matter were achieved simply by controlling its environment. The core of this thesis manuscript focuses on vibrational strong coupling (VSC). We have used this new approach that harnesses light-matter interactions, in order to control chemical reaction landscapes by structuration of the electromagnetic field inside optical cavities. More precisely, a reaction system was designed to demonstrate the ability of VSC to drive the formation of one product relatively to another. Recent preliminary results, obtained with another reaction system, have also shown that VSC could be used for cavity catalysis. Thus, this weak-field room-temperature method has the potential to become an everyday tool for chemists to physically control chemical reactivity without catalysts, pre-functionalization, or chemical changes to the reaction conditions and could also provide a new tool for mechanistic studies.

Keywords : Light-matter Interactions, Vibrational Strong Coupling, Site-selectivity